IAEA
International Atomic Energy Agency

DOSIMETRY FOR RADIO PHARMA CEUTICAL Therapy

Yuni Dewaraja • Katarina Sjögreen-Gleisner

PRINCIPLES OF DOSIMETRY IN RADIOPHARMACEUTICAL THERAPIES

DOSIMETRY FOR RADIOPHARMACEUTICAL THERAPY

The following States are Members of the International Atomic Energy Agency:

AFGHANISTAN
ALBANIA
ALGERIA
ANGOLA
ANTIGUA AND BARBUDA
ARGENTINA
ARMENIA
AUSTRALIA
AUSTRIA
AZERBAIJAN
BAHAMAS
BAHRAIN
BANGLADESH
BARBADOS
BELARUS
BELGIUM
BELIZE
BENIN
BOLIVIA, PLURINATIONAL STATE OF
BOSNIA AND HERZEGOVINA
BOTSWANA
BRAZIL
BRUNEI DARUSSALAM
BULGARIA
BURKINA FASO
BURUNDI
CABO VERDE
CAMBODIA
CAMEROON
CANADA
CENTRAL AFRICAN REPUBLIC
CHAD
CHILE
CHINA
COLOMBIA
COMOROS
CONGO
COSTA RICA
CÔTE D'IVOIRE
CROATIA
CUBA
CYPRUS
CZECH REPUBLIC
DEMOCRATIC REPUBLIC OF THE CONGO
DENMARK
DJIBOUTI
DOMINICA
DOMINICAN REPUBLIC
ECUADOR
EGYPT
EL SALVADOR
ERITREA
ESTONIA
ESWATINI
ETHIOPIA
FIJI
FINLAND
FRANCE
GABON
GAMBIA
GEORGIA
GERMANY
GHANA
GREECE
GRENADA
GUATEMALA
GUINEA
GUYANA
HAITI
HOLY SEE
HONDURAS
HUNGARY
ICELAND
INDIA
INDONESIA
IRAN, ISLAMIC REPUBLIC OF
IRAQ
IRELAND
ISRAEL
ITALY
JAMAICA
JAPAN
JORDAN
KAZAKHSTAN
KENYA
KOREA, REPUBLIC OF
KUWAIT
KYRGYZSTAN
LAO PEOPLE'S DEMOCRATIC REPUBLIC
LATVIA
LEBANON
LESOTHO
LIBERIA
LIBYA
LIECHTENSTEIN
LITHUANIA
LUXEMBOURG
MADAGASCAR
MALAWI
MALAYSIA
MALI
MALTA
MARSHALL ISLANDS
MAURITANIA
MAURITIUS
MEXICO
MONACO
MONGOLIA
MONTENEGRO
MOROCCO
MOZAMBIQUE
MYANMAR
NAMIBIA
NEPAL
NETHERLANDS, KINGDOM OF THE
NEW ZEALAND
NICARAGUA
NIGER
NIGERIA
NORTH MACEDONIA
NORWAY
OMAN
PAKISTAN
PALAU
PANAMA
PAPUA NEW GUINEA
PARAGUAY
PERU
PHILIPPINES
POLAND
PORTUGAL
QATAR
REPUBLIC OF MOLDOVA
ROMANIA
RUSSIAN FEDERATION
RWANDA
SAINT KITTS AND NEVIS
SAINT LUCIA
SAINT VINCENT AND THE GRENADINES
SAMOA
SAN MARINO
SAUDI ARABIA
SENEGAL
SERBIA
SEYCHELLES
SIERRA LEONE
SINGAPORE
SLOVAKIA
SLOVENIA
SOUTH AFRICA
SPAIN
SRI LANKA
SUDAN
SWEDEN
SWITZERLAND
SYRIAN ARAB REPUBLIC
TAJIKISTAN
THAILAND
TOGO
TONGA
TRINIDAD AND TOBAGO
TUNISIA
TÜRKİYE
TURKMENISTAN
UGANDA
UKRAINE
UNITED ARAB EMIRATES
UNITED KINGDOM OF GREAT BRITAIN AND NORTHERN IRELAND
UNITED REPUBLIC OF TANZANIA
UNITED STATES OF AMERICA
URUGUAY
UZBEKISTAN
VANUATU
VENEZUELA, BOLIVARIAN REPUBLIC OF
VIET NAM
YEMEN
ZAMBIA
ZIMBABWE

The Agency's Statute was approved on 23 October 1956 by the Conference on the Statute of the IAEA held at United Nations Headquarters, New York; it entered into force on 29 July 1957. The Headquarters of the Agency are situated in Vienna. Its principal objective is "to accelerate and enlarge the contribution of atomic energy to peace, health and prosperity throughout the world".

DOSIMETRY FOR RADIOPHARMACEUTICAL THERAPY

YUNI DEWARAJA

KATARINA SJÖGREEN-GLEISNER

INTERNATIONAL ATOMIC ENERGY AGENCY
VIENNA, 2024

COPYRIGHT NOTICE

Marketing and Sales Unit, Publishing Section
International Atomic Energy Agency
Vienna International Centre
PO Box 100
1400 Vienna, Austria
fax: +43 1 26007 22529
tel.: +43 1 2600 22417
email: sales.publications@iaea.org
www.iaea.org/publications

Printed by the IAEA in Austria
April 2024
STI/PUB/2065
https://doi.org/10.61092/iaea.xlzb-6h67

IAEA Library Cataloguing in Publication Data

Names: International Atomic Energy Agency.
Title: Dosimetry for radiopharmaceutical therapy / International Atomic Energy Agency.
Description: Vienna : International Atomic Energy Agency, 2024. | Series: -, ISSN - ; no. - | Includes bibliographical references.
Identifiers: IAEAL 23-01643 | ISBN 978-92-0-139523-8 (paperback : alk. paper) | ISBN 978-92-0-139623-5 (pdf) | 978-92-0-139723-2 (epub)
Subjects: LCSH: | Radiopharmaceuticals — Treatment. | Cancer — Treatment. | Radiation dosimetry.
Classification: UDC 615.849 | STI/PUB/2065

FOREWORD

Radiopharmaceutical therapy consists in the use of unsealed radioactive compounds to deliver a toxic level of radiation to tumour cells or other cells that are functioning in a non-normal manner. It usually involves the use of radiopharmaceuticals that target cancer cells by a broad array of physiologic and biochemical mechanisms, but also includes, for example, local delivery of radioactive substances by intra-arterial or intra-articular injections. The efficacy of the therapy depends upon the energy absorbed in the diseased tissue from the radiation emitted by the radionuclide. Similarly, its toxicity is determined by the level of radiation exposure to other radiosensitive tissues. Nuclear medicine provides a unique opportunity to assess the biodistribution of these agents and use this information to evaluate the absorbed dose to tumours and normal tissues, enabling a treatment approach based on dosimetry considerations.

This book aspires to cover the principles of dosimetry in radiopharmaceutical therapy that are common to different therapies performed in nuclear medicine. It will be followed by other publications addressing in more detail the dosimetry aspects of specific radiopharmaceutical therapies. The aim is to fill the existing gaps in education and training of medical physicists on methods for patient-specific dosimetry. The target audience are clinical medical physicists who are responsible for radiation dosimetry for treatment of patients, as well as nuclear medicine physicians performing radiopharmaceutical therapy and other interested health professionals.

The book has been developed by the drafting committee based on the discussions and recommendations raised during three meetings held at the IAEA headquarters in Vienna over a period of four years. The IAEA wishes to thank the American Association of Physicists in Medicine (AAPM), the European Federation of Organizations for Medical Physics (EFOMP), the European Association of Nuclear Medicine (EANM) and the Society of Nuclear Medicine and Molecular Imaging (SNMMI), which supported these meetings through their representatives. This publication has been endorsed by AAPM, EFOMP, EANM and SNMMI.

The IAEA is also grateful for the important contribution of the international experts that drafted and reviewed the 11 chapters of this book. The main authors of each chapter are listed at the beginning of the chapter. The following international experts are gratefully acknowledged for their broad review of this book as technical editors: Y. Dewaraja (United States of America) and K. Sjögreen-Gleisner (Sweden). The IAEA officers responsible for this publication were G.L. Poli and P. Knoll of the Division of Human Health.

PREFACE

Radiopharmaceutical therapy involves the use of radioactive compounds to expose tumour cells to lethal radiation levels by local delivery or using pharmacological mechanisms to concentrate the radionuclide or radiolabelled carrier to a particular target cell population. It is a form of radiation therapy that uses ionizing radiation to kill cancer cells and shrink tumours by damaging the cells' deoxyribonucleic acid (DNA), thereby stopping these cells from continuing to grow and divide. This kind of radiation therapy often makes use of radiopharmaceuticals, consisting of radioactive atoms combined with cell targeting molecules, which can be injected into the patient's bloodstream to deliver radiation directly to or near disease sites. The delivery of the radioactive compounds can also be accomplished by local delivery, via intra-arterial or intra-articular injections. For this publication the term radiopharmaceutical therapy was adopted, although the therapy modality currently runs under several names, such as molecular radiotherapy, radionuclide therapy or endoradiotherapy.

Currently, in many different pharmacological therapies, considerable effort is being made towards more efficacious and safe treatment with an individualized approach. In this context, radiopharmaceutical therapy has a unique advantage in that the emitted radiation, combined with imaging or other measurement techniques, allows for a detailed determination of the biodistribution of the injected therapy agent and the delivered absorbed doses. The agent responsible for the biologic effect can thus be followed in real time, in the individual patient being treated, to a spatial detail that is relevant for interpreting the biologic effects. Furthermore, a tracer quantity of the therapy agent or an imaging analogue can be administered prior to therapy to predict the biodistribution and the delivered absorbed doses from the subsequent therapeutic administration. This offers a tremendous possibility for arriving at absorbed dose estimates that are relevant for understanding patient treatment outcomes and opens the possibility of a dosimetry guided treatment approach. Indeed, such information is not available in any other kind of systemic cancer therapy. However, this unique feature of radiopharmaceutical therapy is typically not exploited; instead, patients are in most cases treated without any imaging or dosimetry (i.e. without utilizing this possibility for a personalized treatment approach).

The IAEA International Basic Safety Standards require the optimization of protection and safety for each medical exposure, including the administration of radiopharmaceuticals for therapeutic purposes. These standards establish that for radiopharmaceutical therapy the type and activity of the radiopharmaceuticals administered to each patient have to be appropriate. However, in current clinical practice, therapeutic radiopharmaceuticals are administered at standard fixed activities (in some cases with adjustments made empirically, or for body weight

or body surface area), despite the fact that it is well known that the administered activity is not a good predictor of the outcome of the treatment. A fundamental tenet of radiation therapy is the association between radiation absorbed dose and radiobiological effects. Thus, toxicity in therapeutic nuclear medicine is expected to be dependent upon the absorbed dose to critical organs and the efficacy of the treatment is expected to be related to the absorbed dose received by malignant tissue tissues. Once robust dose–effect relationships are established, pretreatment estimation of the absorbed doses received by organs at risk and target tissues would allow for therapy planning based on an accurate prediction of toxicity and efficacy of the treatment. The dosimetry calculations performed in this context should account for patient to patient variation in pharmacokinetics and anatomy.

There are many reasons why currently dosimetry is not widely applied or recognized to be a fundamental part of radiopharmaceutical therapy. Dosimetry methods are often considered too complicated — providing results with high uncertainties — and may entail an increased burden on patient management. Moreover, there are no internationally recognized standard methods for calibrating or implementing radiopharmaceutical therapy dosimetry in the clinic. Another reason for not adopting dosimetry methods is the presumed lack of evidence of the absorbed dose–effect relationship, albeit several studies indicate a correlation between the absorbed doses delivered and the response and toxicity. The scientifically demonstrated correlation strongly suggests that dosimetry could be used to guide personalized treatments for an improved patient outcome.

The field of radiopharmaceutical therapy is rapidly changing with research and development of new agents and delivery mechanisms, such as nanotechnology. In parallel, practical tools for performing quantitative imaging based dosimetry, including at the voxel level, are constantly progressing with advances in computational power and machine learning. Progress has been made towards standardization, assessment of uncertainty and traceability. These are essential components to the implementation of dosimetry driven treatment planning. Without these elements, the clinical benefits of radiopharmaceutical therapy treatment planning will not be uniformly assured. Radiobiology is integral to translating absorbed dose to biologic effects (i.e. for treatment planning). Implementation of dosimetry in radiopharmaceutical therapy will not resemble dosimetry in radiotherapy. The diversity of targeting agents, radionuclides and the corresponding variability in dosimetry methods do not make radiopharmaceutical therapy dosimetry amenable to a one size fits all approach. Accordingly, having described a ‘platform’ review of dosimetry methods, this publication will be followed by a series of individual publications that build upon this platform and that describe, in a short, prescriptive manner, recommended dosimetry methodologies for the many radiopharmaceutical therapy agents that are on the horizon.

The IAEA has a long tradition of producing and supporting guidance documents in medical areas that require medical physics support. In 2014, IAEA Human Health Reports No. 9, Quantitative Nuclear Medicine Imaging: Concepts, Requirements and Methods, was published to advise on methods for accurate activity distribution measurements to support patient-specific dosimetry. The role of clinically qualified medical physicists as key members of the clinical team has been emphasized in several IAEA guidance documents. This publication is intended for clinical medical physicists working in nuclear medicine who are responsible for performing the tasks associated with dosimetry in radiopharmaceutical therapy. It will also serve as a resource for other interested health professionals such as, for example, clinicians, radiochemists and medical technologists who would like to familiarize themselves with the general elements of a standardized approach to dosimetry based personalized treatment.

The overall objective of this publication is to highlight the tools and methodologies available to help ensure that radiopharmaceutical therapy is not implemented as if it is 'radioactive chemotherapy'. Medical physicists, together with other health professionals, need to set up a framework on feasible and affordable methods to ensure that radiopharmaceutical therapy is implemented through a dosimetry guided individualized treatment approach, making clear what equipment and resources are needed. This publication will be beneficial in the international recognition of standardized procedures for dosimetry in radiopharmaceutical therapy, which is a multistep procedure, where each step is essential to obtain an accurate estimate of the absorbed dose delivered to one or more malignant or normal tissues. This publication describes the basic principles of radiation physics, imaging and non-imaging instrumentation used, measurement of the administered activity, calibration procedures and methods for obtaining quantitative information on the biodistribution of the radioactive drug, with a focus on the specific approaches to be used with radioisotopes relevant to therapy. It also describes methods for image segmentation and registration of images acquired at different time points, strategies for fitting and integrating activity measurements over the time of treatment, absorbed dose calculation and derived dosimetry indexes with methods to estimate the overall uncertainty. The publication addresses radiobiological considerations that are specific to radiopharmaceutical therapy, including radiobiological indexes. Moreover, the main radiopharmaceutical therapies are presented from a clinical point of view, with focus on the potential impact of a dosimetry approach to therapy. This is a timely publication, considering the recent renewed interest in radiopharmaceutical therapy with multiple new agents approved for clinical practice or undergoing clinical trial. This includes ^{177}Lu labelled therapies for neuroendocrine tumours and prostate cancer and alpha emitter labelled therapies under development for different malignancies. Furthermore, there is added relevance considering the

recent directive of the European Union that for **all** radiotherapy procedures, including radiopharmaceutical therapy, the exposures should be individually planned and verified.

The authors of this book, selected for their experience and in recognition of their contributions to the field, were drawn from around the world and thus this book represents a truly international collaboration. We would like to thank each one of them for their important contribution.

Y. Dewaraja,
P. Knoll,
G.L. Poli,
K. Sjögreen-Gleisner

CONTENTS

Chapter 1

INTRODUCTION

G. SGOUROS, K. SJÖGREEN-GLEISNER, M. KONIJNENBERG, V. SMYTH

Radiopharmaceutical therapy (RPT) may be broadly defined as the use of radionuclides to deliver lethal radiation to tumour cells or other cells that are not functioning normally, such as those of the thyroid gland. In contrast to brachytherapy, in which radiation delivery is controlled by implantation of radionuclides that are sealed in seeds or capsules intended to avoid release of the radionuclide, radiation delivery in RPT involves the use of pharmaceuticals that either bind specifically to tumours or that accumulate by means of a broad array of physiologic mechanisms. In patients who are ineligible for chemo-refractory and external beam radiation therapy (EBRT), RPT offers viable treatment options where none otherwise exist. RPT has yielded durable responses in heavily pretreated, refractory populations [1.1–1.5]. In castrate-resistant metastatic prostate cancer, RPT with the alpha emitter ^{223}Ra has yielded significantly increased survival rates in patients previously considered untreatable [1.6–1.10]. Similarly, promising results have been observed in adult acute myelogenous leukaemia patients treated with antibody-conjugated ^{225}Ac, also an alpha-particle emitter [1.11–1.13]. In Europe, RPT using radiolabelled peptides has demonstrated efficacy in patients with late-stage, neuroendocrine tumours (NETs). Such tumours are substantially more radioresistant than lymphomas and leukaemia. Thousands of patients have benefited from this treatment modality with approximately 25% showing objective tumour responses in the near absence of serious side effects [1.14]. A recent multicentre trial (NETTER-1) rigorously confirmed the benefit of ^{177}Lu RPT for somatostatin-receptor positive patients [1.15] and has led to FDA approval and EMA marketing authorization of Lutathera. In patients whose cancer expresses catecholamine receptors (e.g. NETs such as neuroblastoma and pheochromocytoma), meta-iodobenzylguanidine (mIBG), labelled with ^{131}I, has reduced tumour volumes and the symptoms associated with release of hormones [1.16]. A high specific activity formulation of this RPT has also been approved by the FDA [1.17]. Finally, perhaps the most successful RPT and possibly the most successful systemic cancer therapeutic is radioiodine treatment of differentiated thyroid cancer [1.18, 1.19]. In addition, the treatment of benign thyroid diseases with ^{131}I, which was first proposed in the late 1940s, is still the recommended treatment approach for these patients [1.20].

1.1. DOSIMETRY FOR RADIOPHARMACEUTICAL THERAPY

The efficacy of RPT depends upon delivering a lethal level of radiation to cancer cells while sparing normal cells. The ability to image the biodistribution of RPT agents and use this information to evaluate the absorbed dose to tumours and normal tissues enables a dosimetry-driven treatment planning approach to RPT. The potential advantage of treatment planning as applied to RPT is illustrated in Figs 1.1 and 1.2.

Figure 1.1 shows the red marrow toxicity relative to different potential predictors for a large collection of ^{131}I radioimmunotherapy studies. Studies were selected so that the red marrow absorbed dose was calculated using a consistent methodology [1.21]. The results show that a substantial number of patients could have been treated more aggressively if the red marrow absorbed dose had been used to determine the activity to be administered for therapy. As is evident in Fig. 1.1(c), at red marrow absorbed doses below 1.5 Gy and above 3 Gy, patients experience either low or high platelet toxicity, respectively. Between 1.75 and 3 Gy the biological response is likely dominated by other patient-specific

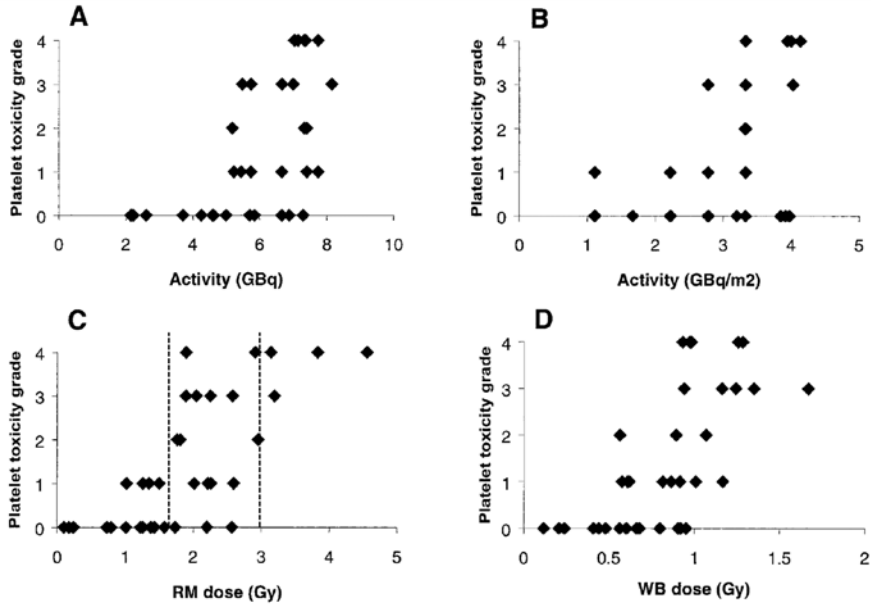

FIG. 1.1. Red marrow (RM) dose-response data for patients treated with different ^{131}I-labelled intact antibodies. Platelet toxicity grade is plotted against (a) administered activity, (b) activity/m^2, (c) red marrow absorbed dose and (d) whole body (WB) absorbed dose (adapted from Ref. [1.21]).

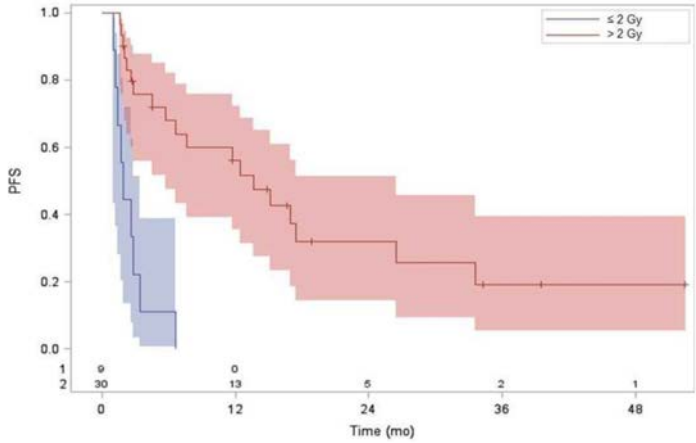

FIG. 1.2. Tumour absorbed dose as a 'biomarker' for progression-free survival. The 2 Gy cut-off value selected is consistent with the known high radiosensitivity of lymphoma [1.23]. Shaded areas represent 95% confidence intervals (adapted from Ref. [1.22], reproduced with permission from Journal of Nuclear Medicine publishing). PFS: progression-free survival.

considerations, such as prior chemotherapy and bone marrow reserve. The figure also highlights the near complete inability to predict toxicity when the administered activity is used as a measure of potential response (Fig. 1.1(a)) while the predictive ability increases as the absorbed dose measures are used (Fig. 1.1(c) and (d)).

Figure 1.2 shows that absorbed dose to tumour can be used as a potential 'biomarker' to identify patients that are more likely to have a longer progression-free survival (PFS) following ^{131}I radioimmunotherapy. The absorbed dose was estimated based on sequential activity measurements from SPECT/CT imaging [1.22]. The median PFS in patients whose tumours received an absorbed dose greater than 2 Gy was 13.6 months; the median PFS for patients whose tumour absorbed dose was less than or equal to 2 Gy was 1.9 months.

Aside from a compromised ability to efficiently identify the tolerable treatment level, selection of administered activity as the escalation variable in phase 1 trials also fails to make the most of a unique opportunity in the development and commercialization of RPT (i.e. to collect critical dose-response data that could much more efficiently guide implementations of the treatment beyond the patient population under study). The evidence base for the use of internal dosimetry was reviewed in [1.24].

The significance of a treatment planning approach to RPT may be understood by comparison with how chemotherapy dose is chosen and administered. Chemotherapy is administered on a per body weight or body

surface area (BSA) basis. Typically, the dose used is obtained from a phase I dose escalation trial in which the dose is escalated until prohibitive toxicity (i.e. the maximum tolerable dose, MTD) is encountered. The MTD is typically defined by the response of a limited number of patients, typically two to four of six patients in a dose group. This MTD is then used to treat all other patients in phase II and subsequent trials. This approach does not account for possible differences in drug clearance, metabolism or pharmacokinetics in different patients. The outcome of such an approach is that patients will either be underdosed (if a dose is chosen to avoid toxicity across most patients) or they will be overdosed and experience toxicity. In RPT it is possible to collect pharmacokinetic and imaging data to calculate tumour and absorbed dose to dose-limiting organs resulting from a particular amount of administered activity. This makes it possible to adjust the administered activity so that the treatment is customized for each patient, to deliver the maximum possible absorbed dose to the tumour while maintaining toxicity at an acceptable level (Fig. 1.3).

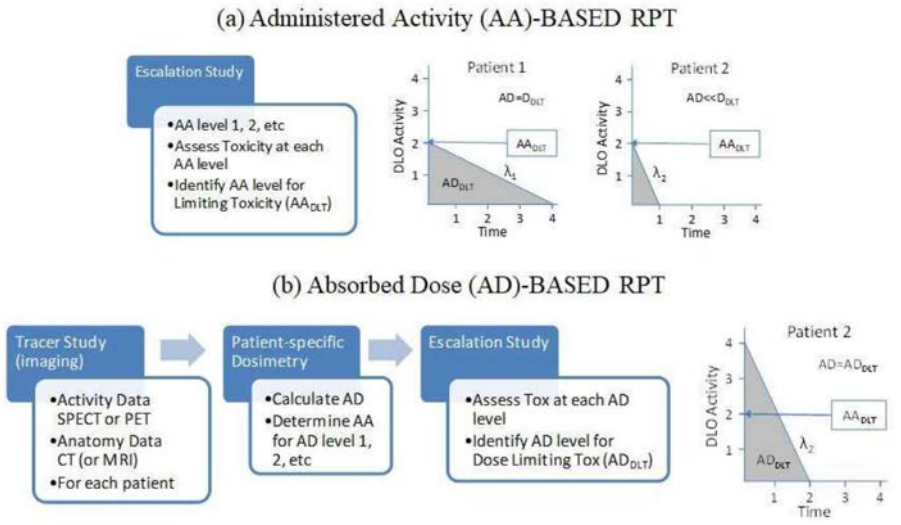

FIG. 1.3. (a) RPT prescription by a previously defined fixed administered activity (AA_{DLT}) may be appropriate for patient 1 but substantially undertreats patient 2, who exhibits more rapid clearance kinetics. In patient 2, the activity corresponding to the dose-limiting organ toxicity is higher than in patient 1. An administered activity based prescription can undertreat or overtreat by not accounting for patient differences in pharmacokinetics (e.g. λ_1 vs λ_2). (b) In absorbed dose based prescriptions, patient-specific dosimetry provides administered activity to deliver AD_{DLT}. This accounts for pharmacokinetic (illustrated here) and other differences among patients (courtesy of G. Sgouros).

FIG. 1.4. Histogram of the activity required to deliver a 0.75 Gy whole body absorbed dose to 634 patients with non-Hodgkin's lymphoma, treated with ^{131}I tositumomab. The figure illustrates the variability in administered activity across a large patient population when treatment is customized to deliver a prescribed absorbed dose to the dose-limiting organ. In the example shown, the most frequently applicable administered activity (~3.7 GBq) would under- or overtreat a substantial fraction of the treated patients. This would be unacceptable in an EBRT setting (adapted from Ref. [1.25]).

Cancer patients will range in age, weight, height and tumour burden. Because of this potential variability, RPT treatment planning is essential to ensure that treatment is appropriate for each individual patient. This concept is well recognized and accepted in EBRT and brachytherapy. It has been implemented for the treatment of non-Hodgkin's lymphoma using ^{131}I-conjugated antibody and whole body absorbed dose as a surrogate for the absorbed dose to marrow, the dose-limiting organ [1.25]. The impact of this approach is illustrated in Fig. 1.4.

1.2. DOSIMETRY FOR DIAGNOSTIC VERSUS THERAPEUTIC PURPOSES

Dosimetry for RPT requires a fundamentally different approach to that used for diagnostic procedures. In diagnostic nuclear medicine, dosimetry is performed for different radiopharmaceuticals to provide estimates of the mean absorbed dose to different organs and the effective dose. These values are primarily intended for radiation protection, to plan and optimize diagnostic procedures in perspective of the risk for cancer induction in the exposed (or imaged) patient population. The effective dose is calculated for a reference person and not an individual, and

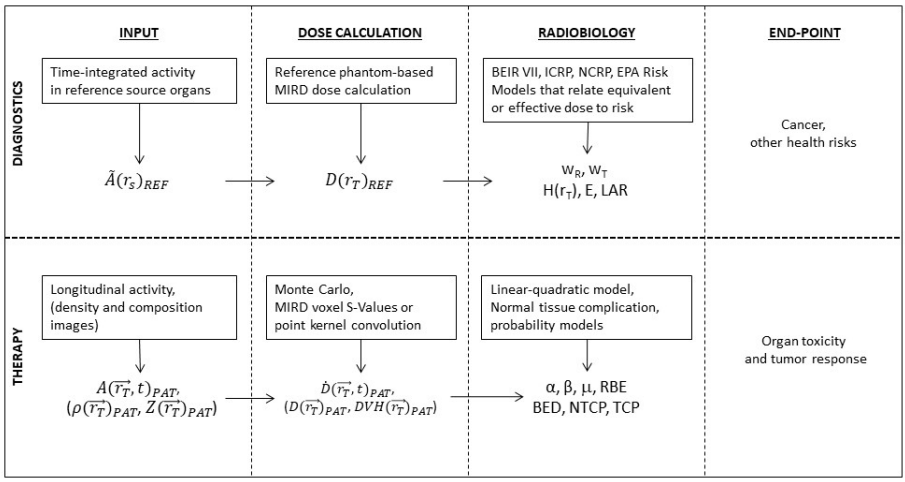

FIG. 1.5. Input, methods and biologic end points for diagnostic dosimetry compared to patient-specific dosimetry for therapy (courtesy of G. Sgouros).

mean organ absorbed doses in a well defined anatomical model, representative of the population, are thus required.

In therapy, the relevant end points are organ toxicity and tumour control for the treated patient. These end points require dosimetry that is considerably more detailed and that focuses on the individual patient instead of using population based estimates. It is well known that the same administered activity can result in different absorbed doses in different patients, mainly due to a variability in the rate of radiopharmaceutical uptake and washout in different organs and tissues, and also in the mass of the relevant target tissues. Such individually varying parameters can be estimated from measurements of the patient being treated.

As shown in Fig. 1.5, a single value, the time-integrated activity in each source organ, is required as input into an absorbed dose calculation for diagnostic imaging for which the end point is the risk of cancer and detriment to health. In contrast, evaluation of therapeutic end points, under some circumstances, could require a series of single photon emission computed tomography (SPECT) or positron emission tomography (PET) images, registered across time, and also a computed tomography (CT) scan. SPECT or PET provide the spatial activity information at different times following injection of the therapeutic radiopharmaceutical, while the CT provides the patient density information required for absorbed dose calculation. Methods to interpret the absorbed dose distribution in terms of radiobiological response may include calculation of the biologically effective dose (BED), normal-tissue complication probability and probability of tumour control. However, the radiobiological models that convert

dosimetry output to organ toxicity and tumour control are still largely based upon experience in external beam radiotherapy and brachytherapy.

TABLE 1.1. DESCRIPTION OF QUANTITIES USED IN FIG. 1.5
(courtesy of G. Sgouros)

Quantity	Description
$\tilde{A}(r_S)_{REF}$	Time-integrated activity in source region, r_S, of a reference anatomical model
$D(r_T)_{REF}$	Absorbed to target region, T, of a reference anatomical model
w_R, w_T	Radiation and tissue weighting factors, respectively
$H(r_T)$, E, LAR	Equivalent dose to target region, T, of a reference model, effective dose to a reference model, lifetime attributable risk
$A(\vec{r}_S,t)_{PAT}$, $\rho(\vec{r}_T)_{PAT}$, $Z(\vec{r}_T)_{PAT}$	Spatio-temporal map of the activity, tissue density and tissue composition (atomic number (Z)-value)
$\dot{D}(\vec{r}_T,t)_{PAT}$, $D(\vec{r}_T)_{PAT}$, $\mathrm{DVH}(\vec{r}_T)_{PAT}$	Spatial map of the absorbed dose rate and absorbed dose, and a dose–volume histogram for a patient-specific tissue volume
α, β	Tissue specific coefficients of radiation damage proportional to dose (single event is lethal) and dose squared (two sublethal events required for lethal damage), respectively
μ, RBE	DNA repair rate assuming exponential repair of DNA damage, relative biological efficacy
BED, NTCP, TCP	Biological effective dose, normal tissue complication probability, tumour control probability

Figure 1.5 and Table 1.1 summarize these concepts. Although the figure depicts dosimetry for therapy as reliant on patient-specific measurements that are represented by a vector to account for the spatial distribution of activity (as

derived from PET or SPECT imaging) within a source region, there are cases in which the spatial distribution may not be needed (e.g. whole body activity measurements over time to approximate red marrow absorbed dose and toxicity).

1.3. DOSIMETRY FOR THERAPY END POINTS

Relevant target tissues are those that are associated with the biological end point and, in principle, it is their volume that should be considered when determining the mean energy imparted and the mass to calculate the mean absorbed dose. Generally, radiopharmaceuticals distribute in the body by molecular mechanisms, and there may be a considerable non-uniformity in their spatial distribution; the non-uniformity may exist on a body-, organ-, sub-organ- or cellular level. The absorbed dose to a sensitive organ structure, to layers of cells, or individual cells can differ significantly from the mean absorbed dose in the whole organ. The degree of non-uniformity in the energy deposition pattern depends both on the distribution of radiopharmaceutical on a small scale, but also on the range of the emitted radiation.

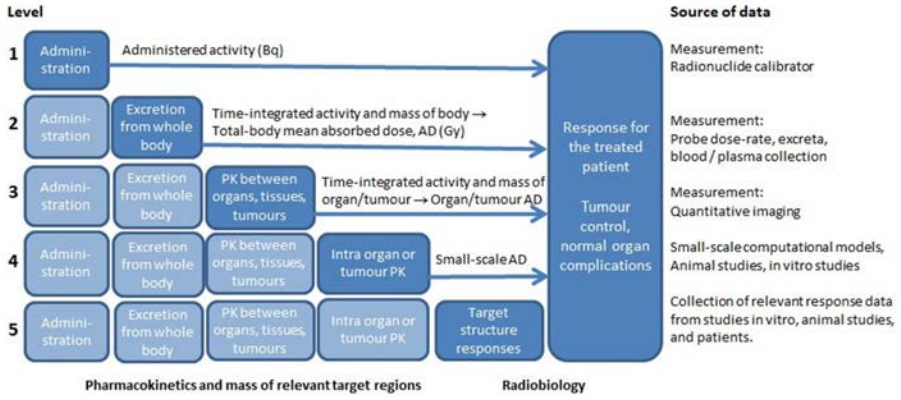

FIG. 1.6. Generalized block scheme of target structures defined on different spatial-scale levels, and the resolution at which the pharmacokinetics (PK), time-integrated activity and masses need to be estimated in order to determine the mean absorbed dose (AD) in Gy. The figure indicates the importance of matching the scale of the calculation to the population of cells most likely to drive toxicity or efficacy, and how a refinement in scale may decrease the gap between the absorbed dose estimates and the relevant target responses. To the right in this figure the techniques available for data collection are indicated, as well as the spatial scales where different kinds of model based estimates become necessary. This figure was inspired by the report, Characterization and Application of Physiologically-based Pharmacokinetic Models in Risk Assessment [1.26] (courtesy of K. Sjögreen-Gleisner).

In order to understand the therapeutic response for normal organs and tumours it is of interest to resolve the non-uniformity in the absorbed dose.

Figure 1.6 is inspired by a report from the World Health Organization [1.26] that mainly relates to risks associated with chemical substances, but which in our context shows how absorbed dose estimates at an increasing spatial resolution may increase the possibility of understanding and describing the treatment responses. Level 1, in which only the administered activity is measured, is included for comparison. This level is still the most commonly applied strategy for clinical RPT (i.e. by administering a fixed level of activity to all patients receiving a particular RPT, possibly modulated based on patient body weight or surface area). However, in terms of its ability to provide information for understanding the relationship between the radiation exposure and the toxic response, this level is probably completely inadequate. Level 2, in which total-body or excreta measurements are included to estimate the total body absorbed dose, is known to provide useful information in some therapies and may in some cases be sufficient. Level 3 includes dosimetry of whole organs or sub-parts of organs whose volume are sufficiently large in comparison to the spatial resolution of the imaging system. This level is in many cases required to provide useful estimates for correlation with the biologic effect, and is regarded to be the highest achievable with currently available macroscopic imaging devices, such as PET/CT or SPECT/CT. Level 4 refers to the redistribution of the radiopharmaceutical for small scale substructures in organs and tumours. This spatial scale is not resolvable on an individual patient level and estimates need to be based on data from animal studies, or possibly from biopsies from patients. Preferably, results of such studies should be generalized using computer modelling tools, such as pharmacokinetic or small scale geometrical models, in order to allow for proper integration and adjustment to patients. Level 5 indicates the estimation of the biologic response. Here, carefully collected animal or in vitro data, and patient data in well controlled, clinical studies are required, which then need to be accompanied by relevant absorbed dose estimates.

1.4. RADIOBIOLOGY

As noted in a 2014 review of radiopharmaceutical therapy [1.27], “[t]he weakest links in both diagnostic and therapeutic dosimetry are the accuracy of the input and the reliability of the radiobiological models used to convert dosimetric data to the relevant biologic end points. Dosimetry for RPT places a greater demand on both of these weak links.”

Examples of these weak links include the estimated distribution of the activity or the target region volumes and the tumour control probability and normal tissue complication probability models and their parameter values.

The linear–quadratic (LQ) model is at the heart of most radiobiological models. The LQ model has been used as the basis for establishing an absorbed dose equivalence between high dose rate 2 Gy per fraction delivery of radiation and the exponentially decreasing dose rate delivery from RPT (e.g. the equivalent dose in 2 Gy fractions (equieffective dose, EQD2) and BED models). It has also been used to account for the effects of non-uniform absorbed dose distributions within tumours (e.g. the tumour control probability (TCP) models) and the potential complication probability to normal tissues resulting from a particular spatial distribution of absorbed dose (e.g. NTCP models). The parameter values for each of these models have typically been obtained from cell or pre-clinical animal model studies, complemented by retrospective analyses of human response to different external beam (or brachytherapy) regimens. These models and their related parameter values have been adopted and used to help guide implementation of RPT. Although both radiotherapy and RPT deliver radiation, their spatial and temporal pattern of delivery are fundamentally different. In the former, delivery is controlled by beam orientation while in the latter, delivery is determined by biologic and physiologic parameters (e.g. target expression on the tumour cells, blood flow to the tumour, penetration depth of the agent). These biologic and physiologic variables are much more difficult to ascertain. Accordingly, radiobiological modelling in RPT requires continued accumulation of dose-response studies to formulate and validate radiobiological models that are confirmed to be relevant to RPT. While these studies are ongoing, continued guidance from external beam radiotherapy is a reasonable approach towards understanding likely absorbed dose versus response but must be implemented with caution, with recognition that delivery of radiation by external beam (or by brachytherapy) is fundamentally different to delivery by RPT.

1.5. TRACEABILITY OF MEASURED DOSIMETRY DATA TO PRIMARY STANDARDS

Dosimetry used in every modality of radiotherapy other than RPT (e.g. external beam, brachytherapy, protons, carbon ions) is based on a system of calibrations, traceable to internationally agreed primary physical standards of absorbed dose. This means that anywhere in the world, if a user follows the agreed calibration and measurement protocol, the obtained absorbed dose values will agree with other users of the same system, within a known tolerance (usually a few per cent). This is essential when the absorbed dose is a critical parameter in

multicentre clinical trials. Broadly speaking, the absorbed dose has not yet been considered an important part of treatment planning in RPT, and so, up until now, there has been no consensus on calibration or measurement protocols to ensure international or even inter-clinic comparability. In RPT the absorbed dose is partly determined by the administered activity and partly by the patient's biokinetics, and measurement is a combination of activity quantification and absorbed dose calculation. This complexity is the other reason for the current lack of a general RPT calibration protocol. Chapter 3 shows how the process of RPT dosimetry can be formulated as a measurement chain and how traceability to primary standards can be achieved. Suggested approaches to standardization of calibration methods are presented. In a recent collaboration between clinical physicists and metrologists [1.28], considerable effort is being made to develop such protocols, with a strong emphasis on traceability to primary standard laboratories.

1.6. STANDARDIZATION OF PATIENT DOSIMETRY PROTOCOLS

Dosimetry standardization is essential for inter-comparability across different institutions, regions and countries. Standardization is also essential to compile consistent dose-response relationships that may be used for radiobiological model development and also to identify model parameters. In a comprehensive evaluation of dose-response data in EBRT [1.29], standardization was identified as the most important requirement in the collection and interpretation of dose-response data [1.30]. The European Association of Nuclear Medicine (EANM) Dosimetry and Medical Internal Radiation Dose (MIRD) committees have published documents related to standardization [1.31–1.33] but greater efforts are required to ensure that these standards are adopted by all physicists performing dosimetry calculations for RPT.

1.7. UNCERTAINTY

Absorbed dose reporting should be accompanied by an assessment of the uncertainty associated with the reported value. A variety of approaches to calculating absorbed dose are available and have been adopted and used to perform patient dosimetry. Some approaches are less accurate than others. The practical implications of requiring an assessment of uncertainty (e.g. in the form of a standard deviation) is that one may easily judge the accuracy of the approach and place it in the context of the uncertainties associated with biological variability. This is particularly important in the reporting of dose versus response data. Chapter 9 on uncertainty analysis describes recently developed guidelines,

along with specific examples on estimating the uncertainty contributions associated with different dosimetry methodologies.

REFERENCES

[1.1] GORDON, L.I., et al., Durable responses after ibritumomab tiuxetan radioimmunotherapy for $CD20^+$ B-cell lymphoma: Long-term follow-up of a phase 1/2 study, Blood **103** 12 (2004) 4429–4431, https://doi.org/10.1182/blood-2003-11-3883

[1.2] WITZIG, T.E., et al., Treatment with ibritumomab tiuxetan radioimmunotherapy in patients with rituximab-refractory follicular non-Hodgkin's lymphoma, J. Clin. Oncol. **20** 15 (2002) 3262–3269, https://doi.org/10.1200/JCO.2002.11.017

[1.3] HORNING, S.J., et al., Efficacy and safety of tositumomab and iodine-131 tositumomab (Bexxar) in B-cell lymphoma, progressive after rituximab, J. Clin. Oncol. **23** 4 (2005) 712–719, https://doi.org/10.1200/JCO.2005.07.040

[1.4] FISHER, R.I., et al., Tositumomab and iodine-131 tositumomab produces durable complete remissions in a subset of heavily pretreated patients with low-grade and transformed non-Hodgkin's lymphomas, J. Clin. Oncol. **23** 30 (2005) 7565–7573, https://doi.org/10.1200/JCO.2004.00.9217

[1.5] KAMINSKI, M.S., et al., Pivotal study of iodine I 131 tositumomab for chemotherapy-refractory low-grade or transformed low-grade B-cell non-Hodgkin's lymphomas, J. Clin. Oncol. **19** 19 (2001) 3918–3928, https://doi.org/10.1200/JCO.2001.19.19.3918

[1.6] NILSSON, S., et al., First clinical experience with alpha-emitting radium-223 in the treatment of skeletal metastases, Clin. Cancer Res. **11** 12 (2005) 4451–4459, https://doi.org/10.1158/1078-0432.CCR-04-2244

[1.7] NILSSON, S., et al., Bone-targeted radium-223 in symptomatic, hormone-refractory prostate cancer: A randomised, multicentre, placebo-controlled phase II study, Lancet Oncol. **8** 7 (2007) 587–594, https://doi.org/10.1016/S1470-2045(07)70147-X

[1.8] NILSSON, S., PARKER, C., BIGGIN, C., BRULAND, O., Clinical experience and radiation safety of the first-in-class alpha-pharmaceutical, Alpharadin (radium-223) in patients with castration-resistant prostate cancer (CRPC) and bone metastases, Int. J. Radiat. Oncol. Biol. Phys. **78** 3 Suppl. 1 (2010) S375–S376, https://doi.org/10.1016/j.ijrobp.2010.07.886

[1.9] PARKER, C., AKSNES, A., HAUGEN, I., BOLSTAD, B., NILSSON, S., Radium-223 chloride, a novel, highly targeted alpha-pharmaceutical for treatment of bone metastases from castration-resistant prostate cancer (CRPC): Hematologic and safety profile with repeated dosing, Ann. Oncol. **21** (2010) 277–278.

[1.10] HENRIKSEN, G., FISHER, D.R., ROESKE, J.C., BRULAND, O.S., LARSEN, R.H., Targeting of osseous sites with alpha-emitting Ra-223: Comparison with the beta-emitter Sr-89 in mice, J. Nucl. Med. **44** 2 (2003) 252–259.

[1.11] ROSENBLAT, T.L., et al., Phase I trial of the targeted alpha-particle nano-generator actinium-225 (^{225}Ac)-HuM195 (Anti-CD33) in acute myeloid leukemia (AML), Blood **110** 11 (2007) 910, https://doi.org/10.1182/blood.V110.11.910.910

[1.12] ROSENBLAT, T.L., et al., Sequential cytarabine and alpha-particle immunotherapy with bismuth-213-lintuzumab (HuM195) for acute myeloid leukemia, Clin. Cancer Res. **16** 21 (2010) 5303–5311, https://doi.org/10.1158/1078-0432.CCR-10-0382

[1.13] JURCIC, J.G., et al., Targeted alpha-particle immunotherapy for myeloid leukemia, Blood **100** 4 (2002) 1233–1239, https://doi.org/10.1182/blood.V100.4.1233.h81602001233_1233_1239

[1.14] AMBROSINI, V., FANI, M., FANTI, S., FORRER, F., MAECKE, H.R., Radiopeptide imaging and therapy in Europe, J. Nucl. Med. **52** Suppl. 2 (2011) 42S–55S, https://doi.org/10.2967/jnumed.110.085753

[1.15] STROSBERG, J., et al., Phase 3 trial of ^{177}Lu-dotatate for midgut neuroendocrine tumors, N. Engl. J. Med. **376** 2 (2017) 125–135, https://doi.org/10.1056/NEJMoa1607427

[1.16] SISSON, J.C., et al., Radiation safety in the treatment of patients with thyroid diseases by radioiodine 131I: Practice recommendations of the American Thyroid Association, Thyroid **21** 4 (2011) 335–346, https://doi.org/10.1089/thy.2010.0403

[1.17] SHARP, S.E., TROUT, A.T., WEISS, B.D., GELFAND, M.J., MIBG in neuroblastoma diagnostic imaging and therapy, Radiographics **36** 1 (2016) 258–278, https://doi.org/10.1148/rg.2016150099

[1.18] MAZZAFERRI, E.L., JHIANG, S.M., Long-term impact of initial surgical and medical therapy of papillary and follicular thyroid cancer, Am. J. Med. **97** 5 (1994) 418–428, https://doi.org/10.1016/0002-9343(94)90321-2

[1.19] HUNDAHL, S.A., FLEMING, I.D., FREMGEN, A.M., MENCK, H.R., A national cancer data base report on 53,856 cases of thyroid carcinoma treated in the U.S., 1985–1995, Cancer **83** 12 (1998) 2638–2648, https://doi.org/10.1002/(SICI)1097-0142(19981215)83:12%3C2638::AID-CNCR31%3E3.0.CO;2-1

[1.20] STOKKEL, M.P., HANDKIEWICZ JUNAK, D., LASSMANN, M., DIETLEIN, M., LUSTER, M., EANM procedure guidelines for therapy of benign thyroid disease, Eur. J. Nucl. Med. Mol. Imaging **37** 11 (2010) 2218–2228, https://doi.org/10.1007/s00259-010-1536-8

[1.21] O'DONOGHUE, J.A., et al., Hematologic toxicity in radioimmunotherapy: Dose-response relationships for I-131 labeled antibody therapy, Cancer Biother. Radiopharm. **17** 4 (2002) 435–443, https://doi.org/10.1089/108497802760363222

[1.22] DEWARAJA, Y.K., et al., Tumor-absorbed dose predicts progression-free survival following ^{131}I-tositumomab radioimmunotherapy, J. Nucl. Med. **55** 7 (2014) 1047–1053, https://doi.org/10.2967/jnumed.113.136044

[1.23] FERTIL, B., MALAISE, E.P., Intrinsic radiosensitivity of human cell lines is correlated with radioresponsiveness of human tumors: Analysis of 101 published survival curves, Int. J. Radiat. Oncol. Biol. Phys. **11** 9 (1985) 1699–1707, https://doi.org/10.1016/0360-3016(85)90223-8

[1.24] STRIGARI, L., et al., The evidence base for the use of internal dosimetry in the clinical practice of molecular radiotherapy, Eur. J. Nucl. Med. Mol. Imaging **41** 10 (2014) 1976–1988, https://doi.org/10.1007/s00259-014-2824-5

[1.25] WAHL, R.L., The clinical importance of dosimetry in radioimmunotherapy with tositumomab and iodine I 131 tositumomab, Semin. Oncol. **30** 2 Suppl. 4 (2003) 31–38, https://doi.org/10.1053/sonc.2003.23799

[1.26] WORLD HEALTH ORGANIZATION, INTERNATIONAL LABOUR ORGANIZATION, UNITED NATIONS ENVIRONMENT PROGRAMME, Characterization and application of physiologically based pharmacokinetic models in risk assessment, Harmonization Project Document No. 9, WHO, Geneva (2010).

[1.27] SGOUROS, G., HOBBS, R.F., Dosimetry for radiopharmaceutical therapy, Semin. Nucl. Med. **44** 3 (2014) 172–178, https://doi.org/10.1053/j.semnuclmed.2014.03.007

[1.28] Metrology for Clinical Implementation of Dosimetry in Molecular Radiotherapy, http://mrtdosimetry-empir.eu

[1.29] BENTZEN, S.M., et al., Quantitative analyses of normal tissue effects in the clinic (QUANTEC): An introduction to the scientific issues, Int. J. Radiat. Oncol. Biol. Phys. **76** 3 Suppl. 1 (2010) S3–S9, https://doi.org/10.1016/j.ijrobp.2009.09.040

[1.30] DEASY, J.O., et al., Improving normal tissue complication probability models: The need to adopt a "data-pooling" culture, Int. J. Radiat. Oncol. Biol. Phys. **76** 3 Suppl. (2010) S151–S154, https://doi.org/10.1016/j.ijrobp.2009.06.094

[1.31] HÄNSCHEID, H., et al., EANM Dosimetry Committee series on standard operational procedures for pre-therapeutic dosimetry II. Dosimetry prior to radioiodine therapy of benign thyroid diseases, Eur. J. Nucl. Med. Mol. Imaging **40** 7 (2013) 1126–1134, https://doi.org/10.1007/s00259-013-2387-x

[1.32] LASSMANN, M., CHIESA, C., FLUX, G., BARDIÈS, M., EANM Dosimetry Committee guidance document: Good practice of clinical dosimetry reporting, Eur. J. Nucl. Med. Mol. Imaging **38** 1 (2011) 192–200, https://doi.org/10.1007/s00259-010-1549-3

[1.33] LONSDALE, M.N., LASSMANN, M., EANM perspective, Radiat. Prot. Dosim. **153** 2 (2013) 166–169, https://doi.org/10.1093/rpd/ncs293

Chapter 2

PHYSICS

K. SJÖGREEN-GLEISNER, A. CELLER, M. MADSEN, B. ZIMMERMAN

The absorbed doses delivered by internally distributed radiopharmaceuticals are the result of emissions emanating from radioactive decay of the radionuclide. The emitted photons and charged particles interact with the tissue, and deposit energy, resulting in excitations and ionizations of atoms. These initiate chemical reactions that may affect sensitive biomolecules such as deoxyribonucleic acid (DNA). The DNA damage may occur either via direct interaction or be mediated by reactive oxygen species generated by radiolysis of water in tissue. Thus, information about the number of radioactive atoms that are present in organs and tissues combined with information about their emissions are both necessary to determine the absorbed doses delivered and the radiobiological effects obtained in radiopharmaceutical therapy (RPT).

There are two types of radioactive emissions — particles (alphas, electrons, positrons, neutrinos and antineutrinos) and electromagnetic radiation (gamma and X ray emissions) — and they can originate from the atomic shells and/or from the nucleus itself. A short discussion of the emissions that are most relevant to RPT follows.

2.1. RADIOACTIVE DECAY

Radioactive decay is the process by which an unstable atomic nucleus loses its excess energy through the emission of radiation. Except for gamma decay or internal conversion from an excited state, the progeny is a chemical element different from the parent radionuclide (i.e. the number of protons in the nucleus changes as a result of radioactive decay). The rate of decay is governed by the radionuclide-specific probability of decay per unit time and is characterized by the decay constant λ. The quantity **activity** describes the number of decays that occur per unit time, with the SI derived unit becquerel (Bq) corresponding to one decay per second. For a source with an initial number of radioactive atoms, N_0, corresponding to the activity A_0, the activity A(t) that remains after time t can be calculated from the following equation:

$$A(t) = \lambda \cdot N_0 \cdot \exp(-\lambda t) = A_0 \cdot \exp(-\lambda t) \tag{2.1}$$

The half-life of a radionuclide, $T_{1/2}$, is the time required to reduce the number of radioactive nuclei in a sample (or sample activity), to half the initial value (i.e. $T_{1/2} = \ln(2)/\lambda$).

In RPT, in addition to radioactive decay, there are also biological and physiological processes that redistribute the radiopharmaceutical and thus the radioactive atoms in the patient's body. Most often, such processes can also be described in terms of exponential functions, and the effective half-life, T_{eff}, is then governed by the combination of the nuclear (in this context called 'physical') and biological half-lives. The effective half-life for an organ for which there is a biological disappearance of the radioactive material with a half-life of T_{biol}, can be calculated using the following formula:

$$\frac{1}{T_{eff}} = \frac{1}{T_{phys}} + \frac{1}{T_{biol}} \tag{2.2}$$

2.2. RADIONUCLIDE EMISSIONS

Radionuclides used in RPT may emit radiation through processes such as alpha decay, beta decay, electron capture and isomeric transition. These decay modes result in emissions of alpha particles, beta particles, gamma photons, internal conversion electrons, characteristic X rays and Auger electrons. The type, energy and yield of the emitted radiation depends on the radionuclide.

2.2.1. Alpha decay and alpha particles

Alpha particles are helium nuclei that are generally emitted from heavy radioactive nuclides (A > 200). The emission energy spectrum of alpha particles is always discrete, with energies typically of the order of a few MeV.

2.2.2. Beta decay

Beta particles are electrons (β^-) or positrons (β^+) emitted as part of the radioactive decay in which a neutron is changed into a proton (with an electron and an antineutrino emission) or a proton is changed into a neutron (with a positron and a neutrino emission). Since in beta decay the total transition energy is shared between a beta particle and a neutrino, the energy spectrum of the emitted beta particles is continuous. Depending on the radionuclide, the maximum beta particle energy ranges from hundreds of keV to several MeV with the mean beta particle energy equal to approximately one third of the maximum energy. For

many beta-decaying radionuclides, the progeny nucleus is left in an exited state and its transition to the ground state causes emission of gamma photons and internal conversion electrons.

2.2.3. Electron capture

Electron capture is a decay process in which one of the atomic electrons (usually from the K or L electron shell) is absorbed by one of the nucleus protons, changing it into a neutron with the emission of a neutrino. After this decay, the atom remains neutral as the captured electron decreases the positive charge of the nucleus by one. As with beta decay, the progeny nucleus may be left in an exited state and its transition to the ground state causes emission of gamma radiation and internal conversion electrons. Additionally, since the vacancy created in the inner shell is filled by an electron from an outer shell, characteristic X rays and Auger electrons are emitted.

2.2.4. Gamma photons and internal conversion electrons

Radioactive decay often leaves the progeny nucleus in an excited state. Its de-excitation occurs with the emission of monoenergetic photons and internal conversion electrons. Internal conversion electrons are inner shell atomic electrons that are ejected from the atom with energies equal to the energy of the associated gamma ray minus the binding energy of the ejected electron. Because the energy of internal conversion electrons is not high, their range is limited, and they contribute only to the locally absorbed radiation energy. In most cases, the contribution to the absorbed dose is small.

2.2.5. Isomeric transition

In situations when the de-excitation of a nucleus involves a quantum mechanically forbidden transition, the excited state persists for a duration much longer than the 10^{-16} s associated with an allowed transition. This is referred to as an isomeric or metastable state. Traditionally, any state with a half-life longer than 10^{-12} s is considered isomeric, although only those with half-lives of the order of several minutes, hours or even days have practical applications in nuclear medicine. A nucleus with such a long half-life is called an isomer and is denoted by a letter ‘m’ next to its atomic number. One example of an isomer is ^{99m}Tc, in which a forbidden transition from a $1/2^-$ excited state to a $9/2^+$ ground state has a half-life of 6 h. The decay of an isomeric state occurs through emission of gamma photons and internal conversion electrons, similar to the decay of any excited state of a nucleus.

2.2.6. Characteristic X rays and Auger electrons

Whenever there is an inner shell atomic vacancy, characteristic X rays and Auger electrons are emitted. Inner shell vacancies occur during electron capture decay and as a result of the emission of internal conversion electrons. Additionally, they may be created as a result of photoelectric absorption or collisions with energetic charged particles. Auger electrons are often emitted in a cascade since the emission of an Auger electron from one shell causes another inner shell vacancy. The probability for Auger emission is higher for low-Z atoms and in this case, the energy of the Auger electrons is typically less than 10 keV, resulting in their very short range. Somewhat unexpectedly, this makes them high linear energy transfer (LET) particles and if they are emitted in the nucleus of a cell, they are associated with enhanced cell killing.

2.2.7. Bremsstrahlung

Bremsstrahlung is electromagnetic radiation (photons) created when charged particles are decelerated in an electric field. Thus, positrons and electrons from beta decay and internal conversion can generate bremsstrahlung radiation as they pass in close proximity to the atomic nuclei of the material they are traversing. Bremsstrahlung spectra are continuous with the maximum energy equal to the energy of the charged particle, and with increasing intensity towards lower energies. Typically, for radionuclides used in RPT, 90–95% of bremsstrahlung photons have energies below 50 keV.

Another source of bremsstrahlung photons is the continuous electromagnetic radiation that accompanies beta and electron capture decay. These photons, referred to as internal bremsstrahlung, are emitted alongside the above mentioned externally generated bremsstrahlung photons [2.1]. Both internal and external bremsstrahlung photons contribute to gamma camera imaging of pure beta emitters such as ^{90}Y.

2.3. RADIONUCLIDE DATA

2.3.1. Evolution and establishment of radionuclide data

The calculation of absorbed dose from radionuclides used in RPT is critically dependent on the radioactive decay properties. Accurate, widely validated decay data are crucial to ensure the accuracy of dosimetry and the safety and effectiveness of these procedures. There are currently two primary repositories of evaluated nuclear decay data. The first of these is the Evaluated

Nuclear Structure Data File (ENSDF), maintained at the National Nuclear Data Center at Brookhaven National Laboratory on behalf of the international Nuclear Structure and Decay Data network [2.2, 2.3]. The second is the Decay Data Evaluation Project (DDEP), maintained at the Laboratoire National Henri Becquerel [2.4, 2.5]. Both of these databases rely on evaluators who are experts in nuclear physics and who review the measurements that form the bases for the tabulated data. While they both provide access to high quality data, the focus of each and the approach taken in their respective evaluations are slightly different. The DDEP focuses primarily on data relevant to the radionuclide metrology community and provides data specifically related to radioactive decay measurement, including X ray and Auger emission energies and probabilities. The data in the ENSDF are focused primarily on nuclear structure and provide comprehensive information about the properties of a particular nucleus, not just those seen in radioactive decay. The ENSDF database is probably the most widely used source of nuclear data in the world, while DDEP is seen as the authoritative source for radioactive decay data, especially by national metrology institutes, who use DDEP data exclusively in their activities.

The data that appear in both ENSDF and DDEP are generally taken from the published peer-reviewed literature and are critically evaluated to determine the weighting factors when calculating a recommended value for a particular data point. Consideration is given to the method used in the measurement, the quality of the data, the magnitude of the uncertainty and the completeness of the uncertainty budget when evaluating any given data set. The individual evaluator's expertise in the field is an important component of the evaluation process.

Coordinating the generation of new nuclear data is done by a number of groups, including the IAEA's Nuclear Data Section (NDS) through a number of coordinated research projects, the International Committee on Radionuclide Metrology (ICRM) and its working groups, and the Nuclear Energy Agency (NEA). These organizations bring researchers and evaluators together to help identify and prioritize needs from all the different user communities.

2.3.2. Radionuclide data for commonly used radionuclides in RPT

Since the purpose of RPT is to deliver radiation energy at an amount that is sufficient to induce a therapeutic effect, the radionuclides are selected such that they emit charged particles (i.e. electrons from beta decay or internal conversion, or alpha particles). Often, radionuclides that emit both charged particles and gamma radiation are preferred, as the gamma emissions enable imaging and measurement of the radionuclide uptake and distribution in the patient after administration. Radionuclides used are selected also based on their physical half-life, which needs to be matched to the pharmacokinetic properties of the

pharmaceutical to which the radionuclide is attached. The physical half-life should be long enough to allow for sufficient radiation energy delivery to the treatment regions once the initial circulation and uptake processes have taken place. On the other hand, it must be short enough not to deliver excessive absorbed doses to radiosensitive normal organs in the patient, and to avoid excessive irradiation of medical personnel and public. Typically, the physical half-life is of the order of days. Table 2.1 provides a list of commonly used electron emitting radionuclides in RPT, their modes of decay and their main emissions.

TABLE 2.1. COMMONLY USED ELECTRON EMITTING RADIONUCLIDES IN RPT, THEIR MODES OF DECAY AND THEIR MAIN EMISSIONS

(data retrieved from Laboratoire National Henri Becquerel, France and National Nuclear Data Center, Brookhaven National Laboratory, USA [2.3, 2.5]; courtesy of K. Sjögreen-Gleisner)

Radio-nuclide	Half-life	Decay mode	Maximum energy of emissions (keV) and probability × 100 *		Energy (keV) and probability × 100 **	Ref.
			Electrons ***	Positrons	Photons	
P-32	14.3 d	β^-	1711 (100%)			[2.5]
Cu-64	12.7 h	β^-, EC, β^+	579 (38%)	653 (18%)	511 (35%)	[2.5]
Cu-67	61.8 h	β^-	468 (22%) 562 (20%)		91 (7%) 93 (16%) 185 (49%)	[2.3]
Ga-67	3.26 d	EC			93 (38%) 185 (21%) 300 (17%) 394 (5%)	[2.5]
Sr-89	50.6 d	β^-	1495 (100%)		909 (0.00956%)	[2.5]
Y-90	2.67 d	β^-	2279 (100%)		511 (0.00638%)	[2.5]
In-111	2.80 d	EC	145 (8%, ce) 219 (5%, ce)		171 (91%) 245 (94%)	[2.5]

TABLE 2.1. COMMONLY USED ELECTRON EMITTING RADIONUCLIDES IN RPT, THEIR MODES OF DECAY AND THEIR MAIN EMISSIONS

(data retrieved from Laboratoire National Henri Becquerel, France and National Nuclear Data Center, Brookhaven National Laboratory, USA [2.3, 2.5]; courtesy of K. Sjögreen-Gleisner) (cont.)

Radio-nuclide	Half-life	Decay mode	Maximum energy of emissions (keV) and probability × 100 *		Energy (keV) and probability × 100 **	Ref.
			Electrons ***	Positrons	Photons	
Sn-117m	14.0 d	IT	127 (66%, ce) 129 (12%, ce) 152 (27%, ce) 155 (6%, ce)		159 (86%)	[2.3]
I-131	8.02 d	β^-	334 (7%) 606 (89%)		80 (3%) 284 (6%) 364 (81%) 637 (7%) 723 (2%)	[2.5]
I-124	4.18 d	EC		1534.9 (12%) 2137.6 (11%)	511 (45%) 603 (63%) 723 (10%) 1691 (11%)	[2.3]
Sm-153	1.93 d	β^-	635 (30%) 705 (49%) 808 (20%)		103 (29%)	[2.5]
Ho-166	26.8 h	β^-	1774 (51%) 1855 (48%)		81 (7%)	[2.5]
Er-169	9.38 d	β^-	345 (44%) 353 (56%)			[2.5]
Lu-177	6.65 d	β^-	101.7 (7%, ce) 177 (12%) 385 (9%) 498 (79%)		113 (6%) 208 (10%)	[2.5]

TABLE 2.1. COMMONLY USED ELECTRON EMITTING RADIONUCLIDES IN RPT, THEIR MODES OF DECAY AND THEIR MAIN EMISSIONS

(data retrieved from Laboratoire National Henri Becquerel, France and National Nuclear Data Center, Brookhaven National Laboratory, USA [2.3, 2.5]; courtesy of K. Sjögreen-Gleisner) (cont.)

Radio-nuclide	Half-life	Decay mode	Maximum energy of emissions (keV) and probability × 100 *		Energy (keV) and probability × 100 **	Ref.
			Electrons ***	Positrons	Photons	
Re-186	3.72 d	EC, β^-	125 (6%, ce) 932 (22%) 1070 (71%)		137 (9%)	[2.5]
Re-188	17.0 h	β^-	143 (6%, ce) 1965 (26%) 2120 (71%)		155 (15%)	[2.5]

Note: IT: isomeric transition; EC: electron capture.

* Listed are those with probability >5% and energy >100 keV.

** Listed are those with energy above approximately 100 keV and the highest occurring probabilities.

*** β particles, unless explicitly stated ce (internal conversion electrons).

Alpha emitters are generally part of a serial decay chain, with emissions from the parent radionuclide as well as its progeny. The decay chain often includes emission of multiple alpha particles, electrons from beta decay, internal conversion and Auger, and photons in the form of gamma radiation and X rays. The energies of alpha particles are typically of the order of 5–6 MeV, and the total energy emitted per radioactive decay is thus considerably higher than for the radionuclides listed in Table 2.1. The most commonly used alpha emitter is ^{223}Ra, for which the decay sequence is illustrated in Fig. 2.1.

Other currently emerging alpha emitters in RPT are, for instance, ^{225}Ac, ^{211}At and ^{227}Th. Figure 2.2 provides an overview of these serial decays.

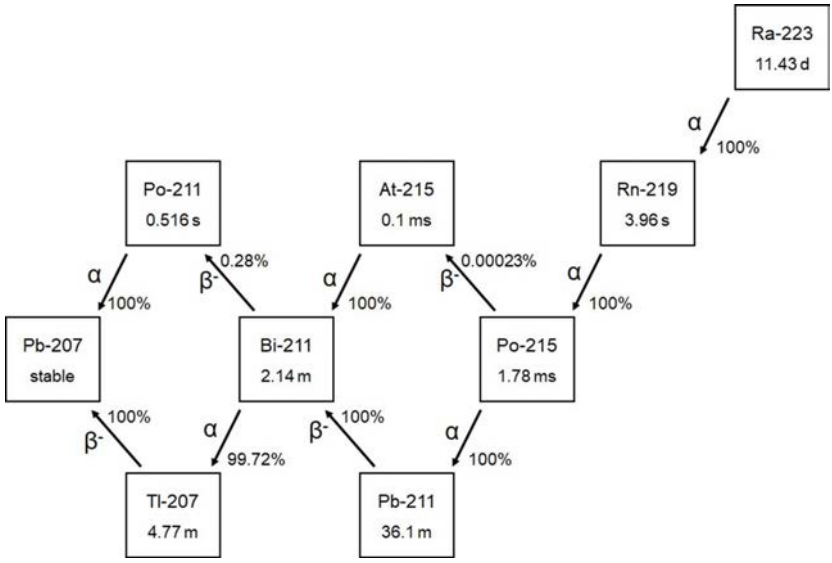

FIG. 2.1. Decay for ^{223}Ra, via its progeny, to the stable radionuclide ^{207}Pb. Courtesy of B.E. Zimmerman.

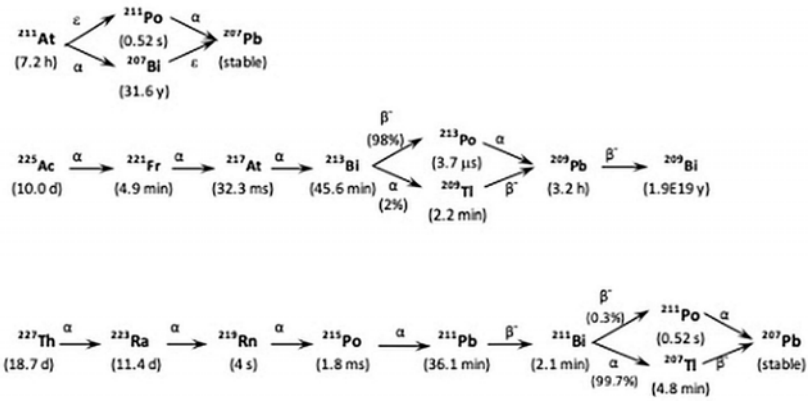

FIG. 2.2. Serial decays of ^{227}Th, ^{211}At and ^{225}Ac. Data retrieved from the National Nuclear Data Center, Brookhaven National Laboratory, USA [2.3]. Courtesy of K. Sjögreen Gleisner.

2.4. INTERACTION AND TRANSPORT OF PHOTONS AND CHARGED PARTICLES IN TISSUE

The interactions of radiation with matter differ between photons and charged particles. Photons can pass through matter without interacting, be totally absorbed or scattered with no or only partial energy deposition. Although photons ionize matter and thus generate a fluence of electrons, they are generally classified as indirectly ionizing because it is the kinetic energy of the subsequent electrons that results in the local energy deposition. Charged particles have a surrounding Coulomb field and will interact with all electrons and nuclei encountered in the material being traversed. Charged particle interactions are therefore classified as directly ionizing.

2.4.1. Photons

In the energy range of relevance for RPT the main interaction mechanisms of photons are photoelectric absorption, Compton scattering and coherent scattering. In the photoelectric effect the total energy of the photon is transferred to an inner shell atomic electron, and as a result an orbital electron is ejected. The probability for this effect depends strongly on the photon energy ($\sim E^{-3.5}$), the atomic number ($\sim Z^{4.5}$) and the mass density of the absorbing medium. In water-like tissues, the photoelectric effect is the dominating interaction for photon energies well below 100 keV. In Compton scattering, a portion of the photon energy is transferred to a loosely bound electron resulting in a secondary photon of altered direction and reduced energy. The probability for Compton scattering is directly proportional to the electron density of the medium, which in most cases is linearly related to its mass density. In coherent scattering, the photon direction changes while its energy remains unchanged, and this process is of some importance for very low photon energies and low-Z materials, such as water-like soft tissue.

The linear attenuation coefficient, μ, describes the probability of photon interaction, per unit thickness of an absorbing material when irradiation and detection are performed under narrow beam conditions. The linear attenuation coefficient can be calculated from the total atomic cross-section for all interaction types and the mass density of the absorbing material and is in units of reciprocal distance. The mass attenuation coefficient is the linear attenuation coefficient normalized to the mass density of the absorbing material, and data of mass attenuation coefficients are made available by the National Institute of Standards and Technology [2.6].

For a narrow beam geometry and an initial number of n_0 photons per second towards a material with linear attenuation coefficient μ [1/cm], the number *n(x)* that are transmitted (i.e. have not interacted) to a depth x [cm] is given by:

$$n(x) = n_0 \cdot \exp(-\mu x) \tag{2.3}$$

As the different interaction mechanisms exhibit energy- and material dependence, so does the value of the linear attenuation coefficient. Figure 2.3 shows examples of the magnitude of attenuation at different depths in water and bone, for a selection of photon energies and Fig. 2.4 shows the linear attenuation coefficient for water as a function of photon energy.

The half-value layer (HVL) is the thickness of material required to reduce a photon intensity to half its initial value. The HVL can be obtained from graphs such as in Fig. 2.3 by determining the depth for a relative intensity of one half (0.5), or be calculated as $HVL = ln(2) / \mu$. Figure 2.4 shows the HVL in water, which is thus approximately between 4 cm and 7 cm for photon energies between 100 keV and 500 keV.

It should be noted that the narrow beam situation is idealized since in practice there is a buildup of photons that have undergone Compton or coherent scattering in the material. For RPT where a photon-emitting radioactive source is situated inside a patient and detection is performed on the outside, these scattered photons will also be detected and add to the intensity of the transmitted

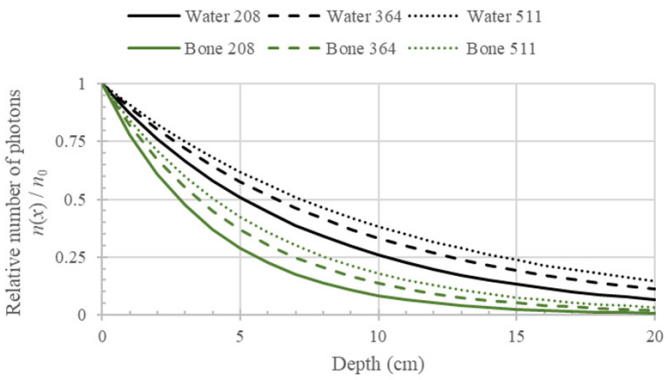

FIG. 2.3. The relative number of photons as a function of depth in water (density 1.0 g/cm^3) indicated by black lines, and cortical bone (density 1.92 g/cm^3) indicated by green lines. Graphs are shown for linear attenuation coefficients for photon energies 208, 364 and 511 keV, representing the main photon emissions from ^{177}Lu, ^{131}I and annihilation radiation from positron emitters. Data underlying the graphs for water and cortical bone (ICRU-44) were retrieved from [2.6]. Courtesy of K. Sjögreen-Gleisner.

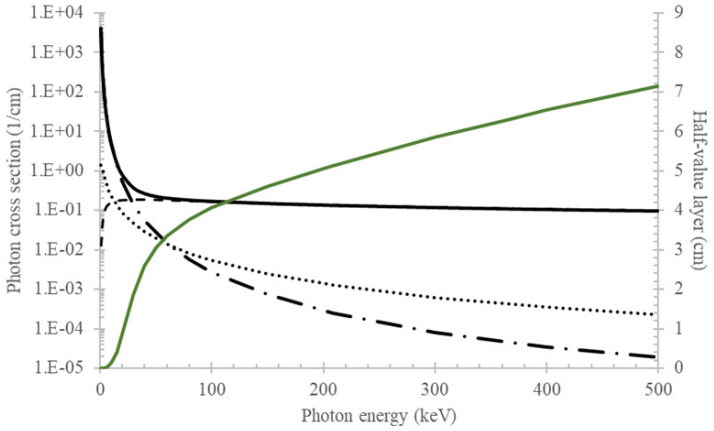

FIG. 2.4. Left hand scale (logarithmic): Photon cross-sections for water (density 1.0 g/cm3) as a function of photon energy. The solid black line is the total photon cross-section (i.e. the linear attenuation coefficient), which is the sum of the cross-sections for photoelectric absorption (dash-dotted line), Compton scattering (dashed line) and coherent scattering (dotted line). Right hand scale (linear) and green line: Half-value layer (i.e. the thickness of water required to reduce the number of photons to half of the initial number). Data underlying the graphs were retrieved from [2.6]. Courtesy of K. Sjögreen-Gleisner.

photons. In RPT, the scattered photons are commonly termed 'scatter', while the photons transmitted under narrow beam conditions are termed 'primary photons' or 'primaries'.

2.4.2. Charged particles

When charged particles such as electrons, positrons and alpha particles pass through tissue they are affected by the Coulomb forces from orbital electrons and atomic nuclei, resulting in excitations, ionizations and radiative energy losses. Because of the small mass of electrons, they have a considerably longer path length and undergo extensively more scattering than the much heavier alpha particles that exhibit comparably straight paths in tissue. While most electron interactions result in small angle scatterings and low energy losses, they can also transfer up to their whole kinetic energy to orbital electrons resulting in large angle scatterings. Positrons lose their kinetic energy in the same way as electrons, but after slowing down and colliding with an electron they annihilate and form two photons (annihilation photons used in PET imaging) emitted in opposite directions, each of energy 511 keV corresponding to the identical rest masses of the electron and the positron. Electrons and positrons also have

much higher probability for energy loss through the emission of bremsstrahlung (radiative energy losses) as compared to heavier charged particles.

Stopping power is a concept used to quantify the average energy loss per path length when charged particles pass through matter [2.7]. There are three contributions to the stopping power, including electronic (or collision), nuclear and radiative stopping power. For electrons and positrons, the nuclear stopping power is negligible, while for alpha particles the radiative stopping power is negligible. When particles pass through tissue, they deposit their kinetic energy along the track, the particle energy decreases and the stopping power typically increases. At the end of a particle track, before the particle stops, there is an increased stopping power called the Bragg peak.

The range of charged particles is characterized by means of the continuous slowing down approximation (CSDA) by the assumption that particles lose kinetic energy continuously along their track with a mean energy loss per path length given by the stopping power [2.7]. Notably, the CSDA range reflects the traversed path length rather than the depth of penetration. For electrons and positrons, which exhibit large angular deflections along their paths, the CSDA range may be considerably larger than the penetration depth along the initial particle direction. Also, since the CSDA range is an average, individual particles can have a much larger or smaller range, in accordance with a statistical distribution. Usually, the stopping power and the CSDA range are normalized to the mass density of the medium, thus forming the mass stopping power and the (mass) CSDA range. Such data are made available by the National Institute of Standards and Technology [2.8].

The linear energy transfer (LET) or more specifically the restricted LET_{Δ}, is a concept used to characterize the ionization density produced by charged particles. LET_{Δ} is defined as the (linear) electronic stopping power subtracted by the mean sum of the kinetic energies in excess of Δ of all the electrons released by the charged particles [2.9]. Energy losses that are below Δ are thus considered to be locally deposited, while energy losses above Δ are considered to be carried away by energetic secondary electrons. LET is of importance in the context of radiobiology, for instance, to understand the relative biological effectiveness (RBE) of different particle types, as further described in Chapter 8.

Figure 2.5 shows the ranges of electrons and alpha particles in water. For beta particles that are considered to be low LET radiation the CSDA range in water is approximately 5 mm/MeV. Because of their higher mass and charge, alpha particles have a high stopping power and short range in tissue (~50 μm in unit density tissue for a 5 MeV alpha particle) and are characterized as high LET particles.

For example, in the β-decay of ^{177}Lu the highest energy of the emitted electrons is 498 keV. This corresponds to a mean energy of 149 keV for which

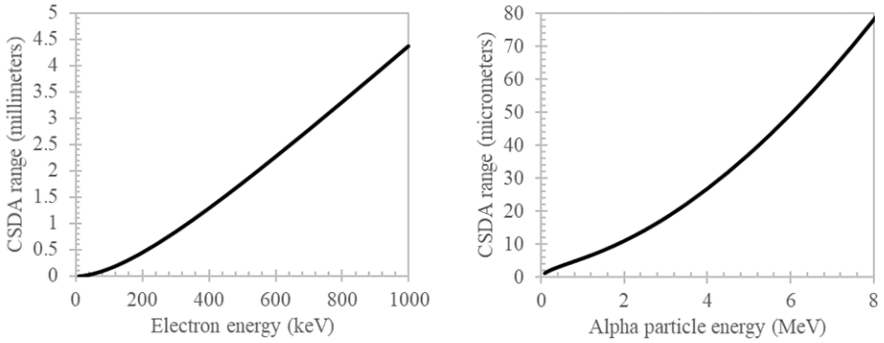

FIG. 2.5. CSDA range in water as a function of energy for electrons (left) and alpha particles (right). Data retrieved from [2.8]. Courtesy of K. Sjögreen-Gleisner.

the CSDA range in water is 0.3 mm. For ^{90}Y with a maximum β^- particle energy of 2279 keV the mean energy is 927 keV for which the CSDA range in water is 4 mm.

2.4.3. Point-source geometry and X_{90} for radionuclide emissions

In RPT, the radionuclides distributed in a patient's body can in many cases be regarded as a collection of point sources and, to a large extent, the distribution of the energy deposition is governed by the geometry. The inverse square law refers to the decreased photon or particle intensity that is obtained when the distance away from a point source increases and can be deduced from the surface of a sphere with a point source located at the centre.

The X_{90} is a concept used to characterize the distribution of the absorbed energy around a radionuclide point source. It is defined as the radius of a sphere in which 90% of the emitted energy from the point source located in the sphere centre is deposited. Calculation of the X_{90} requires Monte Carlo calculations, in which the deposited energy is scored in concentric shells around the point source. Table 2.2. lists CSDA ranges and X_{90} in water calculated for a selection of the electron emitting radionuclides in Table 2.1.

From Table 2.2, it can be noted that the X_{90} is a considerably smaller distance than CSDA range for the maximum electron energy. For instance, for ^{90}Y and ^{188}Re, that have the highest β^- particle energies of those listed, the CSDA range is approximately 1 cm, whereas the X_{90} is only about 4 mm. For RPT, where the radiation energy transport can often be seen as originating from a combination of point sources, the X_{90} is regarded to give a more representative value of the spatial extension of the energy deposited around electron emitters.

TABLE 2.2. CSDA RANGES AND X_{90} VALUES IN WATER FOR A SELECTION OF ELECTRON EMITTING RADIONUCLIDES

(courtesy of K. Sjögreen-Gleisner and M. Bardiès)

Nuclide	CSDA range (mm) for max. energy	X_{90} (mm)
P-32	8.2	3.1
Cu-64	2.2	0.7
Cu-67	2.1	0.4
Sr-89	7.0	2.7
Y-90	11.4	4.6
In-111	0.5	0.3
Sn-117m	0.3	0.2
I-131	2.3	0.6
Sm-153	3.3	0.6
Ho-166	9.0	2.8
Er-169	1.1	0.3
Lu-177	1.8	0.4
Re-186	4.7	1.4
Re-188	10.4	3.7

Note: The CSDA ranges are given for the maximum energy of the emission with the highest energy listed in Table 2.1, retrieved from [2.8]. The X_{90} values were calculated by Monte Carlo simulation, including the energy spectra for beta particles and monoenergetic electrons, kindly provided by M. Bardiès, Cancer Research Institute of Montpellier, France.

2.5. ABSORBED DOSE FOR INTERNALLY DISTRIBUTED RADIONUCLIDES

The absorbed dose is a fundamental quantity used for coupling the energy imparted by ionizing radiation to biologic effects in tissue. Formally, the absorbed dose, D, is defined as the mean energy imparted, $\mathrm{d}\bar{\varepsilon}$, to the matter in an infinitesimal volume, $\mathrm{d}V$, with mass $\mathrm{d}m$ [2.9, 2.10], according to:

$$D = \frac{\mathrm{d}\bar{\varepsilon}}{\mathrm{d}m} \tag{2.4}$$

The unit for the SI derived quantity absorbed dose is the Gray (Gy), with 1 Gy = 1 J/kg. In principle, the absorbed dose is defined at a point, and its value can vary between different regions of an organ or tissue. In RPT, the energy deposition pattern is in most cases non-uniform. The International Commission on Radiological Units and Measurements (ICRU) report 86 [2.11] specifically addresses different situations in which there are non-uniformities in the energy delivery and defines the quantity **mean** absorbed dose, according to:

$$D_{\mathrm{T}} = \frac{1}{m_{\mathrm{T}}} \int_{m_{\mathrm{T}}} D \, \mathrm{d}m \tag{2.5}$$

where m_{T} is the mass of a tissue or organ, or some other target volume for which the absorbed dose is determined [2.11]. Generally, in nuclear medicine applications D_{T} is what is being referred to when discussing an absorbed dose.

The physics of internal dosimetry has been systemized by major organizations, including the ICRU [2.12], the International Commission on Radiological Protection [2.13], the Committee on Medical Internal Radiation Dose (MIRD) and the Radiation Dose Assessment Resource (RADAR) Task Force; the latter two are both part of the Society of Nuclear Medicine and Molecular Imaging [2.14]. These groups approach the physical formulation of estimating absorbed dose in largely the same way but have historically used different nomenclature. In 2009, MIRD Pamphlet No. 21 was published [2.15], with the intent of standardizing the nomenclature (see Table 2.3).

While the ICRU denotes the mean absorbed dose by D_{T}, in the MIRD formalism the same quantity is denoted $D(r_{\mathrm{T}}, T_{\mathrm{D}})$, or $D(r_{\mathrm{T}})$. Thus, following the MIRD schema [2.15] and with notations according to MIRD, the mean absorbed dose to a target region r_{T} is calculated according to:

$$D(r_T) = \frac{1}{M(r_T,t)} \sum_{r_s} \left[\int_0^{T_D} A(r_s,t)\,dt \sum_i \Delta_i \cdot \phi(r_T \leftarrow r_s, E_i, t) \right] \quad (2.6)$$

where $A(r_s, t)$ is the activity in the respective source region r_s at time t. The integral represents the total number of radioactive decays that occur in a given source region and is calculated from the time of administration to the time T_D when the exposure ends, which is most often taken as infinity. This integral is termed the time-integrated activity $\tilde{A}(r_s)$, referred to as cumulated activity in the past.

The factor Δ_i in Eq. (2.6) represents the mean energy emitted from the ith component (alpha, beta, gamma, internal conversion, characteristic X ray or Auger electrons) resulting from the radioactive decay, ϕ is the fraction of the emitted energy that is absorbed in the target region and M is the mass of the target region. In Eq. (2.6), the sum $\sum_i \Delta_i \cdot \phi(r_T \leftarrow r_s, E_i, t)$ represents the mean energy imparted per decay, in turn dependent on the emission spectrum of the radionuclide and the fraction of the emitted energy that is deposited in the target region. The sum over r_s in Eq. (2.6) thus describes the mean energy imparted to a specified target region r_T.

In Eq. (2.6), the terms M, Δ_i and ϕ are often grouped and formulated in terms of the so-called S value, according to:

$$S(r_T \leftarrow r_s, t) = \frac{1}{M(r_T,t)} \sum_i \Delta_i \cdot \phi(r_T \leftarrow r_s, E_i, t) \quad (2.7)$$

The time dependence of the masses, M, and of the absorbed fractions, ϕ, can in most cases be omitted. Thus, Eq. (2.6) can be simplified to the product of the S value and the time-integrated activity, according to:

$$D(r_T) = \sum_{r_s} \tilde{A}(r_s) \cdot S(r_T \leftarrow r_s) \quad (2.8)$$

The S values are specific for each radionuclide and source-target combinations. In principle, the MIRD formalism is valid for any geometry and is not tied to a particular set of S values. However, for practical implementation, S values for uniform distributions of activity located in anthropomorphic geometric models with shapes and masses chosen to mimic the reference manual have been published in numerous pamphlets by the MIRD committee. Such standardized S values are applied for radiation protection purposes, to estimate absorbed doses for populations. For individual patient dosimetry in RPT, the published S values are indeed applicable; however, then the time-integrated activity $\tilde{A}(r_s)$ must be determined for the individual patient, and the reference masses of the target regions r_T must be replaced by an estimate of the target region mass of the

individual patient. In terms of S values this translates into a mass scaling, and Eq. (2.8) becomes:

$$D(r_T) = \frac{M_{ref}(r_T)}{M_{pat}(r_T)} \sum_{r_s} \tilde{A}(r_s) \cdot S(r_T \leftarrow r_s) \tag{2.9}$$

where $M_{ref}(r_T)$ and $M_{pat}(r_T)$ are the masses of the target region for the reference model and patient, respectively. In addition to whole organs, S values have been published for smaller structures, as well as voxels. Details of these calculations will be given in Chapter 7.

Table 2.3 summarizes quantities, units and notations used in the MIRD formalism, for dosimetry of internally distributed radionuclides.

TABLE 2.3. QUANTITIES, UNITS AND NOTATIONS, AS PROVIDED IN REF. [2.15]

(courtesy of K. Sjögreen-Gleisner)

Quantity or parameter	SI derived unit	MIRD 21 notation
Source region		r_S
Target region		r_T
Absorbed dose rate to target region	Gy·s^{-1}	$\dot{D}(r_T,t)$
Activity in source region	Bq	$A(r_S, t)$
Absorbed dose rate per unit activity	Gy·Bq^{-1}·s^{-1}	$S(r_T \leftarrow r_S,t)$
Dose integration period	s	T_D
Absorbed dose to target	Gy	$D(r_T)$ or $D(r_T, T_D)$
Administered activity	Bq	A_0
Source activity fraction		$a(r_S, t) = A(r_S, t)/A_0$
Mean energy of the ith transition	MeV	E_i
Number of ith transition/decay	Bq^{-1}·s^{-1}	Y_i

TABLE 2.3. QUANTITIES, UNITS AND NOTATIONS, AS PROVIDED IN REF. [2.15]

(courtesy of K. Sjögreen-Gleisner) (cont.)

Quantity or parameter	SI derived unit	MIRD 21 notation
Mean energy of *i*th transition/decay	$MeV \cdot Bq^{-1} \cdot s^{-1}$	$\Delta_i = E_i \cdot Y_i$
Mass of target region	kg	$M(r_T, t)$
Absorbed fraction		$\phi(r_T \leftarrow r_S, E_i, t)$
Specific absorbed fraction	kg^{-1}	$\Phi(r_T \leftarrow r_S, E_i, t)$
Time-integrated activity in source region (cumulated activity)	Bq·s	$\tilde{A}(r_S, T_D)$
Time-integrated activity coefficient (residence time)	s	$\tilde{a}(r_S, T_D)$

REFERENCES

[2.1] CENGIZ, A., ALMAZ, E., Internal bremsstrahlung spectra of β^- particle emitters using the Monte Carlo method, Radiat. Phys. Chem. **70** 6 (2004) 661–668, https://doi.org/10.1016/j.radphyschem.2004.03.008

[2.2] BHAT, M.R., "Evaluated Nuclear Structure Data File (ENSDF)", Nuclear Data for Science and Technology (QAIM, S.M., Ed.), Springer, Berlin, Heidelberg (1992) 817–821, https://doi.org/10.1007/978-3-642-58113-7_227

[2.3] NATIONAL NUCLEAR DATA CENTER (NNDC), https://www.nndc.bnl.gov/

[2.4] KELLETT, M.A., BERSILLON, O., The Decay Data Evaluation Project (DDEP) and the JEFF-3.3 radioactive decay data library: Combining international collaborative efforts on evaluated decay data, EPJ Web Conf. **146** (2017) 02009, https://doi.org/10.1051/epjconf/201714602009

[2.5] LABORATOIRE NATIONAL HENRI BECQUEREL, Recommended Data, http://www.lnhb.fr/

[2.6] BERGER, M.J., et al., XCOM: Photon Cross Section Database (Version 1.5), National Institute of Standards and Technology, Gaithersburg, MD (2010).

[2.7] INTERNATIONAL COMMISSION ON RADIATION UNITS AND MEASUREMENTS, Key data for ionizing-radiation dosimetry: Measurement standards and applications, Report No. 90: J. ICRU **14** (2016) 1–110, ICRU, Bethesda, MD.

[2.8] BERGER, M.J., COURSEY, J.S., ZUCKER, M.A., CHANG, J., ESTAR, PSTAR, and ASTAR: Computer Programs for Calculating Stopping-Power and Range Tables for Electrons, Protons, and Helium Ions (Version 1.2.3), National Institute of Standards and Technology, Gaithersburg, MD (2005).

[2.9] INTERNATIONAL COMMISSION ON RADIATION UNITS AND MEASUREMENTS, Report 85: Fundamental quantities and units for ionizing radiation, J. ICRU **11** 1 (2011) 1–31, https://doi.org/10.1093/jicru_ndr011

[2.10] ATTIX, F.H., Introduction to Radiological Physics and Radiation Dosimetry, John Wiley & Sons (1986), https://doi.org/10.1002/9783527617135

[2.11] INTERNATIONAL COMMISSION ON RADIATION UNITS AND MEASUREMENTS, Report 86: Quantification and reporting of low-dose and other heterogeneous exposures, J. ICRU **11** 2 (2011) 1–77, https://doi.org/10.1093/jicru_ndr011

[2.12] INTERNATIONAL COMMISSION ON RADIATION UNITS AND MEASUREMENTS, https://icru.org/

[2.13] INTERNATIONAL COMMISSION ON RADIOLOGICAL PROTECTION, http://www.icrp.org/

[2.14] SOCIETY OF NUCLEAR MEDICINE AND MOLECULAR IMAGING, http://www.snmmi.org

[2.15] BOLCH, W.E., ECKERMAN, K.F., SGOUROS, G., THOMAS, S.R., MIRD Pamphlet No. 21: A generalized schema for radiopharmaceutical dosimetry — standardization of nomenclature, J. Nucl. Med. **50** 3 (2009) 477–484, https://doi.org/10.2967/jnumed.108.056036

Chapter 3

METROLOGY — ACHIEVING ACCURATE AND CONSISTENT ABSORBED DOSE MEASUREMENT

V. SMYTH, M. COX, B. ZIMMERMAN

3.1. PRIMARY STANDARDS AND TRACEABILITY IN RADIOTHERAPY

Any measurement of a quantity that plays a critical role in a process needs to be controlled by the international system of measurement [3.1]. This system means that there exists a traceable path that establishes the measurement as agreeing with the most accurate possible measurement using an internationally validated primary standard, within a known margin of uncertainty. Such agreement ensures universal comparability and is often a legal requirement.

A primary standard is an instrument or material of the highest metrological quality that permits determination of the unit of a quantity from its definition, which has been verified internationally by comparison with the equivalent standards of different institutions at the same level. Many countries have a national standardizing laboratory designated by the government for the purpose of developing, maintaining and improving primary standards in radiation measurement.

The Bureau International des Poids et Mesures (BIPM) was set up by the Metre Convention (originally signed in 1875, with 59 Member States and 42 Associate States and Economies as of 14 November 2018 [3.1]) as the international centre for metrology, with its laboratory and offices in Sèvres (France), in order to ensure worldwide uniformity on matters relating to metrology. Part of its role is to promote and advance the global comparability of measurements and to coordinate international comparisons of national measurement standards agreed to be of the highest priority.

Within the radiotherapy community there is a long history of the development of primary standards to ensure the comparability of the absorbed dose delivered to patients in different centres and countries. For external beam radiotherapy (EBRT), absorbed doses were originally based on measurements of ionization in air, calibrated against primary standards of exposure (coulombs per kilogram of dry air) [3.2]. To obtain the absorbed dose in a patient, a calculation is needed to convert exposure in air to absorbed dose to water, using a number

of factors, including W/e (the average amount of energy required to create an ion pair in air). Successive estimates of W/e did not give good agreement, so an average value was proposed by BIPM [3.3] and adopted by the radiotherapy community. As the technology became available, new standards that obtained absorbed dose to water directly were developed using the method of calorimetry, measuring the temperature rise from the absorption of radiation into a water or graphite phantom. This method avoided the reliance on W/e. A new dosimetry protocol was produced based on the new standards [3.4]. This was a considerable step forward because now radiation dosimeters were calibrated directly in terms of absorbed dose to water, and reference beam output measurements were made in a water phantom rather than air. So, the only correction factor required was an adjustment for any difference in the energy between the calibration beam and the clinical beam. This approach is still used for EBRT.

In the case of photon emitting brachytherapy sources, primary standards are based on ionization chambers exposed in air or on graphite calorimetry, which are in turn used to calibrate well-type ionization chambers that are used for the measurement of brachytherapy source strength.

In EBRT and brachytherapy, the therapeutic dose to the patient is derived from a single measurement of absorbed dose rate using an instrument calibrated against a suitable primary standard. The path to primary standards for radiopharmaceutical therapy (RPT) is not as straightforward. An absorbed dose measurement gives a value in terms of absorbed dose per amount of administered activity (Gy/MBq). So, there are two different primary quantities: activity and absorbed dose.

According to the widely adopted medical internal radiation dose (MIRD) formalism [3.5], as described in Chapter 2, the absorbed dose estimation in RPT relies on the estimation of the time-integrated activity (total number of nuclear disintegrations) within the target region of tissue, and the S factor, which is the mean absorbed dose to the tissue per nuclear decay, see Eq. (2.8).

The time-integrated activity $\tilde{A}$ is derived from measurements of activity that in principle are traceable to primary standards of activity, through the use of a calibrated clinical activity meter. By contrast, the S factor is obtained not from measurement, but from a calculation using nuclear decay data. The critical data are the following:

(a) Particle emission probability;
(b) Particle energy (either discrete energy or spectrum).

The nuclear data are obtained partly by measurement and partly by theoretical calculation, typically for use in applied research and for detector calibrations. In 1995 an international collaboration was formed, the Decay Data

Evaluation Project (DDEP), which includes members of the BNM-CEA/LNHB (France), PTB (Germany), INEEL (United States of America), KRI (Russian Federation), LBNL (USA), NPL (United Kingdom) and CIEMAT (Spain), with the objective of providing carefully produced recommended data [3.6]. The accuracy of the decay data is clearly crucial to the determination of the absorbed dose. Monte Carlo calculation is generally used to model the radiation transport and determine the *S* factor appropriate to the radionuclide and geometry of the source target tissue combination. The calculation of the transport of the radiation within the tissue depends not only on the particle energy, but also on the accuracy of the particular Monte Carlo code used. Both have been thoroughly researched and benchmarked, so there is some confidence in their accuracy. However, there has, up to the present, been no independent measurement of absorbed dose available to test whether the confidence is justified.

Does this method of measurement provide an acceptable level of traceability to a standard of absorbed dose? Traceability to standards of activity is well developed. In principle, it could be possible to combine a 'conventional quantity value', in the terminology of the BIPM International Vocabulary of Metrology [3.7] (quantity value attributed by agreement to a quantity for a given purpose, such as, for example, the gravitational constant) with a traceable quantity value (in this case activity) and to consider the resulting measurand traceable. Such a possibility depends on trusting the nuclear decay data as an 'agreed quantity'. However, even if agreement is interpreted as endorsement by the DDEP, there is no guarantee of correctness in terms of absorbed dose calculation. There is a history of decay data being corrected as new measurement and theoretical methods become available. Traceability is needed not just for consistent dosimetry of a particular radionuclide, but also for consistency of the gray across all radionuclides and even all modalities of radiotherapy (e.g. for the sake of combined therapies, or to transfer data on normal tissue tolerance). There is a need for independent measurement of absorbed dose traceable to a primary standard to validate the calculations of the *S* factor using a given decay dataset before its widespread use can be considered to conform to the principle of traceability.

If we accept that it is, in principle, possible to measure absorbed dose per administered activity in a patient in such a way as to give traceability to primary standards of activity and absorbed dose, the practical realization relies on rigorous procedures that ensure the measurement uncertainty is well determined. While rigorously formulated dosimetry protocols have been developed over several decades to provide the basis for EBRT dosimetry and brachytherapy, dosimetry in RPT has only recently received a comparable level of attention. RPT has not yet developed the culture of dosimetry standardization and auditing (e.g. the dose auditing service provided by the IAEA for EBRT) that ensures

the universal comparability of radiation dosimetry in the same way as for other radiotherapy modalities. Nevertheless, to achieve comparability in the absorbed doses delivered by each of the different radiotherapy modalities it is essential that they all have traceability to the same gray.

3.1.1. Primary standards of absorbed dose for RPT

Work on developing primary absorbed dose standards for RPT is at a very early stage. The only standard dedicated to RPT was developed recently at the National Physical Laboratory, UK [3.8]. This standard uses extrapolation chamber technology to measure the field of radiation exiting the surface of a solution of radioactive material. Monte Carlo simulation then enables the calculation of a conversion factor to obtain the absorbed dose rate per activity concentration at the centre of a large water phantom containing a uniform distribution of radionuclide. The 'large' water phantom is defined as being large enough to achieve equilibrium of all the particles emitted by the nuclei. (Thus, increasing the size of the phantom does not increase the absorbed dose rate at the centre.) This measurement provides the most fundamental test of the absorbed dose rate determined by the radioactive decay data. The quantity is simply the total mean energy of all the emitted particles per nuclear transition per mass. The National Physical Laboratory (NPL) standard relies on the detection of radiation that can transit a few millimetres of air and penetrate the thin entrance window of the extrapolation chamber, so it is not suitable for alpha emitters, or beta particles of energy less than 35 keV. Fortunately, it can be used with the radionuclides most commonly used for RPT (e.g. ^{90}Y, ^{131}I and ^{177}Lu). Work to date indicates that measurements agree with the nuclear decay data within a few per cent. It is to be hoped that the development work will continue to include other technology (possibly calorimetry), allowing measurement of a greater range of radionuclides and other reference geometries.

3.1.2. Primary and secondary standards of activity for RPT

The calculated absorbed dose delivered from an RPT procedure relies on quantitative imaging that requires calibration procedures, which in turn should be based on activity measurements that are traceable to a standard. Primary standards for activity are normally developed using solutions of single radionuclides whose composition is established to maximize chemical stability. These solutions bear little resemblance to those used clinically, as they normally contain an acid or base, depending on the chemistry of the particular element, as well as additional non-active atoms of the same (or a chemically similar) element to prevent adsorption losses.

The methods used to assay the activity are designed to realize assessment of the becquerel without the need to make reference to any other standards. Such measurements are time and resource intensive and, for that reason, most national metrology institutes will calibrate a stable device, such as an ionization chamber, against a primary standard in an established geometry to serve as a secondary standard. For most radionuclides, especially those that decay with accompanying gamma rays, this is the most common way that routine calibration services are provided.

3.1.3. The principle of establishing traceability

According to the BIPM International Vocabulary of Metrology [3.7], the process of calibrating a measuring instrument establishes a relationship between the quantity values (with measurement uncertainties) provided by primary measurement standards and the corresponding indications (with associated measurement uncertainties) produced by the instrument. The term 'metrological traceability' is used to refer to the property of a measurement whereby the result can be related to a reference primary standard through a documented unbroken chain of calibrations. Clearly, an essential element of the measurement chain is that, from the knowledge of the uncertainty of each calibration in the chain, the resulting uncertainty of the final measurement, and hence the distribution of the possible deviations from the primary measurement, can be evaluated.

When a measurement is carried out using a single instrument, such as a thermometer, to measure temperature, the process of achieving metrological traceability is uncomplicated. In many cases it may involve calibration of a transfer instrument against the primary standard, followed by calibration of the thermometer using the transfer instrument. In order that the uncertainty arising from each step can be known, the conditions under which each comparison is performed (the 'reference conditions') need to be the same, or at least prescribed to be within an accepted range. It is the role of a calibration protocol to set the reference conditions and required procedures so that the uncertainty of each calibration can always be determined. When a measurement is taken into the field, the conditions are unlikely to match the reference conditions specified for the calibration procedure. It is then the user's responsibility to be aware of the performance characteristics of the instrument over the intended range of measurement conditions and to evaluate the corresponding uncertainty appropriately.

When a quantity to be measured is derived from several separate physical measurements, as is the case in RPT, each component measurement must be calibrated separately, providing traceability to the relevant primary standard, and the uncertainty due to the (non-reference) clinical measurement conditions

evaluated. In order to achieve traceability of the end value, the overall uncertainty resulting from the contribution from each component measurement and any other links in the measurement chain has to be evaluated. This means that the functional relationship between each measured parameter and the final measurand should be known. In effect, following the definition of metrological traceability, the distribution of the possible deviations of the ultimate measured value from the 'true' value can be assessed.

3.2. THE FORMALISM OF THE MEASUREMENT CHAIN IN RPT

Dosimetry for RPT provides the absorbed dose to a defined region of tissue per unit of administered activity in a patient. This quantity is obtained from a chain of separate procedures. The details of a dosimetry measurement will vary depending upon the clinical application, but, for the sake of example, here we use one common procedure, whereby the time-integrated activity is measured from a sequence of quantitative images. In this scheme, the components of a quantification of absorbed dose within a region of tissue are as follows:

(a) Activity measurements for calibration (using a calibrated activity meter);
(b) Measurement by quantitative imaging of the total activity contained within the region of tissue at a sequence of time points (using SPECT or PET, calibrated using an accepted method);
(c) Determination of the time-integrated activity within the region of tissue, from the area under a curve fitted to the quantitative imaging measurements;
(d) Calculation of absorbed dose from the time-integrated activity.

There are a considerable number of practical challenges presented by the task of determining the value of mean absorbed dose per administered activity from this measurement chain:

(a) Quantitative imaging is very much affected by the geometry of the patient and the size and shape of the region of tissue, which will be different from the reference conditions used for calibration of the single photon emission computed tomography (SPECT) or positron emission tomography (PET) system used. Compensation for this difference must be made in such a way as not to invalidate the calibration, and the ensuing uncertainty must be evaluated. Calibration of the quantification procedure using phantoms having traceable activity content can assist in this process.

(b) Taking a sequence of quantitative imaging measurements with a redistributing and decreasing activity creates a difficulty for co-registration of the images to ensure the same region of tissue is measured each time.
(c) There is no unique method to select and fit a curve to a finite number of time activity points, or to extrapolate to time zero or beyond the final time point. Each method will have an associated uncertainty, part of which will be covariant (e.g. the uncertainty in the calibration of quantitative imaging applies equally at all time points).
(d) Given the estimate of the total number of disintegrations in the region of tissue, there is still a source of uncertainty in the calculation of absorbed dose. Different methods (tabulated *S* factor, local deposition, point-kernel convolution, Monte Carlo) will apply depending on the radionuclide and how well the images represent the true activity distributions. Furthermore, the nuclear data are critical to accurate calculations. For complete traceability to a primary standard of absorbed dose the calculation must be validated against measurements with traceability to the standard.

The conclusion from these considerations is that RPT dosimetry is considerably more complex than dosimetry for EBRT. However, this does not mean that it is not possible to apply the same metrological rigour as for EBRT. A measurement of absorbed dose from a radiopharmaceutical, in effect, depends on determination of the activity within the source region and the absorbed dose calculated from the time-integrated activity. In order for the absorbed dose measurement to be traceable, both of these measurements must be traceable to primary standards of activity or absorbed dose (see Sections 3.1.1 and 3.1.2).

3.3. UNCERTAINTY ANALYSIS

It is clear from the previous section that a rigorous evaluation of the uncertainty in the measurement of absorbed dose to a patient is a complex process. Traceability must be established to two separate primary standards of activity and absorbed dose, and the measurement chain is not simple. The uncertainty of each component measurement must be evaluated and the functional relationship between this quantity and the end result must be determined so that the uncertainties can be propagated. Some of the links in the measurement chain are functionally non-linear and it is not possible to express the uncertainty simply in terms of a percentage of the quantity and sum the percentages in quadrature. This problem arises in the case of the uncertainties due to imaging processes (e.g. the effects of different patient geometries on image reconstruction) and

of the uncertainty in the area under the time activity curve due to the selected curve-fitting and integration methods.

However, once the functional relationships of each of the links in the chain structure have been established, it is possible to follow the methods recommended in the Guide to the Expression of Uncertainty in Measurement (GUM) [3.9] and Supplements 1 [3.10] and 2 [3.11] and carry out a formal uncertainty analysis. An explanation of this process and examples are given in Chapter 9.

In routine clinical practice it is neither necessary nor practical to evaluate the uncertainty of every absorbed dose measurement. However, it is essential that typical uncertainties for the usual range of clinically occurring geometries in each RPT procedure are known for the particular kind of RPT, the equipment and the dosimetry methods used. These uncertainties should be evaluated when commissioning dosimetry on each procedure. Ideally, at this time validation measurements will be made using relevant anthropomorphic phantoms of organs, tumours and so on. This exercise will provide valuable information about which links in the chain are the greatest sources of uncertainty and how much confidence can be placed in routine measurements.

3.4. STANDARDIZATION OF MEASUREMENTS FOR RPT DOSIMETRY

It is important to start this section by explaining what is meant by standardization in the context of this chapter and the purpose it should serve. When a specific measurement is used widely to guide critical decisions (such as absorbed dose for radiotherapy), some degree of standardization in the measurement methods is highly desirable. Such standardization helps to achieve consistency of results, facilitates the training of users and helps reduce operational errors. The IAEA's dosimetry protocol for EBRT is a good example [3.4]. However, RPT, as a modality of radiotherapy, because of the wide diversity of types of procedure, is not as easily amenable to standardization. A standardization scheme must account for different radionuclides emitting different qualities of radiation, different treatments involving different tissues, and different hardware and software for dosimetry. This is not an easy environment in which to formulate standard procedures. Nevertheless, it is possible to use the methods of metrology to achieve comparability between different centres and with other radiotherapy modalities. It is particularly important in multicentre clinical trials that involve dosimetry that there is an accepted basis for ensuring consistent dosimetry amongst all participants.

Any practical measurement has two components:

(1) Calibration of the (or each) measuring instrument under reference conditions against (or traceable to) a known value from a standard measurement. It is normal practice for the calibration procedures and reference conditions to be covered by an agreed standard protocol, to ensure comparability. The use of a standard protocol reduces the dependence on the expertise of the user and helps to avoid errors.
(2) A process of determining correction factors to account for the non-reference conditions of the field measurement. For the ideal type of measuring instrument these correction factors are not very different from unity. If this is not the case, the reference conditions for calibration should be chosen to be as close to the typical measurement conditions as possible, for the same reason of keeping the correction factors close to unity. In this way the accuracy of measurement is not strongly dependent on the competence of the user.

For an activity meter, the reference measurement usually makes use of a standard vial containing a traceable activity. The corrections for non-reference conditions account for measurements in different containers, non-linearity, dead time and so on. For a well-designed meter, and under normal conditions of use, these corrections are small.

Clearly, in these terms, quantitative imaging is not an ideal type of measurement. There is no reference geometry from which all other possible patient geometries represent a small perturbation. Indeed, it is not at all clear at the time of writing which measurement and reference condition/s should be used for calibration. It is important for a reference condition to be easily reproduced by all users if it is to be prescribed in a protocol. Details are discussed in the next section.

Clinical centres that have developed their own calibration methods may be reluctant to adopt a new protocol because of the time and effort already invested. However, metrological comparability will be more reliably guaranteed if all participating centres adopt the method in the protocol. Any centre that chooses to differ has a responsibility to demonstrate rigorously that their method produces results that are consistent with the protocol.

3.5. CALIBRATION OF ACTIVITY MEASUREMENTS — REFERENCE CONDITIONS

3.5.1. Calibration of activity meters

Activity meters (also known as ‘activity calibrators’ or ‘dose calibrators’) are gas-filled re-entrant ionization chambers that provide an assay of the activity content of a source by measuring the ionization current produced in the interaction of the radiation emitted by the source with the gas. (See Chapter 4 for a detailed description.) For many commercial instruments, the manufacturers provide the instrument with a certificate of calibration for measurement of one specific radionuclide, and either pre-set ‘dial settings’ or correction coefficients that must be applied to the measurement of other radionuclides.

A number of publications and guidance documents exist to assist in the calibration of activity meters (cf. ANSI 2004 [3.12], IAEA 2006 [3.13], AAPM Report No. 181 [3.14], Zimmerman and Cessna, 2000 [3.15]). The general procedure consists of transferring a calibrated solution of the radionuclide of interest into the specific type of container that will be used for the clinical measurement or one that very closely simulates it. The transfer should be carried out by mass using a balance whose calibration is traceable to a national standard. The reason for using this procedure is that mass transfers tend to be more accurate and less susceptible to temperature differences, and the calculation of total activity is easier since most national metrology institutes calibrate solutions in terms of activity concentration (in Bq per g). Once the total activity is known (from the calibrated activity concentration and the transferred mass), the calibration coefficient can be calculated by dividing the measured current in the chamber by the total activity. In the case of activity calibrators that use dial settings, the correct dial setting can be determined by changing the dial until the correct activity is shown on the display. Depending on the individual instrument it may be necessary to set up a ‘custom’ dial setting, or to apply a correction factor. The steps necessary to obtain a measurement corresponding to the calibration will need to be detailed in a standard procedure.

The NPL in the UK can provide an ionization chamber that is built to the same specifications as the NPL secondary standard master ionization chamber and is tested at NPL for a range of radionuclides. Calibration coefficients are provided for a large number of radionuclides in various container geometries all traceable to NPL standards.

Following the discussion in the previous section, it is important to note that a calibration is strictly valid only for the **reference** measurement conditions. In this case the calibration conditions are determined by the container used and the volume of radioactive solution contained. Clinical measurements typically

entail the use of a syringe, a capsule or a vial that is different from the reference container. Correction factors must be determined for the effects of the difference in the container type and the liquid volume compared to the reference vial used for calibration. In many cases the differences will be negligible in comparison with the uncertainty of the activity measurement. However, they should always be checked before clinical use.

In practice, the calibration of an activity meter is sometimes not so straightforward. Not all countries have a service able to supply calibrated solutions. Even if they do, the specific radionuclides used for RPT may not be available, so the clinic will need to rely on calibration using a different radionuclide and the 'dial settings', which, depending on the quality standards of manufacture, may not represent the response of each individual instrument particularly well. Every attempt should be made to obtain relevant calibrated sources or at least to take part in regional or international activity measurement inter-comparisons.

3.5.2. Calibration of SPECT or PET camera systems for quantitative imaging

As mentioned above, in terms of the aims of metrology, quantitative imaging is not an ideal type of measurement. It is not at all clear what measurement should be used as a reference condition measurement for calibration. For example, in the case of SPECT quantitative imaging, the following concerns may arise:

(a) At one extreme, the calibration of a SPECT system can be based on a planar measurement of the sensitivity of the collimator-crystal combination using a calibrated point source in air. In this case, the whole process of constructing an image must be considered as a 'correction' for non-reference conditions. This has the advantage of providing a single calibration procedure applicable to all possible measurements and using readily available equipment. However, it is not ideal from a metrological point of view. It is not representative of a typical clinical measurement. There are potential confounding factors (e.g. the size of the 'point', 'backscatter', from the source holder, scatter and attenuation in the air) that do not occur in normal measurements. Further, there is considerable dependence on local expertise to ensure the 'corrections' are correct, which is not desirable for a procedure to be used widely.

(b) At the other extreme, an anthropomorphic phantom can be produced using 3-D printing, and the feature/s to be imaged quantitatively can be filled with a calibrated activity followed by a tomographic (SPECT or PET) acquisition. In this way, the quantitative imaging measurement of the activity within each

selected filled compartment can be calibrated directly. The advantage here is that the reference condition simulates a clinical measurement. But it is not practical as a standard calibration procedure because the phantom would not be widely available, and a different phantom and calibration procedure would be needed for each different treatment type. (However, a procedure of this type is very useful for testing quantitative imaging performance under non-reference conditions; see Section 3.6.)

(c) Ideally, a standard calibration procedure should be somewhere between cases (a) and (b) if it is to be widely used. Suggested procedures based on imaging a uniformly filled phantom are given in Chapter 4. The standard reference condition should be clearly and uniquely specified, and readily available to all users. It should be chosen with the ultimate aim of achieving the maximum uniformity across the greatest possible number of users, taking a realistic account of the range of levels of expertise in clinical centres.

In any SPECT calibration procedure other than that using a point source in air, the applicability of the procedure will be restricted to the image acquisition and reconstruction method and parameters used in the reference measurement. If a particular clinical image requires a change in the imaging details, then a measurement with these settings should be included in the calibration procedure. In practice, it may be best to perform a series of calibration procedures to suit the range of clinical settings and treatments that will be used. It is essential also that the imaging settings are always recorded as part of the calibration procedure.

The procedure for calibration of a PET/CT system for quantitative imaging is generally prescribed by the manufacturer and follows the terms of the standardized uptake value. This procedure is generally based on a phantom measurement and is also covered in Chapter 4.

All of the above effectively illustrate the earlier comment that RPT is not an easy environment in which to formulate standard procedures. At the time of writing there is no consensus on standard methods.

3.6. VALIDATION OF ABSORBED DOSE MEASUREMENTS IN THE CLINIC

3.6.1. Activity measurements under non-reference conditions

The typical clinical determination of absorbed dose is likely to entail measurements under different conditions from those used to calibrate the activity meter and quantitative imaging camera:

(a) There may need to be a correction for use of a syringe rather than a standard vial in the activity meter.
(b) It is important to check that the calibration factor for the camera is valid for the image settings used.
(c) There will be custom corrections to the quantitative imaging images for scatter, attenuation, septal penetration and dead time.
(d) Depending on the size and shape of the region of tissue there will be a need to estimate a recovery coefficient to correct for the partial volume effect.

There are instructions on how to determine the required corrections to activity measurements in Chapters 4 and 6, and their uncertainty contributions are discussed in Chapter 9. They are also listed here to highlight the need to validate the corrections and to estimate the uncertainty their determination adds to the end absorbed dose measurement. If possible, test measurements should be made on anthropomorphic phantoms filled with known activity representing the clinical measurement. This will provide assurance that the corrections are valid and the deviation will give an evaluation of the uncertainty of such a measurement. This exercise must be carried out on a range of typical patient-like geometries before dosimetry is used for patient management. Recent work has provided detailed specifications for anthropomorphic phantom organs based on internationally adopted virtual phantoms, which can be reproduced using 3-D printing techniques [3.16].

3.6.2. Validation of the calculation of absorbed dose from time-integrated activity

In order to calculate absorbed dose from a time sequence of quantitative imaging data the following steps must be carried out:

(a) In the case of voxel level absorbed dose calculation co-registration of the quantitative imaging images of the region where the absorbed dose is to be determined;

(b) Fitting of a curve to the activity in the region at each time point, extrapolated to time zero and to infinity;
(c) Determination of the area under the curve to obtain a total number of disintegrations;
(d) Calculation of the absorbed dose, taking account of the transport of any radiation that is not locally deposited, in the context of images that have been blurred by the imaging method.

Each of these steps is critical to a correct absorbed dose calculation. The commissioning of an absorbed dose calculation package should include a systematic validation and uncertainty analysis of each step. However, unlike the commissioning of a treatment planning system for EBRT, this process cannot be achieved simply by comparing calculations to measurements. Sets of test data are required, covering the typical range of clinical geometries, generated either from computer simulation or based on anthropomorphic phantoms. The 'true' value of the absorbed dose can be calculated and compared with the result obtained by the dosimetry package. The RPT industry is at an early stage in the development and use of commercial dosimetry systems, but work is currently proceeding on the production of test images and data that will be made available on open public databases to enable the testing of systems.

In the absence of independent data, an absorbed dose calculation package can be tested by comparison with another package, if possible, incorporating different algorithms. Another strongly recommended action would be comparison with other clinical centres of dose calculation from a set of imaging data.

REFERENCES

[3.1] BUREAU INTERNATIONAL DES POIDS ET MESURES, The International System of Units (SI), BIPM, Sèvres (2019).
[3.2] INTERNATIONAL ATOMIC ENERGY AGENCY, Absorbed Dose Determination in Photon and Electron Beams, Technical Reports Series No. 277, IAEA, Vienna (1997).
[3.3] BOUTILLON, M., PERROCHE-ROUX, A.M., Re-evaluation of the W value for electrons in dry air, Phys. Med. Biol. **32** 2 (1987) 213–219, https://doi.org/10.1088/0031-9155/32/2/005
[3.4] INTERNATIONAL ATOMIC ENERGY AGENCY, Absorbed Dose Determination in External Beam Radiotherapy, Technical Reports Series No. 398, IAEA, Vienna (2000).

[3.5] BOLCH, W.E., ECKERMAN, K.F., SGOUROS, G., THOMAS, S.R., MIRD Pamphlet No. 21: A generalized schema for radiopharmaceutical dosimetry — standardization of nomenclature, J. Nucl. Med. **50** 3 (2009) 477–484, https://doi.org/10.2967/jnumed.108.056036

[3.6] HELMER, R.G., BROWNE, E., BÉ, M.-M., International decay data evaluation project, J. Nucl. Sci. Technol. **39** Suppl. 2 (2002) 455–458, https://doi.org/10.1080/00223131.2002.10875138

[3.7] BUREAU INTERNATIONAL DES POIDS ET MESURES, International vocabulary of metrology — Basic and general concepts and associated terms, VIM (2012).

[3.8] BILLAS, I., et al., Development of a primary standard for absorbed dose from unsealed radionuclide solutions, Metrologia **53** 6 (2016) 1259–1271, https://doi.org/10.1088/0026-1394/53/6/1259

[3.9] JOINT COMMITTEE ON GUIDES IN METROLOGY, Evaluation of Measurement Data – Guide to the Expression of Uncertainty in Measurement, BIPM, Sèvres (2008).

[3.10] JOINT COMMITTEE ON GUIDES IN METROLOGY, Evaluation of Measurement Data – Supplement 1 to the "Guide to the Expression of Uncertainty in Measurement" – Propagation of distributions using a Monte Carlo method, BIPM, Sèvres (2008).

[3.11] JOINT COMMITTEE ON GUIDES IN METROLOGY, Evaluation of Measurement Data – Supplement 2 to the "Guide to the Expression of Uncertainty in Measurement" – Extension to any number of output quantities, BIPM, Sèvres (2011).

[3.12] AMERICAN NATIONAL STANDARDS INSTITUTE, Calibration and usage of 'dose calibrator' ionization chambers for the assay of radionuclides, ANSI N42.13-2004, ANSI, Washington, DC (2004).

[3.13] INTERNATIONAL ATOMIC ENERGY AGENCY, Quality Assurance for Radioactivity Measurement in Nuclear Medicine, Technical Reports Series No. 454, IAEA, Vienna (2006).

[3.14] AMERICAN ASSOCIATION OF PHYSICISTS IN MEDICINE, The Selection, Use, Calibration, and Quality Assurance of Radionuclide Calibrators Used in Nuclear Medicine, Report No. 181, AAPM, College Park, MD (2012).

[3.15] ZIMMERMAN, B.E., CESSNA, J.T., Experimental determinations of commercial 'dose calibrator' settings for nuclides used in nuclear medicine, Appl. Radiat. Isot. **52** 3 (2000) 615–619, https://doi.org/10.1016/S0969-8043(99)00219-5

[3.16] TRAN-GIA, J., SCHLÖGL, S., LASSMANN, M., Design and fabrication of kidney phantoms for internal radiation dosimetry using 3D printing technology, J. Nucl. Med. **57** 12 (2016) 1998–2005, https://doi.org/10.2967/jnumed.116.178046

Chapter 4

QUANTIFICATION OF ACTIVITY

Y. DEWARAJA, M. MADSEN, M. LJUNGBERG, H. HÄNSCHEID

4.1. INTRODUCTION

Absolute activity quantification is an essential step in absorbed dose calculation because of the linear relationship between activity and absorbed dose (see Section 2.5). This chapter introduces the concepts behind the detection systems used to measure activity or activity concentrations, both prior to and following (in vivo) radiopharmaceutical administration. The basic principle behind radiation detection is the transfer of energy that occurs when radiation passes through the detection medium, which leads to ionization and excitation of atoms and molecules of the medium (see Section 2.4). The manner in which radiation interacts with the detection medium and loses energy varies for charged particles and photons, but in both cases the result is ionizations and excitations that can be used to generate an electric signal. Charged particles mostly transfer energy via collision events that cause ionizations directly, while photons in the energy range relevant to nuclear medicine mostly transfer energy by photoelectric absorption or Compton interactions, leading to secondary ionization. In photoelectric absorption, the total energy of the photon is transferred completely to an inner shell orbital electron, which is ejected from the atom. Thus, the photon disappears and the electron carries an energy equal to the energy of the photon minus the binding energy of the electron shell. In Compton scattering there is only a partial transfer of energy from the photon to an orbital electron. The amount of energy transferred to the electron depends on the scattering angle and ranges from close to zero for small angle scattering to a maximum value at a scattering angle of 180º.

Both imaging (e.g. gamma camera) and non-imaging (e.g. thyroid probe) detection systems are used in activity quantification for dosimetry. Ideal detectors have a constant and well-known efficiency in the activity range of interest, which is high enough to provide a reproducible numerical value with low uncertainty. The detection efficiency depends on the intrinsic efficiency of the detector material and signal collection, and the geometry between source and detector, which must be precisely defined.

4.2. MEASUREMENT EQUIPMENT

4.2.1. Devices for ex vivo measurements

4.2.1.1. Activity meter

Activity meters, also known as radionuclide calibrators or dose calibrators, are designed to accurately determine the activity of radiopharmaceuticals. Typically, vials or syringes are measured in a re-entrant well-shaped ionization chamber filled with highly pressurized inert gases such as argon and xenon. The radioactive material is placed deep enough into the well so that the radiation is detected with approximately the ideal 4π geometry. The radiation emanating from the source enters the chamber and interacts with the gas, causing ionization. Because a voltage is applied across the chamber, the positive and negative ions resulting from the interactions are collected by the negative cathode (typically the chamber wall) and the positive anode of the chamber, respectively. The current generated can be correlated to the energy deposited in the chamber and thus the intensity of radiation emitted by the source. Since the dose calibrator operates in current mode and does not count individual pulses, dead time effects are avoided. This allows the dose calibrator to be used to measure the high levels of activity typical for radionuclide therapy applications. However, at very high activities, recombination of positive and negative ion pairs may lead to a reduction of the measured current. This effect is expected to be <1% when measuring 100 GBq of ^{99m}Tc and is well within the expected accuracy for these devices. However, the amount of current generated per nuclear decay depends on the radionuclide as well as on the source container used for measurement. The sensitivity is strongly dependent on the type of radiation emitted (photons or charged particles), the energy and the emission probability per radioactive decay. Interaction of the radiation in the radioactive source itself and in the container walls influence the chamber current. Thus, to accurately convert the dose calibrator current to activity, a radionuclide and vial specific calibration factor must be applied. The calibration factor can be determined by relating the current measured to the known activity of a standard that is traceable to a national primary standard maintained by institutes such as the National Physical Laboratory (NPL) in the United Kingdom, or the National Institute of Standards (NIST) in the United States of America. The uncertainties of these national standards are typically 1–3%.

Obtaining traceable samples of the relatively short lived radionuclides used in nuclear medicine can, however, be problematic. If samples are offered by a standards laboratory at all, time required for transport directly competes with the isotopes' radioactive decay. Therefore, most activity meters are currently pre-calibrated by the manufacturer for a number of common

radionuclides. Because this reliance on the manufacturer has not always proven satisfactory [4.1–4.3], and also is not usually considered good clinical practice (survey meters and ion chambers, for example, are typically calibrated in a manufacturer-independent manner), recent developments have suggested the use of a dedicated instrument to transfer the calibration for a given isotope from the standards laboratory to the nuclear medicine clinic [4.4–4.6]. Once the calibration factor is known, it is stored in the activity meter's operating software and applied digitally when the pre-set button corresponding to a specific isotope is selected.

Geometry effects: Other factors that can affect the activity measurement are the positioning of the source, the source holder used to place the vial in the chamber and the filling volume of the vial or syringe. Since the detection efficiency decreases at the top and the bottom of the chamber, it is advisable to use the source holder supplied by the manufacturer, which keeps the source centred in the range of maximum sensitivity. Correction factors may be needed to account for differences between the container used to assay the radiopharmaceutical (e.g. a shipping vial or syringe used for administration to the patient) and the container used for the calibration standard. Even if the same vial is used, differences in the filling volume can also lead to different activity measurements because of differences in self-absorption of the emitted radiation and varying sensitivity along the axis of the well. The geometry and volume effects are especially important for low energy photon emitters and pure beta emitters. Due to the much increased photoelectric cross-section and short range of beta particles, respectively, the previously discussed geometric factors are particularly important; therefore, the device should be calibrated specifically for the vials and volumes to be used in the clinic in those cases. Bremsstrahlung photons produced by high energy beta particles interacting in the source volume and container or in the chamber wall are also registered by the dose calibrator and can be used to measure the activity of a pure beta emitter indirectly. The sensitivity, however, is only a fraction of that for photon emitters, because the bremsstrahlung yield is low.

4.2.1.2. Well counters

Dose calibrators are not suitable for measuring specimens with low activity such as blood or urine samples from patients receiving low tracer activities for pre-therapeutic dosimetry. Instead, scintillation detectors configured with a well cavity are used which provide highly sensitive spectroscopic single photon counting. Well counters are commonly used in nuclear medicine laboratories to measure labelled cells in vitro or blood activity.

The structure of a typical well counter is illustrated in Fig. 4.1. The most widely used set-up consists of a solid cylindrical crystal of thallium activated

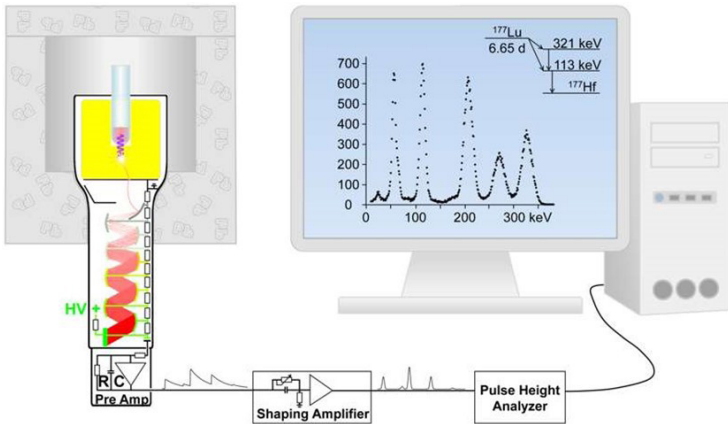

FIG. 4.1. Well-shaped NaI(Tl) detector with photomultiplier and signal processing electronics. Courtesy of H. Hänscheid.

sodium iodide (NaI(Tl)) with a borehole cut into the crystal into which the measuring vial is inserted. Gamma radiation entering the detector ionizes the crystal via secondary electrons and generates excited states which decay approximately exponentially with a decay constant of 0.25 μs under emission of visible light [4.7]. The total number of photons generated, about 30 light photons per keV [4.8], is proportional to the energy deposited in the crystal. A certain amount of the generated light reaches the photocathode of a photomultiplier tube where it releases electrons via the photoelectric effect with a probability of about 25% per photon [4.9]. The number of photoelectrons produced is proportional to the number of scintillation photons, and thus to the energy deposited in the crystal. For example, the 364 keV radiation of ^{131}I will produce on the order of $n = 1000$ photoelectrons with $\sigma = 1/\sqrt{n} \approx 3\%$ statistical uncertainty, which limits the energy resolution to about 2.36 σ ≈ 7.5% full width at half-maximum (FWHM).

The photoelectrons are accelerated in an electric field towards a series of dynodes enclosed in the evacuated glass tube of the photomultiplier. A connection to positive high voltage and a resistive biasing ladder supplies the dynodes with increasingly positive electric potentials. The photoelectrons hit the first dynode and, dependent on their kinetic energy, knock out a number of secondary electrons, which are accelerated towards the next dynode. An increasing cloud of electrons successively hits every dynode and each time the charge multiplies resulting in an almost constant amplification in the range of 10^5–10^6, depending on the high voltage and the number of dynodes. Finally, the charge accumulates in the inverting integrator pre-amplifier (Pre-Amp) in capacitor C, which discharges via resistor R. About 1000 photoelectrons from the example above are converted into

a voltage of approximately 1 V at the output of the Pre-Amp. The minimal rise time of the output signal is defined by the decay of the intensity of the scintillation light. The decay constant of the output signal, defined by R·C, is much longer and in the range of 50 μs. At high counting rates, the rising step caused by the detection of a gamma photon adds to the exponential decay of a previous event before the pre-amplifier output returns to zero. This pulse pile-up induces a varying and increasing baseline of the pre-amplifier output, which causes signal distortion of the output pulses and can, at very high rates of large pulses (i.e. high photomultiplier current), result in saturation, paralyzing the detector.

The output signal of the pre-amplifier is fed into a pulse-shaping linear amplifier, which passes the signal through a filter network with a shaping time constant of about 1 μs or, in modern devices, to a digital signal processor [4.10]. This main amplifier is designed to restore the baseline between the pulses at ground potential, to improve the signal to noise ratio by attenuating low and high frequencies, to further amplify the signal and to produce a unipolar semi-Gaussian output pulse. The pulse height of the output signal, which represents the energy loss in the crystal, is measured in an analogue-to-digital converter in the pulse height analyser and sorted into a histogram known as pulse height spectrum. The dead time of the shaping amplifier is typically an order of magnitude longer than the shaping time constant and exceeds the dead time of the pulse height analyser. Considerable dead time loss is expected at count rates of 10 000 counts per second and higher.

The count rate capability of a given system can be improved by choosing a not too high photomultiplier voltage, a short shaping time constant of the main amplifier and a fast analogue-to-digital conversion. However, these measures tend to compromise the energy resolution.

Geometry effects: The thickness of the crystal of the well counter should be adapted to the energy to be measured. While for the detection of the 30 keV photons from ^{125}I, small crystal thicknesses are sufficient to completely absorb the radiation and several borehole crystals can be operated side by side in sample changers to increase the throughput, the detection of photon energies above 200 keV requires crystal diameters of 5 cm or more. The well itself should have as narrow a diameter as possible adapted to the sample. Since the sample is almost completely surrounded by the crystal, more than 95% of the gamma rays emitted by the sample will traverse the detector crystal. The geometric efficiency decreases with increasing height within the well. It is therefore important to measure with small and fixed quantities in a well defined geometry for which the efficiency is known by calibration. The isotope-specific calibration factors are reported in photopeak count rate per activity (e.g. counts/(s Bq)). For example, the calibration factors of a typical well counter with 3″ × 3″ (7.68 × 7.68 cm)

NaI(Tl) detector are about 0.45 cps/Bq for the 364 keV radiation of ^{131}I and 0.8 cps/Bq for the 140 keV radiation of ^{99m}Tc.

Coincidence summing: Energy spectra measured in well counters may differ considerably from those acquired at some distance for radionuclides emitting more than one gamma ray per nuclear disintegration. Due to the high detection efficiency for individual photons, the probability is high that coincident photons are measured simultaneously and form a peak at the sum of the energies. Figure 4.1 illustrates a computer screen displaying the decay scheme of ^{177}Lu and a spectrum obtained with a well counter. The excited state at 321 keV decays via the successive emission of two photons with energies 208 keV and 113 keV. Besides the corresponding lines, X rays after internal conversion of the excited state at 113 keV are visible at 55 keV as well as sum peaks at 208 + 55 keV and at 208 + 113 keV.

4.2.2. Probe based counting systems

Dosimetry measurements of gamma emitters in vivo can be performed with non-imaging detectors if the activity is concentrated in the tissue to be measured and if the background from other activities in the field of view make only minor contributions to the registered count rate. Such probe systems can be used, for example, to measure the whole body activity time function or the uptake of radioactive iodine into the thyroid gland.

The latter is often done with a dedicated thyroid uptake probe (see Fig. 4.2) in order to determine the activity necessary for the treatment of benign thyroid disease. Such a device usually consists of a scintillation detector in a lead collimator that defines a field of view with 15–20 cm diameter at a distance of about 25 cm [4.11]. The structure and function of the probe are largely identical to those of the well counter. The scintillation light produces photoelectrons in the photocathode of a photomultiplier, which are multiplied in a cascade of electric fields between dynodes. The resulting current is collected in a charge integrator whose output pulses are evaluated by a pulse height analyser after shaping and further amplification in a main amplifier. The detector is mounted on a gantry and can be positioned over the tissue to be measured. Since the solid angle is inversely proportional to the square of the distance between the activity and the detector, the distance to the patient's neck must be precisely set by a spacer during the measurement. An activity of about 1 MBq of ^{131}I and a 2″ × 2″ (5.12 × 5.12 cm) NaI(Tl) detector are appropriate for dosimetry prior to radioiodine therapy of benign thyroid disease. The measured count rate over the thyroid gland one day after the administration is then expected to be in the order of 100 cps in the peak at 364 keV. Such a probe cannot be used for uptake measurements after therapy with several hundred MBq of ^{131}I. In order to perform dosimetry measurements

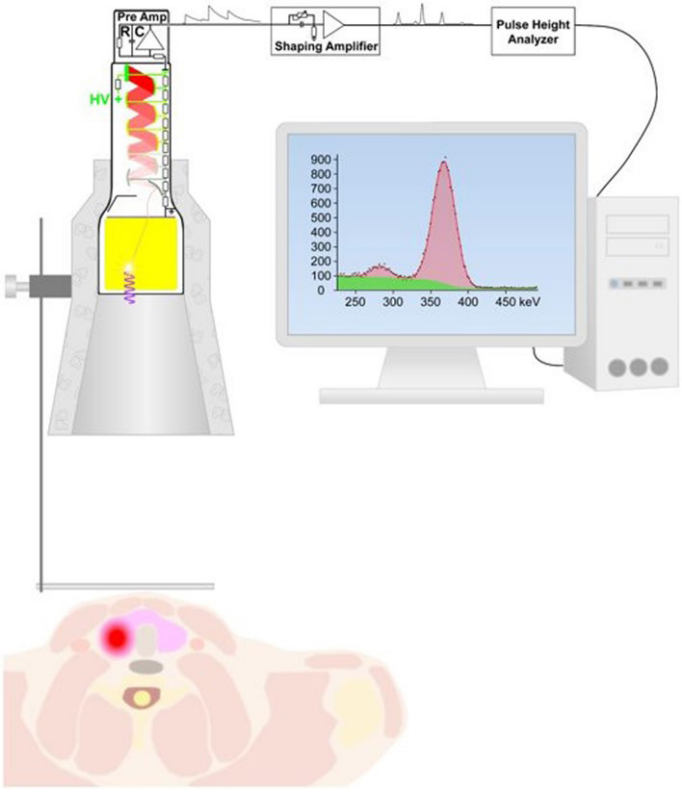

FIG. 4.2. Thyroid uptake probe with a NaI(Tl) detector. Courtesy of H. Hänscheid.

after high activity treatments, the sensitivity of the probe must be reduced to a few per cent by considerably increasing the measuring distance or by using another collimator with only a small aperture in front of the detector.

Geometry effects: Since the mean depth of the activity distribution under the neck surface influences the detection sensitivity by both the distance and the attenuation in the tissue, it is necessary to calibrate a thyroid uptake probe using a phantom that mimics a thyroid gland in a neck. At 25 cm distance between neck and detector and 2.5 cm calibration depth, 0.1 cm deviation of the actual mean depth of activity under the skin from the calibration depth leads to about 1.5% error with approximately equal contributions from solid angle and attenuation.

Whole body counting: Scintillation detectors or, for radionuclides with high dose rate constants and high activities, survey meters are ideally suited for measuring the activity time function in the whole body, especially after radiopharmaceutical therapy (RPT). A first probe count, performed shortly after the administration before any excretion, is used as a 100% value. A series

of subsequent measurements is normalized to this value. Since only relative measurements are needed to calculate the retention function, an absolute calibration of the device by phantom measurements is not necessary. In order to ensure identical sensitivity for all measurements, the measuring distance must be sufficiently large (e.g. 2 m) and must be exactly reproducible. To compensate for possible changes in measuring geometry by redistribution of the activity in the body, each retention value should be determined as the normalized geometric mean of conjugate view (anterior and posterior) net counts.

4.2.3. Devices for imaging based measurements

The basis for nuclear medicine imaging is the detection and localization of photons that are emitted during or following radioactive decay of the administered radionuclides. For macroscopic dosimetry, activity distributions can be imaged by planar (2-D) or emission tomographic (3-D) methods. The advantages of planar imaging are fast acquisition and ease of processing as it does not require multiple angular views and image reconstruction, making it convenient for clinical use. Planar imaging, however, cannot resolve the source depth nor is it reliably correct for counts emanating from activity in tissue overlying or underlying the structure of interest. Furthermore, degrading physical factors such as scatter, attenuation and finite resolution cannot be accurately modelled. Although delineating regions of interest (ROIs) manually on planar views can be done quickly, planar imaging cannot be used to determine target volumes for dosimetry. These limitations are overcome with tomographic imaging that can be further subdivided into single photon emission computed tomography (SPECT), where single photons are imaged, and positron emission tomography (PET), where pairs of photons are imaged in coincidence. The basics of these systems are described below, and the reader is referred elsewhere for more detailed descriptions [4.8, 4.12].

4.2.3.1. The gamma camera for planar and SPECT imaging

The gamma camera, also known as the scintillation camera or Anger camera, used in planar and SPECT imaging, is a position sensitive detector that detects and localizes photons, typically gamma rays that penetrate the body tissue. The major components of the gamma camera (Fig. 4.3) are a collimator as the image forming aperture, a scintillation crystal that acts as the detection medium for the photons transmitted through the collimator, an array of photomultiplier tubes and electronics for determining position and energy associated with the interaction in the crystal and a gantry system for moving the camera. A photon that passes through the collimator (without absorption in the lead walls) interacts with the scintillation crystal to produce light photons in proportion to the deposited energy

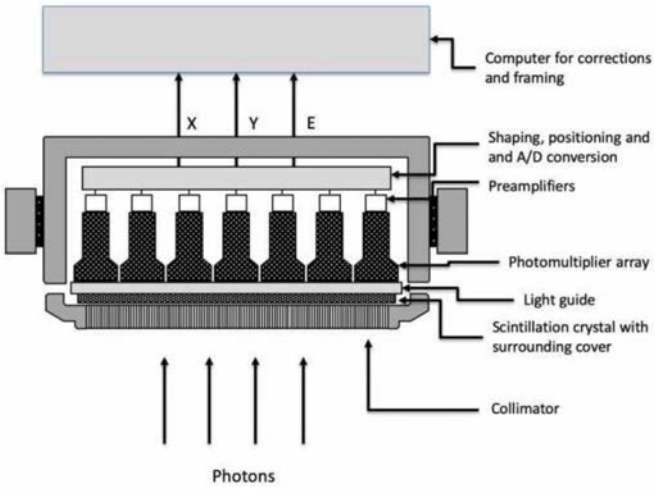

FIG. 4.3. Schematic of the gamma camera. Courtesy of M. Ljungberg.

in the crystal as discussed in Section 4.2.1.2 on well counters. The photomultiplier tubes convert the light pulses into electronic signals, which are then fed to positioning logic circuits that determine the location of each scintillation event within the 2-D matrix by using the weighted average of the signals. The energy of each scintillation event is also determined by summing the signals from all photomultiplier tubes. If the pulse amplitude of the summed signal falls within a pre-set acquisition energy window the pixel value corresponding to the X,Y location of the event is incremented. In this manner the gamma camera generates a 2-D projection image of the activity distribution within the patient. For planar imaging, one or two projection views (typically anterior and posterior) are acquired. For SPECT, a sufficient number of projection images from multiple angles must be acquired. In SPECT systems that use conventional gamma cameras with parallel hole collimators, these projections are acquired as the camera rotates around the patient. Other systems that rely on multiple pinhole collimation can acquire the projections without moving the detectors.

The scintillation crystal in the gamma camera is made of high-Z material, typically NaI(Tl), in order to increase the probability of photoelectric absorption of the incident photon. The thickness of the crystal is selected by considering the trade-off between efficiency, which improves with thickness, and energy resolution, which deteriorates with thickness. The standard gamma camera, designed for detecting photons with energies in the range 100–200 keV, has a crystal thickness of 9.5 mm. With the standard crystal, the (photopeak) detection efficiency is ~80% for ^{99m}Tc but is substantially lower for higher

gamma ray energies associated with some therapy radionuclides. For example, for imaging ^{131}I, the standard scintillation crystal is less than 30% efficient at converting incident gamma rays into photopeak pulses. Therefore, some gamma cameras, specifically meant for oncology applications, are equipped with thicker crystals (e.g. 15 mm thick crystal for imaging in radioiodine therapy applications). Recently, gamma camera systems that use semiconductor material, such as cadmium zinc telluride (CZT) as the detection medium, have become commercially available [4.13, 4.14]. These detection media convert the energy deposited following a photon interaction directly into an electrical signal without the need for photomultiplier tubes. The direct energy conversion results in better energy resolution compared with scintillators, allowing narrower acceptance windows to be used for better discrimination of scattered photons. The intrinsic spatial resolution of semiconductor detectors is typically better than that of conventional scintillation crystals coupled with photomultiplier tubes; however, the detection efficiency is lower for high energy photons. Currently, commercially available CZT based SPECT systems are limited to low energy (e.g. ^{99m}Tc, ^{201}Tl, ^{123}I) and medium energy (e.g. ^{177}Lu) photon emitters and are not suitable for some therapy radionuclides including ^{131}I that has higher energy gamma ray emissions.

The collimator, typically a lead plate consisting of an array of holes and septa (walls), controls which gamma rays are accepted. Photons that are not within the small angular range defined by the collimator holes are rejected by absorption in the septa. Thus, the activity distribution within the patient is projected onto the crystal. A large fraction of the photons emitted by the source is absorbed in the collimator septa, thus limiting the efficiency of gamma cameras. There are four basic types of collimators: pinhole, parallel hole, diverging and converging. However, in nearly all imaging studies relevant to RPT dosimetry, parallel hole collimation is used.

The spatial resolution of the gamma camera depends on the intrinsic resolution of the scintillator crystal and the collimator resolution. The intrinsic resolution becomes poorer at low gamma ray energies and with the thickness of the crystal. Typical values of intrinsic resolution measured for ^{99m}Tc are in the range of 3–4 mm FWHM. The collimator resolution depends on the collimator geometry as well as the source to collimator distance (depth dependent). At source-collimator distances greater than about 5 cm the gamma camera system resolution is dominated by collimator resolution. The collimator hole geometry, which includes diameter, length and wall thickness, greatly impacts both collimator resolution and sensitivity (Table 4.1).

Long narrow holes provide images with the best spatial resolution but result in poor efficiency. The trade-off between resolution and efficiency has been considered when designing the collimators and needs to be considered when

selecting a collimator for a specific radionuclide and application. The categorization of commercial collimators as low, medium or high energy is based on the maximum gamma ray energy for which the thickness of the septa is considered to be adequate (typically, to keep septal penetration below about 5%). The selection of a low, medium or high energy collimator depends on the energy of the imaged photon and any significant higher energy photons associated with the radionuclide decay, as well as the desired balance of spatial resolution and sensitivity.

TABLE 4.1. GAMMA CAMERA SPECIFICATIONS CORRESPONDING TO FIVE DIFFERENT PARALLEL HOLE COLLIMATOR CATEGORIES

(on the same commercial system; courtesy of M. Ljungberg)

Collimator	Isotope	Hole diameter (mm)	Septa thickness (mm)	Hole length (mm)	Resolution at 10 cm FWHM (mm)	Sensitivity * at 10 cm (cps/MBq)
LEAP	Tc-99m	1.45	0.2	24.05	9.4	148
LEHR	Tc-99m	1.11	0.16	24.05	7.5	91
LEUHR	Tc-99m	1.16	0.13	35.8	6.0	45
ME	Ga-67	2.94	1.14	40.64	10.8	124
HE	I-131	4	2	59.7	13.2	61

Note: LEAP: low-energy all-purpose; LEHR: low-energy high-resolution; LEUHR: low-energy ultra-high resolution; ME: medium energy; HE: high energy.

* Values measured in accordance with National Electrical Manufacturers Association (NEMA) Standards Publication NU-1 2018 using 3/8″ crystal.

TABLE 4.2. RECOMMENDED TYPE OF COLLIMATORS FOR SELECTED THERAPY RADIONUCLIDES AND IMAGING SURROGATES

(courtesy of M. Ljungberg)

Low energy	Low or medium energy	Medium energy	Medium or high energy	High energy
Sn-117m, Sm-153, Re-186, Tc-99m	I-123	In-111, Lu-177, Cu-67	Ga-67, Ho-166, Re-188, Y-90	I-131, Y-90

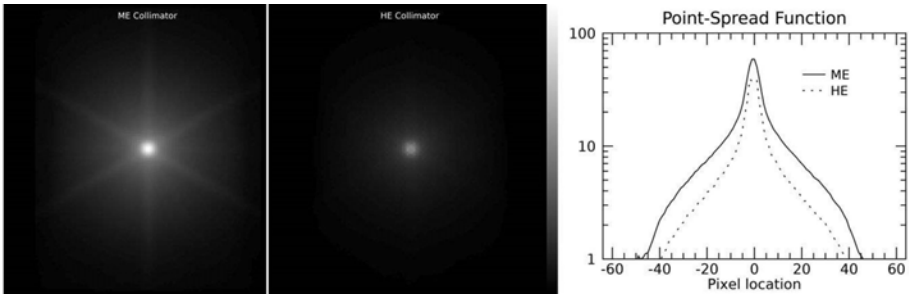

FIG. 4.4. Monte Carlo simulated ^{131}I point source images (left) and profiles across centre (right) for a gamma camera equipped with a medium energy and a high energy collimator demonstrating the higher septal penetration when the medium energy collimator is used. A gamma value of 0.7 was used for the greyscale in order to visualize the penetration effects. Courtesy of M. Ljungberg.

For common radionuclides relevant to therapy applications, the suggested collimators are given in Table 4.2. Note that for some radionuclides that are imaged using a relatively low energy gamma ray, such as ^{166}Ho and ^{188}Re, a medium or high energy collimator is recommended because of septal penetration by higher energy gamma emissions and/or by the considerable amount of bremsstrahlung photon generated by the β emissions as they slow down in tissue.

The impact of septal penetration when an inappropriate collimator is used is demonstrated by Fig. 4.4, in which ^{131}I point source images and point spread functions for a gamma camera equipped with medium and high energy collimators are compared.

The ideal ‘desired’ event in gamma camera imaging is a gamma ray that does not interact in the object or collimator and passes through the collimator holes, followed by photoelectric absorption in the scintillation crystal (Fig. 4.5).

Thus ideally, only events originating along what is referred to as the line of response (LOR), defined as a trajectory parallel to the collimator holes, contribute to the signal detected by the corresponding pixel location. As is evident in Fig. 4.5, the signal intensity recorded by the detector should be proportional to the sum of activities along the LOR. However, because of physical factors such as attenuation and scatter this assumption is not valid. Compensation for these factors is discussed in Section 4.4.

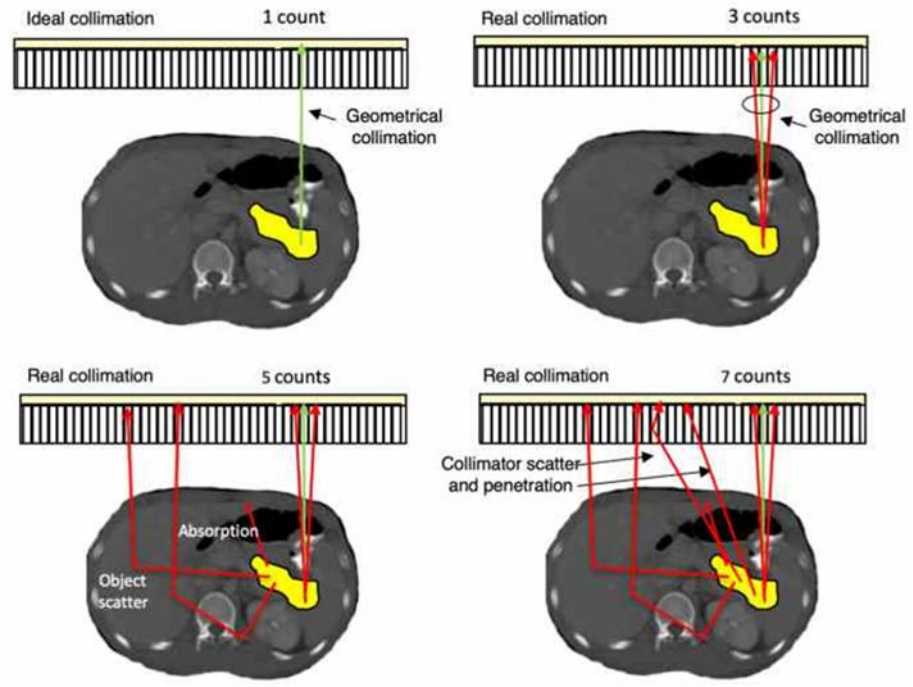

FIG. 4.5. Projected events and image degrading factors. The lines of response depicting the desired projected events are indicated in green. Courtesy of M. Ljungberg.

4.2.3.2. The PET system

PET is an imaging modality that generates tomographic images of the internal distribution of radiopharmaceuticals that are labelled with positron emitting radionuclides [4.8, 4.12, 4.15]. The positron dissipates its energy through electromagnetic interactions with the atomic electrons in the medium that it traverses. At some distance from the site of disintegration, which is defined by the range of the positron, it will very briefly combine with an electron to form a positronium atom and, since it is the antiparticle of the electron, the two particles will mutually annihilate. The most common result of this interaction is the generation of two 511 keV annihilation photons which travel in exactly opposite directions (180°) when the annihilation occurs for a positronium at rest. Most often, the positronium has a momentum which is conserved and transferred to the photon pair, leading to non-collinear photon trajectories with some deviation from a straight line. The simultaneous and anti-parallel nature of annihilation photon emission allows the application of coincidence detection (Fig. 4.6).

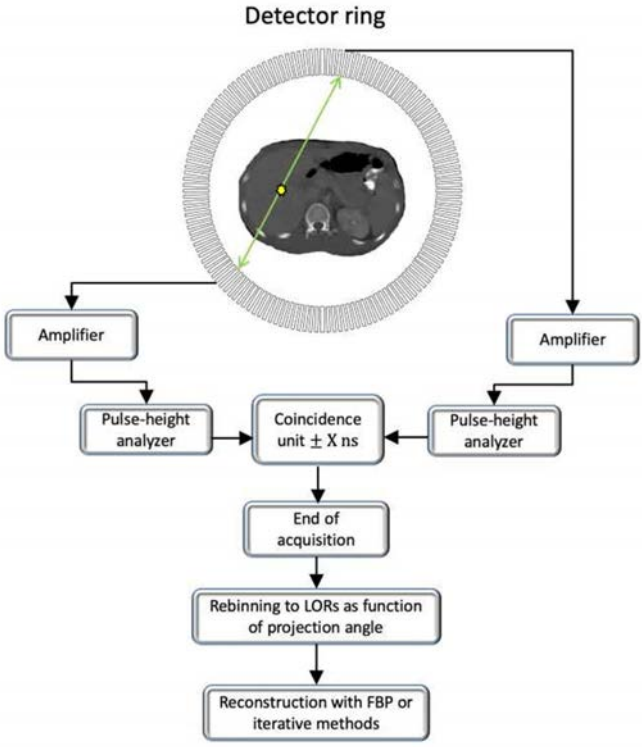

FIG. 4.6. Coincidence detection of annihilation photons and schematic flow chart describing the different components in a PET system. A PET system acquires lines of response (LORs) for all possible projection angles simultaneously. Therefore, a rebinning step is necessary to sort the LORs as a function of angle before reconstruction. FBP: filtered back projection. Courtesy of M. Ljungberg.

With coincidence detection, events are registered only if there is 'simultaneous' detection in two opposed detectors. Simultaneity in this sense is limited by the characteristics of the detectors and the associated electronics resulting in a coincidence time window, which is on the order of 5 nanoseconds for current commercially available PET systems. Coincidence detection provides 'electronic collimation' since a source has to be located in the envelope defined by the front face dimensions of the opposed detector crystal (Fig. 4.7(a)). This feature of coincidence detection eliminates the need for 'physical collimation' and results in substantially higher (~1 to 2 orders of magnitude) system sensitivity for a given spatial resolution than SPECT systems that rely on single photon detection. Coincidence events are registered when any pair of detectors in the system detects annihilation photons within the coincidence time window. The path connecting

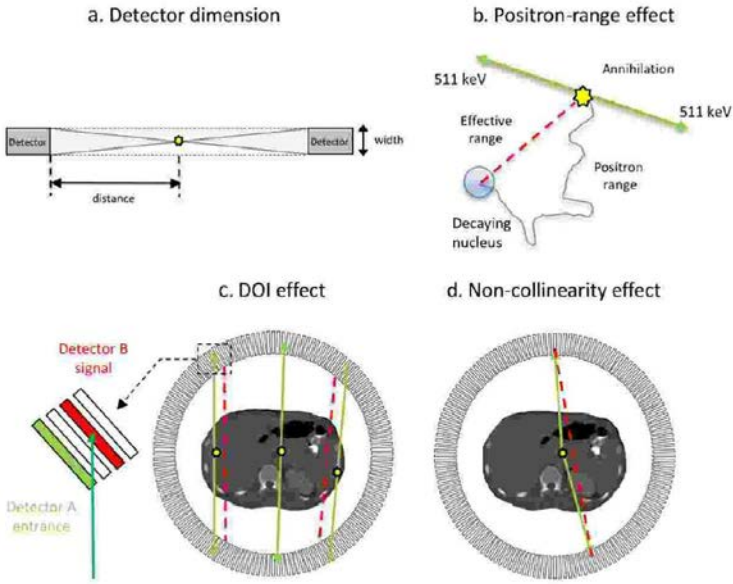

FIG. 4.7. Factors that degrade PET spatial resolution: (a) width of the individual detector elements; (b) positron range effects; (c) depth of interaction (DOI) effect; and (d) non-collinearity effect. Courtesy of M. Ljungberg.

these two detectors is the LOR for PET (green line in Fig. 4.6) and the signal intensity in the detector bin is proportional to the total activity along this LOR. Since coincidence events are possible between any opposed detectors, there are millions of LORs that sample the activity distribution in the patient providing the necessary projection information for tomographic reconstruction. Prior to the late 1990s, lead septa were used to constrain coincidence LORs within an axial plane (2-D PET). This approach allowed direct application of reconstruction algorithms and limited both random coincidences and scattered radiation at the expense of count sensitivity. In the pasttwo decades, new reconstruction algorithms have been developed that can effectively utilize the redundant information provided by 3-D sampling in which LORs from all detector planes are included. Sophisticated algorithms for removing scattered radiation have also been developed to the point where nearly all the PET tomographs in use today operate in 3-D mode.

PET systems consist of a large number of individual detector crystals that are configured to form a cylindrical bore with a length typically of 15 to 25 cm and a diameter of approximately 90 cm. The dimensions of each individual detector vary among manufacturers but are roughly $5 \times 5 \times 20$ mm^3. Recently, systems with detector width down to 3–4 mm have been introduced to improve spatial resolution [4.15]. Because the intrinsic efficiency for coincidence detection

depends on the product of the intrinsic efficiencies of the two detectors involved in the event, it is crucial that the detector material have a high intrinsic efficiency. This requires both high density and, even more importantly, high atomic number. Scintillators best fit these requirements.

Table 4.3 shows the properties associated withlutetium oxyorthosilicate (LSO) and yttrium doped lutetium oxyorthosilicate (LYSO) scintillators that are currently the preferred detectors used in commercial PET systems (properties of sodium iodide, used in SPECT systems, are included for comparison). In addition to intrinsic efficiency, other desirable characteristics include a fast scintillation response and high light output. In traditional PET systems, as with gamma cameras, the crystals are coupled with photomultiplier tubes, but some new systems couple the crystals with silicon photomultipliers (SiPMs) to achieve higher timing resolution [4.15]. In addition to the improved timing resolution, another attractive feature of SiPMs is that unlike photomultiplier tubes they are insensitive to magnetic fields and hence are well suited for integrated PET/magnetic resonance (MR) systems.

Events that are acquired on PET tomographs are classified in three ways: true coincidences, random coincidences and scattered coincidences. A true coincidence is a good event resulting from a single positron annihilation and where the source lies along the LOR (green line in Fig. 4.6).

TABLE 4.3. PROPERTIES OF SCINTILLATORS COMMONLY USED IN PET SYSTEMS IN COMPARISON WITH NaI(Tl) USED IN SPECT SYSTEMS

(adapted from [4.8]; courtesy of M. Ljungberg)

	LSO	LYSO	NaI(Tl)
Effective Z	66	64	50
Density (g/cm^3)	7.4	7.1	3.67
Thickness (mm) to achieve efficiency of 0.875	24	25	60
Light yield (relative %)	75	75	100
Decay constant (ns)	40	45	230

Note: LSO: lutetium oxyorthosilicate; LYSO: yttrium doped lutetium oxyorthosilicate; NaI(TI): sodium iodide.

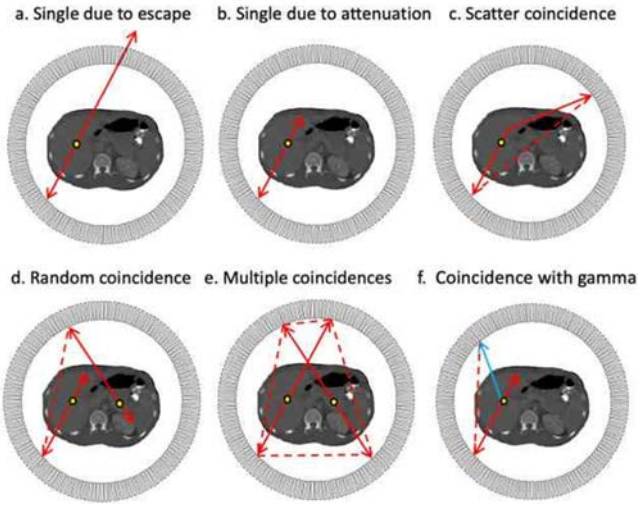

FIG. 4.8. Different types of undesired events that can occur in a PET system. The annihilation photons are indicated in red and prompt gamma rays are indicated in blue. The LORs from undesired coincidence events are indicated with red dashed lines. Note that for the example of multiple coincidences, four false coincidences are possible in addition to the two true coincidences and the camera may not be able to distinguish the true from the false coincidences. Courtesy of M. Ljungberg.

A random coincidence occurs when two uncorrelated annihilation photons from different sources just happen to hit opposing detectors within the coincidence time window. This generates a false LOR, which needs to be removed from the acquired data (Fig. 4.8). Random events are either estimated from the singles count rates at the individual detectors or from a coincidence timing window that is offset from the true coincidence time peak (delayed window). Another process that generates false LOR is scattered radiation. Either one, as shown in Fig. 4.8, or both of the annihilation photons can undergo Compton scattering within the patient. In 3-D PET, the scatter fraction can be greater than 40% and correction requires a sophisticated algorithm that uses photon transport equations to estimate the scatter component for each projection. A further complication in PET with positron emitters such as ^{124}I is coincidence between an annihilation photon and a prompt gamma ray that is associated with the decay.

Conventional PET makes no attempt to localize the source location along the LOR and consequently, projection data are back projected across the entire reconstruction volume. However, the rise time of the scintillation signal from LSO and LYSO is fast enough that the differential arrival times of detected signals participating in the LOR can be measured to within 500 picoseconds or

less [4.16]. This information is used in time-of-flight (TOF) PET and it provides rough localization of the source along the LOR. The TOF information can be used in the reconstruction to achieve a significant improvement in the signal to noise ratio. The improvement associated with TOF PET is more significant for larger sized objects. The spatial resolution of a PET system is determined primarily by the width of the individual detector elements (Fig. 4.7(a)) and the resolution (FWHM) is approximately half of the detector width. Most of the improvement in spatial resolution over the last two decades is the result of using smaller individual detectors. Spatial resolution for whole body PET tomographs typically ranges from 4 to 6 mm FWHM at the centre of the field of view. Factors which degrade spatial resolution include detector parallax (depth of interaction (DOI) effect), non-collinearity of the annihilation photons and the range of the positrons (Fig. 4.7). The parallax problem increases as the source is located toward the periphery of the field of view where the LOR passes obliquely through a number of detectors. Because the depth of the interaction within the interacting detectors is unknown, the exact location of the LORs is unknown. Much research has been devoted to obtaining depth of interaction information, but that has not been incorporated into any widely used commercial system. The non-collinearity effect refers to the fact that annihilation photons are typically not emitted at exactly 180°. The dispersion of the trajectory angle between the annihilation photons adds about 2 mm FWHM to the spatial resolution of whole body PET systems [4.8]. A further degradation associated with annihilation photon physics is the distance that a positron travels prior to annihilation. This positron range effect depends on the energy of the emitted positron and is most significant for higher energy positron emitters such as ^{82}Rb (3.4 MeV vs 0.63 MeV for ^{18}F).

It should be understood that the spatial resolution specifications are for high count density and that the spatial resolution in actual studies is likely to be worse because of the application of smoothing in order to suppress noise in the reconstructed images. Objects that are smaller than twice the spatial resolution (FWHM) of the imaging system will have altered quantitative results because of partial volume effects. As will be discussed in Section 4.4.3, resolution recovery and the application of recovery coefficients can be used to compensate for this effect.

4.2.3.3. Hybrid or multimodality imaging systems

The clinical availability of hybrid (or multimodality) SPECT/CT and PET/CT imaging systems that enable the fusion of physiological and anatomical information has enhanced the accuracy of quantitative emission tomography. In particular, the anatomic image set facilitates the generation of attenuation maps for non-uniform attenuation correction. Computed tomography (CT)

based attenuation maps from SPECT/CT and PET/CT systems generated with negligible acquisition time have replaced those generated by long acquisitions with a transmission source in the past as they offer higher spatial resolution and contrast. Additionally, the anatomic information can be used for some scatter and partial volume correction methods. The sequential acquisitions during a single imaging session with a hybrid system eliminate much of the error and complexity associated with co-registration of functional and anatomical images acquired on different systems.

In addition to improving quantitative imaging in general, the availability of these hybrid systems has facilitated patient-specific 3-D dosimetry. If SPECT/CT or PET/CT is performed at multiple time points to determine pharmacokinetics, CT-CT registration can be used to co-register the emission images. The CT can also be used to derive the density map that is coupled with co-registered PET or SPECT based activity maps, required for patient-specific dosimetry using methods such as Monte Carlo radiation transport. Furthermore, CT based segmentation can be used to define the volume of interest (VOI) for estimating the mean absorbed dose or to generate dose–volume histograms) for the target region. However, in some cases segmentation can be challenging, especially for poorly defined lesions, because unlike diagnostic CT, CT in hybrid systems is typically performed in low dose mode and without contrast enhancement. There have been numerous studies reporting on clinical dosimetry in radionuclide therapy using both pre- and post-therapy images acquired on SPECT/CT and PET/CT systems and examples are presented in Medical Internal Radiation Dose (MIRD) Pamphlets Nos 24 and 26 [4.17, 4.18]. When SPECT/CT or PET/CT is performed at multiple time points for dosimetry applications, consideration of the radiation exposure from the CT component of the study is especially important. If the CT is performed only to generate density and attenuation maps, the tube current can be reduced substantially without significant loss of accuracy [4.19]. If needed, a higher quality CT for segmentation can be performed at one imaging time point with lower dose CT for attenuation correction only at other time points.

While SPECT/MR is still in the research stage, PET/MR has become available commercially. For quantitative imaging, the advantage of PET/MR over PET/CT is the increased soft tissue contrast, simultaneous PET and MR acquisition and potential for improved motion correction [4.20]. However, generation of accurate patient-specific attenuation correction maps, a major requirement for high quantitative accuracy, is a challenge because unlike CT, magnetic resonance imaging (MRI) cannot directly assess tissue density. Methods for MRI based attenuation correction implemented on commercial systems and under development often require a priori information on the object [4.21]. Recently, there has been much interest in deep learning methods for addressing the challenges of PET attenuation correction [4.22]. Some studies report on

convolutional neural networks that are trained to generate pseudo-CT images from the MR images. Reports on the use of PET/MR for clinical radionuclide therapy dosimetry have been limited to ^{90}Y radioembolization [4.23, 4.24] thus far.

4.3. TOMOGRAPHIC IMAGE RECONSTRUCTION

4.3.1. General concepts

The SPECT and PET imaging systems discussed in the previous section provide 2-D angular views measured by detectors that rotate around the patient or are placed around the patient in a ring geometry. The fundamental challenge in emission tomographic imaging is how to make accurate estimates of the 3-D internal distribution of the radiopharmaceutical concentration within the patient from these external measurements. This process, known as tomographic image reconstruction, is possible if the appropriate external data are collected from a sufficient number of angular views. The appropriate data required are LORs or line integrals. A line integral represents the linear sum of the parameter under consideration (measured counts) along a particular trajectory through the internal distribution (Figs 4.5 and 4.6). Collections of line integrals for a particular geometry (e.g. parallel or fan beam) at a given angle are referred to as projections. A complete set of projections that span viewing angles over at least 180° is needed to obtain accurate tomographic reconstructions. For SPECT imaging, the projections are typically (though not always) acquired sequentially as the gamma camera rotates around the patient. The projection geometry is determined by the collimation, which is most often parallel. In PET imaging, the coincidence LOR between a given detector and all the opposed detectors that populate a ring determine the projections. These projections have a fan beam geometry but may be re-binned into a parallel geometry. Under simplified assumption of no photon scatter or attenuation the counts recorded for the LOR in a projection are proportional to the summed activity along the LOR. However, because this is not the case in reality, compensation for image degrading physical factors must be applied in order to achieve accurate tomographic images.

It is often common to reorganize the data from PET and SPECT acquisitions into datasets referred to as sinograms (because of the sinusoidal pattern each point in the projections forms when displayed in this way). A sinogram represents all the acquired data for a particular axial position in one image. Each row in the sinogram corresponds to a particular projection angle, and the values along the rows represent the integrated signal for a particular LOR for that angle. The first row represents the first projection angle while the last row represents the last angle.

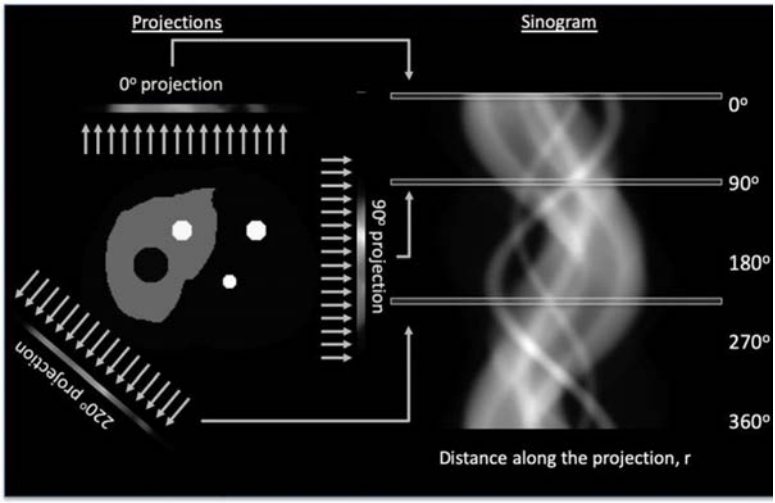

FIG. 4.9. Projection profiles for a tomographic section of the object displayed as a sinogram. The sinogram is a stack of projections ordered by angle. The object corresponds to a liver with a cold and hot spot and two hot spots outside the liver volume. Courtesy of M. Ljungberg.

Figure 4.9 exemplifies a sinogram for a specific tomographic section. The sinogram can be very useful for detecting motion during acquisition since unexpected motion results in a discontinuity that is relatively easy to identify in the otherwise smooth shapes.

The mathematical details of SPECT and PET tomographic image reconstruction are beyond the scope of the current textbook and these details can be found in texts dedicated to emission tomography [4.25, 4.26]. Attenuation compensation and corrections for other factors that degrade the quality of tomographic images will be discussed after the general theory of image reconstruction is presented.

4.3.2. The principles behind back projection

Because the number of counts in a projection bin reflects the number of detected events from photons emitted along a specific LOR for a certain angle (ignoring attenuation), the simplest way of estimating the underlying source

distribution is to back project the detected events along the same trajectory as they were measured. Back projection is mathematically written as:

$$f(x,y) = \int_0^{\pi} p(r,\theta)\,\mathrm{d}\theta \tag{4.1}$$

where $f(x, y)$ is the estimated tomographic source distribution, r is the lateral position of the projection bin and $p(r,\theta)$ represents the measured signal at r acquired for angle θ. Simple back projection does not yield an accurate estimate of the source distribution because the method is a purely additive process that projects data along evenly distributed lines. This results in a blurred image where the amount of blurring depends on the reciprocal of the distance from the true source location. This effect is exemplified by the top row of images of Fig. 4.10. Here, direct back projection is made for 8, 16, 32, 64 and 128 projection angles evenly distributed over 360° for Monte Carlo simulated projection data corresponding to a liver phantom with a cold spot and lesions.

The solution for the severe blurring of direct back projection is to apply a mathematical filter to the projection data, which is constructed as the inverse of the blurring function. The filtering can be performed by convolution in the spatial domain or by a multiplication in the Fourier domain. The appropriate filter in the Fourier domain is called a ramp filter, $|\upsilon|$ (where υ denotes spatial frequency),

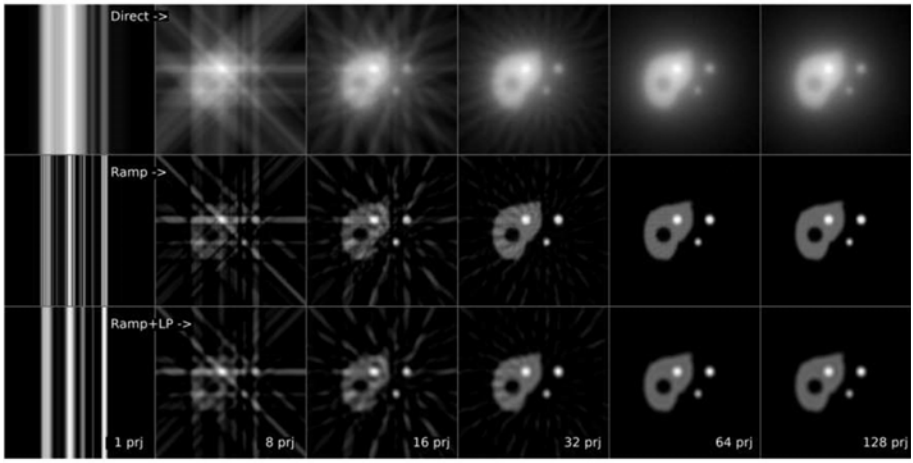

FIG. 4.10. SPECT reconstruction for 8, 16, 32, 64 and 128 projection angles for direct back projection (upper row), a ramp-filtered reconstruction (middle row) and ramp-filter combined with a low-pass Butterworth filtered reconstruction (bottom row). The filter reduces noise but also degrades spatial resolution. Projections were simulated using the SIMIND Monte Carlo code and correspond to the object of Fig. 4.9 with ^{99m}Tc. Courtesy of M. Ljungberg.

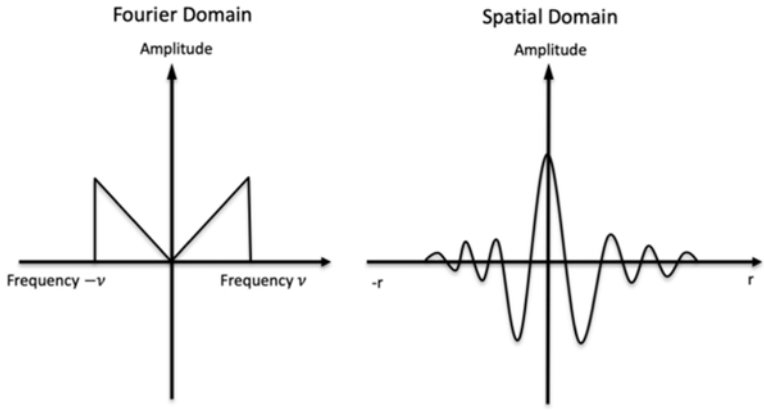

FIG. 4.11. The ramp filter (left) used in the frequency space and its equivalent spatial version (right). Note the negative lobes that reduce the blurring due to the back projection methods. This reduction can be seen in the middle row of Fig. 4.10. Courtesy of M. Ljungberg.

because the filter increases linearly in amplitude as a function of the spatial frequency. In the spatial domain, the equivalent filter is a sinc-shaped function (Fig. 4.11), which includes negative values that reduce the reconstructed image values that are wrongly allocated by the back projection algorithm.

Filtered back projection (FBP) can mathematically be described by the following equation:

$$f(x,y)=\int_0^{\pi}\mathcal{F}^{-1}\left[|\upsilon|\mathcal{F}\left\{p(r,\theta)\right\}\right]\mathrm{d}\theta \tag{4.2}$$

where $\mathcal{F}$ and $\mathcal{F}^{-1}$ symbolize the forward and inverse Fourier transforms, respectively. One of the problems with using a ramp filter is that it is a high-pass filter amplifying signals of high frequencies where statistical fluctuations (noise) are dominant resulting in noise amplification. One common way of reducing noise amplification is by applying a low-pass filter. In the frequency domain, the low-pass filter, *lp(v),* can be directly applied to the ramp filter by multiplication:

$$f(x,y)=\int_0^{\pi}\mathcal{F}^{-1}\left[lp(\upsilon)|\upsilon|\mathcal{F}\left\{p(\mathrm{r},\theta)\right\}\right]\mathrm{d}\theta \tag{4.3}$$

The effect of the low-pass filter can be seen in the lower row of Fig. 4.10.

4.3.3. Limitations with filtered back projection

FBP has been successfully used for many years and this is partly because of its relative simplicity and speed. However, there are several limitations with the method. The ramp filter will only successfully remove the blurring effect if an infinite number of projection angles are used. However, for clinical applications, due to time constraints for the patient, the number of projection angles and acquisition time per projection are both limited and therefore some streak-like artefacts emanate in the final image when ramp filtering is applied. Although some approximate methods are available for correcting for attenuation and spatial resolution, FBP cannot accurately compensate for image degrading physical effects such as non-homogeneous attenuation, scatter or blurring due to the collimator resolution.

Three dimensional PET requires a sophisticated reconstruction algorithm to make use of all the acquired data. Coincidence events that are acquired within the plane of a single detector ring are referred to as direct planes, and these provide sufficient information to perform the reconstruction using conventional reconstruction algorithms similar to those of SPECT. Three dimensional PET also acquires coincidence events between separate rings that sample the object obliquely and provide about a factor of four increase in sensitivity. The incorporation of this information into the reconstruction was an early challenge for PET. A 3-D filtered back projection algorithm was developed by Colsher [4.27] and this is available as a reconstruction option on most PET scanners. Although 3-D filtered back projection is relatively fast, it is susceptible to streak artefacts and is not well suited for incorporating corrections such as resolution recovery.

4.3.4. Iterative reconstruction

An alternative to analytical image reconstruction methods such as FBP is iterative reconstruction. In contrast to FBP, iterative methods can account for the noise structure in the measurements and include realistic models of the emission and detection processes. In iterative reconstruction, one starts with an initial estimate of the source distribution (usually a uniform distribution). The algorithm generates projections from this source distribution by modelling the imaging system. This operation is called forward projection and is the inverse of the previously described back projection. The modelling can include all the physical properties of photon transport and system geometry that are known. The projections generated by this process are compared to the actual acquired projection data. The pixel-wise ratios of the projections are back projected, and the image formed is used to generate an updated estimate. The process of comparing and updating repeats (iterates) until the resulting reconstructed image

estimate approaches convergence. Iterative reconstruction is computationally intensive because, typically, a large number of iterations that involve projection and back projection steps are needed before convergence to an acceptable image.

In iterative reconstruction the model that describes the emission and detection process that relates the object activity distribution to projection measurements is referred to as the system matrix. The system matrix describes the probability that photons emitted from specific voxels within the object distribution will be detected at specific pixels in the projections. In addition to accounting for the system geometry, factors such as attenuation can be incorporated into the system model by simple weighting of the matrix elements. Compared with analytical methods, iterative methods that directly model the system yield reconstructed images with improved noise characteristics and improved quantification accuracy, which are both important for 3-D dosimetry.

4.3.4.1. Maximum-likelihood expectation-maximization (ML-EM) algorithm

Iterative reconstruction consists of a criterion and an iterative algorithm to find the activity distribution that optimizes this criterion. In other words, the optimization of the criterion provides the estimation of the activity distribution which best matches the measured projection data. The most widely used criterion is the maximum likelihood (ML) criterion, which seeks the activity distribution that maximizes the Poisson likelihood of the projection data. In commercially available nuclear medicine imaging systems, iterative ML optimization is usually implemented in the form of the maximum-likelihood expectation-maximization (ML-EM) method introduced by Shepp and Vardi [4.28] and the closely related -ordered-subsets -expectation-maximization (OS-EM) method [4.29]. The ML-EM algorithm can be generally expressed by the following iterative equation:

$$f_j^{n+1} = \frac{f_j^n}{\sum_i a_{ij}} \sum_i a_{ij} \frac{p_i}{\sum_k a_{ik} f_k^n} \tag{4.4}$$

where f_j^n and f_j^{n+1} are the current and the new estimates, respectively, of the image value at the *j*th voxel, p_i is the measured projection data at the *i*th pixel and a_{ij} are the elements of the system matrix. The steps of the ML-EM algorithm are shown by the block diagram of Fig. 4.12.

In its simplest form assuming that no photon attenuation, no scatter contribution and no collimator blur occur, $a_{ij}$is unity along the ray of view for the current projection. In its most general form, the system matrix considers all physical and geometric effects that affect the detected event. Thus, the probability for the photons being absorbed or scattered along the path needs to be included along with effects such as collimator penetration. Combined, these yield a

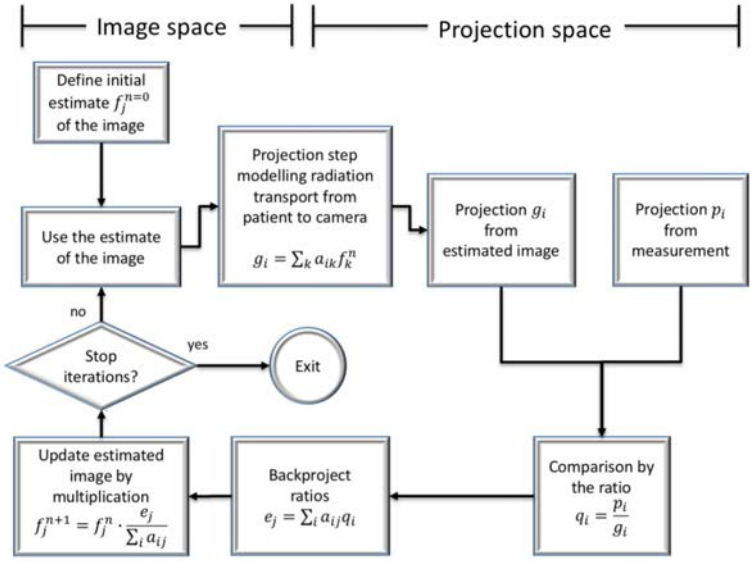

FIG. 4.12. Flow chart describing the main steps of the ML-EM algorithm. Courtesy of M. Ljungberg.

probability for a photon starting at a certain location in the object to be detected in a particular pixel element. These probabilities depend on the projection angle, the patient geometry and the source distribution. Pre-calculating these probabilities leads to a large set of data that increases with the acquisition matrix size and the number of projection angles.

The right side of Eq. (4.4) represents the ratio between the measured and estimated projections that is back projected to generate what is referred to as an error image. After normalization, the error image is multiplied with the previous estimate of the image and the procedure is repeated. This iterative procedure converges to a stable image as the updated image estimate gets closer to the actual source distribution (Fig. 4.13), thus producing estimated projections that more closely approximate the measured projections and ideally the ratio between the two projections should converge to unity. However, continuing the iterations increases the noise levels in the reconstructed image.

4.3.4.2. Ordered-subsets expectation-maximization (OS-EM) algorithm

The number of iterations required for ML-EM to converge is large and this was in the past a problem that prevented the method from being used clinically. However, a method to accelerate the process was introduced by Hudson and

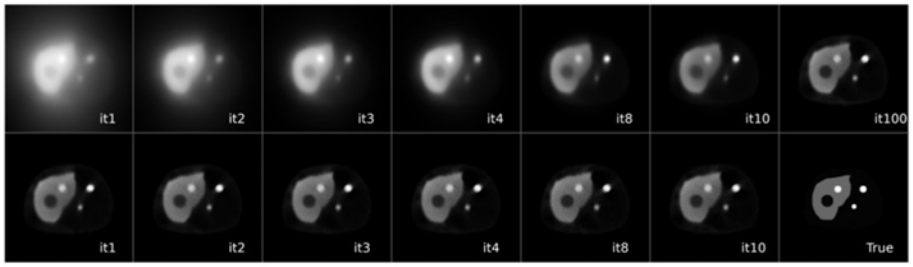

FIG. 4.13. The improvement in the estimate of the source distribution with number of iterations for ML-EM (top row) and OS-EM (bottom row) for the phantom of Fig. 4.9. Note the faster convergence for OS-EM when compared to ML-EM. The number of angles per subset was 8 and the number of updates per iteration for the OS-EM algorithm was 16. Courtesy of M. Ljungberg.

Larkin in 1994 referred to as OS-EM [4.29] and since then has been widely used by different vendors. The fundamental difference between OS-EM and ML-EM is that with OS-EM only a subset of the total dataset is used for each image update. Different subsets of the projection data are used in subsequent sub-iterations until all projections are used. This leads to an acceleration factor compared with ML-EM that is roughly equal to the number of subsets that are used. For 128 projections with a subset size (number of projections per subset) of 8, the number of subsets will be 16 ($8 \times 16 = 128$) and the acceleration factor will be 16.

It can be seen from Fig. 4.13 that the shape of the images stabilizes as the number of iterations increases. This is also true for the count levels in the images. Figure 4.14 compares the convergence of the sum of counts within five volumes of interest (VOIs) corresponding to three hotspots, the cold spot and the liver as a function of number of iterations. The values obtained for each iteration are normalized by the sum counts corresponding to using 100 iterations. With OS-EM, convergence is reached at a lower number of iterations in all cases. One important property to consider is the non-linear convergence. As is evident from Fig. 4.14, large objects converge more rapidly than small objects. In general, more iterations are required for convergence when the system model includes image degrading physical factors.

4.3.4.3. Resolution — noise trade-off

When reconstructing objects from noisy projection data the noise level and edge artefacts tend to increase as the number of iterations increase. The simplest option to overcome this is to stop the iteration procedure after only a few iterations; however, this may result in loss of spatial resolution and quantitative accuracy. Alternatively, the projection data can be pre-filtered with a low-pass

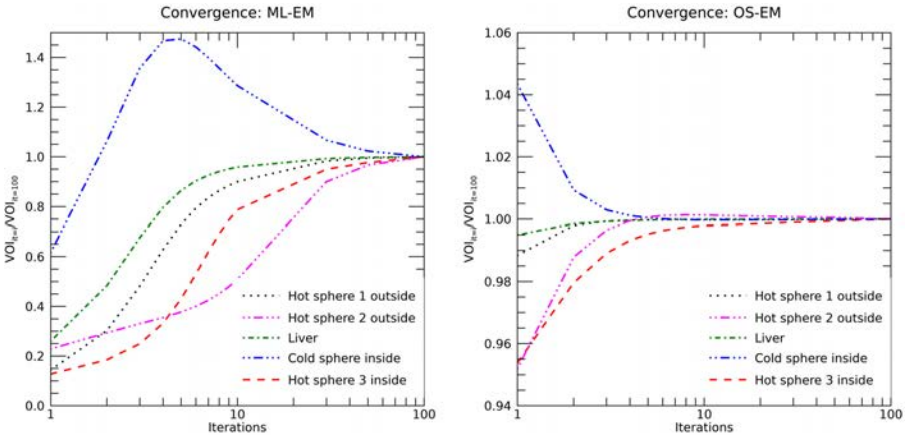

FIG. 4.14. The sum of counts in the VOIs relative to convergence (100 iterations), as a function of number of iterations for ML-EM (left) and OS-EM (right). The results from each iteration have been normalized to the result at 100 iterations. Note that the scale on the ordinate is different between the two graphs. The number of angles per subset was 8 and the number of updates per iteration for the OS-EM algorithm was 16. Courtesy of M. Ljungberg.

filter prior to the reconstruction, but then the Poisson noise characteristic from which both ML-EM and OS-EM methods are derived will be lost. The noisy reconstructed images can also be post-filtered with a smoothing 3-D filter, an option that is widely available in commercial software. However, low-pass filtering always reduces high-frequency components, regardless of whether they reflect true fine details or local changes due to noise, yielding a loss of spatial resolution and quantitative accuracy. The number of iterations and the amount of smoothing should be determined by considering the application and the trade-off between resolution and noise. When the quantity of interest is the mean absorbed dose to a target region, a larger number of iterations can be used because averaging over a VOI will tend to reduce the effects of noise and edge artefacts (both of which increase with the iteration number). However, when the quantity of interest is 3-D dose metrics such as the dose–volume histogram, a smaller number of iterations may be optimal because of sensitivity to noise [4.30].

An alternative to noise regularization by post-filtering or stopping iterations early is to use Bayesian algorithms that incorporate prior information regarding the expected noise. The most widely used is the maximum a posteriori (MAP) algorithm [4.31]. The MAP equation is similar to the ML-EM equation (4.4) with an additional (prior) term in the denominator that constrains the difference between neighbouring voxel count values, hence favouring smooth images with less noise. The MAP-EM algorithm [4.32] is expressed as:

$$f_j^{n+1} = \frac{f_j^n}{\sum_i a_{ij} + \beta \left. \frac{\partial U(\mathbf{F})}{\partial f_j} \right|_{\mathbf{F}=\mathbf{F}^n}} \sum_i a_{ij} \frac{p_i}{\sum_k a_{ik} f_k^n} \tag{4.5}$$

The term U, often called an energy function, determines the probability for a certain source distribution a priori. The constant β is a regularization parameter that determines the balance of weight between the measured data and the impact of the prior. In the one-step-late (OSL) procedure (Eq. (4.5)), the derivative term is evaluated from the previous image estimate. If co-registered anatomical information is available from high resolution CT or MR, these images can then provide prior information to control PET and SPECT resolution loss due to regularization. Typically, the anatomical information is used to constrain smoothing to within organ boundaries defined by the anatomical data.

4.4. COMPENSATION FOR THE MAIN IMAGE DEGRADING FACTORS

Due to noise and physical factors, such as attenuation and scatter, there is always inconsistency between the measured emission data and the true source distribution in the object. The main image degrading factors in emission imaging and compensation for these effects are discussed next.

4.4.1. Photon attenuation

Photon attenuation refers to all interactions that lead to a change in direction and/or energy of the emitted photons as they pass through the body. Photon attenuation thus affects the expected counts or pixel intensity measured by the detector. The expected reduction in counts due to attenuation in tissue equivalent material as a function of energy and tissue thickness is demonstrated in Chapter 2 (Fig. 2.3). The interactions that lead to attenuation can be photoelectric absorption resulting in the disappearance of the photon, Compton scattering resulting in a change in both energy and direction or coherent scattering resulting in only a change in the direction. For photon energies above 1.022 MeV, rarely encountered with therapy radionuclides, pair production can also occur. For a monoenergetic narrow beam of photons of energy E and beam intensity n_o incident on an absorber of thickness d composed of an element of atomic number Z, the fraction of photons that pass through the absorber is given by:

$$\frac{n(d)}{n_o} = e^{-\int_0^d \mu(Z,E)dx} \tag{4.6}$$

where n is the intensity of a transmitted narrow beam and μ is the linear attenuation coefficient, which is an energy and tissue dependent measure of photon attenuation per unit distance (cm^{-1}, for example). For a uniform medium the integral in Eq. (4.6) is replaced by μd.

4.4.1.1. Planar attenuation correction

The most common method for attenuation correction with planar imaging is the conjugate view technique based on measuring two opposing (typically, anterior and posterior) projection images with a gamma camera. By taking the geometric mean of these two measurements it is possible to obtain an expression for counts corrected for attenuation, C_{corr}, that is independent of source depth [4.33]:

$$C_{corr} = \sqrt{\frac{C_{Ant} \cdot C_{Post}}{e^{-\mu t}}} \cdot \left[\frac{\frac{\mu d}{2}}{\sinh\left(\frac{\mu d}{2}\right)} \right] \tag{4.7}$$

where C_{Ant} and C_{Post} are count rates corresponding to ROIs delineated in the raw anterior and posterior projections, t is the thickness of the patient at the source location, and $e^{-\mu t}$ is the transmission fraction through the average thickness t along the defined ROI assuming uniform attenuation μ. The term in brackets accounts for the self-attenuation on the source of thickness d and is ~1 for small source volumes. The transmission fraction is typically determined from the ratio of the measurements with an externally mounted source performed with and without the patient present.

Equation (4.7) was derived assuming a narrow beam geometry without significant contribution from scattered radiation. Correction for scattered radiation can be performed as described in MIRD 16 [4.33]. Furthermore, typically, background corrections are needed because activity in tissue overlying or underlying the structures of interest will contribute with counts to the anterior and posterior views, thereby overestimating the activity.

4.4.1.2. SPECT and PET attenuation correction

Attenuation correction in SPECT and PET is discussed in Refs [4.34, 4.35]. The two main classes of attenuation correction are based on the use of uniform

or non-uniform linear attenuation coefficients. For the uniform correction a fixed body contour is assumed, or the contour is estimated from the emission data and a constant value of the linear attenuation coefficient is assumed within the contour. Ideally, a patient-specific non-uniform attenuation map should be measured for each patient because the tissue in the body is heterogeneously distributed with different densities for lungs, soft tissue and bone. The attenuation map is a distribution of the non-uniform linear attenuation coefficients within the body contour. Once the attenuation coefficients are determined they can be included as weighting factors in the system matrix a_{ij} for the forward and back projection steps (Eq. (4.4)).

In PET, the amount of attenuation is independent of the source location and depends only on the total path length of the LOR through the body. This is a consequence of the fact that the two annihilation photons must traverse the full thickness of the body along the LOR before being measured by the opposing detectors, irrespective of where the decay originated. Correction factors for PET attenuation can be obtained by a transmission measurement with an external photon source directed towards the body along each LOR without and with the patient present in the field of view. In SPECT, unlike in PET, the amount of attenuation is a function of source location because when only a single photon is emitted, the distance the photon must traverse through the body before detection depends on the point of origin of the decay. Therefore, unlike in PET, SPECT attenuation correction cannot be performed by simple multiplication by transmission factors. Attenuation coefficient maps for SPECT are estimated based on transmission measurements followed by tomographic reconstruction of the transmission data.

One of the main advantages with iterative reconstruction over analytical methods is that image degrading physical effects can be included in the system model, which then automatically acts as a compensation for that effect. Physical factors can be included in the system model either as multiplicative factors or as additive factors. For example, typically, attenuation is included as a multiplicative factor in the system matrix while scatter is included as an additive term in the system model because inclusion of scatter in the system matrix is computationally very demanding. Typically, attenuation and geometric effects are incorporated in the system model for both the forward and back projection steps, while for computational efficiency, scatter is only incorporated in the forward projection step.

4.4.1.3. CT based attenuation correction

In the past, external radionuclide sources, such as ^{68}Ge for PET or ^{153}Gd for SPECT, were used to obtain transmission projections to generate non-uniform

attenuation maps. With the advent of combined SPECT/CT and PET/CT systems, the co-registered CT is used to generate patient-specific attenuation maps for the emission image. The advantages of using an X ray source over a radionuclide source are superior spatial resolution, high signal to noise ratio, lack of cross talk from the administered radionuclide and a fast acquisition.

The CT numbers or Hounsfield units (HUs) are directly related to the linear attenuation coefficient at the effective energy of the polyenergetic X ray beam. A calibration curve is needed to convert the linear attenuation coefficient values at the X ray effective energy to the values corresponding to the gamma ray energies in SPECT or 511 keV in PET. The CT image typically also needs to be down-sampled to the SPECT or PET image matrix size and slice thickness matched when generating the CT derived attenuation map. To convert the attenuation coefficient values from the X ray effective energy to the photon energy of the emission image, a calibration measurement is typically performed by scanning a phantom consisting of multiple tissue-equivalent rods of known composition [4.34]. The calibration curve is then generated by plotting the mean CT number corresponding to each rod versus the known attenuation coefficient at the photon energy of interest. Despite the advantages and ease of CT based attenuation correction (CT-AC), potential artefacts need to be considered, including those caused by mis-registration between the CT and the emission study, CT truncation, respiratory motion and the presence of metal inserts or a contrast agent.

4.4.2. Scatter contribution

Compton scattering and coherent scattering (important only at low photon energies) lead to loss of contrast that can significantly impact visual image quality and quantitative accuracy of SPECT and PET. This is because photons that originate from decays some distance away from an LOR can be scattered into the LOR and then be detected in the same projection bin as the ideal unscattered (primary) photons (Figs 4.5 and 4.8). Typically, scatter events contribute to 30–50% of all events in the energy window in SPECT and 40–60% in 3-D PET [4.36]. Scatter counts do not reflect the true origin of the photon but cannot be avoided because of the finite energy resolution of the detector. Because of the poor energy resolution, it is necessary to use a relatively wide acquisition window to avoid loss of counting statistics. The energy resolution of NaI(Tl) scintillator based systems is ~10% FWHM leading to a typical energy window setting of about 15–20% for SPECT. Figure 4.15 shows two energy/pulse height distributions without (left) and with (right) simulation of a typical energy resolution for a NaI(Tl)) based gamma camera. While the main interaction type in the detection medium for SPECT below 200 keV is photoelectric absorption,

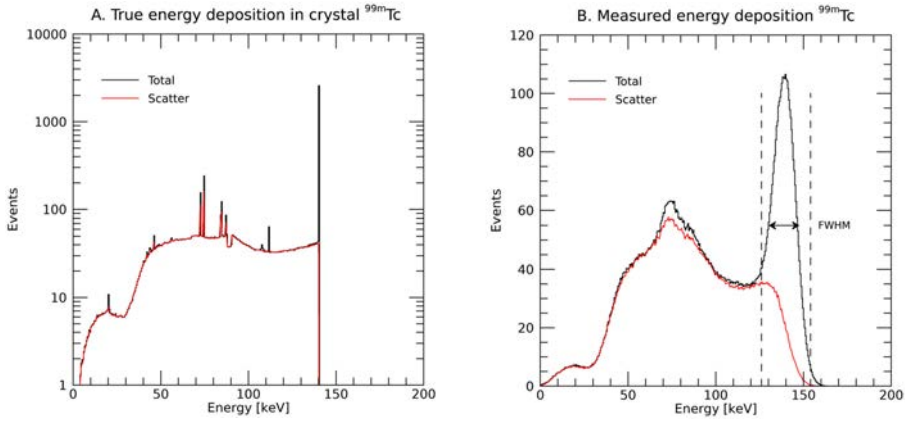

FIG. 4.15. Monte Carlo simulated energy spectrum of the true deposited energy of ^{99m}Tc in the NaI(Tl) crystal (left). Due to the stochastic nature of the conversion from deposited energy to scintillation light and the following conversion to electrical signals in the photomultiplier tubes, the uncertainty in the energy measurement will be quite large and in the order of 9–10% FWHM at 140 keV (right). If a wide energy window is used (usually with a width of ~2 FWHM) for acquiring counts (as is indicated in the right graph), then there will be a fraction of photons scattered in the patient that also will be accepted in the energy window. In this particular example, the fraction of scatter in the energy window is about 30%. Courtesy of M. Ljungberg.

in PET it is Compton scattering, due to the higher energy of the annihilation photons. Hence, to increase detection efficiency for photons that undergo scatter in the crystal, the acquisition window used in PET is substantially wider than that used in SPECT. Apart from energy resolution and energy window setting, the ratio of the number of scatter events to total number of events within the energy window (scatter fraction) depends on the material composition of the object and the source location within the object.

4.4.2.1. Scatter compensation — planar and SPECT

Several methods for SPECT scatter compensation have been developed over the years and are summarized in Refs [4.37] and [4.38]. A first order correction for scatter can be made by replacing the narrow beam attenuation coefficient with a broad beam attenuation coefficient, but this approach does not account for the spatial distribution of scattered events. The most commonly used methods in the clinic are energy window based where data acquired in additional acquisition windows are used to estimate the scatter in the main photopeak window. In the dual energy window method suggested by Jaszczak et al. [4.39] the scatter in the main energy window was compensated for by subtracting the counts acquired

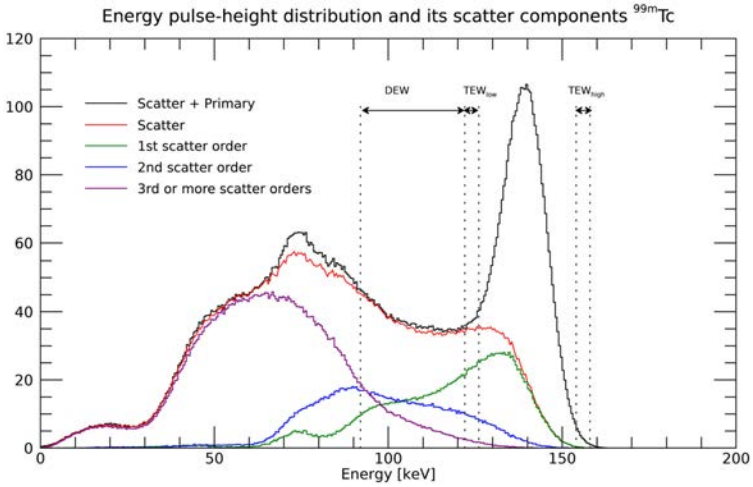

FIG. 4.16. Monte Carlo simulated energy spectrum where the scatter distribution has been separated as curves for different scatter orders. The vertical lines indicate typical energy window settings for dual energy window and TEW methods. Note that for the dual energy window setting, more events that originate from multiple scattering are collected in the scatter window as compared to the photopeak energy window. Courtesy of M. Ljungberg.

in a wide scatter window after scaling by a constant factor. This method had limitations since the lower energy window acquired more multiple-scattering events that had a different distribution as compared to the small angle scatter events that appear in the photopeak window (Fig. 4.16). Ogawa et al. [4.40] suggested an alternative, called the triple-energy window (TEW) method. This method uses two narrow energy windows adjacent to the main window (Fig. 4.16) to estimate the scatter counts in the main window. The pixel level TEW scatter estimate is expressed as:

$$g_i^{\text{scatt}} = \left[\frac{g_i^{\text{lower}}}{w_{\text{lower}}} + \frac{g_i^{\text{upper}}}{w_{\text{upper}}} \right] \cdot \frac{w_{\text{peak}}}{2} \tag{4.8}$$

where g_i^{lower} and g_i^{upper} are the lower and upper energy scatter window counts at pixel i and w_{peak}, w_{lower} and w_{upper} are the photopeak and scatter window widths.

When there is little or no contribution from down scatter by photons with energy above the photopeak window, the upper energy window is typically not used (e.g. for the ^{99m}Tc photopeak and the 208 keV photopeak of ^{177}Lu). The TEW scatter correction (TEW-SC) has demonstrated high accuracy for multiple radionuclides' applications, including dosimetry (see Refs [4.41–4.43]), but this method can be noisy because of the narrow scatter windows.

An alternative to simple energy window based scatter correction in SPECT is the model based approach. These methods include analytical calculations using the Klein–Nishina formula for Compton scattering [4.44] and the effective source scatter estimation (ESSE) method [4.45] where a scatter profile is calculated from an attenuation map of the patient and an initial SPECT reconstruction (without scatter correction) of the activity distribution. The ESSE method requires access to a Monte Carlo program to calculate the scatter kernels since it is challenging to experimentally measure them. The method assumes that the contribution from large-angle scattering is negligible. Other more sophisticated approaches to scatter modelling, which are expected to provide the best quantitative accuracy, include Monte Carlo simulation based methods [4.46, 4.47]. These methods require extensive computations and have been mostly used in research studies. However, as computational power advances, they are expected to enter the clinical arena in the near future. An advantage of model based methods is that they do not require additional acquisition windows and optimization of parameters such as the window width and filtering. In addition, window based methods are not well suited for bremsstrahlung SPECT because of the continuous energy distribution of the photons (discussed in the next chapter), hence the model based correction is well justified in this case. Recently, machine learning based methods have been evaluated for SPECT scatter estimation, including convolutional neural networks trained to address the challenges of bremsstrahlung scatter [4.48].

The scatter contribution estimated from different methods can be subtracted from the acquired emission projections prior to reconstruction. However, for both SPECT and PET, to improve noise properties, it is recommended to include scatter directly in the iterative process as an additive term in the forward projection step instead of subtraction [4.38]. The scatter estimate at voxel j, g_i^{scatt}, can be incorporated into the previously described ML-EM equation as follows:

$$f_j^{n+1} = \frac{f_j^n}{\sum_i a_{ij}} \sum_i a_{ij} \frac{p_i}{\sum_k a_{ik} f_k^n + g_i^{\text{scatt}}} \tag{4.9}$$

Any scatter estimate (e.g. energy window based, or model based) can be included in Eq. (4.9) in this manner. Additionally, for model based scatter correction methods, including Monte Carlo based, the scatter term, g_i^{scatt}, can be updated with improved estimates during the iterative process.

4.4.2.2. Scatter compensation — PET

In PET, either one or both of the annihilation photons can undergo Compton or coherent interactions and contribute to the image. The fraction of scattered photons in 3-D PET can be higher than in SPECT because a wider energy window

is used due to the poorer energy resolution of the PET scintillators and to include events that undergo Compton scatter in the crystal, which is the main detection mode for 511 keV photons. Scatter compensation methods in PET have been reviewed by Zaidi and Montandon [4.49]. In 2-D PET scanners where scatter comprises less than 20% of the events, the magnitude of scattered radiation could be adequately estimated by fitting the detected events in the projections that extended beyond the body boundary as these events are mispositioned due to scatter. For 3-D PET, a more sophisticated approach that relies on first order photon transport modelling is typically used. Here, the scatter contribution to each LOR is estimated based on the Klein–Nishina formula for Compton scattering using information from an initial reconstruction of the emission data (without scatter correction) that reflects the activity distribution in conjunction with the CT based attenuation map. Typically, a simplifying assumption is that scatter is dominated by single scatter events. With the recent advances in machine learning methods in medical imaging, convolutional neural network based scatter estimation is also being evaluated for PET [4.22].

4.4.3. Resolution modelling

Resolution modelling, also known as resolution recovery or point spread function modelling, is routinely available in commercial PET and SPECT iterative reconstruction software. In this case, the resolution degrading effects are modelled within the reconstruction algorithm itself. Although resolution recovery leads to improved reconstruction, it is not possible to completely recover all information that was lost due to resolution effects; hence, even when resolution recovery is used it is common to use further corrections for partial volume effects (discussed in Section 4.7.2). Use of resolution recovery should be approached with caution because some studies have shown that the improvement in resolution comes at the expense of increased variability and edge artefacts [4.50].

As discussed previously, for SPECT the major contributor to the poor spatial resolution is the collimator and the degradation becomes worse with increasing source to collimator distance. Additionally, the intrinsic resolution of the detector (excluding the collimator) also contributes to the spatial resolution of the system, hence the term collimator detector response (CDR) is used to describe the image corresponding to a point source. The components of the CDR are the intrinsic, geometric, septal penetration and septal scatter responses. If collimator scatter/penetration is insignificant the CDR can be approximated by a Gaussian function. If collimator scatter/penetration is significant (e.g. with ^{131}I and ^{123}I that have high energy gamma ray emissions) the CDR for different distances should be generated using Monte Carlo simulation. Alternatively, the depth dependent

CDR can be experimentally determined using planar acquisitions of a point source placed at several different distances from the collimator.

Figure 4.17 demonstrates the impact, including CDR as well as attenuation and scatter effects, in a system model of the OS-EM SPECT reconstruction.

In PET, resolution effects that are typically incorporated into the system matrix of the reconstruction algorithm are the detector related effects and sometimes positron range effects for higher energy positron emitters such as ^{82}Rb. Both image and projection space based resolution modelling have been proposed as discussed in an extensive review article on resolution modelling in PET [4.50]. As with SPECT, the resolution model can be approximated by a Gaussian simulation or can be determined from Monte Carlo simulation. The best spatial resolution in a PET scanner is achieved at the centre of the field of view and the spatial resolution becomes increasingly worse as the source location moves away from the centre and toward the edge of the field of view. Algorithms are now available that incorporate the point spread functions measured at locations across the field of view into the 3-D iterative reconstruction algorithm.

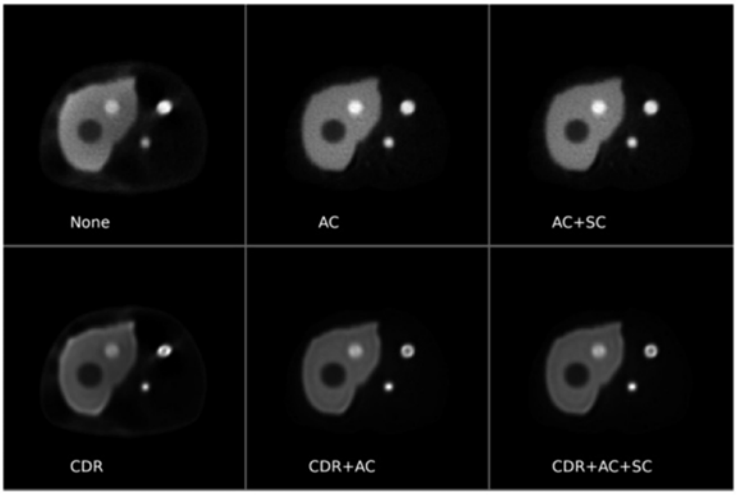

FIG. 4.17. Technetium-99m SPECT images with three physical factors — non-uniform attenuation (AC), model based scatter (SC) and collimator detector response (CDR) — included in the OS-EM reconstruction (eight iterations and eight projections/subset) model. Visually, the impact of scatter compensation is hard to see in this case (AC vs AC + SC). Despite less blurring, also note the enhancement in counts at the liver boundary and the artefact in the centre of the larger tumour outside the liver that appear in the images with CDR modelling. The grey levels of the images have been individually normalized and therefore the difference in intensity between the images does not reflect differences in counts. Courtesy of M. Ljungberg.

This approach substantially decreases the variation in the spatial resolution as a function of source location and improves image quality.

4.4.4. Random coincidences correction in PET

As discussed in Section 4.2.3.2, random coincidences provide false information, which results in loss of contrast and quantitative accuracy. As with scatter correction, it is preferred that the random coincidence correction is performed as part of the iterative reconstruction instead of direct subtraction. In this case, the random coincidences are included as an additive term in the denominator of the ML-EM equation (Eq. (4.9)).

The two methods commonly used for random coincidence correction are the delayed timing window method and the single count rate method. A time spectrum of coincidence events shows a peak corresponding to prompt coincidences, which includes the true events that are desired as well as scattered events and random coincidences. This peak sits on a background that is the result of random coincidences. The widely used delayed timing window method uses a second coincidence circuit that has a time delay that positions it away from the true coincidence peak so that it only samples the random coincidence event rate. Because the random coincidence rate is relatively time independent, the information in the delayed time window can be used to estimate the contribution of random coincidences to the prompts detected in the undelayed window. The second method for random coincidences correction is based on the relationship between the random coincidence rate (R_{random}) and the singles rate ($R_1 \cdot R_2$) in a detector pair:

$$R_{\text{random}} = \Delta T \cdot R_1 \cdot R_2 \tag{4.10}$$

where ΔT is the coincidence timing window. As long as the count rates at each individual detector pair are known, the random coincidence rate along any LOR can be estimated from Eq. (4.10) and removed.

4.5. MOTION CORRECTION

The three types of motion that impact qualitative and quantitative PET and SPECT imaging can be classified as (1) subject motion, (2) respiratory motion and (3) cardiac motion. The first of these is generally considered as a rigid motion of the entire organ while respiratory and cardiac motion are classified as non-rigid motion that can include organ deformation. Although improvements in detector technology have led to improved spatial resolution of nuclear medicine

imaging systems, with PET spatial resolution <5 mm, the full capabilities cannot be achieved in practice because of the blurring due to motion. In hybrid PET/CT and SPECT/CT systems, motion impacts the CT derived information that forms the basis for correction of the emission image. This is because the emission image is acquired over several minutes and therefore over multiple respiratory/cardiac cycles, but the sequentially performed CT, sometimes acquired with breadth hold, is performed only at one or two time points of the cycle. This leads to inconsistency between emission image acquisition and the attenuation coefficient map used for attenuation correction and for some scatter correction methods. Furthermore, motion artefacts impact the accuracy of the CT derived VOI used for activity quantification and the CT derived density maps used for patient-specific dosimetry with methods such as Monte Carlo radiation transport. Although CT has to be acquired before or after the emission acquisition, some newer PET/MR systems allow simultaneous acquisitions by the two modalities, thus mitigating some of the problems associated with misalignment of the anatomic image.

The most basic approaches that are used in the clinic to reduce motion artefacts due to gross patient movement employ devices that limit movement and in the case of hybrid imaging, perform image registration, typically to reduce rigid body misalignment. The most commonly performed cardiac and respiratory motion correction methods in the clinic are based on cardiac and respiratory gating of the data into frames representing different phases. In the conventional gating schemes the individual frames are independently reconstructed, which leads to noisy images due to loss of statistics because fewer data are available for each reconstruction. This can be especially problematic when imaging under low count conditions, such as those encountered in ^{90}Y PET after liver radioembolization [4.51]. More advanced motion correction algorithms use all recorded events to considerably improve counting statistics compared with conventional gating techniques [4.52]. Data driven or software based motion estimation methods that rely solely on the analysis of the emission data are an attractive alternative to conventionally used external tracking devices owing to practicality and potentially poor correlation between internal organ motion and externally recorded motion [4.53, 4.54].

A valuable tool for evaluating the impact of motion on PET and SPECT activity quantification/dosimetry is the 4-D XCAT non-uniform rational b-spline (NURBS) based 4-D XCAT computational phantom that models temporal and spatial changes in internal organs associated with cardiac and respiratory cycles. The 4-D XCAT has been used in a study evaluating the impact of respiratory motion on internal radiation dosimetry [4.55]. Motion can have a particularly large impact on some applications related to radionuclide therapy dosimetry, such as respiratory motion artefacts, when quantifying activity in liver lesions that are close to the lung. This is highly relevant in therapies such as liver

radioembolization and peptide receptor radionuclide therapy of neuroendocrine tumours (NETs), where the liver is the most common site of metastases. Respiratory motion also has a substantial impact on lung shunt estimation performed prior to radioembolization [4.56].

4.6. DEAD TIME CORRECTIONS

The dead time in radiation detection systems is related to the finite time associated with processing individual events. Events that occur within the resolving time of the detector cannot be recorded as separate events. This leads to count loss and also event mis-positioning in the case of imaging systems. Distortions can occur in the energy spectrum when energies of two photons are summed and recorded as a single higher energy photon and also in the spatial domain, where summed photons may increase count levels in areas lying between regions containing high activity.

Detection systems are defined as paralyzable when each event extends the dead time or non-paralyzable when subsequent events occurring during dead time are ignored [4.8]. Dead time effects become significant at high count rates and are particularly significant in systems with high detection efficiency. In diagnostic SPECT imaging dead time effects are minimal due to the low count rates but can be a significant factor in SPECT imaging after therapeutic administrations for which injected activities can be over 4 GBq. In PET, the count rate for single events is higher than for coincidence events and dead time effects can be considerable. In PET systems, dead time correction factors that compensate for the count loss are typically applied to the recorded events in real time prior to image reconstruction. The dead time model used in most PET systems is empirical and is based on measurements (performed by the manufacturer) of the observed count rate as a function of activity concentration in a range of objects. In single photon imaging, such real time correction for dead time losses is not generally available and measurements to determine dead time correction factors must be performed by the user.

One of the simplest methods for dead time correction is based on monitoring counts corresponding to a reference source placed at the edge of the camera field of view. The correction factor is the ratio of counts recorded in the ROI for the reference source without and with the patient present. Then, the true counts corrected for dead time are estimated by multiplying the measured counts by the correction factor. However, because of interference between photons emitted from the patient and those emitted by the reference source, implementing such a correction is problematic. Therefore, dead time correction methods based on mathematic models that characterize the system as paralyzable

or non-paralyzable are preferable. Such corrections require prior knowledge of the system dead time, which can be measured experimentally using methods such as the two-source method or the decaying source method [4.8]. Once the dead time of the system and the measured (observed) counts are known, the dead time corrected (true) counts can be determined from an analytic expression if the system is non-paralyzable or can be estimated by graphical or numeric methods if the system is paralyzable.

For a non-paralyzable system the relationship between the true count rate (R_t) and the observed count rate (R_o) is given by:

$$R_o = \frac{R_t}{\left(1 - R_t \tau\right)} \tag{4.11}$$

where τ is the dead time.

For a paralyzable system:

$$R_o = R_t e^{-R_t \tau} \tag{4.12}$$

Measurements of the observed count rate over a range of different activity levels can be performed to empirically determine if a particular imaging system behaves as a paralyzable or non-paralyzable system. If the system is best approximated by a non-paralyzable model the observed count rate increases asymptotically towards a maximum as the activity increases whereas it reaches a maximum and then decreases in the case of a paralyzable model.

4.7. ACTIVITY QUANTIFICATION

For absorbed dose calculation, the planar or tomographic images representing the distribution of the radiopharmaceutical in the patient's body must be expressed in absolute activity units. The sensitivity of the camera must be known to translate image counts into activity. When quantifying activity within source regions that are small relative to the spatial resolution of the system, corrections for the partial volume effect are also needed for accurate quantification. The process for absolute quantification of images is discussed next.

4.7.1. Conversion of counts to activity

Camera sensitivity: To make an image quantitative (i.e. voxel values in units of activity) the voxel values in the reconstructed image that are in units of counts (or recorded 'events') have to be scaled by the system sensitivity and the acquisition time. The sensitivity is expressed in units of count rate per unit activity (e.g. cps/MBq). The sensitivity can be determined by measurements performed with a source of known activity. The sensitivity, S, relates the count rate, C_j, in an image voxel j of the reconstructed image to the activity, A_j, by:

$$A_j = \frac{C_j}{S} \tag{4.13}$$

In most SPECT systems the sensitivity measurement is performed by the user and Eq. (4.13) is applied off-line to convert the reconstructed counts to activity. For PET cameras, the sensitivity factor determined by the manufacturer is embedded in the system software and images are presented in units of activity concentration (e.g. Bq/mL). This is multiplied by the voxel volume to obtain the absolute activity in the voxel. The user has to periodically check that the sensitivity does not deviate substantially (typically, <5%) from the manufacturer's specified value. For PET this measurement is usually performed using an extended source (a cylinder) filled with a uniform solution of a known concentration of a positron emitting radioisotope (typically, ^{18}F or ^{68}Ga). For newer PET radionuclides that are not supported as a selectable radionuclide option in the PET acquisition software (e.g. ^{90}Y in some systems) it is necessary to select a suitable other long lived radionuclide from the available list and correct the displayed Bq/mL values for differences in positron yield. The requirement for a long lived radionuclide (e.g. ^{22}Na) is to avoid any scanner decay correction during acquisition, which is otherwise applied for short lived PET radionuclides.

The sensitivity measurement for a gamma camera needs to be performed for each radionuclide and the corresponding energy window with the specific collimator that will be used for patient imaging. The simplest approach to determining the sensitivity is with a planar measurement using a 'point-like' source of known activity attached to a minimal attenuating fixture, if available on the system, or placed on a low attenuation/low scatter medium such as Styrofoam at a fixed distance from the collimator surface. The source is made as small as possible to minimize scatter and attenuation effects. As stated in IAEA Human Health Reports No. 9 [4.57], a 5–10 mL syringe and activities of 10–40 MBq (for most radionuclides) are considered appropriate. Another possible source geometry is to use a thin layer of activity placed in a Petri dish, following the quality assurance procedures by the National Electrical Manufacturers

Association (NEMA) [4.58]. The recommended acquisition time should be such that a total of 10^5–10^6 counts are obtained to ensure high precision of the sensitivity measurement. The measured count rate should be corrected for the background to determine the net count rate of the source activity. Although object scatter is minimal in the case of a point source, contribution from scatter in the collimator or other camera components can be significant. Hence, the scatter counts, estimated by the TEW method, for example, should be subtracted from the main window counts of the planar acquisition. If C_{ref} is the total scatter- and background-corrected count rate corresponding to the planar projection of the reference source and A_{ref} is the known source activity, then the gamma camera sensitivity (count rate per unit activity) is expressed as:

$$S = \frac{C_{\text{ref}}}{A_{\text{ref}}} \cdot e^{\lambda \Delta t} \cdot \frac{\lambda t_{\text{acq}}}{1 - e^{-\lambda t_{\text{acq}}}} \tag{4.14}$$

where the two factors at the end account for the decay during the time delay Δt between the time that the true activity was measured and the start time of the acquisition, and for the decay during the acquisition time t_{acq}, respectively.

The activity used in the above sensitivity measurement should be determined with high accuracy using a well calibrated activity meter that is traceable to a primary standards laboratory for the specific isotope being imaged [4.59]. Some state of the art SPECT/CT systems now come with an integrated source holder and a manufacturer provided traceable source that can be used for camera sensitivity measurement. In some systems, the sensitivity (measured periodically) can be saved in the software, allowing the option of directly obtaining the image in activity concentration units (e.g. Bq/mL) as in PET/CT.

SPECT calibration factor for quantifying VOI activity: When converting the reconstructed SPECT counts within a VOI to activity, a sensitivity factor based on a planar acquisition with a point-like source (described above), though practical, is not ideal due to imperfect corrections for image degrading factors (e.g. scatter and attenuation). The impact of imperfect corrections can be reduced by performing a phantom based calibration with a tomographic acquisition of a source geometry and distribution that to some extent matches the patient. For example, a large sphere (large enough to minimize partial volume effects) of known activity in a ‘warm’ phantom can be used to determine the calibration factor for quantifying activity in lesions. Other source geometries that can be used for determining the calibration factor include a cylinder filled with uniform activity or inserts in a torso phantom that model organs of interest such as kidney or liver (i.e. organ specific calibration factors) [4.60]. The ready access to 3-D printing technology has facilitated the use of non-spherical objects for calibration measurements [4.60, 4.61]. The same imaging and reconstruction

protocol and procedure for defining VOIs used in the patient study should be used in the calibration experiment. The previous expression Eq. (4.14) for the sensitivity factor is valid for determining the phantom based calibration factor, but in this case the reference count rate corresponds to the VOI counts in the reconstructed image instead of the counts in the planar projection. Under ideal conditions (perfect correction for effects such as scatter, attenuation and resolution effects) the phantom based calibration factor will approach the camera sensitivity factor. The calibration factor relates the patient's measured VOI count rate, C_{VOI}, to activity, A_{VOI}, by:

$$A_{VOI} = \frac{C_{VOI}}{CF} \tag{4.15}$$

4.7.2. Partial volume correction

Partial volume effects due to finite spatial resolution of the system are reduced to some extent in both PET and SPECT by incorporating the point spread function into the system matrix of the iterative reconstruction (resolution recovery) as described in Section 4.4.3. However, this does not lead to complete count recovery, even when a high number of iterations are used. When quantifying objects that are small compared to the spatial resolution of the imaging system (less than 2–3 times the FWHM of the resolution), partial volume correction (PVC) is needed to improve quantification accuracy. A number of PVC methods have been proposed for correction of mean activity as well as for voxel level correction [4.62–4.64]. One of the most practical and most widely used PVCs in radionuclide therapy dosimetry applications is based on using volume dependent recovery coefficients (*RC*s) that correct the mean activity in a target. The *RC* is defined as follows:

$$RC = \frac{\text{measured activity in object VOI}}{\text{true activity in object VOI}} \tag{4.16}$$

Then, the measured activity within the source region VOI, A_{VOI}, (from Eq. (4.15) can be scaled to obtain the PVC corrected activity A'_{VOI}:

$$A'_{VOI} = \frac{A_{VOI}}{RC} \tag{4.17}$$

In addition to the widely used Eq. (4.16), there are other definitions of the *RC*. Gear et al. [4.65] define the *RC* as the ratio of the count rate measured in

the object VOI to the total count rate in the image. Regardless of the definition, ideally, the *RC*s should be determined from phantom studies performed on the same imaging system used in the patient study [4.17, 4.66]. If a Monte Carlo code that is well validated for the particular imaging system is available, they can also be determined by Monte Carlo simulation. The *RC* depends strongly on volume and the number of iterations used in the reconstruction [4.30]. The most widely used approach is to generate a fit function for *RC* versus volume data from phantom studies performed under similar imaging/reconstruction conditions and to use this function to determine the *RC*s for the VOIs in the patient images.

Figure 4.18 shows the *RC*s for ^{131}I SPECT measured as a function of sphere volume and number of iterations with VOIs corresponding to physical size (inner volume) defined on the CT of SPECT/CT. Note that *RC* ~1 for the largest objects after about 35 iterations, but more iterations are needed for convergence of the smaller objects. The figure also demonstrates the substantial improvement in recovery with CDR modelling. Phantom based PVC has limitations because in reality *RC*s depend not only on the volume of the object and image acquisition and reconstruction parameters, but also on other factors such as object shape and target to background ratio. To reduce the geometry dependence, the use of organ specific *RC*s, based on phantom measurements with kidney, liver and spleen shaped inserts, for example, have been proposed [4.67, 4.68]. This method, though practical, also has limitations because of patient-to-patient variations in organ size, geometry and uptake relative to background tissue. For lesions, due to the impracticality of performing measurements for the numerous possibilities for geometry, spherical shapes are generally considered as representative, but this correction will be less accurate the more the lesion volume differs from a sphere shape. The quantification accuracy that can be achieved for non-spherical objects using *RC*s based on spheres has been investigated; the results from one study for ^{177}Lu SPECT/CT are summarized in Table 4.4.

First, measurements with a multi-sphere phantom were performed to determine the *RC* versus volume curve and then additional measurements with a phantom with non-spherical inserts were performed to test quantification accuracy with and without the use of *RC*s extrapolated from the sphere based *RC* curve. As indicated by the results of Table 4.4, although in general there is a substantial improvement in quantification accuracy with the use of the volume-dependent *RC*s, the error can still be large (up to 25% underestimation for the toroid shaped insert). Table 4.4 also shows quantification accuracy that was achieved for organ inserts using volume-based *RC*s extrapolated from a curve generated for the same organs, but with different activity distributions. This study did not evaluate the impact of the background activity on *RC*s since measurements were performed with cold or very low background activity.

The *RC*s' based PVCs of Fig. 4.18 are region level corrections for quantifying mean activity in a target, which is applicable when estimating mean absorbed dose to a target region. Other more complex techniques that require an accurate measure of the scanner point spread function and segmented anatomical regions are available, but the sensitivity of these methods to segmentation and registration errors have not been well investigated. In addition to inter-regional PVC, deconvolution methods that correct for between voxel partial volume effects, without the need for segmentation, are also available [4.69]. These voxel-to-voxel techniques have not yet been evaluated for voxel-level dosimetry.

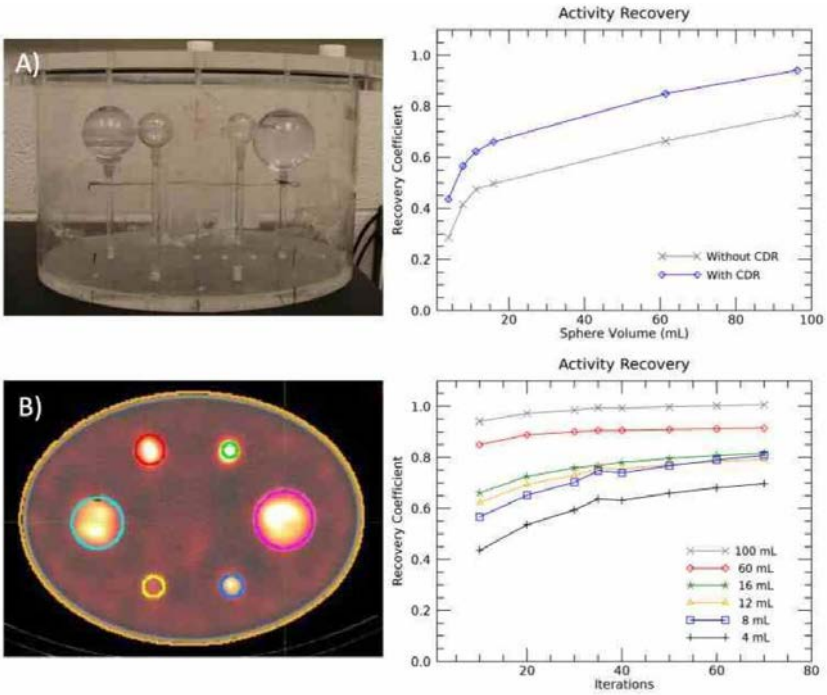

FIG. 4.18. Phantom set-up used to measure RCs for ^{131}I and the corresponding SPECT/CT image (left column). RCs as a function of volume and number of OS-EM iterations with six subsets (right column). The impact of collimator detector response (CDR) on the RCs is also shown (at 35 iterations). The calibration factor was based on the counts in the total phantom. Courtesy of M. Ljungberg.

TABLE 4.4. ACCURACY OF LESION AND ORGAN ACTIVITY QUANTIFICATION IN ^{177}Lu SPECT/CT PHANTOM MEASUREMENTS WITH AND WITHOUT PVC USING VOLUME DEPENDENT RCs

(values taken from Ref. [4.68]; courtesy of M. Ljungberg)

Phantom	Shape and volume	% difference * between quantified activity ** and true activity with (and without) PVC using *** RCs.
Multi-lesion geometric phantom, 6713 mL All lesion inserts 1.53 MBq/mL, cold background	Ellipsoid, 6 mL	–38% (22%)
	Ellipsoid, 15 mL	–18% (15%)
	Ellipsoid, 29 mL	–18% (8%)
	Toroid, 3 mL	–78% (–25%)
	Toroid, 10 mL	–45% (–20%)
	Tube, 30 mL	–15% (10%)
	'Pear' shape, 30 mL	–22% (8%)
Multi-organ anthropomorphic phantom, 8153 mL Organs 0.53–1.1 MBq/mL, background 0.03 MBq/mL	Pancreas, 92 mL	–36% (5%)
	Right kidney, 142 mL	–22% (–1%)
	Left kidney, 142 mL	–23% (–2%)
	Spleen, 156 mL	–8% (11%)
	Liver, 1470 mL	–3% (3%)

* Negative % difference indicates underestimation of activity compared with truth.

** Quantification similar to the approach of Eqs (4.14) to (4.16) with the calibration factor determined from a measurement with a cylindrical uniform activity phantom. The VOIs were defined on CT. Iterative (ten iterations, eight subsets, 4.8 mm Gaussian filter) SPECT reconstruction with attenuation correction, CDR and window based scatter correction for the two ^{177}Lu photopeaks was used.

*** Volume dependent *RC*s for the non-spherical lesions were extrapolated from an *RC* curve corresponding to spheres. Volume dependent *RC*s for the organs were extrapolated from an *RC* curve corresponding to a different scan of the same phantom with the same organs, but with different activity concentrations.

REFERENCES

[4.1] BAKER, M., CHARI, K., JUDGE, S., MacMAHON, T., STROAK, A., A Review of Commercial Radionuclide Calibrators, NPL Report DQL-RN 003, NPL, Teddington, UK (2005).

[4.2] OROPESA, P., WOODS, M.J., OLŠOVCOVÁ, V., DOS SANTOS, J.A., Radionuclide calibrator comparisons and quality improvement in nuclear medicine, Appl. Radiat. Isot. **66** 3 (2008) 353–361, https://doi.org/10.1016/j.apradiso.2007.07.008

[4.3] WOOTEN, A.L., et al., Calibration setting numbers for dose calibrators for the PET isotopes ^{52}Mn, ^{64}Cu, ^{76}Br, ^{86}Y, ^{89}Zr, ^{124}I, Appl. Radiat. Isot. **113** (2016) 89–95, https://doi.org/10.1016/j.apradiso.2016.04.025

[4.4] OLIVEIRA, P.A., SANTOS, J.A.M., Innovative methodology for intercomparison of radionuclide calibrators using short half-life in situ prepared radioactive sources, Med. Phys. **41** 7 (2014) 072507, https://doi.org/10.1118/1.4884035

[4.5] GALEA, R., GAMEIL, K., Renewing the radiopharmaceutical accuracy check service for Canadian radionuclide calibrators, Appl. Radiat. Isot. **109** (2016) 254–256, https://doi.org/10.1016/j.apradiso.2015.11.068

[4.6] JANS, H.-S., Activity cross-calibration of unsealed radionuclides utilizing a portable ion chamber, Med. Phys. **43** 12 (2016) 6536, https://doi.org/10.1118/1.4967484

[4.7] AN34 Experiments in Nuclear Science, Experiment 3: Gamma-Ray Spectroscopy Using NaI(Tl), ORTEC, http://ortec-online.com/service-and-support/library/educational-experiments

[4.8] CHERRY, S.R., SORENSON, J.A., PHELPS, M.E., Physics in Nuclear Medicine, Elsevier Health Sciences, Philadelphia, PA (2012), https://doi.org/10.1016/B978-1-4160-5198-5.00001-0

[4.9] Photomultiplier Tubes Hamamatsu, https://www.hamamatsu.com/resources/pdf/etd/PMT_TPMZ0002E.pdf

[4.10] Introduction to Amplifiers, ORTEC, https://www.ortec-online.com/-/media/ametekortec/other/amplifier-introduction.pdf

[4.11] HÄNSCHEID, H., et al., EANM Dosimetry Committee series on standard operational procedures for pre-therapeutic dosimetry II. Dosimetry prior to radioiodine therapy of benign thyroid diseases, Eur. J. Nucl. Med. Mol. Imaging **40** 7 (2013) 1126–1134, https://doi.org/10.1007/s00259-013-2387-x

[4.12] BAILEY, D.L., HUMM, J.L., TODD-POKROPEK, A., VAN ASWEGEN, A., Eds, Nuclear Medicine Physics: A Handbook for Teachers and Students, IAEA, Vienna (2014).

[4.13] LIU, C.-J., CHENG, J.-S., CHEN, Y.-C., HUANG, Y-.H., YEN, R.-F., A performance comparison of novel cadmium-zinc-telluride camera and conventional SPECT/CT using anthropomorphic torso phantom and water bags to simulate soft tissue and breast attenuation, Ann. Nucl. Med. **29** 4 (2015) 342–350, https://doi.org/10.1007/s12149-015-0952-z

[4.14] GOSHEN, E., et al., Feasibility study of a novel general purpose CZT-based digital SPECT camera: Initial clinical results, EJNMMI Phys. **5** 1 (2018) 6, https://doi.org/10.1186/s40658-018-0205-z

[4.15] SLOMKA, P.J., PAN, T., GERMANO, G., Recent advances and future progress in PET instrumentation, Semin. Nucl. Med. **46** 1 (2016) 5–19, https://doi.org/10.1053/j.semnuclmed.2015.09.006

[4.16] SURTI, S., KARP, J.S., Advances in time-of-flight PET, Phys. Medica **32** 1 (2016) 12–22, https://doi.org/10.1016/j.ejmp.2015.12.007

[4.17] DEWARAJA, Y.K., LJUNGBERG, M., GREEN, A.J., ZANCONICO, P.B., FREY, E.C., MIRD Pamphlet No. 24: Guidelines for quantitative ^{131}I SPECT in dosimetry applications, J. Nucl. Med. **54** (2013) 2182–2188, https://doi.org/10.2967/jnumed.113.122390

[4.18] LJUNGBERG, M., et al., MIRD Pamphlet No. 26: Joint EANM/MIRD guidelines for quantitative ^{177}Lu SPECT applied for dosimetry of radiopharmaceutical therapy, J. Nucl. Med. **57** 1 (2016) 151–162, https://doi.org/10.2967/jnumed.115.159012

[4.19] BUCK, A.K., et al., SPECT/CT, J. Nucl. Med. **49** 8 (2008) 1305–1319, https://doi.org/10.2967/jnumed.107.050195

[4.20] EHMAN, E.C., et al., PET/MRI: Where might it replace PET/CT? J. Magn. Reson. Imaging **46** 5 (2017) 1247–1262, https://doi.org/10.1002/jmri.25711

[4.21] DELSO, G., NUYTS, J., "PET/MRI: Attenuation correction", PET/MRI in Oncology: Current Clinical Applications (IGARU, A., HOPE, T., VEIT-HAIBACH, P., Eds), Springer, Cham, Switzerland (2018) 53–75, https://doi.org/10.1007/978-3-319-68517-5_4

[4.22] GONG, K., BERG, E., CHERRY, S.R., QI, J., Machine learning in PET: From photon detection to quantitative image reconstruction, Proc. IEEE **108** 1 (2020) 51–68, https://doi.org/10.1109/JPROC.2019.2936809

[4.23] FOWLER, K.J., et al., PET/MRI of hepatic ^{90}Y microsphere deposition determines individual tumor response, Cardiovasc. Interv. Radiol. **39** 6 (2016) 855–864, https://doi.org/10.1007/s00270-015-1285-y

[4.24] KNEŠAUREK, K., TULI, A., KIM, E., HEIBA, S., KOSTAKOGLU, L., Comparison of PET/CT and PET/MR imaging and dosimetry of yttrium-90 (^{90}Y) in patients with unresectable hepatic tumors who have received intra-arterial radioembolization therapy with ^{90}Y microspheres, EJNMMI Phys. **5** 1 (2018) 23, https://doi.org/10.1186/s40658-018-0222-y

[4.25] WERNICK, M., AARSVOLD, J. (Eds), Emission Tomography. The Fundamentals of PET and SPECT, Elsevier, Amsterdam (2004).

[4.26] ZAIDI, H. (Ed.), Quantitative Analysis in Nuclear Medicine Imaging, Springer, New York (2006), https://doi.org/10.1007/b107410

[4.27] COLSHER, J.G., Fully three-dimensional positron emission tomography, Phys. Med. Biol. **25** 1 (1980) 103–115, https://doi.org/10.1088/0031-9155/25/1/010

[4.28] SHEPP, L.A., VARDI, Y., Maximum likelihood reconstruction for emission tomography, IEEE Trans. Med. Imaging **1** 2 (1982) 113–122, https://doi.org/10.1109/TMI.1982.4307558

[4.29] HUDSON, H.M., LARKIN, R.S., Accelerated image reconstruction using ordered subsets of projection data, IEEE Trans. Med. Imaging **13** 4 (1994) 601–609, https://doi.org/10.1109/42.363108

[4.30] DEWARAJA, Y.K., et al., MIRD Pamphlet No. 23: Quantitative SPECT for patient-specific 3-dimensional dosimetry in internal radionuclide therapy, J. Nucl. Med. **53** 8 (2012) 1310–1325, https://doi.org/10.2967/jnumed.111.100123

[4.31] BRUYANT, P.P., Analytic and iterative reconstruction algorithms in SPECT, J. Nucl. Med. **43** 10 (2002) 1343–1358.

[4.32] GREEN, P.J., Bayesian reconstructions from emission tomography data using a modified EM algorithm, IEEE Trans. Med. Imaging **9** 1 (1990) 84–93, https://doi.org/10.1109/42.52985

[4.33] SIEGEL, J.A., et al., MIRD Pamphlet No. 16: Techniques for quantitative radiopharmaceutical biodistribution data acquisition and analysis for use in human radiation dose estimates, J. Nucl. Med. **40** 2 (1999) 37s–61s.

[4.34] ZAIDI, H., MONTANDON, M.-L., ALAVI, A., Advances in attenuation correction techniques in PET, PET Clin. **2** 2 (2007) 191–217, https://doi.org/10.1016/j.cpet.2007.12.002

[4.35] PATTON, J.A., TURKINGTON, T.G., SPECT/CT physical principles and attenuation correction, J. Nucl. Med. Technol. **36** 1 (2008) 1–10, https://doi.org/10.2967/jnmt.107.046839

[4.36] RAHMIM, A., ZAIDI, H., PET versus SPECT: Strengths, limitations and challenges, Nucl. Med. Commun. **29** 3 (2008) 193–207, https://doi.org/10.1097/MNM.0b013e3282f3a515

[4.37] ZAIDI, H., KORAL, K.F., Scatter modelling and compensation in emission tomography, Eur. J. Nucl. Med. Mol. Imaging **31** 5 (2004) 761–782, https://doi.org/10.1007/s00259-004-1495-z

[4.38] HUTTON, B.F., BUVAT, I., BEEKMAN, F.J., Review and current status of SPECT scatter correction, Phys. Med. Biol. **56** 14 (2011) R85–112, https://doi.org/10.1088/0031-9155/56/14/R01

[4.39] JASZCZAK, R.J., GREER, K.L., FLOYD, C.E., Jr., HARRIS, C.C., COLEMAN, R.E., Improved SPECT quantification using compensation for scattered photons, J. Nucl. Med. **25** 8 (1984) 893–900.

[4.40] OGAWA, K., HARATA, Y., ICHIHARA, T., KUBO, A., HASHIMOTO, S., A practical method for position-dependent Compton-scatter correction in single photon emission CT, IEEE Trans. Med. Imaging **10** 3 (1991) 408–412, https://doi.org/10.1109/42.97591

[4.41] DEWARAJA, Y.K., LJUNGBERG, M., FESSLER, J.A., 3-D Monte Carlo-based scatter compensation in quantitative I-131 SPECT reconstruction, IEEE Trans. Nucl. Sci. **53** 1 (2006) 181–188, https://doi.org/10.1109/TNS.2005.862956

[4.42] DE NIJS, R., LAGERBURG, V., KLAUSEN, T.L., HOLM, S., Improving quantitative dosimetry in ^{177}Lu-DOTATATE SPECT by energy window-based scatter corrections, Nucl. Med. Commun. **35** 5 (2014) 522–533, https://doi.org/10.1097/MNM.0000000000000079

[4.43] URIBE, C.F., et al., Accuracy of ^{177}Lu activity quantification in SPECT imaging: A phantom study, EJNMMI Phys. **4** 1 (2017) 2, https://doi.org/10.1186/s40658-016-0170-3

[4.44] VANDERVOORT, E., et al., Implementation of an analytically based scatter correction in SPECT reconstructions, IEEE Trans. Nucl. Sci. **52** 3 (2005) 645–653, https://doi.org/10.1109/TNS.2005.851463

[4.45] FREY, E.C., TSUI, B.M.W., "A new method for modeling the spatially-variant, object-dependent scatter response function in SPECT", Proc. IEEE Nucl. Sci. Symp., Anaheim, 1996, IEEE (1996) 1082–1086.

[4.46] BEEKMAN, F.J., DE JONG, H.W., VAN GELOVEN, S., Efficient fully 3-D iterative SPECT reconstruction with Monte Carlo-based scatter compensation, IEEE Trans. Med. Imaging **21** 8 (2002) 867–877, https://doi.org/10.1109/TMI.2002.803130

[4.47] DEWARAJA, Y.K., et al., Improved quantitative ^{90}Y bremsstrahlung SPECT/CT reconstruction with Monte Carlo scatter modeling, Med. Phys. **44** 12 (2017) 6364–6376, https://doi.org/10.1002/mp.12597

[4.48] XIANG, H., LIM, H., FESSLER, J.A., DEWARAJA, Y.K., A deep neural network for fast and accurate scatter estimation in quantitative SPECT/CT under challenging scatter conditions, Eur. J. Nucl. Med. Mol. Imaging **47** 13 (2020) 2956–2967, https://doi.org/10.1007/s00259-020-04840-9

[4.49] ZAIDI, H., MONTANDON, M.-L., Scatter compensation techniques in PET, PET Clin. **2** 2 (2007) 219–234, https://doi.org/10.1016/j.cpet.2007.10.003

[4.50] RAHMIM, A., QI, J., SOSSI, V., Resolution modeling in PET imaging: Theory, practice, benefits, and pitfalls, Med. Phys. **40** 6 (2013) 064301, https://doi.org/10.1118/1.4800806

[4.51] OSBORNE, D.R., et al., 90Y liver radioembolization imaging using amplitude-based gated PET/CT, Clin. Nucl. Med. **42** 5 (2017) 373–374, https://doi.org/10.1097/RLU.0000000000001613

[4.52] RAHMIM, A., ROUSSET, O., ZAIDI, H., Strategies for motion tracking and correction in PET, PET Clin. **2** 2 (2007) 251–266, https://doi.org/10.1016/j.cpet.2007.08.002

[4.53] MUKHERJEE, J.M., HUTTON, B.F., JOHNSON, K.L., PRETORIUS, P.H., KING, M.A., An evaluation of data-driven motion estimation in comparison to the usage of external-surrogates in cardiac SPECT imaging, Phys. Med. Biol. **58** 21 (2013) 7625–7646, https://doi.org/10.1088/0031-9155/58/21/7625

[4.54] KESNER, A., SCHMIDTLEIN, C.R., KUNTNER, C., Real-time data-driven motion correction in PET, EJNMMI Phys. **6** 1 (2019) 3, https://doi.org/10.1186/s40658-018-0240-9

[4.55] XIE, T., ZAIDI, H., Effect of respiratory motion on internal radiation dosimetry, Med. Phys. **41** 11 (2014) 112506, https://doi.org/10.1118/1.4898118

[4.56] ALLRED, J.D., et al., The value of ^{99m}Tc-MAA SPECT/CT for lung shunt estimation in ^{90}Y radioembolization: A phantom and patient study, EJNMMI Res. **8** 1 (2018) 50, https://doi.org/10.1186/s13550-018-0402-8

[4.57] INTERNATIONAL ATOMIC ENERGY AGENCY, Quantitative Nuclear Medicine Imaging: Concepts, Requirements and Methods, IAEA Human Health Reports No. 9, IAEA, Vienna (2014).

[4.58] NATIONAL ELECTRICAL MANUFACTURERS ASSOCIATION, NEMA Standards Publication NU 1-2012: Performance Measurements of Gamma Cameras, NEMA, Rosslyn, VA (2012).

[4.59] INTERNATIONAL ATOMIC ENERGY AGENCY, Quality Assurance for Radioactivity Measurement in Nuclear Medicine, Technical Reports Series No. 454, IAEA, Vienna (2006).

[4.60] PRICE, E., et al., Improving molecular radiotherapy dosimetry using anthropomorphic calibration, Phys. Med. **58** (2019) 40–46, https://doi.org/10.1016/j.ejmp.2019.01.013

[4.61] TRAN-GIA, J., SCHLÖGL, S., LASSMANN, M., Design and fabrication of kidney phantoms for internal radiation dosimetry using 3D printing technology, J. Nucl. Med. **57** 12 (2016) 1998–2005, https://doi.org/10.2967/jnumed.116.178046

[4.62] SORET, M., BACHARACH, S.L., BUVAT, I., Partial-volume effect in PET tumor imaging, J. Nucl. Med. **48** 6 (2007) 932–945, https://doi.org/10.2967/jnumed.106.035774

[4.63] ROUSSET, O., RAHMIM, A., ALAVI, A., ZAIDI, H., Partial volume correction strategies in PET, PET Clin. **2** 2 (2007) 235–249, https://doi.org/10.1016/j.cpet.2007.10.005

[4.64] ERLANDSSON, K., BUVAT, I., PRETORIUS, P.H., THOMAS, B.A., HUTTON, B.F., A review of partial volume correction techniques for emission tomography and their applications in neurology, cardiology and oncology, Phys. Med. Biol. **57** 21 (2012) R119–159, https://doi.org/10.1088/0031-9155/57/21/R119

[4.65] GEAR, J.I., et al., EANM practical guidance on uncertainty analysis for molecular radiotherapy absorbed dose calculations, Eur. J. Nucl. Med. Mol. Imaging **45** 13 (2018) 2456–2474, https://doi.org/10.1007/s00259-018-4136-7

[4.66] JENTZEN, W., Experimental investigation of factors affecting the absolute recovery coefficients in iodine-124 PET lesion imaging, Phys. Med. Biol. **55** 8 (2010) 2365–2398, https://doi.org/10.1088/0031-9155/55/8/016

[4.67] TRAN-GIA, J., LASSMANN, M., Optimizing image quantification for ^{177}Lu SPECT/CT based on a 3D printed 2-compartment kidney phantom, J. Nucl. Med. **59** 4 (2018) 616–624, https://doi.org/10.2967/jnumed.117.200170

[4.68] FINOCCHIARO, D., et al., Partial volume effect of SPECT images in PRRT with ^{177}Lu labelled somatostatin analogues: A practical solution, Phys. Med. **57** (2019) 153–159, https://doi.org/10.1016/j.ejmp.2018.12.029

[4.69] THOMAS, B.A., et al., PETPVC: A toolbox for performing partial volume correction techniques in positron emission tomography, Phys. Med. Biol. **61** 22 (2016) 7975–7993, https://doi.org/10.1088/0031-9155/61/22/7975

Chapter 5

QUANTITATIVE IMAGING OF RADIONUCLIDES RELEVANT TO RADIOPHARMACEUTICAL THERAPY

Y. DEWARAJA, M. LJUNGBERG

5.1. OVERVIEW

Traditionally, planar imaging with a gamma camera has been the most widely used method to quantify activity in internal dosimetry. However, planar imaging cannot determine the source depth or reliably correct for counts emanating from activity in tissues overlying or underlying the structures of interest. It is well established that 3-D tomographic imaging modalities such as SPECT (singles photon emission computed tomography) and PET (positron emission tomography) offer improved quantitative imaging capabilities over 2-D planar imaging [5.1–5.3], but planar imaging continues to be used because it offers the advantages of fast acquisition, good axial coverage and low cost associated with data processing and computer resources. Of the two tomographic nuclear medicine modalities, the main advantage of PET over SPECT is the ability to detect and record a higher number of the emitted photons [5.4]. The lower sensitivity of SPECT, by 2–3 orders of magnitude compared with PET, results from the low efficiency of physical collimators that are necessary to localize events in single photon imaging (planar scintigraphy and SPECT) but not in PET, as discussed in Chapter 4. The possibility of coincidence counting also leads to higher spatial resolution for PET compared with SPECT (4–6 mm full width at half-maximum (FWHM) compared with 7–12 mm FWHM for SPECT). Despite these advantages, SPECT imaging is used more frequently than PET in dosimetry applications because most therapeutic radionuclides are not positron emitters but emit gamma rays suitable for single photon imaging (Table 2.1 in Chapter 2). For example, ^{131}I, widely used in radioiodine therapy, has a 364 keV gamma ray that can be directly imaged by SPECT, but PET imaging involves the use of a surrogate positron emitting tracer, ^{124}I.

Typically, for absorbed dose estimation, serial quantitative imaging must be performed at multiple time points to determine the time-integrated activity as radiopharmaceuticals redistribute with time. Historically, the inaccuracy in estimating time-integrated activity from serial quantitative imaging has been considered to be the largest contributor to the error in absorbed dose estimation.

Both the quantitative imaging process and fitting of the time activity curves that describe the uptake and washout of the radiopharmaceutical contribute to this error. Accurate quantitative imaging of radionuclides associated with therapy is typically more complex than imaging radionuclides used in diagnosis, which usually display more favourable imaging properties. For example, SPECT imaging of therapeutic radioisotopes such as ^{131}I and ^{177}Lu, both of which have multiple photopeaks, and ^{90}Y, which has a continuous bremsstrahlung energy spectrum, is more difficult than imaging diagnostic isotopes such as ^{99m}Tc, which has a single photopeak at 140 keV. Compensation for scatter and collimator septal penetration becomes very important when imaging therapy radionuclides because of the high fraction of high energy photons that will down scatter and contaminate the low energy photopeak signal and will contribute to the tails of the collimator detector response (CDR). This is evident in Table 5.1, where for ^{99m}Tc imaged with a low energy collimator the fraction of primary events in the photopeak energy window is ~70%, but for ^{131}I it is only ~40%. Additionally, iterative reconstruction with resolution recovery (discussed in Chapter 4), not always used with diagnostic radionuclides, is very important because of the poor spatial resolution associated with medium and high energy collimators typically used in SPECT imaging of therapy radionuclides. As in SPECT, PET imaging associated with radionuclide therapy (e.g. ^{90}Y PET, ^{124}I PET and ^{68}Ga PET) is more complex than the standard ^{18}FDG-PET imaging. This is because of the low positron yields, high energy positrons and accompanying gamma rays or bremsstrahlung photons associated with the decays of these isotopes (Table 5.1).

Despite these complexities, by combining hybrid imaging (SPECT/CT, PET/CT) with iterative reconstruction that incorporates image degrading physical factors in the system model, it is feasible to achieve good accuracy in activity quantification for most therapy radionuclides when quantifying activity in structures that are large compared to the system spatial resolution. An exception is SPECT imaging of radionuclides used in α emitter therapies, which are associated with very low count rates, such as ^{223}Ra. Further insights into the physical properties and behavior of the radionuclides used in PET imaging, essential for understanding their applications in radionuclide therapy, can be found in Table 5.2. Table 5.3 summarizes quantification accuracies reported for SPECT and PET imaging of radionuclides relevant to therapy in selected phantom measurement studies. These studies demonstrate that it is possible to achieve quantification accuracies of better than 20% for most large organs and lesions. For smaller structures (<2–3 times the FWHM of the system resolution), such accuracies can be achieved if partial volume correction (PVC) is included, but accurately quantifying structures <4 mL with SPECT and <1 mL with PET is challenging because of the large correction factors involved. When there is little or no activity in the surrounding tissue, a larger volume of interest (VOI) can be

TABLE 5.1. COMPARISON OF COUNT RATE PER UNIT ACTIVITY AND THE PRIMARY TO TOTAL FRACTION FOR DIFFERENT RADIONUCLIDES RELEVANT TO RADIONUCLIDE THERAPY

(The collimators, peak energies and energy window widths used in the simulations are also listed. The phantom geometry and camera used in the Monte Carlo simulation model is described at the end of this section. Courtesy of M. Ljungberg)

Radionuclide	Collimator	Energy window centre (keV) *	cps/MBq		Primary/total count ratio (%)	
			15% window	20% window	15% window	20% window
Tc-99m	LEHR	140.5	37.0	40.7	75	72
Lu-177	LEHR	208.4	32.8	34.8	41	40
	LEHR	113.0	4.7	5.7	3	34
	ME	208.4	6.1	6.5	78	75
	ME	113.0	5.3	6.2	53	48
ln-111	ME	245.4	51.3	54.3	76	73
	ME	171.3	67.6	75.7	66	61
I-131	ME	364.5	167.8	186.7	28	26
	HE		36.0	39.9	52	47
I-123	LEHR	159.0	85.7	103.1	36	31
	ME		57.6	63.4	72	68
Ho-166	ME	80.6	8.3	10.9	22	19
	HE		3.8	5.0	30	27
Ba-133	HE	356	23.2	25.5	65	62
Sm-153	LEHR	103	13.3	14.8	62	59

TABLE 5.1. COMPARISON OF COUNT RATE PER UNIT ACTIVITY AND THE PRIMARY TO TOTAL FRACTION FOR DIFFERENT RADIONUCLIDES RELEVANT TO RADIONUCLIDE THERAPY

(The collimators, peak energies and energy window widths used in the simulations are also listed. The phantom geometry and camera used in the Monte Carlo simulation model is described at the end of this section. Courtesy of M. Ljungberg) (cont.)

Radionuclide	Collimator	Energy window centre (keV) *	cps/MBq		Primary/total count ratio (%)	
			15% window	20% window	15% window	20% window
Re-188	ME	155	24.8	29.7	31	27
	HE		12.1	13.9	48	43
Ra-223	LEHR	82	89.0	115.4	12	10
	ME		32.1	38.9	47	44
Y-90	ME	150	1.4	5.4 (60% window)	9	9 (60% window)
	HE		0.5	2.1 (60% window)	17	17 (60% window)

* Typical values.

Note: HE: high energy; LEHR: low-energy high-resolution; ME: medium energy.

TABLE 5.2. PROPERTIES OF SOME RADIONUCLIDES USED IN PET IMAGING THAT ARE RELEVANT TO RADIONUCLIDE THERAPY, ALSO INCLUDING ^{18}F FOR COMPARISON [5.5]

(courtesy of M. Ljungberg)

Radionuclide	Half-life	Positron yield (%)	Mean energy (MeV)	Maximum energy (MeV)	Mean range (mm)	Maximum range (mm)	γ rays/ bremsstrahlung (MeV)
F-18	110 m	96.9	0.250	0.634	0.6	2.4	

TABLE 5.2. PROPERTIES OF SOME RADIONUCLIDES USED IN PET IMAGING THAT ARE RELEVANT TO RADIONUCLIDE THERAPY, ALSO INCLUDING ^{18}F FOR COMPARISON [5.5]

(courtesy of M. Ljungberg) (cont.)

Radionuclide	Half-life	Positron yield (%)	Mean energy (MeV)	Maximum energy (MeV)	Mean range (mm)	Maximum range (mm)	γ rays/ bremsstrahlung (MeV)
I-124	4.18 d	11.7 10.7	0.687 0.975	1.535 2.138	2.8 4.4	7.1 10.0	0.603 (63%), 0.723 (10%) 1.691 (11%)
Ga-68	67.8 m	87.7 1.2	0.836 0.352	1.899 0.821	3.5 1.1	9.2 3.4	1.077 (3%)
Y-90	2.67 d	0.0032	*	0.739	*	*	Bremsstrahlung photons up to 2.279 MeV

* Published data not available.

TABLE 5.3. REPORTED SPECT AND PET QUANTIFICATION ACCURACY FOR RADIONUCLIDES RELEVANT TO INTERNAL RADIONUCLIDE THERAPY

(data correspond to select studies where physical phantom measurements were used; courtesy of M. Ljungberg)

Nuclide	Ref.	Modality and reconstruction	Absolute quantification accuracy
Tc-99m	[5.6]	SPECT: OS-EM, CDR, CT-AC, EW-SC, PVC	<6.8% error for 0.5 to 16 mL spheres
	[5.7]	SPECT: OS-EM, CT-AC, TR-SC, PVC	<2% error for cylindrical phantom; <4% error for liver and cardiac chambers
I-131	[5.8]	SPECT: OS-EM, CDR, CT-AC, MC-SC	<1% error for background in NEMA phantom; <83% for spheres ranging from 0.5 to 6 mL
	[5.9]	SPECT: OS-EM, CDR, CT-AC, EW-SC	<17% error for 8 to 95 mL spheres; 31% for 4 mL sphere

TABLE 5.3. REPORTED SPECT AND PET QUANTIFICATION ACCURACY FOR RADIONUCLIDES RELEVANT TO INTERNAL RADIONUCLIDE THERAPY

(data correspond to select studies where physical phantom measurements were used; courtesy of M. Ljungberg) (cont.)

Nuclide	Ref.	Modality and reconstruction	Absolute quantification accuracy
Ba-133	[5.10]	SPECT: OS-EM, CT-AC, TEW-SC	<2% average error for sphere volumes; 2–23 mL in 'cold' phantom
Lu-177	[5.11]	SPECT: OS-CG, CDR, CT-AC, TEW-SC, PVC	<1.5% error for kidney compartments
	[5.12]	SPECT: OS-EM, CDR, CT-AC, MC-SC	Activity concentration recovery 70, 75 and 85% for spheres of volumes of 2.6, 11.5 and 26.2 mL, respectively
	[5.13]	SPECT: OS-EM, CDR, CT-AC, ESSE-SC	<6% error for liver and kidneys
	[5.14]	SPECT: OS-EM, CDR, CT-AC, AN-SC	<18% error for small objects; <5% for objects >100 mL
	[5.15]	SPECT: OS-EM, CDR, CT-AC, EW-SC	<15% for large cylinder
In-111	[5.16]	SPECT: OS-EM, CT-AC, EW-SC, PVC	<20% error for organs and 2 to 32 mL spheres; 48% error for 0.5 mL sphere
	[5.3]	SPECT: OS-EM, CDR, CT-AC, ESSE-SC, PVC	<12% error for organs; 8 to 23 mL spheres
Y-90	[5.17]	SPECT: OS-EM, CDR, CT-AC, ESSE-SC	<11% error for liver and 100 mL sphere
	[5.18]	SPECT: OS-EM, CDR, CT-AC, ESSE-SC	7% for 90 mL sphere, 10% for 2 mL sphere
	[5.19]	SPECT: OS-EM, CDR, CT-AC, MC-SC	5% for liver and 14–31 mL objects
Ho-166	[5.20]	SPECT: OS-EM, CDR, TR-AC, MC-SC	16% average error for 22 mL bottles

TABLE 5.3. REPORTED SPECT AND PET QUANTIFICATION ACCURACY FOR RADIONUCLIDES RELEVANT TO INTERNAL RADIONUCLIDE THERAPY

(data correspond to select studies where physical phantom measurements were used; courtesy of M. Ljungberg) (cont.)

Nuclide	Ref.	Modality and reconstruction	Absolute quantification accuracy
Re-188	[5.21]	SPECT: OS-EM, CDR, CT-AC, TEW-SC	<10% error for background concentration; 2–200 mL objects in cold background
Y-90	[5.22]	PET: OS-EM, TOF, RR, CT-AC, SC	<20% for 11–26 mL spheres; <40% for spheres down to 0.5 mL
	[5.23]	PET: OS-EM, TOF, RR, CT-AC, SC	<20% for 11–26 mL spheres; <50% for spheres down to 0.5 mL
I-124	[5.24]	PET: OS-EM, CT-AC, SC, PVC	<10% error for spheres down to 1 mL; <21% error for a 0.5 mL sphere

Note: AN-SC: analytical scatter correction; CDR: collimator detector response; CT-AC: CT based attenuation correction; ESSE-SC: effective source scatter estimation scatter correction; EW-SC: energy-window based scatter correction; MC-SC: Monte Carlo based scatter correction; OS-CG: ordered-subset conjugate gradient; OS-EM: ordered-subsets expectation-maximization; PVC: partial volume correction; RR: resolution recovery; TEW-SC: triple-energy-window scatter correction; TOF: time-of-flight; TR-SC: transmission based scatter correction.

used to encompass the whole uptake region, to increase quantification accuracy by minimizing partial volume effects.

In this chapter, in vivo gamma camera and PET imaging of the most widely used therapy radionuclides and imaging surrogates are discussed, focusing on dosimetry applications. To exemplify the characteristics of the radionuclides, presented in Table 5.3 (excluding ^{124}I) when imaged with a gamma camera, Monte Carlo simulations were performed using the SIMIND Monte Carlo code. This approach allows the detected events to be separated into components of 'primary' events and 'non-primary' events. Here, primary refers to the desired geometrically collimated photons that do not penetrate the collimator septa or undergo scatter in the phantom or collimator. All other events ('non-primary'), represent events that degrade the image quality and/or the ability to accurately quantify activity. The computer phantom used in the simulations resembled the

physical National Electrical Manufacturers Association (NEMA) 2012 PET phantom, with six spheres and a 'cold' lung insert. The camera was positioned at a 2 cm distance from the surface of the phantom. The sphere sizes were increased to be more relevant for SPECT resolution capabilities (1.7, 3.6, 7.5, 15.7, 27.5 and 104 cm^3) and the relative activity concentrations were defined to be 12, 10, 9, 8, 7 and 6, respectively, for the six spheres and one for the background. The simulated camera included a 5/8″ NaI(Tl) crystal with an energy resolution of 9.3% FWHM at 140 keV. Three different collimators, namely low-energy high-resolution (LEHR), medium energy and high energy (see Table 4.1 for specifications) were simulated and calculations of expected count rate (cps/MBq) and primary to total fraction for different energy window settings were made. The energy spectra shown in this chapter represent an average of acquired counts for eight equally spaced projections around a 360° rotation orbit. The energy spectra have all been normalized to a total activity in the phantom of 1 MBq and 1 s acquisition time. Dashed vertical lines in the spectra indicate typical energy window settings.

5.2. IMAGING SURROGATE ISOTOPES

In cases where the radionuclide used for therapy does not emit photons that could be used for imaging, a chemically equivalent positron or gamma emitting analogue can be used for pre-therapy imaging to make decisions on the therapy administration. These two isotopes, one for therapeutic and one for dosimetry (diagnostic imaging) purposes are also referred to as a 'theragnostic pair'. For example, ^{111}In labelled antibodies and peptides, with analogous or similar chemical properties as the ^{90}Y or ^{177}Lu labelled analogue, have been developed as surrogate gamma emitting imaging agents for pharmacokinetics assessment in pre-therapy dosimetry. PET with ^{124}I or SPECT with ^{123}I is used as a surrogate for ^{131}I in radioiodine therapy. Another usage of an analogue is ^{99m}Tc macroaggregated albumin (MAA) particles as a surrogate for ^{90}Y labelled microspheres in radioembolization. If the surrogate imaging agent is used to quantify time varying biological distributions over several days, the half-life must be sufficiently long. For example, the surrogates ^{111}In and ^{124}I have a half-life of 2.8 and 4.2 days, respectively. This requirement does not apply in the case of radioembolization, because the microspheres are permanently trapped and there is no redistribution of activity.

When a surrogate isotope is used for quantitative imaging, the assumption is made that the biological half-life of the surrogate and the therapy radionuclide is equal. Then, the differences in physical half-lives can be accounted for by a simple scaling factor based on the decay constants of the two radionuclides.

If $A(t)'$ is the measured activity of the surrogate at time t post-injection, the predicted activity of the therapy radionuclide is given by:

$$A(t) = A(t)' \cdot \frac{A_0}{A_0'} \cdot \frac{e^{-\lambda t}}{e^{-\lambda' t}} \tag{5.1}$$

where A_0 and A_0' are the administered activities and λ and λ' are the physical decay constants of the therapy radionuclide and the surrogate, respectively. In the following section imaging of some common surrogate tracers is discussed.

5.2.1. Iodine-124

Most common positron emitting radionuclides have short half-lives, making them unsuitable as imaging surrogates for in vivo quantification of biological distributions over time. Iodine-124 is the only positron emitting isotope of iodine that is long lived and has emerged as a surrogate imaging agent for therapies with ^{131}I, which is not ideally suited for direct gamma camera imaging because of the relatively high energy of the main gamma rays. Iodine-124 PET has been used as a surrogate for ^{131}I radiolabelled antibodies, ^{131}I m-iodobenzylguanidine (^{131}I-mIBG) and ^{131}I radioiodine, where quantitative imaging over several days is needed to determine biokinetics for dosimetry. Iodine-124 PET is particularly attractive for lesion dosimetry prior to radioiodine therapy of differential thyroid cancer because of the superior spatial resolution of PET compared with SPECT and because pre-therapy imaging with ^{131}I may cause the phenomenon of stunning, which potentially reduces the uptake of the therapeutic administration. However, ^{124}I PET has not been widely used because ^{124}I is a non-pure positron emitter with a complex decay scheme that includes several high energy gamma rays. Additionally, the positrons of ^{124}I have a low yield (23%) and a relatively high energy, which increases the positron range effect discussed in Chapter 4.

The complexities related to quantification of ^{124}I PET are associated with the cascade of gamma rays, as is evident from the decay scheme of Fig. 5.1. About half of the positrons are followed by 603 keV gamma rays that are emitted within the typical coincidence timing window of the PET scanner. The energy of the primary gamma ray or its energy after undergoing small angle scattering is mostly within the standard acquisition energy window of PET systems (e.g. 425–650 keV). Additionally, two gamma ray photons associated with two cascade gamma transitions can be recorded in coincidence. Thus, for ^{124}I PET the detection of a (prompt) coincidence consists of the following events: (1) true coincidences between an annihilation photon pair (desired event); (2) true coincidences between an annihilation photon and the 603 keV cascade gamma ray; and (3) true coincidences between two cascade gamma rays.

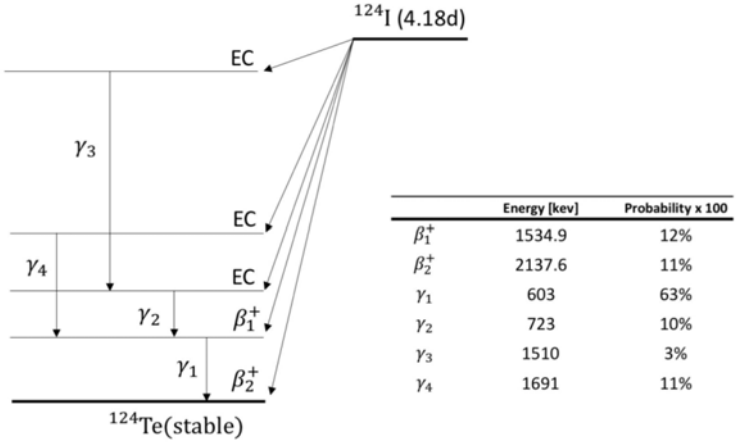

FIG. 5.1. Iodine-124 decay scheme. Courtesy of M. Ljungberg.

The undesired coincidence events are indistinguishable from the annihilation photon pair coincidences. However, because these coincidence photon pairs were not emitted at 180° from one another they provide little position information, will contribute to spurious counts in the PET image and will appear as an approximately uniform background spread over the field of view. Additionally, the increased singles rate due to the gamma rays leads to increased random coincidences. The random coincidences can be corrected with standard methods, such as the delayed window method discussed in Chapter 4.

Despite the complex decay scheme, promising quantitative results have been reported for ^{124}I PET using standard PET systems and standard ordered-subsets expectation-maximization (OS-EM) reconstruction with scatter, attenuation and random correction methods, the same as those used with ^{18}F imaging [5.25]. Quantification accuracies within 10% have been reported for spheres >12.6 mm in diameter by Jentzen et al. [5.24]. Attempts have been made to reduce the effects of false coincidences involving gamma rays (sometimes called prompt gammas) by narrowing the energy window as well as by sophisticated background subtraction. Some improvements have been achieved recently with prompt gamma correction methods designed for non-pure positron emitting isotopes that have been integrated into commercial PET reconstruction software [5.5].

Figure 5.2 compares activity recovery as a function of sphere diameter for ^{124}I PET (with and without prompt gamma correction), ^{18}F PET and ^{68}Ga PET. The ^{124}I recovery coefficients are higher than for ^{68}Ga and with prompt gamma correction, similar to those for ^{18}F.

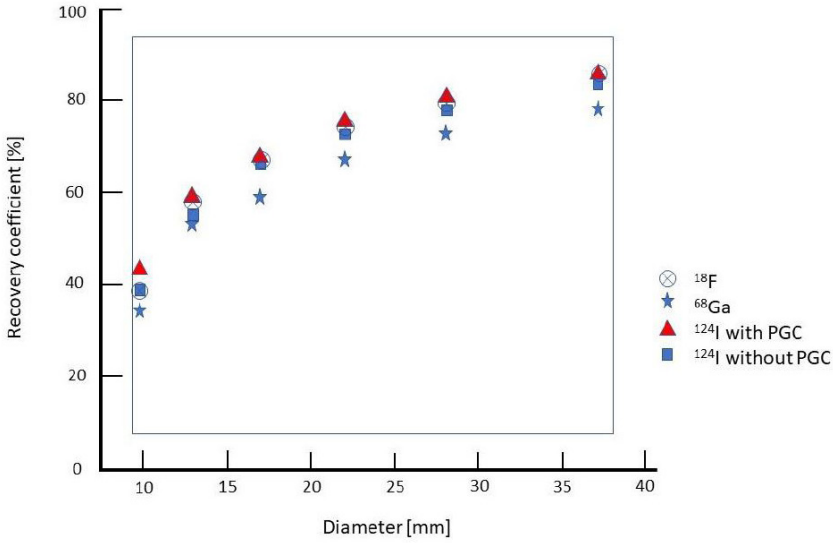

FIG. 5.2. Comparison of recovery coefficients for ^{18}F, ^{68}Ga and ^{124}I PET with and without prompt gamma correction (PGC) from a sphere phantom measurement (sphere: background 10:1). Reconstruction was made with iterative methods together with a 2 mm FWHM Gaussian post filter. Adapted from [5.27].

In addition to the complexities of ^{124}I PET, another important factor in quantitative imaging of this radionuclide is related to the activity meter measurements; because of several low energy photons (58% abundance of X rays in 20–40 keV range) there is a strong geometry dependency when measuring ^{124}I in a dose calibrator. To avoid this problem, the use of a copper filter that absorbs these X rays has been recommended [5.26].

5.2.2. Gallium-68

Pretreatment PET imaging with ^{68}Ga labelled pharmaceuticals is used for patient selection and therapy decisions in radionuclide therapies. For example, ^{68}Ga PET imaging is performed to identify patients with increased expression of somatostatin receptors in ^{177}Lu and ^{90}Y labelled peptide receptor radionuclide therapy (PRRT) of neuroendocrine tumours (NETs). For imaging NETs, PET with ^{68}Ga labelled peptides has advantages over conventional scintigraphy with ^{111}In labelled peptides such as ^{111}In-octreotide due to the inherent imaging advantages of PET. Although PET with ^{68}Ga ($T_{1/2}$ = 68 min) is not used to determine pharmacokinetics for dosimetry, because typically the effective half-lives of the radiolabelled peptides in normal organs are >40 h, a study has shown a correlation

between pretreatment standardized uptake value and absorbed doses from the therapy [5.28]. Also, ^{68}Ga-DOTATATE PET/CT uptake has shown potential for use as an early predictor of response in patients with NETs treated with PRRT [5.29]. Another application of pre-therapy ^{68}Ga PET imaging is in ^{177}Lu-PSMA (prostate-specific membrane antigen) radioligand therapy of prostate cancer.

The decay of ^{68}Ga has a pure positron branch with an abundance of 87.7%. There is also a low yield (1.2%) positron branch to an excited level of ^{68}Zn, which is followed by a gamma emission of 1.08 MeV to the ground state. Thus, there is the possibility for coincidence between annihilation photons and the prompt gamma rays if they undergo scatter and fall within the PET acquisition energy window. Although the prompt gamma contribution to coincidences is much lower than in the case of ^{124}I PET, prompt gamma correction is recommended even for ^{68}Ga. Additionally, the relative long range of ^{68}Ga positrons (Table 5.1) can lead to some loss of spatial resolution; however, for clinical PET scanners the difference in resolution compared with ^{18}F has been shown to be small [5.30].

5.2.3. Technetium-99m

Technetium-99m macroaggregated albumin (^{99m}Tc-MAA) planar and SPECT/CT imaging is used to estimate the lung shunt fraction prior to ^{90}Y microsphere radioembolization of liver malignancies under the assumption that the MAA particles mimic the vascular distribution of the microspheres. Though typically not part of the clinical protocol currently, the ^{99m}Tc-MAA SPECT/CT image can also be used to predict the absorbed dose delivered by the ^{90}Y therapy to lesions and the normal liver. Unlike most other radionuclide therapies where multi-time point imaging is needed to determine biokinetics for dosimetry, absorbed dose estimation in radioembolization is performed with only imaging at a single time point (preferably soon after the administration), because the MAA particles and microspheres do not redistribute. Hence, the relatively short half-life of ^{99m}Tc is not a disadvantage when using it as a surrogate imaging agent for this application. However, MAA is not the ideal surrogate considering reported differences between the intrahepatic distributions, potentially due to differences between MAA particles and the microspheres [5.31].

Technetium-99m with only a single gamma ray emission at 140 keV (Fig. 5.3) is ideally suited for quantitative SPECT with standard gamma cameras that are optimized for this energy range. Low-energy general-purpose (LEGP) and low-energy high-resolution (LEHR) collimators are used. Due to the lack of down scatter of higher energy photons, a single low energy scatter window adjacent to the photopeak window is sufficient for window based scatter estimation. Collimator detector response can be modelled by a simple Gaussian function, because contribution from septal penetration is not a significant concern. Using

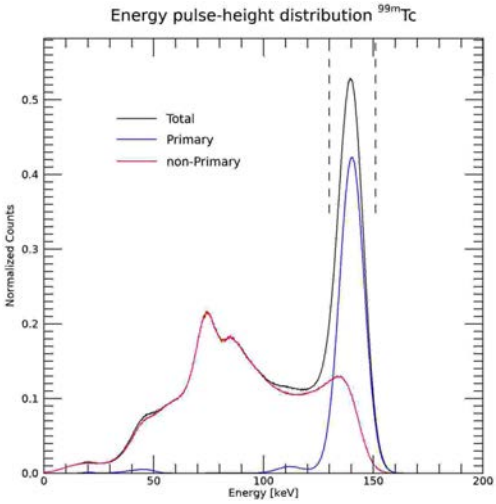

FIG. 5.3. Monte Carlo simulated energy spectrum for ^{99m}Tc as would be measured by a gamma camera equipped with an LEHR collimator. The phantom and camera are described in Section 5.1. Courtesy of M. Ljungberg.

SPECT/CT imaging and iterative reconstruction with the standard corrections, quantitative accuracies within 10% are readily achieved for this radionuclide as has been demonstrated by phantom and in vivo studies [5.32].

5.2.4. Iodine-123

Iodine-123 is used for diagnostic planar and SPECT imaging prior to therapeutic administrations of ^{131}I in both radioiodine therapy and mIBG therapy because it has superior quantitative imaging capabilities compared with ^{131}I. The lower energy of the main gamma ray (159 keV) compared with the main gamma ray of ^{131}I results in more efficient detection in the crystal and a higher spatial resolution is achieved with a low energy collimator than with medium or high energy collimators used for ^{131}I imaging. There are also fewer radiation safety issues with ^{123}I compared with ^{131}I. A limitation of ^{123}I radiolabelled pharmaceuticals is that they are only suitable for the study of relatively fast metabolic processes due to the relatively short physical half-life (13.2 h). Unlike ^{124}I, which has a longer half-life, ^{123}I is typically not used for predicting absorbed doses prior to ^{131}I therapies.

Iodine-123 is typically imaged with a 15–20% acquisition window centered on the 159 keV photopeak, which has an abundance of 83%. There are multiple gamma rays with energies above 500 keV that are low in abundance (sum less

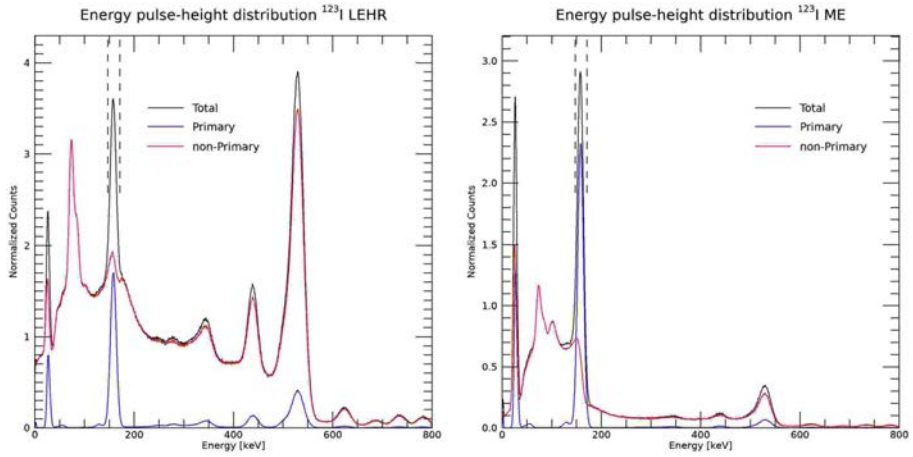

FIG. 5.4. Monte Carlo simulated ^{123}I energy spectrum as would be measured by a gamma camera equipped with an LEHR (left) and medium energy (ME) (right) collimator. The phantom and camera are described in Section 5.1. Courtesy of M. Ljungberg.

than 2%), but these photons penetrate the septa of the low energy collimator and down scatter into the acquisition window. The triple-energy window (TEW) scatter correction (TEW-SC) with scatter windows located above and below the main window can be used to correct for down scatter. For ^{123}I imaging either low or medium energy collimators can be used. Although there is an increase in sensitivity when a low energy collimator is used, much of the gain in sensitivity over the medium energy collimator comes from down scattered counts.

Figure 5.4 compares the ^{123}I energy spectra detected by a gamma camera equipped with an LEHR and a medium energy collimator. Despite their low abundance, the high energy gamma rays appear prominently in the energy spectrum corresponding to the LEHR collimator, but substantially less in the spectrum corresponding to the medium energy collimator because of the lower probability of septal penetration with its thicker septa (also see Table 5.1).

5.2.5. Indium-111

Indium-111 has been widely used as a surrogate imaging agent for therapies with ^{177}Lu and ^{90}Y. The 2.8 d half-life makes it suitable for pre-therapy biodistribution/pharmacokinetics assessment for predicting absorbed doses delivered by therapies such as PRRT and radioimmunotherapy. For example, ^{111}In-DOTATOC/DOTATATE has been used to perform kidney dosimetry to predict toxicity in ^{90}Y-DOTATOC and ^{177}Lu-DOTATATE therapy of NETs [5.33] and ^{111}In labelled antibodies have been used to perform bone marrow dosimetry

to predict toxicity in ^{90}Y radioimmunotherapy [5.34, 5.35]. Some studies have reported on differences in the biodistribution of the therapeutic agent and the ^{111}In labelled analogue [5.36]. Due to the superior sensitivity and spatial resolution of PET compared with SPECT, somatostatin analogues radiolabelled with ^{68}Ga instead of ^{111}In are increasingly used for pre-therapy imaging of NETs, but unlike ^{68}Ga, imaging with ^{111}In also enables absorbed dose estimation.

Gamma camera imaging of ^{111}In is similar in many respects to ^{177}Lu imaging because they both have a low energy and a medium energy gamma ray emission. However, the ^{111}In gamma rays have a much higher abundance (171 keV, 91% and 245 keV, 94%) than the gamma rays of ^{177}Lu, hence ^{111}In is suitable for imaging with tracer quantities of the radionuclide. Typically, a medium energy collimator is used to reduce septal penetration of the 245 keV gamma rays. As is evident in the spectra of Fig. 5.5, a large fraction of the lower energy window counts is due to down scatter of the 245 keV gamma rays. Scatter correction with the TEW method is suitable for the 171 keV peak to include correction for down scatter while only the lower energy scatter window is needed for the 245 keV peak. High quantitative accuracies have also been reported for ^{111}In SPECT with specialized reconstruction methods that include model based [5.3] and Monte Carlo based scatter correction [5.37].

The two datasets corresponding to the 171 and 245 keV energy widows can be acquired into separate projection files and reconstructed into two separate images with each image individually compensated for energy-dependent

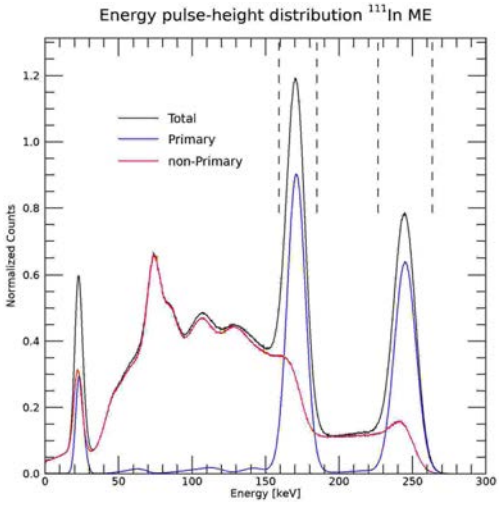

FIG. 5.5. Monte Carlo simulated ^{111}In energy spectrum measured by a gamma camera equipped with a medium energy (ME) collimator. The phantom and camera are described in Section 5.1. Courtesy of M. Ljungberg.

attenuation, CDR and scatter and then summed. Alternatively, joint multi-window iterative SPECT reconstruction for efficient processing of projection data corresponding to both windows, has been proposed [5.37].

5.2.6. Barium-133

Although not used in in vivo imaging this radionuclide is used as a long lived (half-life 10.5 y) surrogate for the relatively short lived ^{131}I (half-life 8.02 d) in phantom studies to evaluate ^{131}I SPECT quantification capabilities and as a calibration standard. The main gamma ray emission of ^{133}Ba has a similar energy and intensity (356 keV, 62%) as that of ^{131}I (364 keV, 81%). Like ^{131}I, ^{133}Ba is imaged with a high energy collimator and a thicker crystal because of the relatively high energy of the gamma ray. Triple energy scatter correction, including both the lower and upper scatter windows, is recommended because of the presence of a gamma ray at 384 keV (9%) that can down scatter and contribute counts to the 356 keV photopeak window. However, the down scatter, backscatter and septal penetration contribution in ^{133}Ba imaging is smaller than that encountered in ^{131}I imaging because the higher energy gamma rays associated with ^{131}I (634 and 723 keV) have a much higher probability of penetrating the septa, even when a high energy collimator is used, than the 384 keV gamma ray of ^{133}Ba. This is evident in Table 5.1 where the primary to total ratio for a 20% photopeak

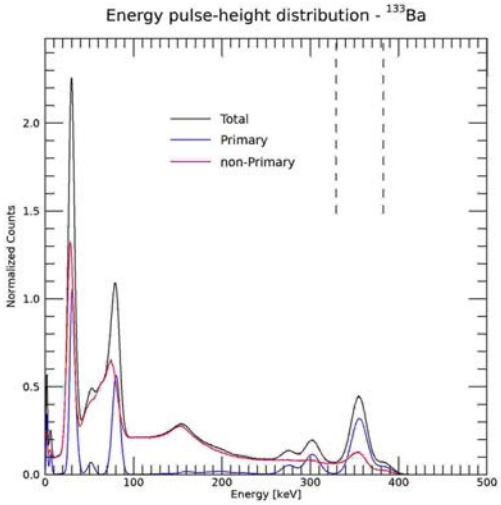

FIG. 5.6. Monte Carlo simulated ^{133}Ba energy spectrum measured by a gamma camera equipped with a high energy collimator. Note the absence of significant high energy gamma rays that can contaminate the main photopeak energy window by down scatter like in the case of ^{131}I (Fig. 5.7). The phantom and camera are described in Section 5.1. Courtesy of M. Ljungberg.

window is 62% for ^{133}Ba but only 47% for ^{131}I with a high energy collimator. This is also evident when comparing the simulated ^{133}Ba spectrum (Fig. 5.6) with that for ^{131}I presented in Section 5.3.1 (Fig. 5.7). Because of these differences in down scatter/septal penetration, ^{133}Ba is not the ideal surrogate for evaluating ^{131}I quantification accuracies but has been used in multicentre phantom comparison studies where the relatively short half-life made it infeasible to prepare and ship ^{131}I sources that are traceable to a single standard [5.38].

5.3. IMAGING OF THERAPY RADIONUCLIDES

Pre-therapy imaging analogues may not always accurately predict the biodistribution and pharmacokinetics of the therapy administration, hence direct post-therapy imaging is important for verification of safe delivery of activity to the target with minimal unplanned non-targeted activity deposition. Additionally, for assessing dose–outcome relationships, accurate absorbed dose calculation based on post-therapy quantitative imaging may be preferred over calculations based on pre-therapy assessment with a surrogate. For example, direct post-therapy ^{90}Y imaging by bremsstrahlung SPECT or ^{90}Y PET is used to assess for inadvertent extra-hepatic deposition of microspheres following radioembolization and has been used in dose–outcome studies [5.39, 5.40]. Post-therapy ^{90}Y imaging is possible because the high levels of activity administered for therapy mitigates the problems associated with the low probability of bremsstrahlung generation and low abundance of positrons that makes ^{90}Y imaging after a tracer-level administration challenging. Similarly, high therapy activities mitigate the problems associated with the low abundance of the ^{177}Lu gamma rays, so direct imaging can be used after each cycle of ^{177}Lu peptide receptor radionuclide therapy to plan subsequent cycles. In the following section, imaging methods for some commonly used therapy radionuclides are reviewed.

5.3.1. Iodine-131

Therapeutic use of ^{131}I includes radioiodine for treatment of thyroid cancer and hyperthyroidism, ^{131}I-mIBG for treatment of neuroblastoma and ^{131}I radioimmunotherapy for treatment of non-Hodgkin's lymphoma. Iodine-131 is considered to be the first theragnostic agent; it is efficient for therapy (emits β^- particles with a maximum energy of 606 keV, maximum range 2.3 mm [5.41]) and is suitable for single photon imaging with a gamma camera for diagnostics and treatment planning purposes. Quantitative ^{131}I SPECT imaging can be used both pre-therapy to predict absorbed doses from the therapy administration and post-therapy to determine the delivered absorbed doses.

Iodine-131 is not ideally suited for gamma camera imaging because of the relatively high energy (364 keV, 81%) of the predominant gamma ray and the prevalence of higher energy emissions at 637 keV (7%) and 723 keV (2%) that are low in intensity but have a high probability of penetrating the collimator septa, thereby contributing disproportionally to the image counts (Fig. 5.7). Iodine-131 image quality and activity quantification are degraded by the poor spatial resolution associated with high energy collimators, collimator septal penetration, scatter of the 364 keV photons and down scatter of higher energy gamma rays into the 364 keV energy window. Additionally, the relatively high energy of the 364 keV gamma ray results in lower intrinsic efficiency of the gamma camera crystal. At 364 keV, a standard gamma camera with a 3/8″ crystal thickness is less than 30% efficient in converting the incident gamma rays into photopeak pulses. When imaging following tracer administration, a gamma camera system equipped with a thicker NaI(Tl) crystal (e.g. 5/8″) is preferred instead of the standard crystal (3/8″) typically used in ^{99m}Tc imaging. This can increase the efficiency for detecting the 364 keV gamma ray by approximately a factor of 2, with only a small loss of intrinsic spatial resolution. However, a thinner crystal with lower sensitivity might be more appropriate for imaging following therapeutic administrations of ^{131}I due to dead time effects that may preclude early imaging with a more sensitive camera.

Although the system sensitivity is higher with a medium energy collimator than with a high energy collimator, the majority of the additional counts are due to collimator scatter and septal penetration events that require subsequent compensation, hence a high energy collimator is preferred. This is evident from comparing the Monte Carlo simulated energy spectra corresponding to medium and high energy collimators (Fig. 5.7).

Note the higher fraction of non-primary events corresponding to the 364 keV photopeak in the case of the medium energy collimator, also evident in Table 5.1. In typical ^{131}I patient imaging studies with a high energy collimator, the scatter and penetration contribution to the photopeak counts is about 50%. TEW-SC with both scatter windows is suitable for ^{131}I because the higher energy scatter window accounts for down scatter of the 637 and 723 keV gamma rays into the photopeak window. Model/Monte Carlo based down scatter estimation using specialized software has also been evaluated for improving the quantitative accuracy [5.42, 5.43]. Modelling the full CDR in the iterative reconstruction is important because of the high probability of collimator scatter and septal penetration, although sometimes only the intrinsic and geometric components of the CDR are modelled. Either experimental measurements or Monte Carlo simulation of a point source at varying distances can be used to determine the ^{131}I CDR [5.44].

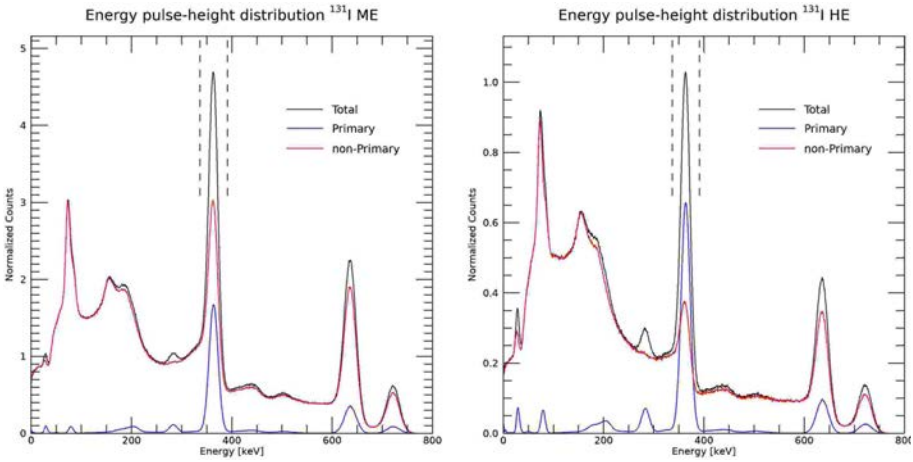

FIG. 5.7. Monte Carlo simulated ^{131}I energy spectrum measured by a gamma camera equipped with medium energy (ME) (left) and high energy (HE) (right) collimators. The phantom and camera are described in Section 5.1. Courtesy of M. Ljungberg.

Despite the challenges of ^{131}I SPECT, the possibility for both therapy and imaging with the same radionuclide makes it an attractive radionuclide for theragnostics. As is evident in Table 5.3, reasonable quantitative accuracy can be achieved with appropriate SPECT/CT acquisition parameters and iterative reconstruction that include compensation for the image degrading factors discussed above.

5.3.2. Lutetium-177

The main therapeutic applications of ^{177}Lu include peptide receptor radionuclide therapy of NETs, radioimmunotherapy of non-Hodgkin's lymphomas and PSMA radioligand therapy of prostate cancer. Lutetium-177 is a β^- emitter (maximum energy 498 keV, maximum range 1.8 mm [5.41]) that also emits gamma ray photons that can be used for imaging. Lutetium-177 image quality and activity quantification are degraded by the relatively low intensity of the main gamma rays, 113 keV (6%) and 208 keV (10%), and the down scatter associated with the presence of multiple high energy gamma rays. Under typical imaging conditions, the fraction of scatter events in the photopeak window cantered on 113 keV and 208 keV has been estimated to be 0.5 to 0.6, and 0.2 to 0.3, respectively [5.45]. This is also evident in Table 5.1. Because of the low yield of ^{177}Lu photons, when available, choosing a thicker gamma camera crystal to increase the probability of detection is important. For example, for a 5/8″ crystal

thickness, the number of photons detected in a 20% energy window centred at 208 keV increases by about 35% as compared with that for a 3/8″ thick crystal.

Because of the high contribution of down scatter to the 113 keV photopeak window (Fig. 5.8), if count rates are sufficiently high, it is recommended that only the 208 keV photopeak be used for imaging. In this case, a 15–20% energy window, a medium energy collimator and a system with a thicker crystal are recommended. If low count rates are a concern, a second energy window centred on the 113 keV photopeak can be used to increase counting statistics. In this case, the two datasets corresponding to the two energy windows should be acquired into separate projection files and reconstructed into two separate images with each image individually compensated for attenuation and scatter. If the images obtained from the two windows have a similar image quality, they can be summed for further analysis. If only an LEHR collimator is available, only the 113 keV photopeak should be used for imaging because of the high fraction of septal penetration events associated with the 208 keV photopeak window (Fig. 5.8). Because of the low yield of gamma rays emitted in the decay of ^{177}Lu and the very small bremsstrahlung contribution, count losses due to dead time effects are relatively small but should be considered if imaging soon after a therapy administration [5.46].

For ^{177}Lu, relatively good quantification accuracy can be achieved with the TEW-SC applied to each photopeak. If the medium energy collimator is used, the high energy scatter window corresponding to the 208 keV photopeak can be omitted as there will be very few counts in this window, hence the scatter estimate can be obtained with a triangular approximation based only on the counts in the lower energy scatter window. However, if a low energy collimator is used the counts in the upper scatter window will be significant due to penetration/down scatter by the lower abundance photopeak at 249.7 and 321.3 keV (Fig. 5.8), hence both scatter windows should be used. For the 113 keV photopeak the use of both scatter windows is necessary, regardless of the collimator used, because of the significant contribution from down scatter of the 208 keV photons. The width of the scatter windows must be chosen carefully because of potential interference from X ray photons in the case of the 113 keV photopeak and other gamma ray emissions in the case of the 208 keV photopeak. A study evaluating 4 keV versus 10 keV scatter windows for the 113 and 208 keV photopeaks of ^{177}Lu reported that both sets of windows gave comparable quantitative results [5.47]. Other scatter estimation methods have also been investigated for ^{177}Lu and may be more suitable than the TEW method at low count rates, including the effective scatter source estimation (ESSE) and the analytic photon distribution interpolative method [5.47, 5.48].

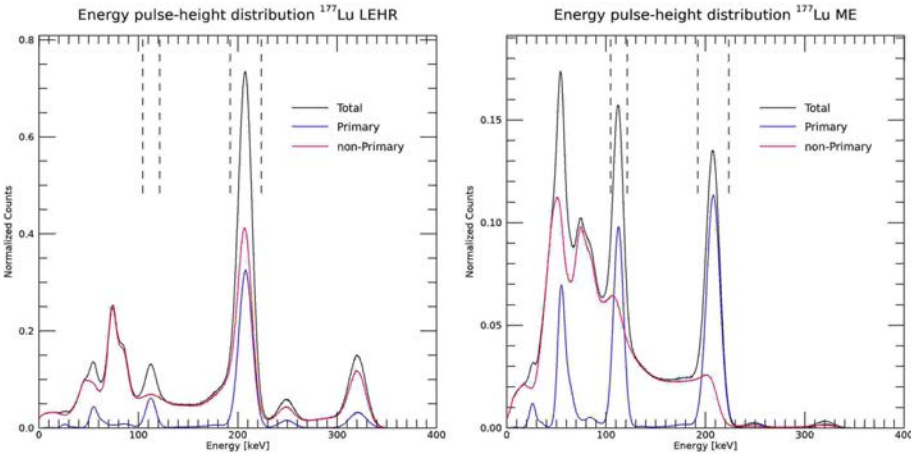

FIG. 5.8. Monte Carlo simulated ^{177}Lu energy spectrum measured by a gamma camera equipped with an LEHR (left) and medium energy (ME) (right) collimator. The phantom and camera are described in Section 5.1. Courtesy of M. Ljungberg.

5.3.3. Rhenium-188

The main application of ^{188}Re is in palliative therapy for bone metastases and in radiation synovectomy for treatment of inflammation in the synovium membrane. Additionally, ^{188}Re microspheres are used as a cost effective alternative to ^{90}Y microspheres in the trans-arterial treatment of liver malignancies. An advantage of ^{188}Re over ^{90}Y, an almost pure β emitter, is that ^{188}Re is a β emitter that also emits a gamma ray that is suitable for gamma camera imaging. Gamma camera imaging of ^{188}Re is challenging due to the presence of multiple high energy gamma rays above the main 155 keV gamma ray that is used for imaging (Fig. 5.9). Though low in abundance, the high energy gamma rays that undergo scatter can penetrate the collimator and down scatter into the photopeak acquisition window. Therefore, although the main photopeak energy is similar to that of ^{99m}Tc, a medium or high energy collimator is recommended for ^{188}Re. Since the abundance of the 155 keV gamma ray is only 15%, the loss of sensitivity when using these collimators is a challenge and prolonged acquisition times must be considered. Scatter correction with the TEW method is suitable for ^{188}Re as it enables correction for down scatter. The high energy β^- particles associated with the decay of ^{188}Re (maximum energy 2.1 MeV, maximum range 10.4 mm [5.41]) result in the generation of bremsstrahlung photons that can also interfere with the photopeak window acquisition. However, simulation studies have shown this contribution to be negligible [5.14]. Quantification

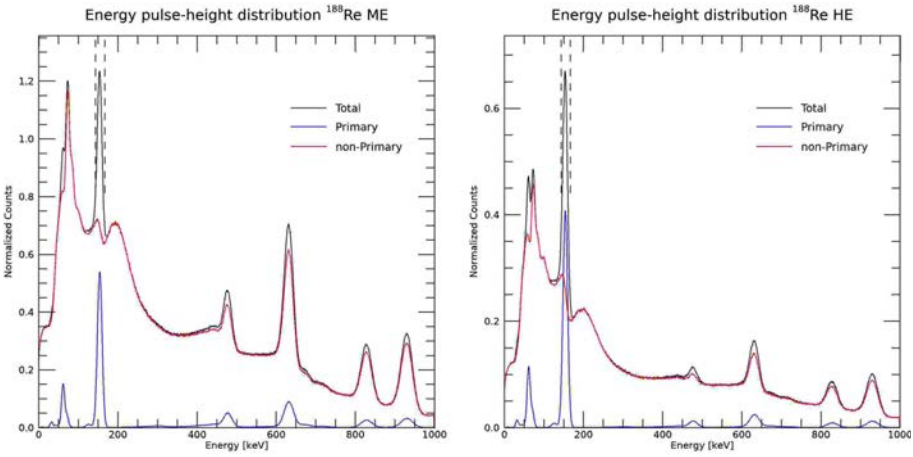

FIG. 5.9. Monte Carlo simulated ^{188}Re energy spectrum measured by a gamma camera equipped with a medium energy (ME) (left) and a high energy (HE) (right) collimator. The phantom and camera are described in Section 5.1. Courtesy of M. Ljungberg.

accuracies within 10% have been reported for activity concentration in a uniform phantom and for hot objects (2–200 mL) in a phantom with cold background in a study using standard OS-EM reconstruction with CT-AC, TEW-SC and CDR compensation [5.21].

5.3.4. Holmium-166

Over the years there has been interest in ^{166}Ho as an attractive theranostic radionuclide for therapeutic applications [5.49]. In addition to the high energy beta particle emission for treatment and the 81 keV (7%) gamma ray suitable for SPECT imaging it has a high magnetic susceptibility for magnetic resonance imaging. Holmium-166 labelled antibodies and peptides have been investigated, and recently ^{166}Ho microspheres have become commercially available for intra-arterial liver radioembolization as an alternative to ^{90}Y microspheres. The advantages over ^{90}Y are that the same microspheres can be used for both pre-therapy diagnostic imaging and for the therapy itself. Pre-therapy ^{166}Ho imaging can be used for lung shunt estimation and to predict the absorbed doses that will be delivered to tumour and non-tumoural liver from the therapy.

Like some of the other therapy radionuclides, quantitative ^{166}Ho SPECT is complicated by the presence of multiple low intensity gamma ray emissions with energies above the main photopeak energy (Fig. 5.10). Furthermore, because of the high energy of the ^{166}Ho β^- particles (maximum energy 1.86 MeV, maximum

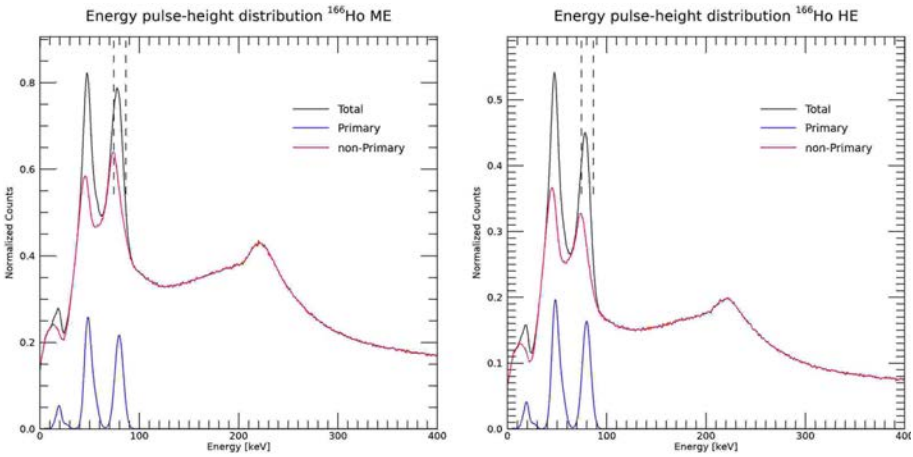

FIG. 5.10. Monte Carlo simulated ^{166}Ho energy spectrum measured by a gamma camera equipped with a medium energy (ME) (left) and a high energy (HE) (right) collimator. The phantom and camera are described in Section 5.1. The peaks around 200 keV are due to backscattering from material behind the crystal. The 'background' of non-primary events is due to septum penetration in the collimator followed by partial energy depositions from Compton scattering in the crystal from the low intensity photons having high energies up to 1.83 MeV. Courtesy of M. Ljungberg.

range 9 mm [5.41]) the contribution from bremsstrahlung photons (extending from 0 to 1.86 MeV) must also be considered. Gamma rays and photons that undergo septal penetration, down scatter and camera backscatter can contribute to the photopeak window image and degrade the quantification accuracy. To reduce the impact of septal penetration, a medium or high energy collimator should be used. Although the TEW method can be used for scatter correction, the inclusion of characteristic Pb X rays (74 keV) in the main acquisition window at 81 keV and the adjacent lower energy scatter window must be considered. To improve the quantitative accuracy of ^{166}Ho SPECT, Monte Carlo based compensation for image degrading factors has been investigated [5.50].

5.3.5. Samarium-153

The bone seeking ^{153}Sm ethylene-diaminetetramethylene phosphonic acid (^{153}Sm-EDTMP) is used to selectively deliver radiation to osteoblastic bone metastases and osteosarcoma. Although no survival benefits in these patients have been reported for radionuclide therapy with beta emitting radionuclides, a meta-analysis has provided evidence that pain relief is achieved after a single

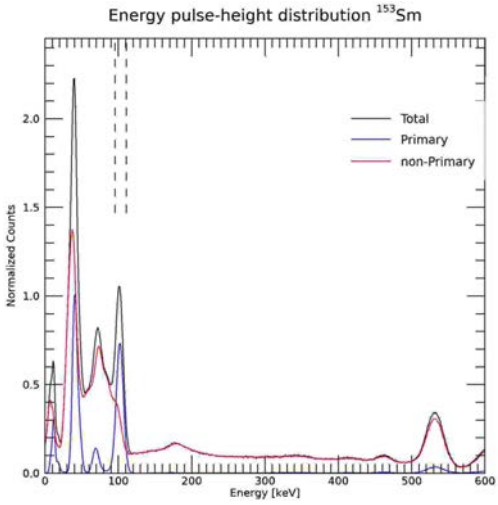

FIG. 5.11. Monte Carlo simulated ^{153}Sm energy spectrum measured by a gamma camera equipped with an LEHR collimator. The phantom and camera are described in Section 5.1. Courtesy of M. Ljungberg.

treatment with ^{153}Sm in 70% of patients [5.51]. Most of the evaluated patients had prostate cancer with bone metastases.

Samarium-153 is a beta emitter with a 1.93 d half-life that also emits a 103 keV (29%) gamma ray suitable for gamma camera imaging (Fig. 5.11). Because of low tissue penetration of the betas (the average beta particle energy is 233 keV and the average range is 1.7 mm in bone) the radiation exposure to bone marrow is limited [5.52]. Planar and SPECT imaging is performed with low energy collimators using a 20% photopeak window and an adjacent low energy scatter correction window. In a study reporting on high dose treatment with 16.7 GBq of ^{153}Sm-EDTMP followed by external beam radiotherapy (EBRT), the importance of correcting for gamma camera saturation effects was emphasized [5.53]. In that study, SPECT/CT imaging was performed at 4 h and 48 h after therapy infusion and images were reconstructed with an OS-EM algorithm that included model based scatter correction, CT-AC and collimator detector response modelling. The voxel-level dose map based on the SPECT/CT imaging was used to plan the EBRT. A similar quantitative SPECT/CT imaging and reconstruction protocol was used in a study reporting on tumour dosimetry and response following ^{153}Sm-EDTMP in osteosarcoma [5.54].

5.3.6. Yttrium-90

Novel therapeutic applications with ^{90}Y loaded microspheres and ^{90}Y labelled antibodies and peptides have sparked growing interest in quantitative imaging of ^{90}Y, an almost pure high energy β^- emitter (Fig. 5.12). The relatively high energy and range in tissue of ^{90}Y β^- particles (maximum energy 2.3 MeV, maximum range 11.3 mm [5.41]) allows for high absorbed dose deposition and eradication of tumour cells that are not directly targeted. Additionally, the half-life (64 h) is well suited for a variety of radionuclide therapy applications. The lack of gamma photons simplifies the radioprotection of surrounding organs and personnel but makes direct imaging of ^{90}Y complex; it involves SPECT via bremsstrahlung photons associated with the β^- particles or PET via a very low abundance positron emission from internal pair production.

PET has the advantage of superior resolution that can lead to better quantification of smaller lesions, but a disadvantage is the high noise associated with a low true coincidence count rate in the presence of a high random coincidence count rate due to the bremsstrahlung photons. Accurate quantitative ^{90}Y imaging either by SPECT or PET requires very high activity concentrations, such as those seen in trans-arterial radioembolization treatment in which up to several GBq of ^{90}Y microspheres are focally administered to parts of the liver. Because of the complexities associated with direct ^{90}Y imaging, ^{99m}Tc labelled MAA particles are used as a pre-therapy gamma emitting surrogate for predicting shunting to the lung and absorbed doses to lesions and non-tumoural liver from the radioembolization. Similarly, in radionuclide therapies, ^{111}In labelled antibodies and peptides, with analogous chemical properties as the ^{90}Y labelled analogue, have been developed as surrogate gamma emitting pre-therapy imaging agents for pharmacokinetics assessment for dosimetry. However, these surrogates may not always accurately predict the ^{90}Y biodistribution/pharmacokinetics from the therapy administration, hence direct post-treatment ^{90}Y imaging is often performed.

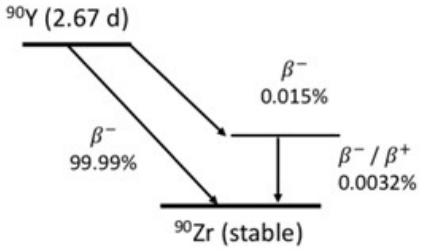

FIG. 5.12. Yttrium-90 decay scheme. Courtesy of M. Ljungberg.

5.3.6.1. Yttrium-90 bremsstrahlung imaging

The β^- particles emitted by ^{90}Y decay lose kinetic energy and slow down as they interact with atoms in the tissue media. Most of the interactions occur between the β^- particle and orbital electrons, but sometimes the interaction is with the atomic nucleus, resulting in deflection of the β^- particle and generation of **external** bremsstrahlung photons that can potentially be imaged by a gamma camera [5.55]. The bremsstrahlung energy spectrum is continuous, ranging from nearly zero, if the particle is only slightly deflected, to up to the full energy of the incident β^- particle (2.3 MeV for ^{90}Y), in which case the particle is stopped. A second source of bremsstrahlung photons, **internal** bremsstrahlung, is the continuous energy electromagnetic radiation that accompanies β^- and electron capture decay [5.56]. These photons are emitted alongside externally generated bremsstrahlung photons. Like the external bremsstrahlung spectrum, the internal bremsstrahlung spectrum extends from zero to the β^- end point energy.

Bremsstrahlung production accounts for only a small fraction of β^- particle energy loss, hence the ^{90}Y photon yield is typically low. The probability of bremsstrahlung production increases with the atomic number of the absorber and the β^- particle energy. In the case of ^{90}Y, less than 3% of β^- interactions in water results in photons of energy >50 keV [5.14], hence bremsstrahlung imaging with a gamma camera is an inefficient process. Additionally, standard gamma camera

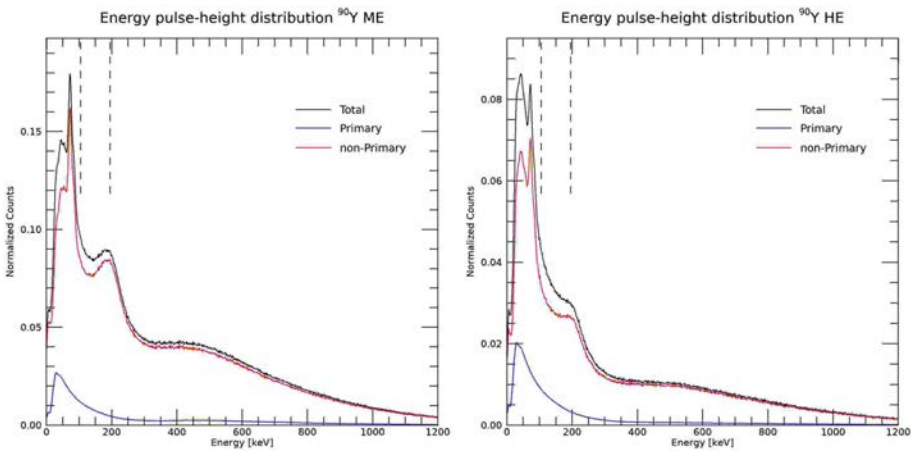

FIG. 5.13. Monte Carlo simulated ^{90}Y bremsstrahlung energy spectrum measured by a gamma camera equipped with a medium energy (ME) collimator (left) and a high energy (HE) collimator (right). The peak around 200 keV is a contribution of events from photons backscattered in the compartment behind the NaI(Tl) crystal. The phantom and camera are described in Section 5.1. Courtesy of M. Ljungberg.

systems and the corresponding reconstruction algorithms typically available in the clinic are designed for gamma rays with well defined energies and not for photons that have a continuous energy spectrum extending up to high energies. Complexities of ^{90}Y imaging with a gamma camera are primarily associated with the penetration and down scatter of high energy photons that contribute to counts in the lower energy acquisition window and inadequacy of standard energy window based scatter correction with a continuous energy spectrum. The energy dependence of the attenuation map also contributes to the complexity of imaging photons with a continuous energy spectrum. Another consideration is the degradation in spatial resolution because of the finite distance between the location of the ^{90}Y decay and the location where the external bremsstrahlung photons are generated, akin to positron range effects in PET. A further complication is that the bremsstrahlung yield and energy spectrum are tissue dependent [5.57], but this effect is not significant when imaging homogenous regions such as the liver.

Despite the complexities, images sufficient in quality to assess post-therapy ^{90}Y distributions have been achieved with bremsstrahlung imaging and standard reconstruction methods, especially with the use of SPECT/CT systems. Proper choice of collimators and energy windows is a simple step that can improve image quality and quantification. While both medium and high energy collimators have been used for ^{90}Y bremsstrahlung imaging, the high energy collimator reduces the down scatter and penetration contribution (Fig. 5.13), thereby improving image contrast. The loss in sensitivity due to the use of high energy versus medium energy collimators is estimated as ~30% when considering only the desired primary (unscattered) events. A relatively low energy window in the 100–200 keV range avoids the characteristic lead X ray peaks at lower energies and the rapid decrease in the fraction of primary photons at higher energies evident in Fig. 5.13. Although moving the window to allow lower energy photons will increase sensitivity this will also increase the fraction of multiple-order scatter events, which increases dramatically at lower energies. If count rates are high enough to permit the use of a single narrow window, or if a multiple narrow window reconstruction model is used, then the inaccuracies associated with using a single energy attenuation coefficient map and CDR over a wide window can be reduced. In some studies, to account for the energy dependence of the bremsstrahlung yield, the attenuation coefficient map and CDR are determined at the mean energy of the respective window. To overcome some of the limitations of using standard SPECT reconstruction for bremsstrahlung photons, empirical methods for scatter correction [5.58] and specialized reconstruction methods that rely on Monte Carlo based (Fig. 5.14) or model based methods for scatter estimation have been developed [5.17, 5.19, 5.59, 5.60]. Some of these methods use a multi-window modelling approach in the reconstruction that enables

accurate quantitative imaging with a wide energy window (e.g. 100–500 keV), which is important in applications such as radioimmunotherapy and PRRT, where the uptake concentration in lesions and normal organs can be substantially lower than in radioembolization. Recently, a deep learning based method was reported for bremsstrahlung SPECT scatter correction, in which a convolutional neural network was trained to predict the scatter estimate based on the measured ^{90}Y emission projections and the CT based attenuation projections [5.61].

5.3.6.2. Yttrium-90 PET

Yttrium-90, an almost 'pure' β^- emitter, also has a low probability branch to the first excited state of ^{90}Zr where a transition may occur by electron–positron internal pair production (Fig. 5.12). Though the probability for positron emission is extremely low (Table 5.2) it has been successfully exploited for PET imaging [5.22, 5.62]. The spatial resolution of ^{90}Y PET has been reported to be similar to that of ^{18}F PET [5.30], but reported recovery coefficients are generally lower [5.22]. Yttrium-90 PET is typically performed with a longer acquisition time compared with conventional PET (20–30 min per bed position is typical, compared with the 2–5 min per bed position used in FDG PET/CT).

Yttrium-90 PET imaging is complex especially because the low abundance positrons have to be imaged in the presence of a high flux of bremsstrahlung photons generated by β^- interactions. Although the bremsstrahlung yield in tissue drops off rapidly with energy, some photons fall within the acquisition energy window for the 511 keV annihilation photons. This results in a singles count rate that substantially exceeds the true coincidence count rate of the annihilation photons from the positron interactions. The high flux of bremsstrahlung photons results in a high contribution of random coincidences that can occur between two bremsstrahlung photons or between a bremsstrahlung photon and an annihilation photon. The probability of these events occurring in true coincidence is extremely low, so the true coincidences are mainly between two annihilation photons. An additional challenge when imaging at very low true coincidence count rates, which is not a concern at the rates associated with conventional ^{18}F PET, is the presence of natural radioactivity in lutetium oxyorthosilicate (LSO) and yttrium doped lutetium oxyorthosilicate (LYSO) crystals commonly used as the scintillator material in PET systems. Lutetium contains traces of ^{176}Lu, which decays by β^- emission with a cascade of prompt gamma rays that can lead to both random and true coincidences in PET systems. As a result of the ^{176}Lu background radiation and presence of bremsstrahlung photons, the randoms fraction typically associated with ^{90}Y PET far exceeds that of typical ^{18}F PET (>80% compared with 30–50%). One important consideration in ^{90}Y PET is the manner in which random coincidences are corrected. For randoms estimation based on acquisition

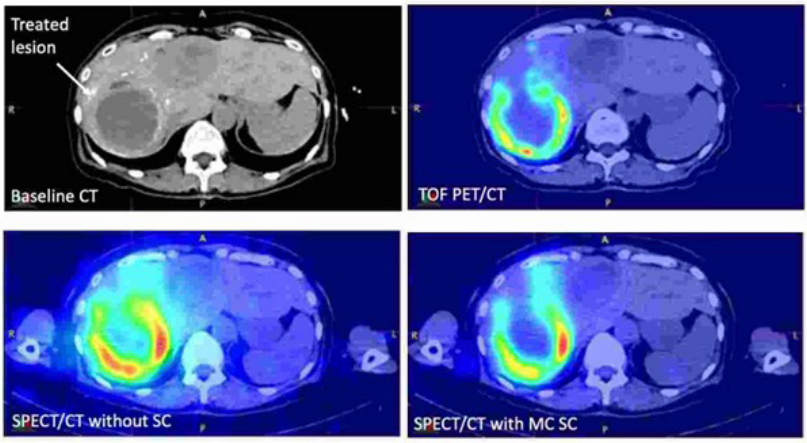

FIG. 5.14. Comparison of ^{90}Y SPECT/CT without and with Monte Carlo based scatter correction and ^{90}Y time-of-flight PET/CT. SPECT/CT and PET/CT were acquired within 2 h of ^{90}Y radioembolization with glass microspheres (3.9 GBq). Acquisition time was ~30 min for each scan. The large neuroendocrine tumour indicated on the baseline CT has a necrotic centre and enhancing rim. The contrast between the rim and the necrotic centre is better visualized on SPECT/CT with scatter correction and PET/CT. The superior resolution of PET/CT over SPECT/CT is evident. Courtesy of Y. Dewaraja.

in a delayed window discussed in Chapter 4, it has been shown that smoothing of the delayed coincidence events prior to randoms correction leads to less noise and better quantification [5.22]. Another consideration in quantitative imaging at low count rates (high noise) is potential inaccuracies in scatter correction. With very noisy data, PET scatter correction methods that rely on scatter simulations/models followed by scaling based on tail fitting are expected to lead to large under- or overestimation of scatter [5.23].

Due to the noisy images, a lower number of iterations are used in ^{90}Y PET OS-EM reconstruction compared with conventional PET, with 1–2 iterations (21–24 subsets) being typical for ^{90}Y. Including time-of-flight (TOF) information reduces the impact of the high randoms fraction and studies have demonstrated improved image quality and quantification with TOF PET compared with standard PET [5.22]. With appropriate selection of imaging and reconstruction parameters suitable for low count rates, ^{90}Y TOF PET/CT has demonstrated quantitative capabilities that allow application in dosimetry under conditions where there is high focal uptake (Fig. 5.14). Phantom studies show high accuracy for activity quantification in uniform background regions; however, contrast recovery and activity recovery in hot spheres are lower than that achieved with ^{18}F PET [5.22]. In the multicentre phantom study of Willowson et al. [5.22], underestimation of

activity concentration with TOF PET/CT with parameters optimized for ^{90}Y was up to 20% even for the largest sphere with a diameter of 37 mm. A limitation of quantitative ^{90}Y PET is the bias associated with the non-negativity constraint of standard OS-EM reconstruction algorithms where negative sinogram values are set to zero following randoms correction. While this bias does not significantly impact imaging with conventional radiotracers where image noise is low, the impact on ^{90}Y PET is substantial. Specialized reconstruction methods tailored for low count conditions are needed to further improve image noise and quantitative capabilities with ^{90}Y PET [5.63].

Acquisition software on some PET workstations does not support ^{90}Y as a radionuclide option. Hence, an additional re-scaling step is required to obtain the ^{90}Y distribution in activity concentration units (e.g. Bq/mL). This involves selecting a surrogate radionuclide from the list of available radionuclides for the acquisition and then scaling the reconstructed ^{90}Y PET image by the ratio of the positron emission probability of ^{90}Y and that of the selected radionuclide. The chosen radionuclide should have a half-life that is much longer than the scan time (e.g. ^{22}Na) to avoid any impact of scanner decay correction.

5.4. IMAGING IN ALPHA PARTICLE THERAPIES

Clinical trials of radionuclide therapy with α emitters are showing much promise in the treatment of various malignancies. The short range (~6 cell diameters or 50–100 μm in tissue) and high linear energy transfer (LET) associated with α particles make them an attractive choice for therapy compared with beta particles, especially for treating micro-metastases. Currently available α emitters that have favourable characteristics for therapy include ^{211}At, ^{225}Ac, ^{213}Bi, ^{227}Th, ^{212}Pb and ^{223}Ra. Although there are therapeutic advantages, accurate in vivo quantitative imaging of the biodistribution and kinetics of the alpha-labelled radiopharmaceuticals for dosimetry is challenging. The primary decay mode for these radionuclides is the emission of an α particle, but some, such as ^{223}Ra, also have associated X ray and gamma ray photons that can potentially be used for gamma camera imaging of the biodistribution in the patient after a therapeutic administration. The activities administered in α particle therapies are, however, very low, hence quantitative imaging of these low abundance photons by conventional gamma camera systems and software is challenging. Furthermore, the complex decay chains associated with α emitters, with photons' emissions from progeny, adds to the challenge.

Much of the work on in vivo photon imaging of α emitters has focused on ^{223}Ra, which is a bone seeking radionuclide currently used in clinical practice for the treatment of bone metastases of prostate cancer. Although the administered

activity to patients is very low (typically 55 kBq per kg body weight, hence <5 MBq), multiple studies have demonstrated the feasibility of gamma camera imaging of ^{223}Ra as summarized in a review article [5.64]. In these studies, both phantom and patient results have demonstrated the feasibility of semi-quantitative imaging or fully quantitative imaging for dosimetry. In clinical studies, good correlation between ^{223}Ra dichloride and ^{99m}Tc-methylene diphosphonate (MDP) images when comparing the uptake in lesions and lesion to background ratios has been demonstrated. Furthermore, reasonable reproducibility (within ~20%) between cycles has been demonstrated for lesion absorbed doses in patients imaged after successive therapy cycles.

Radium-223 decays to stable ^{207}Pb through a series of short lived progeny. The main X rays and photons associated with the ^{223}Ra decay chain are listed in Table 5.4 together with their emission probabilities. Some of these photons have too low or too high energies for imaging with conventional gamma cameras that are not designed to handle energies outside the range 50–500 keV. The most suitable photons for gamma camera imaging are considered to be the X rays at 83.8 keV (25%) and 81.1 keV (15%). An energy window centred around 82 keV can encompass both of these X rays. Depending on the width of the acquisition window, the 94.6 keV X rays of ^{223}Ra and the 72.9 keV X rays of its progeny ^{211}Bi can also contribute to counts acquired in this window. Additionally, characteristic Pb X rays generated in the collimator septa can be detected in this energy window. It has been shown that inclusion of these Pb X rays increases the sensitivity, without degrading image contrast or quantification [5.65, 5.66]. In addition to these lower energy X rays, the most suitable gamma rays for imaging are at 154 keV (6%) and at 270 keV (13%). Three energy windows centred at 82, 154 and 270 keV were evaluated for quantitative planar imaging of ^{223}Ra by Hindorf et al. [5.65]. Based on the sensitivity, spatial resolution and partial volume effects measured for the three different energy windows, the use of the 82 keV energy window was recommended. Using a medium energy collimator, the planar in ‘air’ sensitivity and spatial resolution they reported for this window on their system were 69 cps/MBq and 10.7 mm FWHM, respectively (the corresponding values for ^{99m}Tc on the same system were 55 cps/MBq and 8.3 mm). Since energy window based scatter correction is not well suited for low count conditions, for their quantitative studies they used an effective mass attenuation coefficient that included the effects of scatter. For the 82 keV window, the reported quantitative accuracies were within 10% for a 200 mL volume and within 40% for a 0.5 mL volume imaged under clinically relevant count rates. For patient studies, a planar static acquisition time of 30 min for a 100 kBq/kg administration was recommended. The multiple imaging time points for determining pharmacokinetics for dosimetry must be selected considering both the low count rates and the relatively long half-life (11.4 d) of ^{223}Ra. A late

TABLE 5.4. THE MAIN GAMMA RAYS AND CHARACTERISTIC X RAYS ASSOCIATED WITH THE DECAY OF RADIUM-223 THAT ARE RELEVANT TO GAMMA CAMERA IMAGING [5.68]

(courtesy of M. Ljungberg)

Parent	Energy (keV)	Emission probability per disintegration	Type of photon
Ra-223	122.3	0.0130	γ ray
	144.3	0.0351	γ ray
	154.2	0.0608	γ ray
	269.5	0.1324	γ ray
	323.9	0.0363	γ ray
	338.5	0.0259	γ ray
	445.0	0.0122	γ ray
	83.8	0.251	characteristic X ray
	81.1	0.152	characteristic X ray
	94.9	0.115	characteristic X ray
Rn-219	271.2	0.1069	γ ray
	401.8	0.0656	γ ray
Pb-211	404.8	0.0401	γ ray
	427.2	0.0189	γ ray
	704.7	0.0050	γ ray
	766.7	0.0069	γ ray
	832.0	0.0348	γ ray
Bi-211	351.0	0.1311	γ ray
	72.9	0.0126	characteristic X ray

time point is desirable but may be unfeasible because of low counts. Studies where multi-time point imaging was reported have relied on 4–6 time points at day 0, day 1, days 2–4, days 4–6 and days 7–9 [5.65, 5.67].

Due to the low count rates, the collimator and energy window selected for ^{223}Ra imaging must have high sensitivity. However, a large fraction of counts detected in the acquisition window may originate from higher energy photons associated with the ^{223}Ra decay chain that down scatter to the lower energy windows. This includes photons that may have undergone septal penetration in addition to scatter. In order to reduce the fraction of 'contamination' events, a medium or high energy collimator is preferred over a low energy collimator even when using the 82 keV acquisition window. Figure 5.15 compares the Monte Carlo simulated gamma camera energy spectra corresponding to high,

medium and low energy collimators. As Fig. 5.15 shows, the LEHR collimator has the highest sensitivity, but due to increased penetration/down scatter events the fraction of primary photons in the 82 keV window is lower than with the medium and high energy collimators (see also Table 5.1). To increase sensitivity for SPECT studies while keeping the acquisition time at 30 min, a wider window than is typical has been suggested in a past study [5.66] that reported 50% higher contrast to noise ratios with a 40% window at 84 keV compared with a 20% window at 82 keV. For the phantom and camera described in Section 5.1, a comparison of simulated noise-free planar images shows that there is no loss in image quality and contrast when the wider window is used (Fig. 5.16). Thus, a 40% window at 84 keV can be considered for single peak imaging, but when multi-peak imaging capabilities are available the 154 and 270 keV windows can also be utilized to boost counts, especially for SPECT acquisitions.

SPECT imaging with iterative image reconstruction offers several advantages over planar imaging, especially for radionuclides that are challenging to image. The image degrading physical factors can be included in the system model of the iterative reconstruction. Additionally, the inability to distinguish between activity in overlying and underlying tissue with planar imaging is particularly problematic for prostate cancer application because metastases occur mostly in the pelvic and lumbar spine regions and there is high activity in the intestines due to excretion of ^{223}Ra. Because of the very low photon count rates, quantitative gamma camera imaging of α emitters was originally focused only on planar imaging and SPECT was considered unfeasible. However, a few recent studies have shown that with careful selection of imaging parameters and/or use of specialized reconstruction software, quantitative SPECT imaging of ^{223}Ra as well as some other α emitters is feasible. The SPECT study by Owaki et al. [5.66] used a clinically relevant body phantom simulating activity in bowel and lumbar

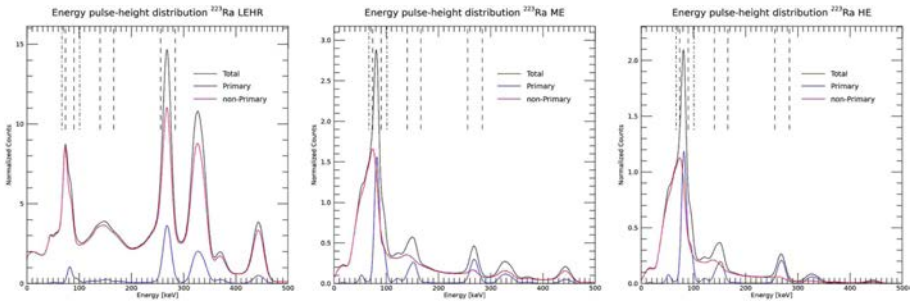

FIG. 5.15. Radium-223 gamma camera energy spectra imaged with LEHR, medium energy (ME) and high energy (HE) collimators. The phantom and camera are described in Section 5.1. Courtesy of M. Ljungberg.

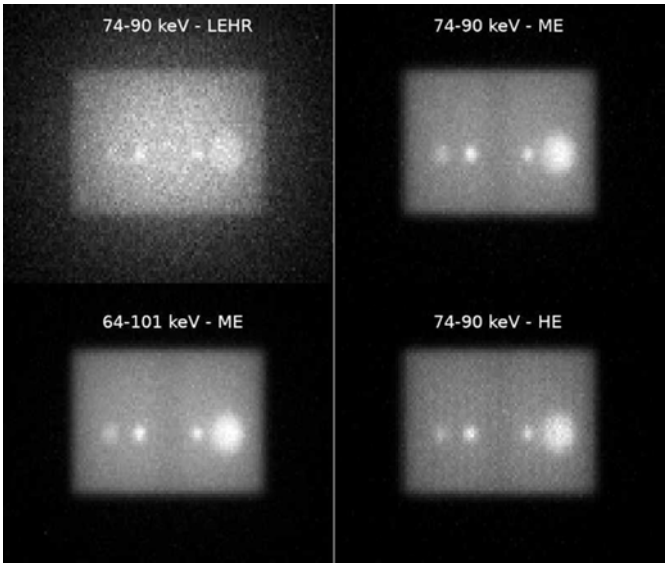

FIG. 5.16. Noise-free simulations of planar ^{223}Ra images corresponding to the sphere phantom of Section 5.1 for different collimators and a 20% energy window at 82 keV. For the medium energy (ME) collimator, an image corresponding to a wider window (40% at 84 keV) is also shown. Note that the dark vertical band across the centre, due to the 'cold' lung insert at the centre of the phantom, is not distinguishable with the LEHR collimator due to the higher fraction of scatter and septal penetration. Courtesy of M. Ljungberg.

spine metastases to show the superior (semi-quantitative) performance of SPECT over planar imaging in the presence of overlapping activity. Based on their phantom and clinical SPECT evaluations they recommended a high energy collimator and a wide energy window of 40% at 84 keV to include multiple X rays including characteristic Pb X rays around this energy. They used standard 3-D OS-EM reconstruction software, but without scatter and AC. Using these parameters and a 30 min acquisition they performed semi-quantitative SPECT imaging of patients 2 h after the injection of ^{223}Ra (55 kBq/kg). Comparison with ^{99m}Tc-MDP SPECT imaging of the same patients showed ^{223}Ra SPECT to be less sensitive and lesion to background ratios to be substantially lower, which was attributed to differences in spatial resolution and lack of compensation for scatter, attenuation and CDR in the ^{223}Ra reconstruction while including them in the ^{99m}Tc reconstruction. However, the visual quality of the SPECT image was encouraging, and it was possible to separate the uptake in bone metastases in the lumbar spine from intense bowel activity. They showed a reasonable correlation between lesion to background ratios in ^{99m}Tc and ^{223}Ra SPECT (r = 0.67 with the medium energy and 0.69 with the high energy collimator).

SPECT imaging of α emitting radionuclides is in the developmental stage, and hardware and software specialized for this challenging imaging situation can play an important role in the future. Solid state detectors that offer higher energy resolution and hence improved scatter rejection, compared with standard gamma camera systems that are based on the scintillator-photomultiplier tube combination, have the potential to enhance image quality and quantitative accuracy. Use of iterative reconstruction that allows multi-window reconstruction with energy dependent system models; use of model based scatter correction; full modelling of the CDR, including septal penetration tails and characteristic Pb X rays; have the potential for achieving improved image quality and quantification over what has been achieved with standard reconstruction. Preliminary results with specialized reconstruction algorithms for SPECT imaging of ^{223}Ra, as well as ^{227}Th with cross-talk correction for contributions from its progeny, ^{223}Ra, are promising, but these methods are still under development [5.69]. Furthermore, because PET and SPECT resolution is inadequate for microscale level imaging, studies on alpha particle microdosimetry, where pre-clinical data are translated to the patient using pharmacokinetic models, are ongoing [5.70].

REFERENCES

[5.1] SIEGEL, J.A., et al., MIRD Pamphlet No. 16: Techniques for quantitative radiopharmaceutical biodistribution data acquisition and analysis for use in human radiation dose estimates, J. Nucl. Med. **40** 2 (1999) 37s–61s.

[5.2] FLUX, G., CHITTENDEN, S., SARAN, F., GAZE, M., Clinical applications of dosimetry for mIBG therapy, Q. J. Nucl. Med. Mol. Imaging **55** 2 (2011) 116–125.

[5.3] HE, B., DU, Y., SONG, X., SEGARS, W.P., FREY, E.C., A Monte Carlo and physical phantom evaluation of quantitative In-111 SPECT, Phys. Med. Biol. **50** 17 (2005) 4169–4185, https://doi.org/10.1088/0031-9155/50/17/018

[5.4] RAHMIM, A., ZAIDI, H., PET versus SPECT: Strengths, limitations and challenges, Nucl. Med. Commun. **29** 3 (2008) 193–207, https://doi.org/10.1097/MNM.0b013e3282f3a515

[5.5] CONTI, M., ERIKSSON, L., Physics of pure and non-pure positron emitters for PET: A review and a discussion, EJNMMI Phys. **3** 1 (2016) 8, https://doi.org/10.1186/s40658-016-0144-5

[5.6] ZEINTL, J., VIJA, A.H., YAHIL, A., HORNEGGER, J., KUWERT, T., Quantitative accuracy of clinical ^{99m}Tc SPECT/CT using ordered-subset expectation maximization with 3-dimensional resolution recovery, attenuation, and scatter correction, J. Nucl. Med. **51** 6 (2010) 921–928, https://doi.org/10.2967/jnumed.109.071571

[5.7] WILLOWSON, K., BAILEY, D.L., BALDOCK, C., Quantitative SPECT reconstruction using CT-derived corrections, Phys. Med. Biol. **53** (2008) 3099–3112, https://doi.org/10.1088/0031-9155/53/12/002

[5.8] VAN GILS, C.A., BEIJST, C., VAN ROOIJ, R., DE JONG, H.W., Impact of reconstruction parameters on quantitative I-131 SPECT, Phys. Med. Biol. **61** 14 (2016) 5166–5182, https://doi.org/10.1088/0031-9155/61/14/5166

[5.9] DEWARAJA, Y.K., et al., ^{131}I-tositumomab radioimmunotherapy: Initial tumor dose–response results using 3-dimensional dosimetry including radiobiologic modeling, J. Nucl. Med. **51** 7 (2010) 1155–1162, https://doi.org/10.2967/jnumed.110.075176

[5.10] ZIMMERMAN, B.E., et al., Multi-centre evaluation of accuracy and reproducibility of planar and SPECT image quantification: An IAEA phantom study, Z. Med. Phys. **27** (2017) 98–112, https://doi.org/10.1016/j.zemedi.2016.03.008

[5.11] TRAN-GIA, J., LASSMANN, M., Optimizing image quantification for ^{177}Lu SPECT/CT based on a 3D printed 2-compartment kidney phantom, J. Nucl. Med. **59** 4 (2018) 616–624, https://doi.org/10.2967/jnumed.117.200170

[5.12] HIPPELÄINEN, E., TENHUNEN, M., MÄENPÄÄ, H., SOHLBERG, A., Quantitative accuracy of ^{177}Lu SPECT reconstruction using different compensation methods: Phantom and patient studies, EJNMMI Res. **6** 1 (2016) 16, https://doi.org/10.1186/s13550-016-0172-0

[5.13] GUSTAFSSON, J., et al., Uncertainty propagation for SPECT/CT-based renal dosimetry in ^{177}Lu peptide receptor radionuclide therapy, Phys. Med. Biol. **60** 21 (2015) 8329–8346, https://doi.org/10.1088/0031-9155/60/21/8329

[5.14] URIBE, C.F., ESQUINAS, P.L., GONZALEZ, M., CELLER, A., Characteristics of Bremsstrahlung emissions of ^{177}Lu, ^{188}Re, and ^{90}Y for SPECT/CT quantification in radionuclide therapy, Phys. Med. **32** 5 (2016) 691–700, https://doi.org/10.1016/j.ejmp.2016.04.014

[5.15] BEAUREGARD, J.M., HOFMAN, M.S., PEREIRA, J.M., EU, P., HICKS, R.J., Quantitative ^{177}Lu SPECT (QSPECT) imaging using a commercially available SPECT/CT system, Cancer Imaging **11** (2011) 56–66, https://doi.org/10.1102/1470-7330.2011.0012

[5.16] ASSIÉ, K., GARDIN, I., VÉRA, P., BUVAT, I., Validation of the Monte Carlo simulator GATE for indium-111 imaging, Phys. Med. Biol. **50** 13 (2005) 3113–3125, https://doi.org/10.1088/0031-9155/50/13/010

[5.17] MINARIK, D., SJÖGREEN GLEISNER, K., LJUNGBERG, M., Evaluation of quantitative ^{90}Y SPECT based on experimental phantom studies, Phys. Med. Biol. **53** (2008) 5689–5703, https://doi.org/10.1088/0031-9155/53/20/008

[5.18] RONG, X., DU, Y., LJUNGBERG, M., FREY, E., Experimental evaluation of quantitative accuracy of activity estimates from a new Y-90 Bremsstrahlung SPECT method, J. Nucl. Med. **52** Suppl. 1 (2011) 2019.

[5.19] DEWARAJA, Y.K., et al., Improved quantitative ^{90}Y bremsstrahlung SPECT/CT reconstruction with Monte Carlo scatter modeling, Med. Phys. **44** 12 (2017) 6364–6376, https://doi.org/10.1002/mp.12597

[5.20] DE WIT, T.C., et al., Hybrid scatter correction applied to quantitative holmium-166 SPECT, Phys. Med. Biol. **51** 19 (2006) 4773–4787, https://doi.org/10.1088/0031-9155/51/19/004

[5.21] ESQUINAS, P.L., et al., Accuracy of Rhenium-188 SPECT/CT activity quantification for applications in radionuclide therapy using clinical reconstruction methods, Phys. Med. Biol. **62** 16 (2017) 6379–6396, https://doi.org/10.1088/1361-6560/aa7926

[5.22] WILLOWSON, K.P., TAPNER, M., TEAM, Q.I., BAILEY, D.L., A multicentre comparison of quantitative ^{90}Y PET/CT for dosimetric purposes after radioembolization with resin microspheres: The QUEST Phantom Study, Eur. J. Nucl. Med. Mol. Imaging **42** 8 (2015) 1202–1222, https://doi.org/10.1007/s00259-015-3059-9

[5.23] CARLIER, T., et al., ^{90}Y-PET imaging: Exploring limitations and accuracy under conditions of low counts and high random fraction, Med. Phys. **42** 7 (2015) 4295–4309, https://doi.org/10.1118/1.4922685

[5.24] JENTZEN, W., et al., Iodine-124 PET dosimetry in differentiated thyroid cancer: Recovery coefficient in 2D and 3D modes for PET(/CT) systems, Eur. J. Nucl. Med. Mol. Imaging **35** 3 (2008) 611–623, https://doi.org/10.1007/s00259-007-0554-7

[5.25] LUBBERINK, M., HERZOG, H., Quantitative imaging of ^{124}I and ^{86}Y with PET, Eur. J. Nucl. Med. Mol. Imaging **38** Suppl. 1 (2011) S10–18, https://doi.org/10.1007/s00259-011-1768-2

[5.26] BEATTIE, B.J., PENTLOW, K.S., O'DONOGHUE, J., HUMM, J.L., A recommendation for revised dose calibrator measurement procedures for ^{89}Zr and ^{124}I, PLoS One **9** 9 (2014) e106868, https://doi.org/10.1371/journal.pone.0106868

[5.27] PREYLOWSKI, V., et al., Is the image quality of I-124-PET impaired by an automatic correction of prompt gammas? PLoS One **8** 8 (2013) e71729, https://doi.org/10.1371/journal.pone.0071729

[5.28] EZZIDDIN, S., et al., Does the pretherapeutic tumor SUV in ^{68}Ga DOTATOC PET predict the absorbed dose of ^{177}Lu octreotate? Clin. Nucl. Med. **37** 6 (2012) e141–147, https://doi.org/10.1097/RLU.0b013e31823926e5

[5.29] HAUG, A.R., et al., ^{68}Ga-DOTATATE PET/CT for the early prediction of response to somatostatin receptor-mediated radionuclide therapy in patients with well-differentiated neuroendocrine tumors, J. Nucl. Med. **51** 9 (2010) 1349–1356, https://doi.org/10.2967/jnumed.110.075002

[5.30] SODERLUND, A.T., et al., Beyond ^{18}F-FDG: Characterization of PET/CT and PET/MR scanners for a comprehensive set of positron emitters of growing application—^{18}F, ^{11}C, ^{89}Zr, ^{124}I, ^{68}Ga, and ^{90}Y, J. Nucl. Med. **56** 8 (2015) 1285–1291, https://doi.org/10.2967/jnumed.115.156711

[5.31] CREMONESI, M., et al., Radioembolization of hepatic lesions from a radiobiology and dosimetric perspective, Front. Oncol. **4** (2014) 210, https://doi.org/10.3389/fonc.2014.00210

[5.32] BAILEY, D.L., WILLOWSON, K.P., An evidence-based review of quantitative SPECT imaging and potential clinical applications, J. Nucl. Med. **54** 1 (2013) 83–89, https://doi.org/10.2967/jnumed.112.111476

[5.33] CREMONESI, M., FERRARI, M., BODEI, L., TOSI, G., PAGANELLI, G., Dosimetry in peptide radionuclide receptor therapy: A review, J. Nucl. Med. **47** 9 (2006) 1467–1475.

[5.34] FERRER, L., et al., Three methods assessing red marrow dosimetry in lymphoma patients treated with radioimmunotherapy, Cancer **116** Suppl. 4 (2010) 1093–1100, https://doi.org/10.1002/cncr.24797

[5.35] WISEMAN, G.A., et al., Radiation dosimetry results for Zevalin radioimmunotherapy of rituximab-refractory non-Hodgkin lymphoma, Cancer **94** Suppl. 4 (2002) 1349–1357, https://doi.org/10.1002/cncr.10305

[5.36] CARRASQUILLO, J.A., et al., Similarities and differences in ^{111}In- and ^{90}Y-labeled 1B4M-DTPA antiTac monoclonal antibody distribution, J. Nucl. Med. **40** 2 (1999) 268–276.

[5.37] MOORE, S.C., OUYANG, J., PARK, M.A., EL FAKHRI, G., Monte Carlo-based compensation for patient scatter, detector scatter, and crosstalk contamination in In-111 SPECT imaging, Nucl. Instrum. Methods Phys. Res. Sect. A **569** 2 (2006) 472–476, https://doi.org/10.1016/j.nima.2006.08.079

[5.38] ZIMMERMAN, B.E., et al., Calibration of traceable solid mock ^{131}I phantoms used in an international SPECT image quantification comparison, J. Res. Natl. Inst. Stand. Technol. **118** (2013) 359–374, https://doi.org/10.6028/jres.118.017

[5.39] DEWARAJA, Y.K., et al., Prediction of tumor control in ^{90}Y radioembolization by logit models with PET/CT-based dose metrics, J. Nucl. Med. **61** 1 (2020) 104–111, https://doi.org/10.2967/jnumed.119.226472

[5.40] KAPPADATH, S.C., et al., Hepatocellular carcinoma tumor dose response after ^{90}Y-radioembolization with glass microspheres using ^{90}Y-SPECT/CT-based voxel dosimetry, Int. J. Radiat. Oncol. Biol. Phys. **102** 2 (2018) 451–461, https://doi.org/10.1016/j.ijrobp.2018.05.062

[5.41] KASSIS, A.I., Therapeutic radionuclides: Biophysical and radiobiologic principles, Semin. Nucl. Med. **38** 5 (2008) 358–366, https://doi.org/10.1053/j.semnuclmed.2008.05.002

[5.42] SONG, N., DU, Y., HE, B., FREY, E.C., Development and evaluation of a model-based downscatter compensation method for quantitative I-131 SPECT, Med. Phys. **38** 6 (2011) 3193–3204, https://doi.org/10.1118/1.3590382

[5.43] DEWARAJA, Y.K., LJUNGBERG, M., FESSLER, J.A., 3-D Monte Carlo-based scatter compensation in quantitative I-131 SPECT reconstruction, IEEE Trans. Nucl. Sci. **53** 1 (2006) 181–188, https://doi.org/10.1109/TNS.2005.862956

[5.44] DEWARAJA, Y.K., et al., MIRD Pamphlet No. 23: Quantitative SPECT for patient-specific 3-dimensional dosimetry in internal radionuclide therapy, J. Nucl. Med. **53** 8 (2012) 1310–1325, https://doi.org/10.2967/jnumed.111.100123

[5.45] LJUNGBERG, M., et al., MIRD Pamphlet No. 26: Joint EANM/MIRD guidelines for quantitative ^{177}Lu SPECT applied for dosimetry of radiopharmaceutical therapy, J. Nucl. Med. **57** 1 (2016) 151–162, https://doi.org/10.2967/jnumed.115.159012

[5.46] URIBE, C.F., et al., Deadtime effects in quantification of ^{177}Lu activity for radionuclide therapy, EJNMMI Phys. **5** 1 (2018) 2, https://doi.org/10.1186/s40658-017-0202-7

[5.47] DE NIJS, R., LAGERBURG, V., KLAUSEN, T.L., HOLM, S., Improving quantitative dosimetry in ^{177}Lu-DOTATATE SPECT by energy window-based scatter corrections, Nucl. Med. Commun. **35** 5 (2014) 522–533, https://doi.org/10.1097/MNM.0000000000000079

[5.48] SHCHERBININ, S., PIWOWARSKA-BILSKA, H., CELLER, A., BIRKENFELD, B., Quantitative SPECT/CT reconstruction for ^{177}Lu and ^{177}Lu/^{90}Y targeted radionuclide therapies, Phys. Med. Biol. **57** 18 (2012) 5733–5747, https://doi.org/10.1088/0031-9155/57/18/5733

[5.49] KLAASSEN, N.J.M., ARNTZ, M.J., GIL ARRANJA, A., ROOSEN, J., NIJSEN, J.F.W., The various therapeutic applications of the medical isotope holmium-166: A narrative review, EJNMMI Radiopharm. Chem. **4** 1 (2019) 19, https://doi.org/10.1186/s41181-019-0066-3

[5.50] ELSCHOT, M., et al., Quantitative Monte Carlo-based holmium-166 SPECT reconstruction, Med. Phys. **40** 11 (2013) 112502, https://doi.org/10.1118/1.4823788

[5.51] HANDKIEWICZ-JUNAK, D., et al., EANM guidelines for radionuclide therapy of bone metastases with beta-emitting radionuclides, Eur. J. Nucl. Med. Mol. Imaging **45** 5 (2018) 846–859, https://doi.org/10.1007/s00259-018-3947-x

[5.52] PARLAK, Y., GUMUSER, G., SAYIT, E., Samarium-153 therapy for prostate cancer: The evaluation of urine activity, staff exposure and dose rate from patients, Radiat. Prot. Dosim. **163** 4 (2015) 468–472, https://doi.org/10.1093/rpd/ncu237

[5.53] HOBBS, R.F., et al., A treatment planning method for sequentially combining radiopharmaceutical therapy (RPT) and external radiation therapy (XRT), Int. J. Radiat. Oncol. Biol. Phys. **80** 4 (2011) 1256–1262, https://doi.org/10.1016/j.ijrobp.2010.08.022

[5.54] SENTHAMIZHCHELVAN, S., et al., Tumor dosimetry and response for ^{153}Sm-ethylenediamine tetramethylene phosphonic acid therapy of high-risk osteosarcoma, J. Nucl. Med. **53** 2 (2012) 215–224, https://doi.org/10.2967/jnumed.111.096677

[5.55] CHERRY, S.R., SORENSON, J.A., PHELPS, M.E., Physics in Nuclear Medicine, Elsevier Health Sciences, Philadelphia, PA (2012), https://doi.org/10.1016/B978-1-4160-5198-5.00001-0

[5.56] CENGIZ, A., ALMAZ, E., Internal bremsstrahlung spectra of beta(-) particle emitters using the Monte Carlo method, Radiat. Phys. Chem. **70** 6 (2004) 661–668, https://doi.org/10.1016/j.radphyschem.2004.03.008

[5.57] LIM, H., FESSLER, J.A., WILDERMAN, S.J., BROOKS, A.F., DEWARAJA, Y.K., Y-90 SPECT ML image reconstruction with a new model for tissue-dependent bremsstrahlung production using CT information: A proof-of-concept study, Phys. Med. Biol. **63** 11 (2018) 115001, https://doi.org/10.1088/1361-6560/aac1ad

[5.58] SIMAN, W., MIKELL, J.K., KAPPADATH, S.C., Practical reconstruction protocol for quantitative ^{90}Y bremsstrahlung SPECT/CT, Med. Phys. **43** 9 (2016) 5093, https://doi.org/10.1118/1.4960629

[5.59] ELSCHOT, M., LAM, M.G., VAN DEN BOSCH, M.A., VIERGEVER, M.A., DE JONG, H.W., Quantitative Monte Carlo-based ^{90}Y SPECT reconstruction, J. Nucl. Med. **54** 9 (2013) 1557–1563, https://doi.org/10.2967/jnumed.112.119131

[5.60] RONG, X., et al., Development and evaluation of an improved quantitative ^{90}Y bremsstrahlung SPECT method, Med. Phys. **39** 5 (2012) 2346–2358, https://doi.org/10.1118/1.3700174

[5.61] XIANG, H., LIM, H., FESSLER, J.A., DEWARAJA, Y.K., A deep neural network for fast and accurate scatter estimation in quantitative SPECT/CT under challenging scatter conditions, Eur. J. Nucl. Med. Mol. Imaging **47** 13 (2020) 2956–2967, https://doi.org/10.1007/s00259-020-04840-9

[5.62] D'ARIENZO, M., FILIPPI, L., BAGNI, O., "Quantitative postradioembolization imaging using PET/CT", Handbook of Radioembolization: Physics, Biology, Nuclear Medicine, and Imaging (PASCIAK, A.S., McKINNEY, J.M., BRADLEY, Y.C., Eds), CRC, Boca Raton, FL (2017).

[5.63] LIM, H., DEWARAJA, Y.K., FESSLER, J.A., A PET reconstruction formulation that enforces non-negativity in projection space for bias reduction in Y-90 imaging, Phys. Med. Biol. **63** 3 (2018) 035042, https://doi.org/10.1088/1361-6560/aaa71b

[5.64] FLUX, G.D., Imaging and dosimetry for radium-223: The potential for personalized treatment, Br. J. Radiol. **90** 1077 (2017) 20160748, https://doi.org/10.1259/bjr.20160748

[5.65] HINDORF, C., CHITTENDEN, S., AKSNES, A.-K., PARKER, C., FLUX, G.D., Quantitative imaging of ^{223}Ra-chloride (Alpharadin) for targeted alpha-emitting radionuclide therapy of bone metastases, Nucl. Med. Commun. **33** 7 (2012) 726–732, https://doi.org/10.1097/MNM.0b013e328353bb6e

[5.66] OWAKI, Y., et al., Ra-223 SPECT for semi-quantitative analysis in comparison with Tc-99m HMDP SPECT: Phantom study and initial clinical experience, EJNMMI Res. **7** 1 (2017) 81, https://doi.org/10.1186/s13550-017-0330-z

[5.67] PACILIO, M., et al., A case report of image-based dosimetry of bone metastases with Alpharadin (^{223}Ra-dichloride) therapy: Inter-fraction variability of absorbed dose and follow-up, Ann. Nucl. Med. **30** 2 (2016) 163–168, https://doi.org/10.1007/s12149-015-1044-9

[5.68] PIBIDA, L., et al., Determination of photon emission probabilities for the main gamma-rays of ^{223}Ra in equilibrium with its progeny, Appl. Radiat. Isot. **101** (2015) 15–19, https://doi.org/10.1016/j.apradiso.2015.03.011

[5.69] GHALY, M., DU, Y., THOREK, D., SGOUROS, G., FREY, E., Quantitative SPECT imaging of the alpha-emitter Th-227 with Ra-223 crosstalk correction, J. Nucl. Med. **59** Suppl. 1 (2018) 578.

[5.70] SGOUROS, G., HOBBS, R.F., SONG, H., Modelling and dosimetry for alpha-particle therapy, Curr. Radiopharm. **4** 3 (2011) 261–265, https://doi.org/10.2174/1874471011104030261

Chapter 6

ANALYSIS OF TEMPORALLY VARYING DATA

A. CELLER, K. SJÖGREEN-GLEISNER

6.1. TEMPORAL CHANGES OF ACTIVITY DISTRIBUTIONS

Pharmacokinetics is a general term describing the uptake, metabolism and excretion of substances administered to a living organism. A complete description of the pharmacokinetics of a drug may include a vast number of physical, chemical and biological processes and can be very complex in its nature.

In contrast to most pharmaceutical therapies, radiopharmaceutical therapy (RPT) often offers the opportunity to follow the pattern of changes in the pharmaceutical distribution over time in a patient's body due to radioactive emissions of the RPT agents and the relatively long physical half-lives of the radionuclides used. By imaging these emissions, information about the pharmacokinetics of the RPT agent, critically important for personalized dosimetry calculations, can be obtained.

Therapeutic radiopharmaceuticals are often administered intravenously, although oral, intra-cavity, and intra-arterial administrations are also employed. Upon entrance to the bloodstream and circulation, the radiopharmaceutical is transported across microvascular endothelia mainly driven by passive processes such as convection and diffusion. The rate of transport varies between tissues and depends on the capillary permeability and other factors such as the hydrostatic and colloid-osmotic pressure [6.1]. The uptake of the radiopharmaceutical in tumour cells is often associated with active processes, mediated by membrane proteins such as symporters, receptors or antigens present on the cell surface [6.2].

Several studies have demonstrated that the uptake and effective half-lives of radiopharmaceutical washout [6.3–6.7] in normal organs and tumours exhibit a large inter-patient variation [6.8]. Additionally, large intra-patient variations in tumour uptake have been observed [6.8]. These observations provide a strong argument for personalized dosimetry, clearly indicating that RTP pharmacokinetics needs to be determined for each individual patient and each organ and region of interest (ROI) (Chapter 1, Figs 1.3 and 1.4). The rate constants may also be of interest in themselves as they carry information about the turnover of the radiopharmaceutical in tissues.

In order to perform RPT dosimetry calculations, the total number of decays that occur in different body regions from the moment of the radiopharmaceutical administration to infinity, must be determined. This total number of decays per injected activity, or time-integrated activity coefficient, corresponds to the integral of the area under the time activity curve (TAC) divided by the injected activity. The TAC describes the combined effects of the radiopharmaceutical kinetics (rates of absorption, distribution and excretion) in different tissues and the physical decay of the radioisotope. It allows us to determine the total absorbed dose to any given tissue (organ and/or tumour). Additionally, in many situations, the rate of absorbed dose delivery may be of interest.

The temporal changes of activity distributions in any given organ or tissue of interest, described by the corresponding TAC, can be determined from a time series of quantitative measurements of this activity. Quantification of activity in source regions is discussed in Chapters 4 and 5. Determination of TACs can be performed in different ways, depending on the type and the quality of the acquired data. Additionally, it may also be of interest to combine the measured data with models, such as small scale dosimetry models or compartmental models, in order to extrapolate dosimetry data to tissues for which absorbed doses cannot be easily determined [6.9–6.14].

The approaches, which can be used to determine the activity located in different regions of the patient's body, can be classified in the following way.

Non-imaging determination of the total activity in the patient's body. Using this approach, the shape of the temporal changes of activity in the entire patient's body is determined from a series of whole body counting (using, e.g., a thyroid probe detector or a Geiger–Müller counter). However, it must be noted that no information about the activity distribution is collected with this approach. When performing multiple measurements over time, care must be taken to ensure consistency of the geometry in these measurements (in particular, the patient–detector distance must be kept constant), but no further processing of the data is required (such as image registration or segmentation).

Planar-only imaging. This approach can be used to determine the shape of the time activity curve for organs and tumours that do not suffer from extensive overlap with other tissues with high activity accumulation. Typically, a series of whole body planar images is acquired over time, often on different days. In order to determine the TAC, the whole organ or tumour activity is determined from the different time point images by ROI drawing (image segmentation). These ROIs need to be placed at the same anatomical location in each image and cover the same number of pixels. This can be accomplished by: (1) defining the ROI in the image acquired at one time point (reference image) and applying it to all other time points following co-registration of these images; or (2) defining the ROIs individually in images corresponding to each time point (without co-registration).

Attenuation and scatter corrections can be applied to the count rate data determined from the images. In addition, background correction for overlapping activities needs to be performed. It has to be noted, however, that due to the two dimensional nature of the technique, planar imaging is known to have inherent limitations in its ability to quantify activity, especially for smaller structures such as tumours and/or when there is activity in overlying and underlying tissue.

Tomographic-only imaging. A time series of tomographic scans (typically single photon emission computed tomography (SPECT)/computed tomography (CT) but positron emission tomography (PET)/CT) is also possible), followed by fully quantitative reconstructions with attenuation and scatter corrections, allows the user to obtain the most accurate 3-D quantitative information about activity distribution and its changes in the patient's body [6.15]. In order to create TACs for every organ or tumour, 3-D image segmentation (i.e. delineation of volumes of interest (VOIs)) of organs and tumours is required. When possible, image registration of the quantitatively reconstructed tomographic images can be made as it enables the use of the same VOIs for the complete series of 3-D images and also allows for calculation of the absorbed dose on a voxel by voxel level. However, it has to be noted that the uncertainty associated with voxel-level estimation can be significantly higher than the uncertainty of the mean value in a larger VOI.

Hybrid method: planar + tomographic. To improve the accuracy of activity quantitation from planar images, a time series of planar scans can be combined with one (or more) tomographic acquisition(s) [6.16]. The tomographic scan(s) should be performed in the time period between the first and the last planar scan and should cover the entire region containing organs and tumours for which the absorbed doses are to be determined. Determination of TACs for organs and tumours requires segmentation in planar images (similar to that performed in point b). At the next step, each of these TACs (expressed in relative units) needs to be re-normalized into activity units (Fig. 6.1) based on the quantitative SPECT. This is performed by segmenting the quantitatively reconstructed tomographic image(s) for the same organs and tumours as those analysed in planar scans. If planar and SPECT acquisitions are performed with a short time interval between them, the activity in the source regions can be assumed to be equivalent at the times of the SPECT and static scans. Otherwise, if there is a time difference between the scans, the value of the planar derived TAC needs to be calculated by interpolation (possibly via curve fitting) to the time corresponding to the SPECT scan. Thus, the activity for the planar derived data at any time point j can be calculated by rescaling according to:

$$A_j = \frac{A_{\mathrm{SPECT},i}}{C_{\mathrm{planar},i}} \cdot C_{\mathrm{planar},j} \tag{6.1}$$

where $A_{\mathrm{SPECT},i}$ is the activity in the source region measured using quantitative SPECT at time point i, $C_{\mathrm{planar},i}$ is the planar derived value at the same time point i, and $C_{\mathrm{planar},j}$ is the corresponding value at other time points j.

6.2. IMAGE REGISTRATION FOR DETERMINATION OF THE TIME ACTIVITY CURVE

As discussed, the determination of individual patient pharmacokinetics requires performing a series of scans (planar and/or tomographic) over the time period following radiopharmaceutical administration. For the analysis of temporal changes of activity in organs and tumours, the resulting images (often acquired on different days) may need to be co-registered. Considering that not only activity concentration and its distribution, but also patient positioning, and shapes and sizes of organs and tumours may vary between scans acquired at different times post-injection, co-registration of these scans may be challenging.

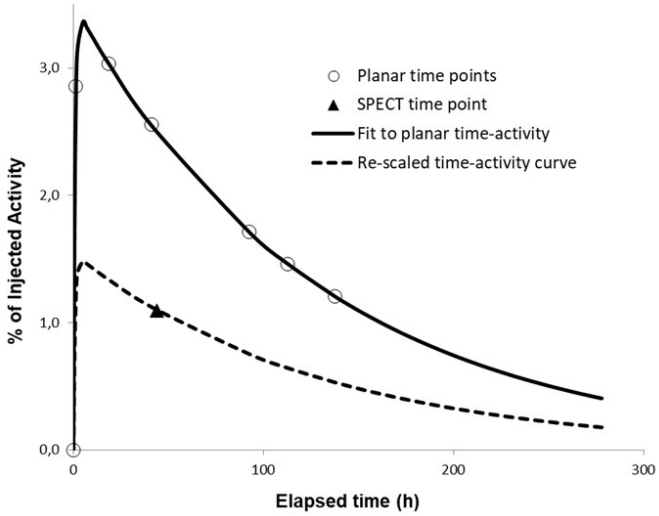

FIG. 6.1. Tumour time activity curve (TAC) of a patient imaged using a hybrid planar/SPECT protocol (Koral et al. 2003 [6.17]) following administration of ^{131}I-tositumomab. The top curve is the multi-exponential fit to six data points obtained from planar measurements while the lower curve is the same curve rescaled after normalization to the quantitative SPECT time point. Courtesy of Y. Dewaraja.

Many different software packages can be used to perform image registration for RPT dosimetry [6.18, 6.19]. In general, the objective of image registration is to match corresponding anatomical locations in two or more images. Image registration usually involves the use of a series of geometric transformations to align these images. The task of finding the matrix of these transformations (T) is usually achieved by minimizing the cost function (C), also called the similarity metric, which measures the misalignment between the images (Fig. 6.2).

The addition of a regularization term is often required to restrict the space of allowed transformations. Regularization may include such image characteristics as local rigidity (bones), incompressibility and/or smoothness of tissues. Similarity metrics can be classified as feature based (using the correspondence between landmarks, external fiducial markers or organ/region boundaries) or intensity based (analysing image intensities or features extracted from image intensities, including entropy or mutual information analysis).

The transformation models that are used to describe deformations used in registrations can be classified into rigid and non-rigid (or elastic) transformations. Rigid transformations are linear transformations that have a fixed number of degrees of freedom allowing the image to be translated, rotated, scaled and sheared. On the other hand, non-rigid (elastic) transformations can be parametrized with a vector displacement field allowing a set of control points, which in the extreme case may correspond to every element of the image (pixel or voxel), to be moved independently according to the neighbouring

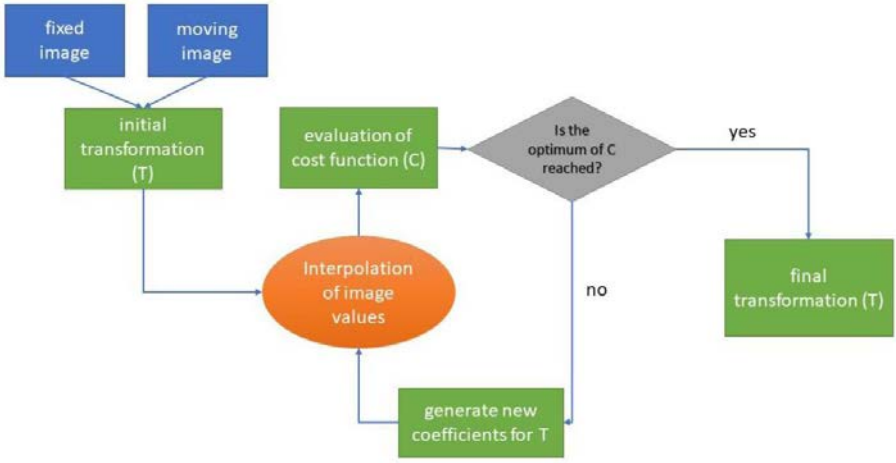

FIG. 6.2. Example flow chart of the registration process. The task to be solved is the estimation of the geometric transformation parameters, T, such that the moving image becomes geometrically aligned with the fixed image. The cost function (similarity metric) is used to quantify the degree of non-correspondence and is minimized during image registration by iterative optimization.

displacement vectors, hence giving more local flexibility than that which can be achieved in rigid registrations. Interpolation of the displacement field between the control points then becomes important. Non-rigid transformations and interpolation can be performed using B-splines or thin plate splines, physical and diffeomorphic models.

Although elasticity of the human body justifies, to a certain degree, the use of non-rigid transformation, too much freedom in parameter selection may lead to unrealistic body shapes and/or wrong new organ locations. Therefore, great care should be taken when using non-rigid transformations so that the resulting images (thus activity distributions) do not substantially alter the shapes of body parts and organs.

Investigations of new and/or improved algorithms for registration of medical images is an active area of research. However, the majority of studies focus on registration of anatomical images (magnetic resonance imaging (MRI) and CT) as registration of functional images (SPECT and PET) is considered to be more difficult. This is because the resolution of functional images is much poorer than that of MRI and CT. Additional problems may arise if the distribution of radiotracer in the images that are being registered does not correspond to the anatomical shapes of the organs or other landmarks, or if this distribution changes over time.

For these reasons, in situations when images from a series of studies acquired on a hybrid camera are being registered (SPECT/CT, PET/CT or PET/MRI), it has been suggested that the registration be first performed using the CT or MRI part of each study [6.20]. Subsequently, once the transformation required to register CT images is determined, the same transformation can be applied to the functional (SPECT or PET) images. This approach assumes that the anatomical and functional images, which were acquired on the same camera (but in practice sequentially), were already registered and that the patient did not move between scans.

Even with hybrid anatomical-functional imaging, due to differences in patient positions, breathing cycle and other factors, the relative location of organs in one image may still differ from that in the second image. In such situations, registration may be easier if only a part of the image is considered (e.g. registration is performed for regions which only include liver, or only lungs).

A procedure aiming to separately determine patterns of activity changes for each individual voxel, resulting in a series of TACs, one for every voxel [6.20–6.23] poses a very special challenge. This task would require the existence of a reliable procedure, which could match individual voxels in a time series of increasingly fuzzy images representing decreasing activity distributions. The main difficulty would be related to the high statistical noise in typical nuclear medical images and to the partial volume effects, which cause the activity from

each voxel to spread over neighbouring voxels. For these reasons, the voxel based registration should be undertaken with great care [6.21]. Alternatively, the determination of a TAC can be made for VOIs covering parts of an organ for sub-organ level dosimetry.

6.3. ORGAN/TUMOUR QUANTIFICATION FOR DETERMINATION OF THE TIME ACTIVITY CURVE

Absorbed dose is defined as the energy deposited by radiation in tissue per unit mass. Therefore, in order to calculate the absorbed dose, not only is the information about the activity contained in an organ/tumour required, but also the mass of this organ, tumour or other tissues must be known.

The information about activity, since it changes over time, has to be obtained from each image of the registered time series of images. This is necessary for determination of the shape of the TAC describing the biokinetics of the investigated agent and, as mentioned, typically requires image segmentation. However, in most cases, the volume of the organ or tumour receiving treatment does not change rapidly and therefore a single volume determination during TAC data acquisition is usually sufficient. Nevertheless, there have been reports of tumour shrinkage after a single therapy cycle [6.24]. Such cases would require multiple volume measurements.

Although determination of physical boundaries of an organ or tumour in anatomical images (CT and MRI) is often difficult, segmentation of organs and tumours in nuclear medical images is even more challenging. In fact, the limited image spatial resolution causes partial volume effect (PVE) and results in some activity to ‘spill-out’ and appear outside the physical boundary of the analysed region, while the background activity can ‘spill-in’ to the object (see Chapter 4).

Several methods have been designed to compensate for PVE [6.25]. None of these methods, however, can completely restore the true size and shape of the object in the reconstructed image. Simpler approaches try to correct for activity losses due to spill-out effects by using mean value recovery coefficients, discussed in Chapter 4 [6.26–6.28]. The curves, representing dependence of the recovery coefficients on the object size, are usually determined experimentally by scanning phantoms containing hot objects of different sizes (attempting to model the patient’s organs and tumours) placed in a warm background (modelling background tissues). These scans should be reconstructed with the same method as that used for the reconstruction of patient studies and the same organ/tumour segmentation method should be applied. Then, the curves representing the ratios of objects’ activities determined from these images to their true activities for different object sizes can be derived. Since typically it can be assumed that the

lesion/organ size does not vary over the imaging time points of the TAC, a single recovery coefficient corresponding to the target size at the first time point can be used for the subsequent time points.

6.4. SEGMENTING IMAGES FOR TIME ACTIVITY DETERMINATION IN ORGANS AND TUMOURS

Image segmentation (i.e. the outlining of organs and tumours in images) is required to estimate both the activity in source regions and their mass. Due to effects of limited resolution, the activity distribution in the image may extend outside the physical organ border and the volume required to encompass the total activity of the organ can thus be larger than the physical size of the organ. Organ mass, on the other hand, is directly proportional to the volume, therefore it can be determined using anatomical images (CT or MRI). For this reason, segmentation used in accurate dosimetry calculations may use two different volumes, one (larger) for the activity determination and another (smaller) for mass determination [6.29].

Over the last several years, a large number of different segmentation techniques have been investigated. Although the number of CT and MRI based segmentation studies still far exceeds those related to PET, and in particular SPECT, a substantial increase of interest in segmentation of nuclear medical images has been observed [6.30, 6.31]. Automated segmentation of planar images in the context of radionuclide therapy is still a scarcely researched area [6.32], although this approach has been used for many years.

In general, segmentation methods, which have been used in the analysis of nuclear medical images, can be divided into the following categories:

— **Manual segmentation methods.** Manual segmentation is usually considered to be the simplest, although defining organ boundaries may be very challenging in planar images when different organs and/or tumours overlap, and very time consuming when segmentation needs to be performed manually on every slice contributing to the 3-D volume. Additionally, the results obtained from manual segmentation are usually highly subjective, as different users will often define different boundaries for the same region. Ideally, manual segmentation should be performed by a nuclear medicine physician, radiologist or another person with appropriate training. This is especially important when segmenting lesions. Manual segmentation of nuclear medical images may be aided by using higher resolution anatomical CT images (e.g. from SPECT/CT or PET/CT) if tumour/region boundaries are visible in these images. However, due to PVE in nuclear medical images,

anatomical volumes determined from CT or MRI images will always be too small to provide the true measure of total organ/tumour activity.

— **Threshold based methods.** Another, relatively simple approach is to use fixed thresholds and while values ranging from 25 to 70% have been reported, the thresholds set at around 40% of the maximum counts in the analysed region are most commonly used in clinical studies [6.31]. The fixed threshold approach, however, provides very unreliable results, as they are highly dependent on the signal to background ratio and noise. To address some of these problems several adaptive or iterative thresholding methods have been suggested [6.33, 6.34]. Typically, the adaptive thresholding techniques adjust the segmentation thresholds by using prior information about the size of the lesions (e.g. from CT) and the estimated ratio of signal to background activity concentrations (sometimes combined with other parameters, such as scanner resolution or motion artefacts). On the other hand, the iterative thresholding methods calculate thresholds iteratively without information about the lesion size; instead, they employ calibration curves determined from phantom experiments. These two approaches can also be combined [6.35]. Unfortunately, all thresholding methods are very sensitive to image noise, do not perform well when segmenting small regions, and tend to underestimate volumes when lesion activity is non-uniform (contains hot and/or necrotic cold regions).

— **Boundary based methods.** The methods in this category attempt to use information about the boundary of a lesion to find its edges, a task which may be very challenging considering the relatively poor resolution and high noise of nuclear medical images [6.31]. Boundary based methods (e.g. level set, active contours, gradient based edge detection), initially developed for segmentation of anatomical (CT and MRI) images, require the user to define the initial ROI inside which the algorithm actively searches for object boundaries [6.36]. Digital filtering to remove noise or enhance contrast may be employed. The gradient based edge detection has been shown to perform well even when the activity distribution inside and outside the target boundary is non-uniform, which is an advantage over methods based on thresholding [6.37, 6.38].

— **Stochastic and machine learning based methods.** The last group comprises a large variety of sophisticated computerized methods that frequently involve statistical analysis of the textures and other image characteristics, employ fuzzy logic and machine learning algorithms (e.g. artificial neural networks (ANN)) and other techniques. Often these methods can be further enhanced by incorporating some prior knowledge into the segmentation algorithms; for example, by mixing information from anatomical and functional nuclear medical images. In the analysis, large sets of image derived parameters

may be defined and analysed, in order to be input into the deep-learning neural network schemes to perform segmentation tasks. This is a rapidly developing field aiming at full automation of medical image analysis. Application of learning based segmentation in PET is discussed in the review by Hatt et al. [6.31].

6.5. SMALL VOLUME ABSORBED DOSE ESTIMATES

As determination of activity in an entire organ based on segmentation of nuclear medical images is difficult and may be prone to errors, a simplified small volume method has been proposed instead [6.39]. This approach assumes that for organs with relatively uniform radiopharmaceutical uptake, the absorbed dose can be estimated using activity concentration determined from only a small volume defined within this organ. The small volume approach has been applied in dosimetry calculations of kidneys in RPT with ^{177}LuDOTATATE [6.40, 6.41].

6.6. TECHNIQUES USED FOR DETERMINATION OF THE TIME-INTEGRATED ACTIVITY

Once the images acquired at different time points are registered and the activity in any given tissue region is determined, a time activity curve for this region can be generated. As already mentioned, the area under each TAC, integrated over time, from the moment of activity administration (time zero; t_0) to infinity, corresponds to the time-integrated activity (or the older term cumulated activity), $\tilde{A}$, for this particular region. $\tilde{A}$ represents the total number of radioactive decays in a source region from t_0 to infinity (see Chapter 2). Several different methods to calculate $\tilde{A}$ have been proposed [6.42, 6.43].

The simplest situation occurs for localized administrations, such as, for example, radioembolization procedures in which microspheres labelled with a therapy radioisotope are injected. In this case, the microspheres cause the activity to be trapped in the body (typically in the liver) and only physical decay of the radioisotope needs to be considered in calculating $\tilde{A}$. Another locally administered procedure is synovectomy. However, for RPTs that are not administered locally, the activity redistributes over time and is governed by the pharmacokinetics of the tracer, therefore TAC determination and integration must be performed.

A relatively simple and straightforward method to calculate time-integrated activity is to apply a trapezoidal method from the time t_0 to the last acquired time point. When using this method, however, some assumption about activity changes beyond this last point to infinity must be made. One option is to ignore biological

elimination and assume that the TAC shape will follow the radionuclide physical decay (physical half-life; $T_{1/2}^{phys}$. This method usually overestimates the values of $\tilde{A}$ and, depending on the extent of the area under the curve that lies beyond the last data point, this extrapolation may introduce large errors. An alternative would be to use the sum of trapezoids up to the last data point and then, from the last time point to infinity, to use the mono-exponential curve fitted to the last two data points. This approach takes into account the biological component of the washout and usually provides better accuracy in $\tilde{A}$ determination.

A preferable, although more complex, method is to fit a curve to the time activity data. The most commonly used curve shapes are sums of exponential functions with different rate constants and amplitudes, where the number of included terms is generally limited by the number of data points available [6.44]. Since typically no more than three data points are available, a mono-exponential curve is used to fit the data. Alternatively, a combination of the trapezoidal method (to be applied between the first two data points) and the mono-exponential fit to data points 2 and 3 can be applied. The motivation behind this approach is that the pharmacokinetics of the tracer in the early stages may be governed by the simultaneous uptake and washout while later pure washout occurs. In such situations, the mono-exponential curve would not properly reproduce the TAC shape for the early data.

Finally, since at least two data points are required for each exponential component, when several scans can be performed (thus multiple data points are collected), a bi-exponential fit may be performed to capture the uptake and clearance phases. A multi-exponential is especially well suited for lesions

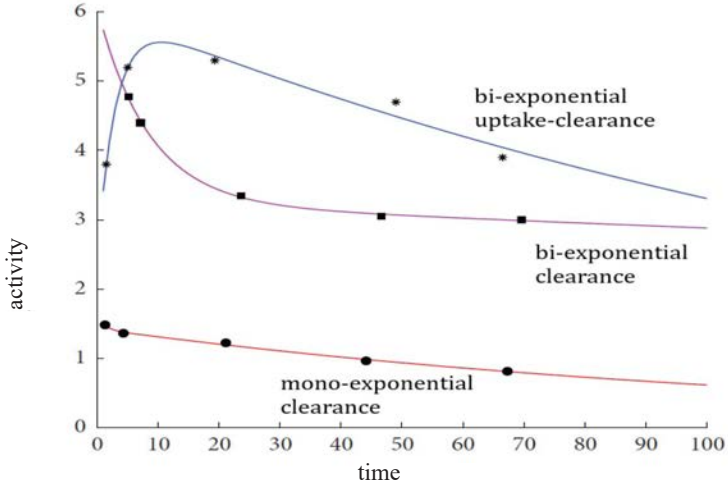

FIG. 6.3. Examples of mono- and bi-exponential time activity curves fit to five data points.

where the uptake phase can extend to multiple days. Examples of mono- and bi-exponential TACs fit to five data points can be seen in Fig. 6.3.

From the fitted curve parameters, the time-integrated activity is determined by analytical integration of the function describing the curve. For instance, the TAC for a source region, r_S, that exhibits a mono-exponentially decreasing activity as function of time, $A(t)$, is described as:

$$A(t) = A_0 \cdot a(r_s,0) \cdot \exp(-\lambda_{eff} \cdot t) \tag{6.2}$$

where A_0 is the administered activity to the patient, $a(r_S,0)$ is the fraction of the administered activity in the source region r_S extrapolated to time zero, and λ_{eff} is the effective rate constant, from which the effective half-life is obtained as $T_{eff} = \ln(2) / \lambda_{eff}$. The curve parameters in this case, determined by curve fitting, are $a(r_S,0)$ and λ_{eff}. Integration from time zero to infinity yields the time-integrated activity, $\tilde{A}(r_S,\infty)$, according to:

$$\tilde{A}(r_s,\infty) = \frac{A_0 \cdot a(r_s,0)}{\lambda_{eff}} \tag{6.3}$$

While the effective decay constant reflects a disappearance of activity from r_S due to both radioactive decay and biological washout, it is often of interest to separately study the biological half-life of the radiopharmaceutical for the particular tissue. From the effective half-life the biological half-life is obtained following:

$$\lambda_{eff} = \lambda_{phys} + \lambda_{biol} \Leftrightarrow T_{biol} = \frac{T_{phys} \cdot T_{eff}}{T_{phys} - T_{eff}} \tag{6.4}$$

6.7. CURVE FITTING METHODS FOR SETS OF EXPONENTIAL FUNCTIONS

In general, a continuous function of the activity as function of time, $A(t)$, can be written as:

$$A(t) = A_0 \sum_{k=1}^{M} a_k \cdot \exp\left(-\frac{\ln(2)}{T_k} \cdot t\right) \tag{6.5}$$

where a_k is the respective $a(r_S,0)$ for each phase k (i.e. the fraction of the administered activity in the source region extrapolated to time zero)) and $T_{\text{eff},k}$ is the effective half-time of phase k with a total of M phases.

The purpose of the curve fitting is to estimate the unknown parameters, a_k and T_k, such that the curve describes the time course of the measured data points. The most commonly used method is the least squares estimation, which finds the optimal parameter values by minimizing the residual sum of squares:

$$RSS = \sum_{i=1}^{N} \left(A_i - A(t_i) \right)^2 \tag{6.6}$$

where N is the number of time points, A_i (i = 1 to N) are the acquired activity data at times t_i and $A(t_i)$ is the model value of the activity at each of these times, calculated according to Eq. (6.5). The actual fitting is usually performed by use of some optimization method, where the sum in Eq. (6.6) is minimized. Optimization methods are available in different software packages, and can, for example, be executed using the Excel solver tool.

When the data A_i have different uncertainty (variance), the use of Eq. (6.6) may not yield optimal results. This is often the case for data in RPT where the activity decreases, and thus the noise in the image increases, as a function of time. In such cases, data weighting should be incorporated in Eq. (6.6), where, theoretically, the optimal choice of weights, w_i, is the inverse of the variance of the data [6.45]. The sum to be minimized becomes:

$$RSS = \sum_{i=1}^{N} w_i \left(A_i - A(t_i) \right)^2 \tag{6.7}$$

When performing the curve fitting, the initial estimates of the parameter values must be carefully selected, since depending on these initial values, the optimizer may find different solutions, thus producing different values of a_k and T_k. Preferably, a consistent strategy for all patients should be applied and one way is to use a data driven approach. For instance, the initial value of the effective half-time can be assumed to be equal to the time when the particular phase reaches half of its maximum value, and the relations between the different amplitudes, a_k, can be estimated from the intersections of the phases with the ordinate.

The choice of a model, such as those in Eqs (6.2) and (6.5), is also of importance. A useful approach to investigate this model validity with respect to the underlying kinetics is to plot differences between the measured activity and the activity calculated by application of the model equation with the fitted parameter values. Ideally, the residuals should be scattered randomly around zero. If the plot exhibits a pattern, then possibly another curve shape should be

employed. Statistical testing of different types of curves can also be performed by systematically applying different curves for fitting, and then by using a criterion, such as the Akaike or F-test, to determine which model yields the best fit [6.46].

Preferably, the curve fitting procedure should provide estimates of the uncertainties of the values of the fitted parameter. The parameter uncertainties can then be propagated to estimate the uncertainty in the cumulated activity and the absorbed dose, as discussed in Chapter 9 [6.47].

6.8. OPTIMAL TIMING OF DATA ACQUISITION

Accurate determination of the time-integrated activity requires performing multiple scans over a period of several hours or days following radiotherapy administration. The number of these scans and the timing of data acquisitions is usually a compromise between the aim of obtaining a high accuracy in the TAC determination, for which acquiring multiple data points is favourable, and the increased burden for the patient and the clinical staff caused by labour intensive multi-acquisition protocols.

Therefore, the relationships between the lowest possible number of scans and their optimum timing and the achieved accuracies have been investigated [6.42]. An additional motivation is that existence of such simplified protocols could increase the number of centres performing RPT dosimetry.

In particular, it has been suggested that a relatively high accuracy of $\tilde{A}$ determination can be achieved when using data from a single time point acquisition [6.48–6.50]. However, the optimum timing of this single scan requires prior knowledge of the pharmacokinetics of the given radiotherapy agent. For ^{177}Lu-DOTATATE it has been shown that the errors will remain below 10% if the sampling time is selected to be within the range of 0.75 to 2.25 of the effective half-life of the radiotracer in a given organ. Therefore, in practice, before using this approach, the effective half-life for any combination of the radiotracer and the organ must be determined as a mean from a series scan of a given patient population.

Alternatively, in the case when insufficient data are acquired for a particular patient, but data are available from previous patients for the same radiopharmaceutical, or when the data are noisy, an interesting approach based on Bayesian techniques has been proposed [6.51]. In this work a non-linear mixed model was used, in which fixed and random effects were combined to analyse data for the individual patient, using the data from previous patients for guidance. The authors tested this approach by comparing predictions from pre-therapy with the data acquired during therapy and a good correlation was obtained.

6.9. PHARMACOKINETIC MODELLING

In order to provide better understanding of the radiopharmaceutical distribution in the body, a kinetic model can be applied to the patient's data. This approach is particularly useful when choosing the curve shape, which would be most appropriate for subsequent descriptive analyses of time activity data for extrapolation to other patients when only limited data are available, for extrapolation between a diagnostic and pre-therapeutic administration of therapy using the same or chemically analogous radiopharmaceuticals and for extrapolation between species. In the dosimetry context, pharmacokinetic modelling can be applied to separate an organ activity into different compartments, which subsequently can be separately employed in dosimetry models. Parametric imaging is an extension of this approach, in which compartment modelling is applied to each voxel in an image. A map of the distribution of the radiopharmaceutical in different compartments can then be obtained at a scale that is not accessible directly from the image. This approach may enhance the contrast and help in tumour detection [6.52, 6.53].

The mechanisms driving the distribution of a radiopharmaceutical in the body can be very complex, and for modelling applications, it is often necessary to make simplifications. Compartments can be chosen to represent organs and/or specific tissues or fluids with similar characteristics of the radiopharmaceutical distribution. When data on whole body and plasma are available, the patient's body can be viewed as a closed system, with well defined input (the plasma curve) and output (excretion) functions. In this way, very stable solutions can be obtained. Physiologically based pharmacokinetic models constitute an extension of the compartment modelling approach, in which the parameters representing actual processes in the body have real physical meaning, such as flow or permeability, or the rate of binding to the molecular target structures on tumour cells. Usually, to make the system solvable, such models require additional input from reference data.

Examples of studies in RPT where compartmental modelling approaches have been attempted to guide treatment planning or for optimization of treatments include, for example, Refs [6.54–6.59].

REFERENCES

[6.1] RIPPE, B., HARALDSSON, B., Transport of macromolecules across microvascular walls: The two-pore theory, Physiol. Rev. **74** 1 (1994) 163–219, https://doi.org/10.1152/physrev.1994.74.1.163

[6.2] CARLSSON, J., FORSSELL-ARONSSON, E., HIETALA, S.O., STIGBRAND, T., TENNVALL, J., Tumour therapy with radionuclides: Assessment of progress and problems, Radiother. Oncol. **66** 2 (2003) 107–117, https://doi.org/10.1016/S0167-8140(02)00374-2

[6.3] SUNDLÖV, A., et al., Individualised ^{177}Lu-DOTATATE treatment of neuroendocrine tumours based on kidney dosimetry, Eur. J. Nucl. Med. Mol. Imaging **44** 9 (2017) 1480–1489, https://doi.org/10.1007/s00259-017-3678-4

[6.4] SANDSTRÖM, M., et al., Individualized dosimetry of kidney and bone marrow in patients undergoing 177Lu-DOTA-octreotate treatment, J. Nucl. Med. **54** 1 (2013) 33–41, https://doi.org/10.2967/jnumed.112.107524

[6.5] DENIS-BACELAR, A.M., et al., Phase I/II trials of ^{186}Re-HEDP in metastatic castration-resistant prostate cancer: Post-hoc analysis of the impact of administered activity and dosimetry on survival, Eur. J. Nucl. Med. Mol. Imaging **44** 4 (2017) 620–629, https://doi.org/10.1007/s00259-016-3543-x

[6.6] JENTZEN, W., et al., Pre-therapeutic ^{124}I PET(/CT) dosimetry confirms low average absorbed doses per administered ^{131}I activity to the salivary glands in radioiodine therapy of differentiated thyroid cancer, Eur. J. Nucl. Med. Mol. Imaging **37** 5 (2010) 884–895, https://doi.org/10.1007/s00259-009-1351-2

[6.7] MÍNGUEZ, P., et al., Whole-remnant and maximum-voxel SPECT/CT dosimetry in ^{131}I-NaI treatments of differentiated thyroid cancer, Med. Phys. **43** 10 (2016) 5279–5287, https://doi.org/10.1118/1.4961742

[6.8] HINDORF, C., et al., Dosimetry for ^{90}Y-DOTATOC therapies in patients with neuroendocrine tumors, Cancer Biother. Radiopharm. **22** 1 (2007) 130–135, https://doi.org/10.1089/cbr.2007.306

[6.9] MEERKHAN, S.A., SJÖGREEN-GLEISNER, K., LARSSON, E., STRAND, S.-E., JÖNSSON, B.-A., Testis dosimetry in individual patients by combining a small-scale dosimetry model and pharmacokinetic modeling-application of ^{111}In-Ibritumomab Tiuxetan (Zevalin ®), Phys. Med. Biol. **59** 24 (2014) 7889–7904, https://doi.org/10.1088/0031-9155/59/24/7889

[6.10] HOBBS, R.F., et al., Arterial wall dosimetry for non-Hodgkin lymphoma patients treated with radioimmunotherapy, J. Nucl. Med. **51** 3 (2010) 368–375, https://doi.org/10.2967/jnumed.109.069575

[6.11] HOBBS, R.F., et al., A bone marrow toxicity model for ^{223}Ra alpha-emitter radiopharmaceutical therapy, Phys. Med. Biol. **57** 10 (2012) 3207–3222, https://doi.org/10.1088/0031-9155/57/10/3207

[6.12] SHAH, A.P., BOLCH, W.E., RAJON, D.A., PATTON, P.W., JOKISCH, D.W., A paired-image radiation transport model for skeletal dosimetry, J. Nucl. Med. **46** 2 (2005) 344–353.

[6.13] KLETTING, P., MAAß, C., RESKE, S., BEER, A.J., GLATTING, G., Physiologically based pharmacokinetic modeling is essential in ^{90}Y-labeled anti-CD66 radioimmunotherapy, PLoS One **10** 5 (2015) e0127934, https://doi.org/10.1371/journal.pone.0127934

[6.14] HARDIANSYAH, D., GUO, W., KLETTING, P., MOTTAGHY, F.M., GLATTING, G., Time-integrated activity coefficient estimation for radionuclide therapy using PET and a pharmacokinetic model: A simulation study on the effect of sampling schedule and noise, Med. Phys. **43** 9 (2016) 5145–5154, https://doi.org/10.1118/1.4961012

[6.15] DEWARAJA, Y.K., et al., MIRD Pamphlet No. 23: Quantitative SPECT for patient-specific 3-dimensional dosimetry in internal radionuclide therapy, J. Nucl. Med. **53** 8 (2012) 1310–1325, https://doi.org/10.2967/jnumed.111.100123

[6.16] GRIMES, J., et al., Patient-specific radiation dosimetry of ^{99m}Tc-HYNIC-Tyr3-octreotide in neuroendocrine tumors, J. Nucl. Med. **52** 9 (2011) 1474–1481, https://doi.org/10.2967/jnumed.111.088203

[6.17] KORAL, K.F., et al., Update on hybrid conjugate-view SPECT tumor dosimetry and response in ^{131}I-tositumomab therapy of previously untreated lymphoma patients, J. Nucl. Med. **44** 3 (2003) 457–464.

[6.18] OLIVEIRA, F.P., TAVARES, J.M.R., Medical image registration: A review, Comput. Methods Biomech. Biomed. Eng. **17** 2 (2014) 73–93, https://doi.org/10.1080/10255842.2012.670855

[6.19] HAJNAL, J.V., HILL, D.L.G. (Eds), Medical Image Registration, CRC Press, Boca Raton, FL (2001), https://doi.org/10.1201/9781420042474

[6.20] SJÖGREEN-GLEISNER, K., RUECKERT, D., LJUNGBERG, M., Registration of serial SPECT/CT images for three-dimensional dosimetry in radionuclide therapy, Phys. Med. Biol. **54** 20 (2009) 6181–6200, https://doi.org/10.1088/0031-9155/54/20/010

[6.21] SARRUT, D., HALTY, A., BADEL, J.-N., FERRER, L., BARDIÈS, M., Voxel-based multimodel fitting method for modeling time activity curves in SPECT images, Med. Phys. **44** 12 (2017) 6280–6288, https://doi.org/10.1002/mp.12586

[6.22] JACKSON, P.A., et al., An automated voxelized dosimetry tool for radionuclide therapy based on serial quantitative SPECT/CT imaging, Med. Phys. **40** 11 (2013) 112503, https://doi.org/10.1118/1.4824318

[6.23] SGOUROS, G., et al., Patient-specific dosimetry for ^{131}I thyroid cancer therapy using ^{124}I PET and 3-dimensional-internal dosimetry (3D-ID) software, J. Nucl. Med. **45** 8 (2004) 1366–1372.

[6.24] DEWARAJA, Y.K., et al., ^{131}I-tositumomab radioimmunotherapy: Initial tumor dose–response results using 3-dimensional dosimetry including radiobiologic modeling, J. Nucl. Med. **51** 7 (2010) 1155–1162, https://doi.org/10.2967/jnumed.110.075176

[6.25] ERLANDSSON, K., BUVAT, I., PRETORIUS, P.H., THOMAS, B.A., HUTTON, B.F., A review of partial volume correction techniques for emission tomography and their applications in neurology, cardiology and oncology, Phys. Med. Biol. **57** 21 (2012) R119–159, https://doi.org/10.1088/0031-9155/57/21/R119

[6.26] KORAL, K.F., DEWARAJA, Y., I-131 SPECT activity recovery coefficients with implicit or triple-energy-window scatter correction, Nucl. Instrum. Methods Phys. Res., Sect. A **422** 1–3 (1999) 688–692, https://doi.org/10.1016/S0168-9002(98)01018-3

[6.27] ZINGERMAN, Y., GOLAN, H., MOALEM, A., Spatial linear recovery coefficients for quantitative evaluations in SPECT, Nucl. Instrum. Methods Phys. Res., Sect. A **602** 2 (2009) 607–613, https://doi.org/10.1016/j.nima.2009.01.015

[6.28] JENTZEN, W., et al., Iodine-124 PET dosimetry in differentiated thyroid cancer: Recovery coefficient in 2D and 3D modes for PET(/CT) systems, Eur. J. Nucl. Med. Mol. Imaging **35** 3 (2008) 611–623, https://doi.org/10.1007/s00259-007-0554-7

[6.29] SHCHERBININ, S., CELLER, A., BELHOCINE, T., VANDERWERF, R., DRIEDGER, A., Accuracy of quantitative reconstructions in SPECT/CT imaging, Phys. Med. Biol. **53** 17 (2008) 4595–4604, https://doi.org/10.1088/0031-9155/53/17/009

[6.30] FOSTER, B., BAGCI, U., MANSOOR, A., XU, Z., MOLLURA, D.J., A review on segmentation of positron emission tomography images, Comput. Biol. Med. **50** (2014) 76–96, https://doi.org/10.1016/j.compbiomed.2014.04.014

[6.31] HATT, M., et al., Classification and evaluation strategies of auto-segmentation approaches for PET: Report of AAPM task group No. 211, Med. Phys. **44** 6 (2017) e1–e42, https://doi.org/10.1002/mp.12124

[6.32] ROTH, D., GUSTAFSSON, J., SUNDLÖV, A., SJÖGREEN GLEISNER, K., A method for tumor dosimetry based on hybrid planar-SPECT/CT images and semiautomatic segmentation, Med. Phys. **45** 11 (2018) 5004–5018, https://doi.org/10.1002/mp.13178

[6.33] MORTELMANS, L., et al., A new thresholding method for volume determination by SPECT, Eur. J. Nucl. Med. **12** 5–6 (1986) 284–290, https://doi.org/10.1007/BF00251989

[6.34] OTSU, N., A threshold selection method from gray-level histograms, IEEE Trans. Syst. Man Cybern. **9** 1 (1979) 62–66, https://doi.org/10.1109/TSMC.1979.4310076

[6.35] GRIMES, J., CELLER, A., SHCHERBININ, S., PIWOWARSKA-BILSKA, H., BIRKENFELD, B., The accuracy and reproducibility of SPECT target volumes and activities estimated using an iterative adaptive thresholding technique, Nucl. Med. Commun. **33** 12 (2012) 1254–1266, https://doi.org/10.1097/MNM.0b013e3283598395

[6.36] GUSTAFSSON, J., SUNDLÖV, A., SJÖGREEN GLEISNER, K., SPECT image segmentation for estimation of tumour volume and activity concentration in ^{177}Lu-DOTATATE radionuclide therapy, EJNMMI Res. **7** 1 (2017) 18, https://doi.org/10.1186/s13550-017-0262-7

[6.37] MIKELL, J.K., et al., Impact of ^{90}Y PET gradient-based tumor segmentation on voxel-level dosimetry in liver radioembolization, EJNMMI Phys. **5** 1 (2018) 31, https://doi.org/10.1186/s40658-018-0230-y

[6.38] GEETS, X., LEE, J.A., BOL, A., LONNEUX, M., GRÉGOIRE, V., A gradient-based method for segmenting FDG-PET images: Methodology and validation, Eur. J. Nucl. Med. Mol. Imaging **34** 9 (2007) 1427–1438, https://doi.org/10.1007/s00259-006-0363-4

[6.39] SANDSTRÖM, M., GARSKE, U., GRANBERG, D., SUNDIN, A., LUNDQVIST, H., Individualized dosimetry in patients undergoing therapy with ^{177}Lu-DOTA-D-Phe^{1}-Tyr^{3}-octreotate, Eur. J. Nucl. Med. Mol. Imaging **37** 2 (2010) 212–225, https://doi.org/10.1007/s00259-009-1216-8

[6.40] HEIKKONEN, J., MÄENPÄÄ, H., HIPPELÄINEN, E., REIJONEN, V., TENHUNEN, M., Effect of calculation method on kidney dosimetry in ^{177}Lu-octreotate treatment, Acta Oncol. **55** 9–10 (2016) 1069–1076, https://doi.org/10.1080/0284186X.2016.1182642

[6.41] DEL PRETE, M., BUTEAU, F.-A., BEAUREGARD, J.-M., Personalized ^{177}Lu-octreotate peptide receptor radionuclide therapy of neuroendocrine tumours: A simulation study, Eur. J. Nucl. Med. Mol. Imaging **44** 9 (2017) 1490–1500, https://doi.org/10.1007/s00259-017-3688-2

[6.42] GUERRIERO, F., et al., Kidney dosimetry in ^{177}Lu and ^{90}Y peptide receptor radionuclide therapy: Influence of image timing, time-activity integration method, and risk factors, Biomed. Res. Int. **2013** (2013) 12, https://doi.org/10.1155/2013/935351

[6.43] KLETTING, P., et al., Molecular radiotherapy: The NUKFIT software for calculating the time-integrated activity coefficient, Med. Phys. **40** 10 (2013) 102504, https://doi.org/10.1118/1.4820367

[6.44] SIEGEL, J.A., et al., MIRD Pamphlet No. 16: Techniques for quantitative radiopharmaceutical biodistribution data acquisition and analysis for use in human radiation dose estimates, J. Nucl. Med. **40** 2 (1999) 37s–61s.

[6.45] CARSON, R.E., "Tracer kinetic modeling in PET", Positron Emission Tomography: Basic Sciences (BAILEY, D.L., TOWNSEND, D.W., VALK, P.E., MAISEY, M.N., Eds), Springer, London (2005) 127–159, https://doi.org/10.1007/1-84628-007-9_6

[6.46] KLETTING, P., GLATTING, G., Model selection for time-activity curves: The corrected Akaike information criterion and the F-test, Z. Med. Phys. **19** 3 (2009) 200–206, https://doi.org/10.1016/j.zemedi.2009.05.003

[6.47] COX, M.G., "Modelling clinical decay data using exponential functions", Approximation Algorithms for Complex Systems, Vol 3 (GEORGOULIS, E.H., ISKE, A., LEVESLEY, J., Eds), Springer, Berlin (2011) 183–203, https://doi.org/10.1007/978-3-642-16876-5_8

[6.48] MADSEN, M.T., MENDA, Y., O'DORISIO, T.M., O'DORISIO, M.S., Technical note: Single time point dose estimate for exponential clearance, Med. Phys. **45** 5 (2018) 2318–2324, https://doi.org/10.1002/mp.12886

[6.49] HÄNSCHEID, H., LAPA, C., BUCK, A.K., LASSMANN, M., WERNER, R.A., Dose mapping after endoradiotherapy with ^{177}Lu-DOTATATE/DOTATOC by a single measurement after 4 days, J. Nucl. Med. **59** 1 (2018) 75–81, https://doi.org/10.2967/jnumed.117.193706

[6.50] MADSEN, M., Single time point dose estimate for bi-exponential clearance, J. Nucl. Med. **58** Suppl. 1 (2017) 834.

[6.51] SCHIPPER, M.J., KORAL, K.F., AVRAM, A.M., KAMINSKI, M.S., DEWARAJA, Y.K., Prediction of therapy tumor-absorbed dose estimates in I-131 radioimmunotherapy using tracer data via a mixed-model fit to time activity, Cancer Biother. Radiopharm. **27** 7 (2012) 403–411, https://doi.org/10.1089/cbr.2011.1053

[6.52] SJÖGREEN GLEISNER, K., et al., Parametric images of antibody pharmacokinetics based on serial quantitative whole-body imaging and blood sampling, J. Nucl. Med. **48** 8 (2007) 1369–1378, https://doi.org/10.2967/jnumed.107.039503

[6.53] ILAN, E., et al., Parametric net influx rate images of ^{68}Ga-DOTATOC and ^{68}Ga-DOTATATE: Quantitative accuracy and improved image contrast, J. Nucl. Med. **58** 5 (2017) 744–749, https://doi.org/10.2967/jnumed.116.180380

[6.54] NICKEL, M., et al., Development and evaluation of a pharmacokinetic model for prediction of radioimmunotherapy based on pretherapy data, Cancer Biother. Radiopharm. **24** 1 (2009) 111–122, https://doi.org/10.1089/cbr.2008.0530

[6.55] BUFFA, F.M., et al., A model-based method for the prediction of whole-body absorbed dose and bone marrow toxicity for 186Re-HEDP treatment of skeletal metastases from prostate cancer, Eur. J. Nucl. Med. Mol. Imaging **30** 8 (2003) 1114–1124, https://doi.org/10.1007/s00259-003-1197-y

[6.56] KLETTING, P., et al., Differences in predicted and actually absorbed doses in peptide receptor radionuclide therapy, Med. Phys. **39** 9 (2012) 5708–5717, https://doi.org/10.1118/1.4747266

[6.57] KLETTING, P., KIRYAKOS, H., RESKE, S.N., GLATTING, G., Analysing saturable antibody binding based on serum data and pharmacokinetic modelling, Phys. Med. Biol. **56** 1 (2011) 73–86, https://doi.org/10.1088/0031-9155/56/1/005

[6.58] KLETTING, P., et al., Radioimmunotherapy with anti-CD66 antibody: Improving the biodistribution using a physiologically based pharmacokinetic model, J. Nucl. Med. **51** 3 (2010) 484–491, https://doi.org/10.2967/jnumed.109.067546

[6.59] KLETTING, P., MEYER, C., RESKE, S.N., GLATTING, G., Potential of optimal preloading in anti-CD20 antibody radioimmunotherapy: An investigation based on pharmacokinetic modeling, Cancer Biother. Radiopharm. **25** 3 (2010) 279–287, https://doi.org/10.1089/cbr.2009.0746

Chapter 7

ABSORBED DOSE CALCULATION

M. BARDIÈS, A. VERGARA GIL

7.1. INTRODUCTION

Clinical dosimetry is a multistep procedure. As presented in Chapter 2, dosimetry requires the determination of the following:

(1) The spatial distribution of activity (Chapter 4);
(2) The temporal distribution of activity and its integration with time (Chapter 6);
(3) How the energy emitted by the radioactive source is absorbed in organs and tissues of interest.

The present chapter deals with this third aspect of the dosimetry procedure.

The first section considers the relationship between radiation range and the geometry/sampling of the target regions. This will condition the choice of the absorbed dose calculation approach. In the second section, different algorithms allowing computing absorbed doses from time-integrated activity distributions in different media are considered. Here, we assume perfectly well defined time-integrated activity distributions, in order to focus on the absorbed dose calculation process (i.e. the radiation transport and energy deposition). The third section deals with broad categories of absorbed dose calculation approaches in clinical practice. Model based and patient-specific dosimetry (as well as intermediary adjusted model based dosimetry) are presented and discussed.

7.2. RADIATION RANGE VERSUS GEOMETRY: PENETRATING AND NON-PENETRATING RADIATION

Alpha particles used in radiopharmaceutical therapy (RPT) typically have a range of about 50–80 μm in water (soft tissue). In the same context, the maximum range of the most energetic beta emitter proposed for RPT (^{90}Y) is around 1 cm in soft tissue (see Table 2.2). The consequences are that, as long as the parameter of interest is the **mean** absorbed dose **at the organ or tissue scale**, these radiations can be qualified as **non-penetrating** for the volumes considered.

In non-penetrating radiation conditions, the calculation of the absorbed dose is simple, as the knowledge of the emitted energy (a physical characteristic of the isotope, usually well known) is directly proving the absorbed energy by using the local energy deposition assumption. Under this assumption, there is no need to implement radiation transport to estimate the absorbed dose. As a matter of fact, the non-penetrating nature of radiation is an essential requirement for RPT: the selectiveness of the biologic vector must be associated to short range radiation to ensure local irradiation of the targeted structure (the tumour).

For clinical dosimetry, non-penetrating radiation conditions are usually assumed for electrons and alpha particles at the organ scale or for tissue dosimetry. Non-penetrating radiation conditions are never met for photons. In fact, given the photon production resulting from electron—matter interactions (bremsstrahlung), one could argue that, strictly speaking, non-penetrating radiation conditions are never met at all, even for electrons or beta and alpha particles.

From a **practical** point of view, non-penetrating conditions are met when, for a given type of radiation combined with a given geometry, the fraction of the energy that escapes the source volume can be safely considered as negligible. Here, 'safely' means that the fraction of energy that escapes the source region is smaller than the value set by the user, in view of all the parameters and uncertainties that impact on the absorbed dose determination.

The penetrating/non-penetrating nature of radiation depends on the radiation type and the energy in relation to the spatial extension of the considered geometry.

Figure 7.1 presents the cumulative energy per decay ($MeV \cdot Bq^{-1} \cdot s^{-1}$) absorbed at a distance of a point source of ^{131}I in water. As can be seen, electrons (beta particles) deposit their energy within the first mm, whereas the absorbed energy from photons becomes significant above 1 cm only.

As a consequence, beta emissions of ^{131}I must be considered as **penetrating** radiation for sphere radii below 1 mm. At that scale, the gamma contribution to the absorbed energy can be neglected. Between 0.1 and 1 cm, beta can be considered as **non-penetrating** radiation, and the gamma contribution to the absorbed energy is still very low. Above 1 cm, the contribution of gammas to the absorbed energy can no longer be neglected.

For a given isotope, the geometry and the spatial sampling condition the choice of the absorbed dose calculation algorithm.

In RPT, whenever a volume can be considered as a radiation source, irradiation **in that volume** (self-irradiation) is mostly coming from short range radiation (alpha, beta, monoenergetic electrons). This is true for human organs/tissues, and even at the voxel level for the typical spatial sampling of single photon emission computed tomography (SPECT) and positron emission tomography (PET).

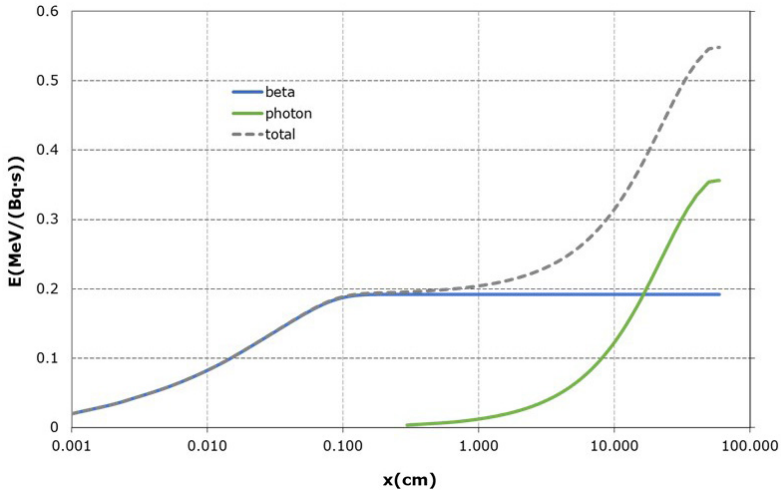

FIG. 7.1. Total absorbed energy per decay (MeV·Bq^{-1}·s^{-1}) in a water sphere as a function of the radius x from a point source of ^{131}I, located at the centre of the sphere. The mean energy of the electron (monoenergetic and ß) and photon emissions are 0.192 and 0.375 MeV·Bq^{-1}·s^{-1}, respectively. Courtesy of M. Bardiès.

Voxel *S* values were introduced by Bolch et al. [7.1] to allow for absorbed dose calculations in 3-D digital images. Voxel *S* values give the absorbed dose at a distance from a central source voxel. They are the analogue of *S* values in sampled geometries, and likewise are expressed in Gy·Bq^{-1}·s^{-1} (or equivalent).

An interesting example is given in the database of voxel *S* values described by Lanconelli et al. [7.2], with example data reproduced in Table 7.1.

For ^{131}I, and for voxel sizes (4.42 mm) encountered in clinical SPECT imaging, the absorbed dose to the first neighbouring voxel is only 2% of that of the source voxel, considering both electron and photon components. The electron cross-irradiation between voxels can be neglected in most cases, and electrons/beta emitted by ^{131}I can safely be considered as non-penetrating, even at the voxel level.

For the most energetic beta emitter used in RPT (^{90}Y), however, the variation of voxel *S* values from the source voxel to the first neighbour is about 14%. Electrons/beta should probably not be considered as non-penetrating in that case. However, in a context of selective internal radiotherapy with ^{90}Y microspheres, some authors recommend using local energy deposition to compute voxel based absorbed dose distributions, as the accuracy of activity quantification at the voxel level is hampered by the limited spatial resolution of SPECT and PET images, which already yields a blurred activity distribution.

TABLE 7.1. ABSORBED DOSE PER 10^6 DECAYS DELIVERED TO THE VOXEL OF COORDINATES *i, j, k* FOR ^{90}Y AND ^{131}I FOR CUBIC VOXELS OF 4.42 mm

i	*j*	*k*	Voxel *S* value (mGy·MBq^{-1}·s^{-1})	
			Y-90	I-131
0	0	0	6.89×10^{-1}	3.00×10^{-1}
0	0	1	$9\ 73 \times 10^{-2}$	7.33×10^{-3}
0	0	2	2.10×10^{-4}	2.15×10^{-4}

Obviously, what is true for voxel based dosimetry is generally true at the organ level. However, one should bear in mind that the **photon** contribution to self-irradiation will increase with volume size and may not be negligible for large volumes. For example, ^{131}I self-absorbed dose to the liver calculated for the International Commission on Radiological Protection (ICRP) 110 adult male with IDAC V2.1 [7.3] is 1.25×10^{-1} mGy/MBq for a hypothetical time-integrated activity coefficient (formerly called residence time) of 2 hours. This value is the sum of the beta contribution (9.30×10^{-2} mGy/MBq) and gamma contribution (3.18×10^{-2} mGy/MBq), not negligible in that situation (25% of the total absorbed dose per activity administered). This means that absorbed dose calculation may be split to consider independently two components (penetrating and non-penetrating radiation), that is, different calculation algorithms can be implemented for different radiation types of the same radiopharmaceutical.

What was presented so far has applied to the absorbed dose from a single source. In that context, it can be safely assumed that most of the irradiation in a given source region is coming from non-penetrating radiation emitted within the source region. A further aspect to bear in mind is the impact of **cross-irradiation** (i.e. the contribution to the absorbed dose from a source region distinct from the target region). In the case of multiple sources, depending on the activity concentration in the different source regions, the cross dose can be significant compared to the self-dose.

For example, always in the case of ^{131}I, the *S* values from OLINDA V1 for an adult male [7.4] are:

$$S_{(\text{Liver}\leftarrow\text{Liver})} = 2.15\times10^{-5}\,\text{mGy MBq}^{-1}\text{s}^{-1} \quad (7.1)$$

$$S_{(\text{Kidney}\leftarrow\text{Kidney})} = 1.18\times10^{-4}\,\text{mGy MBq}^{-1}\text{s}^{-1} \quad (7.2)$$

$$S_{(\text{Kidney}\leftarrow\text{Liver})} = S_{(\text{Liver}\leftarrow\text{Kidneys})} = 8.19\times10^{-7}\,\text{mGy MBq}^{-1}\text{s}^{-1} \quad (7.3)$$

This means that if the time-integrated activities in the liver and the kidneys are the same, the absorbed dose in the liver imparted by the activity in the liver itself (the self-absorbed dose) is 26 times higher than the cross absorbed dose from the activity in the kidneys. Correspondingly, the cross absorbed dose from activity in the liver to the kidneys is 144 times lower than the self-absorbed dose from the activity in the kidneys.

For 'target-only'volumes (i.e. volumes where **no radiopharmaceutical is present**), the radiation is coming from neighbouring source regions, and is therefore predominantly delivered by photons at a distance from the emission point. This is a situation where the exposure is due to penetrating radiation, and radiation transport algorithms should therefore always be implemented.

In clinical dosimetry, several combinations of source and target regions are considered. Depending on the radionuclide (type and abundance of emissions) and source target geometry, the various situations mentioned above can be encountered.

The next example will consider absorbed dose calculations performed at the voxel level using recent dosimetry models (as proposed in ICRP Publication 110, or the Radiation Dose Assessment Resource (RADAR) models available in OLINDA V2), but considering constant activity concentrations in source regions. Table 7.2 presentss the absorbed dose per unit of administered activity obtained from a voxel based adult female model, where ^{177}Lu is uniformly distributed in liver, kidneys and spleen.

As a general observation, the total absorbed doses delivered to **source** regions (liver, kidneys and spleen in the example) are always an order of magnitude higher than those delivered to **target-only** regions:

(a) For **source** regions, the main contributor to the absorbed dose is always the beta/electron component.
(b) For **target-only** regions, the major contributor to the absorbed dose is the photon component, by orders of magnitude, and beta contribution (which can be calculated for voxel based models where neighbouring voxels can belong to different organ/tissues) is most often low (with the exception of kidney irradiation of adrenals, where the beta contribution can be up to 20%, and liver irradiation of the lungs).

TABLE 7.2. ABSORBED DOSE PER UNIT OF ACTIVITY ADMINISTERED (ABSORBED DOSE COEFFICIENTS) OBTAINED IN A VOXEL BASED ADULT FEMALE MODEL, WHERE ^{177}Lu IS CONSIDERED UNIFORMLY DISTRIBUTED IN THREE SOURCE REGIONS (LIVER, KIDNEYS AND SPLEEN) OBTAINED WITH OLINDA V2

(courtesy of M. Bardiès)

Target organ	Beta (mGy/MBq)	Gamma (mGy/MBq)	Total (mGy/MBq)	Beta/total ratio (%)	Gamma/total ratio (%)
Adrenals	1.20E-02	4.73E-02	5.93E-02	20	80
Brain	1.06E-07	1.28E-04	1.28E-04	0	100
Breasts	0.00E+00	4.58E-03	4.58E-03	0	100
Oesophagus	3.05E-05	2.10E-02	2.10E-02	0	100
Eyes	0.00E+00	1.59E-04	1.59E-04	0	100
Gallbladder wall	2.26E-04	4.04E-02	4.06E-02	1	99
Left colon	2.67E-06	6.90E-03	6.90E-03	0	100
Small intestine	1.28E-05	8.25E-03	8.26E-03	0	100
Stomach wall	3.88E-04	1.36E-02	1.40E-02	3	97
Right colon	5.85E-04	1.22E-02	1.28E-02	5	95
Rectum	7.63E-11	9.16E-04	9.16E-04	0	100
Heart wall	2.06E-05	1.15E-02	1.15E-02	0	100
Kidneys	4.99E-01	3.24E-02	5.31E-01	94	6
Liver	2.34E+00	9.55E-02	2.44E+00	96	4
Lungs	2.77E-03	1.39E-02	1.67E-02	17	83
Ovaries	2.36E-11	1.79E-03	1.79E-03	0	100
Pancreas	3.02E-03	3.44E-02	3.74E-02	8	92

TABLE 7.2. ABSORBED DOSE PER UNIT OF ACTIVITY ADMINISTERED (ABSORBED DOSE COEFFICIENTS) OBTAINED IN A VOXEL BASED ADULT FEMALE MODEL, WHERE ^{177}Lu IS CONSIDERED UNIFORMLY DISTRIBUTED IN THREE SOURCE REGIONS (LIVER, KIDNEYS AND SPLEEN) OBTAINED WITH OLINDA V2

(courtesy of M. Bardiès) (cont.)

Target organ	Beta (mGy/MBq)	Gamma (mGy/MBq)	Total (mGy/MBq)	Beta/total ratio (%)	Gamma/total ratio (%)
Salivary glands	6.93E-13	4.31E-04	4.31E-04	0	100
Red marrow	0.00E+00	5.88E-03	5.88E-03	0	100
Osteogenic cells	0.00E+00	7.60E-03	7.60E-03	0	100
Spleen	4.85E-01	1.74E-02	5.02E 01	97	3
Thymus	4.54E-12	7.10E-03	7.10E-03	0	100
Thyroid	2.73E-06	2.51E-03	2.51E-03	0	100
Urinary bladder wall	1.05E-11	7.62E-04	7.62E-04	0	100
Uterus	4.14E-07	1.45E-03	1.45E-03	0	100

Note: Activity distribution of ^{177}Lu is present in liver, kidneys and spleen.

Conclusions extracted from this specific example are quite general. They certainly may be adjusted depending on the relative time-integrated activity present in the sources and isotope characteristics (abundance and energy of the different types of radiation).

7.3. ABSORBED DOSE CALCULATION ALGORITHMS

Three broad categories of absorbed dose calculation algorithms can be defined, presented in what follows in increasing level of complexity. The choice of an algorithm impacts accuracy and computation time.

Figure 7.2 shows qualitatively that, for example, very quick algorithms are available, but rely on simplifying assumptions that must be verified. It has to be

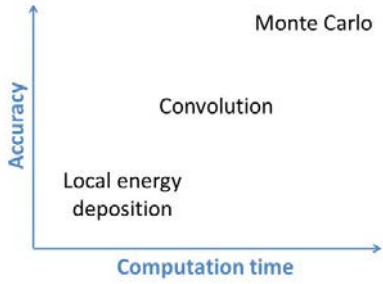

FIG. 7.2. Absorbed dose calculation algorithms. The accuracy/speed compromise presented in the figure is only qualitative. Courtesy of Manuel Bardiès.

noted, however, that there are situations where local energy deposition is at the same time fast and accurate, for example, when self-absorbed dose is dominating.

7.3.1. Local energy deposition

Local energy deposition assumes that the emitted radiations are non-penetrating (*np*) (i.e. all emitted energy is absorbed locally). In that context, the absorbed fraction of the energy from the source region r_S to the target region r_T is [7.5, 7.6]:

$$\phi_{np}\left(r_{\mathrm{T}} \leftarrow r_{\mathrm{s}}\right) = 1 \text{ if source region = target region} \tag{7.4}$$

$$\phi_{np}\left(r_{\mathrm{T}} \leftarrow r_{\mathrm{s}}\right) = 0 \text{ if source region} \neq \text{target region} \tag{7.5}$$

$$S\left(r_{\mathrm{T}} \leftarrow r_{\mathrm{s}}\right) = \frac{1}{M\left(r_{\mathrm{T}}\right)} \sum_i \Delta_i \cdot \phi_{np}\left(r_{\mathrm{T}} \leftarrow r_{\mathrm{s}}, E_i\right) \tag{7.6}$$

where Δ is the emitted energy per decay ($\mathrm{J \cdot Bq^{-1} \cdot s^{-1}}$) for each radionuclide particle emission (in accordance with Chapter 2, Eq. (2.7)).

If we simplify the notation and replace the summation sign by Δ to represent the total emitted energy per decay, we get:

$$S\left(r_{\mathrm{T}} \leftarrow r_{\mathrm{s}}\right) = \frac{\Delta}{M\left(r_{\mathrm{T}}\right)} \text{ if source region = target region} \tag{7.7}$$

$$S(r_T \leftarrow r_s) = 0 \text{ if source region} \neq \text{target region} \quad (7.8)$$

Absorbed dose calculation then becomes simple and can be performed very quickly by multiplication of $S(r_T \leftarrow r_S)$ and the time-integrated activity in the source region $\tilde{A}(r_S)$:

$$D(r_T) = \tilde{A}(r_s) \cdot S(r_T \leftarrow r_s) \quad (7.9)$$

Therefore:

$$D(r_T) = \tilde{A}(r_s) \frac{\Delta}{M(r_T)} \text{ if source region = target region} \quad (7.10)$$

$$D(r_T) = 0 \text{ if source region} \neq \text{target region} \quad (7.11)$$

This can be implemented at the scale of an organ, or for voxels if the range of radiation is low when compared to the voxel dimensions. As long as it can be demonstrated that, for a given geometry, non-penetrating radiation conditions are met, local energy deposition is a very fast and attractive option.

7.3.2. Absorbed dose calculation by convolution with point kernels

If radiation is propagating in a homogeneous medium, energy deposition at a distance r of a point source is a function of the distance to the source and can be represented by the scaled absorbed dose point kernel $F(r/r_0)$:

$$F(r / r_0) = \frac{\delta E(r) / E_0}{\delta r / r_0} \quad (7.12)$$

where δr is the spherical shell thickness, $\delta E(r)$ is the energy deposited in the shell (between r and r + δr), E_0 is the initial electron kinetic energy and r_0 is the continuous slowing down approximation (CSDA) range (see Chapter 2). Integrating deposited energy in concentric shells of increasing radii is a nice way to remove the impact of the inverse square law that precludes giving results for $r = 0$ (Fig. 7.3).

In addition, as an extended source region can be considered as a collection of independent point sources, assessing the variation of the absorbed dose at a distance from a point source represents the first step towards the determination of the absorbed dose for any source geometry. This forms the basis of the absorbed dose point kernel approaches [7.7].

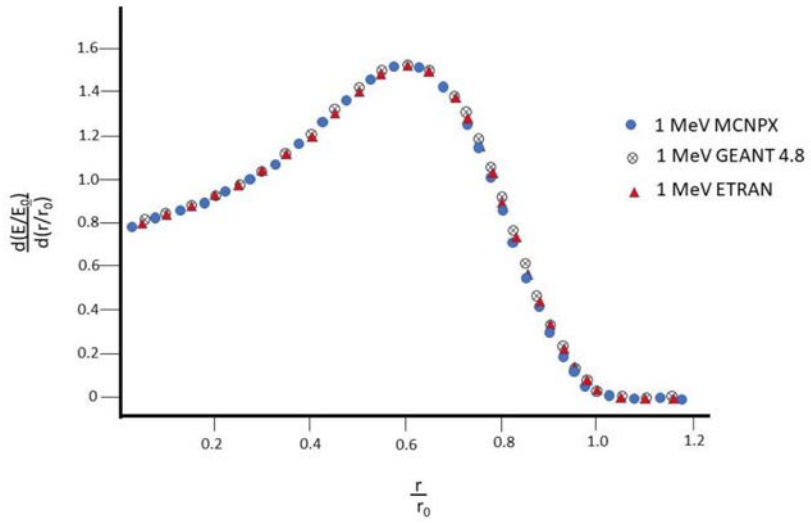

FIG. 7.3. Electron scaled 1 MeV absorbed dose point kernels in water, $F(r/r_0)$ The scaling factor r_0 is the continuous slowing down approximation range of electrons in water. Adapted from [7.8].

Absorbed dosepoint kernels (or dose point kernels, DPKs) can be obtained analytically, determined experimentally or by Monte Carlo modelling of radiation transport. Most DPKs recently presented in the literature were obtained from Monte Carlo modelling of radiation transport. Differences between DPKs obtained using current Monte Carlo codes are small and generating DPK can nowadays be considered as a means to verify Monte Carlo code implementation or version update (Fig. 7.3), at least for the energies and radiation types used in nuclear medicine dosimetry [7.8].

Initially, DPKs were mostly proposed for monoenergetic electrons (at a small scale) or monoenergetic photons.

Subsequently, scaled beta point kernels were generated by integration of DPKs over radionuclide emission spectra [7.9]. Here, E_0 in Eq. (7.12) is replaced by $E_{\beta_{\text{mean}}}$, the average energy over the beta spectrum, and the CSDA range is replaced by X_{90}, the distance at which 90% of the emitted energy is absorbed:

$$F\left(r / X_{90}\right) = \frac{\delta E(r) / E_{\beta_{\text{mean}}}}{\delta r / X_{90}} \tag{7.13}$$

It is also possible to generate radionuclide point kernels that consider all emission types. Figure 7.4 presents the variation of absorbed dose delivered

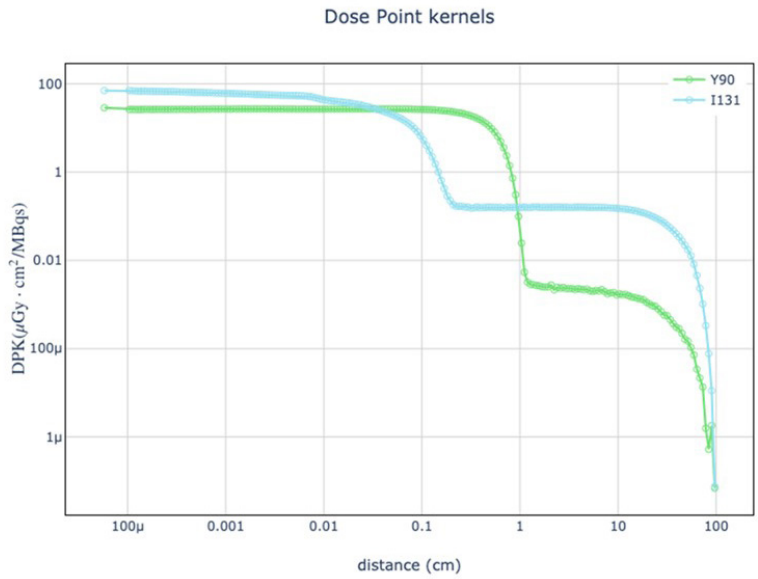

FIG. 7.4. Absorbed dose point kernel (μGy·cm^2·Bq^{-1}·s^{-1}) in water (radial distance cm) from a point source of ^{131}I and ^{90}Y. Electron (ß) contributions vanish after 2 mm for ^{131}I and after 11 mm for ^{90}Y, while photon contributions (gammas and bremsstrahlung) are present up to 1 m distance. Courtesy of A. Vergara Gil.

by a point source of ^{90}Y and ^{131}I. The electron (β) contribution vanishes after approximately 2 mm for ^{131}I and after 11 mm for ^{90}Y, while the photon contribution remains up to 1 m distance. Figures 7.1 and 7.4 both present the energy deposited at a distance of a point source of ^{131}I.

The use of DPKs in more complex geometries (still in homogeneous medium) can be performed by integrating DPKs analytically when possible, or by convolving DPKs with activity or cumulated activity distributions.

The mean absorbed dose $D(\vec{r})$, in Gy, at any location $\vec{r}$ can be obtained by means of the convolution kernel $K_D(\vec{r})$ and the time-integrated activity $\tilde{A}(r_s, \vec{r})$ in Bq·s, as follows:

$$D(\vec{r}) = K_D(\vec{r}) \otimes \tilde{A}(r_s, \vec{r}) \tag{7.14}$$

This formulation is also valid as:

$$\dot{D}(\vec{r}) = K_D(\vec{r}) \otimes A(r_s, \vec{r}) \tag{7.15}$$

where $\dot{D}(\vec{r})$ is the mean absorbed dose rate ($\mathrm{Gy} \times \mathrm{s}^{-1} \times \mathrm{s}^{-1}$) and $A(r_s, \vec{r})$ is the activity (Bq) at a given time point at a position $\vec{r}$ away from the point source.

Or, using the Fourier transform in a source geometry sampled with voxels:

$$D = \mathcal{F}^{-1}\left\{\mathcal{F}\left[K_D\right] \cdot \mathcal{F}\left[\tilde{A}(r_s)\right]\right\} \tag{7.16}$$

or:

$$\dot{D} = \mathcal{F}^{-1}\left\{\mathcal{F}\left[K_D\right] \cdot \mathcal{F}\left[A(r_s)\right]\right\} \tag{7.17}$$

where $\mathcal{F}^{-1}$ and $\mathcal{F}$ are the operators for the discrete Fourier transform representing the inverse and forward Fourier transforms, respectively.

Additionally, K_D (i, j, k), A_{Source} (l, m, n) and $\tilde{A}_{\text{Source}}$ (l, m, n) are the 3-D voxel level representation of kernel, activity and cumulated activity, respectively.

If quantitative imaging can provide activity in a sampled geometry (voxels), then discrete convolution of DPK is an appealing option to generate absorbed dose rate distributions at the voxel level (Fig. 7.5) [7.10].

The convolution process requires the generation of voxel *S* values sampled at the scale of activity or cumulated activity [7.1]. A free database of those is available for use in RPT dosimetry [7.2]. Other authors proposed a way to generate voxel *S* values for any size from finely sampled voxel *S* values [7.11, 7.12]. Depending on the authors, the voxel source can consider a point source located at the centre of the voxel, or a homogeneous distribution of activity in the source voxel. Adaptations of the convolution approach in a context of heterogeneous media have also been proposed [7.13].

Convolution of voxel *S* values is a relatively easy and fast way to perform dosimetry in RPT, which explains why it is often proposed as an absorbed dose calculational algorithm in many academic or commercial work packages [7.14–7.16]. It can provide absorbed dose (rate) distributions at the voxel level, and therefore allows the representation of results under the form of absorbed dose volume histograms, or the computation of refined dosimetry indexes such as the equivalent uniform dose (EUD).

7.3.3. Monte Carlo modelling of radiation transport

Explicit radiation transport modelling via Monte Carlo simulation is the most advanced/refined available approach, but there is a price to pay, in terms

of computation time. It is (in principle) able to cope with any situation involving radiation transport — including those for which no simplified approach (local energy, convolution, deposition, convolution) is adequate. In particular, Monte Carlo modelling of radiation transport can be performed in heterogeneous media (bone, lungs, soft tissues), even at a low scale (complex bone marrow structure at the microscopic level).

Monte Carlo simulations can be used to generate *S* values (for organ/tissues or voxels), or to perform direct absorbed dose rate (or absorbed dose) calculation if the geometry (its mass density) and (time-integrated) activity distributions are well characterized.

Monte Carlo codes used for dosimetry mostly derive from codes developed in nuclear/particle physics research centres [7.17]. These codes became progressively available to the scientific community, their algorithms and cross-sections adapted and validated for the range of energies encountered in nuclear medicine (i.e. from keV to some MeV).

The availability and accuracy of Monte Carlo codes for energies below some tenth of keV will not be discussed here, as they fall outside the relevant scale for patient dosimetry (even voxel based). For example, a 10 keV electron in water will have a CSDA range of about 2.5 µm, and 90% of its energy (X_{90}) will be absorbed within the first 2 µm.

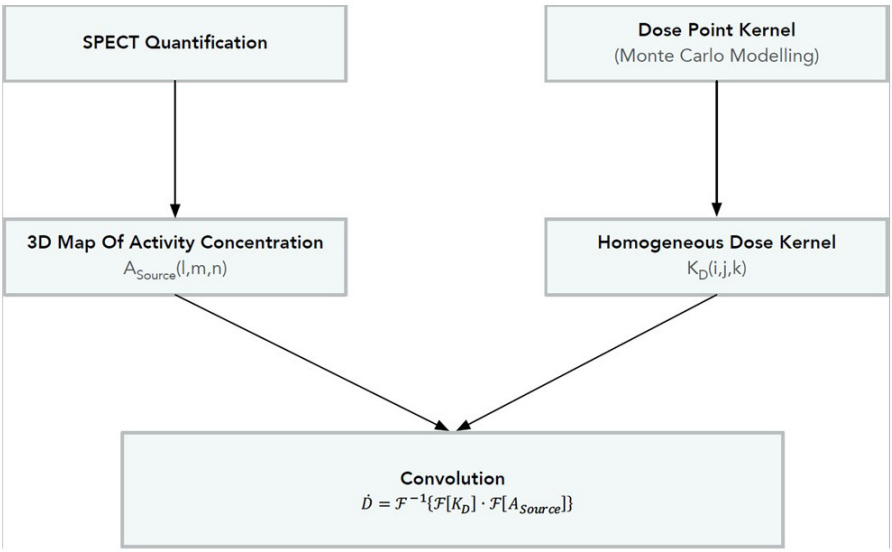

FIG. 7.5. Flowchart of the DPK convolution approach. © Institute of Physics and Engineering in Medicine. Reproduced by permission of IOP Publishing. All rights reserved.

ETRAN was historically the first Monte Carlo code used for nuclear medicine dosimetry [7.18]. The medical internal radiation dose (MIRD) *S* factors published in MIRD 11 [7.19] were obtained partly using a Monte Carlo code (ALGAM) later adapted for several computing models of the ORNL series [7.20–7.26]. The wider application of Monte Carlo codes to radionuclide dosimetry is more recent [7.27].

There is currently a wide availability of the major Monte Carlo codes: MCNP(X) [7.28], EGS5 [7.29], EGS_{NRC} [7.30], GEANT/GATE [7.31, 7.32], FLUKA [7.33] and PENELOPE [7.34]. These can be used to compute the absorbed dose in (almost) any situation encountered in RPT, at least at the organ/tissue scale. Some of them are also able to model nuclear medicine imaging (including hybrid imaging devices). GATE [7.35] is probably the most widely used in that context since it was specifically designed for use in medical imaging and dosimetry.

7.3.4. Selecting the absorbed dose calculation algorithm

The three major algorithms designed for absorbed dose calculation have been reported in Section 7.3.3. For a given situation (i.e. radiation type and energy in relation with the spatial sampling of the geometry), it is possible to select the most adequate algorithm, as described in Fig. 7.6.

This decision tree is valid at any scale, including microscopic, if needed, but only for radiation transport problems where activity and media determination

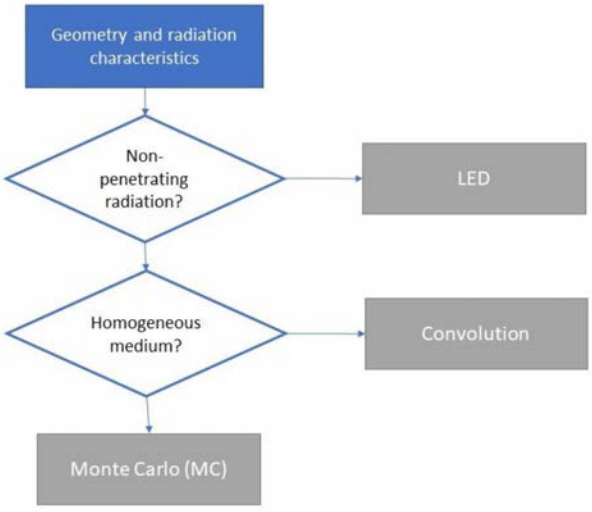

FIG. 7.6. Dosimetry algorithm selection.

are perfectly defined. In other words, in clinical dosimetry, the algorithm selection process should consider the whole context: how source and media are characterized (associated uncertainties), and also the rationale and objectives of the dosimetry approach, to finally decide on the most appropriate radiation transport algorithm to implement or use. This will be addressed in Section 7.4.

7.4. DOSIMETRIC APPROACHES

There are two broad dosimetry approach types, **model based** or **patient-specific** dosimetry.

Model based dosimetry is often (but not exclusively) used in the context of reference dosimetry, for example, during the development phase of a new diagnostic radiopharmaceutical. The absorbed dose is given not for an individual, but for a reference dosimetry model such as those presented by the ICRP [7.36]. **Model based dosimetry** originates from the need for reference values allowing the comparison of irradiation delivered to the patient by radiopharmaceuticals in a diagnostic context. The dosimetry approach follows the recommendations of the ICRP. Therefore, *S* values are generated from a referenced, fully described and traceable model. Some of the most famous models are the adult mathematical model used for generating *S* values in MIRD Pamphlet No. 11 [7.19], followed by Cristy and Eckerman's mathematical paediatric series [7.20–7.26] and Stabin's models of females at various stages of pregnancy. These have been used extensively and *S* values were integrated in codes such as MIRDOSE [7.37] and OLINDA (V1) [7.4].

The calculation of *S* values is done using the algorithms mentioned in the Section 7.3.4. Obviously, for reference dosimetry, one aims usually for the best possible accuracy and Monte Carlo codes are most often used nowadays to derive *S* values [7.38]. However, in principle, nothing prevents one from using alternative absorbed dose calculation algorithms (local energy deposition of convolution) to compute *S* values, if the context allows for it (i.e. if these faster algorithms are as accurate as Monte Carlo).

The time-integrated activity and the time-integrated activity coefficients in the context of reference dosimetry are assessed for a group of patients, or healthy volunteers, or extrapolated from animal experiments to provide a 'reference' pharmacokinetics. Absorbed doses (and derivate indexes like the effective doses) are therefore obtained for a model and should not be used for an individual. Dosimetry results are often presented in MIRD dose estimate reports and are integrated in ICRP reports. Figure 7.7 presents the evolution of dosimetry models with time [7.39].

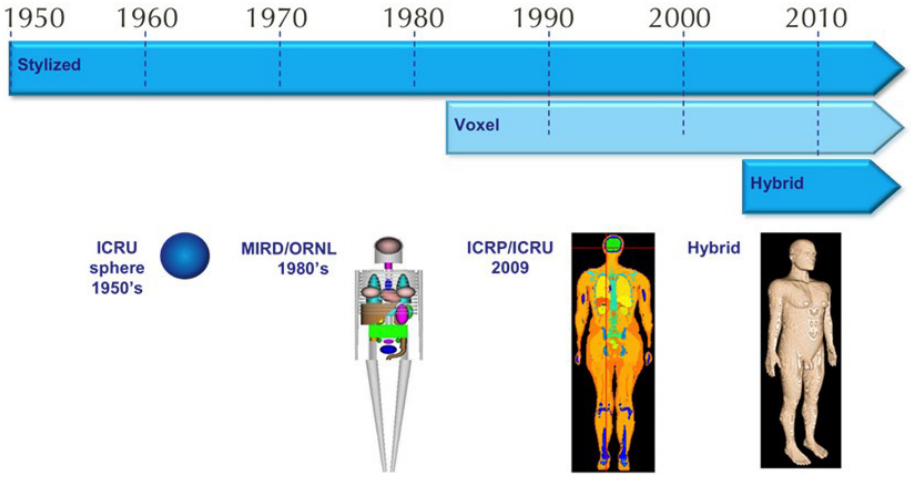

FIG. 7.7. Computing models developed for radiopharmaceutical dosimetry [7.40]. Reproduced with permission from CORDIS Publications Office.

Moving from the diagnostic to a therapy context implies aiming for more accuracy. This justifies the implementation of **patient-specific dosimetry**.

The first step is usually to derive pharmacokinetic parameters specifically for each patient. This has long been acknowledged as a requirement for **patient-specific dosimetry**. However, the specific calculation of the irradiation delivered to the patient (i.e. on the basis of each patient geometry) has long been impossible — and still represents a challenge for most clinical departments. Therefore, efforts aiming at the personalization of clinical dosimetry involved an adaptation of the model based *S* values to consider the actual geometry of the patient.

This is made possible (at least at the scale of an organ or a tissue) by *S* value adjustment. It can be shown that for the self-absorbed dose ($r_T = r_S$), adjusting the reference *S* value by the mass ratio between reference and patient-specific target region mass (e.g. an organ) provides a good approximation of the patient-specific *S* value:

$$S\left(r_T \leftarrow r_s\right)_{pat} = S\left(r_T \leftarrow r_s\right)_{ref} \times \frac{M_{ref}\left(r_T\right)}{M_{pat}\left(r_T\right)} \tag{7.18}$$

This assumption is strictly speaking valid only in conditions of non-penetrating radiation and if the organ mass does not change while the absorbed dose is being delivered.

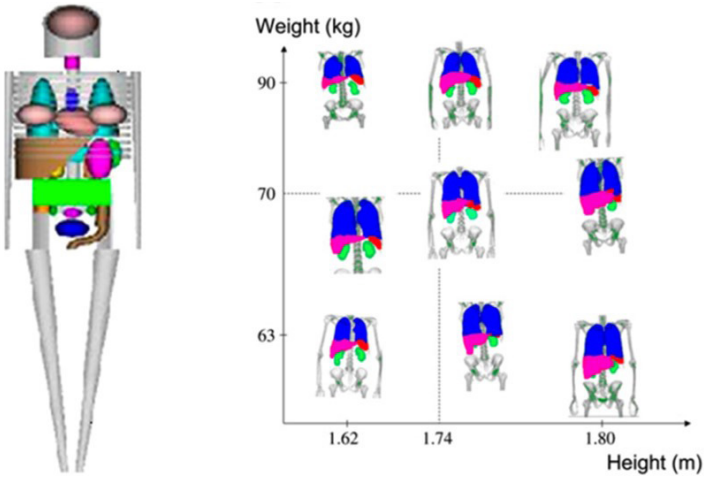

FIG. 7.8. Size and weight distribution of the nine patients from Divoli et al. 2009 [7.41]. Reproduced with permission from Journal of Nuclear Medicine publishing.

In the following example from Divoli et al. [7.41], *S* values from nine patients of variable morphology were obtained by Monte Carlo simulation (MCNPX 2.5.0). The size and weight were varied around the size and weight of the reference OLINDA male model (1.74 m, 70 kg), as presented in Fig. 7.8.

For ^{131}I, the *S* values for the kidneys (self-absorbed dose) are presented in Fig. 7.9. The standard *S* values are taken from OLINDA (V1) without mass adjustment (i.e. the *S* values are the same for all patients regardless of kidney volume/mass). Patient-specific *S* values were obtained using MCNPX after segmentation of the kidneys for each patient. As can be seen there is an important difference (more than a factor 2 sometimes) between standard and patient-specific *S* values. When the mass adjustment is performed, standard-adjusted values are within a few per cent of the patient-specific *S* values.

From a practical point of view, adjusting *S* values is an excellent way to personalize dosimetry as patient-specific organ/tissue masses are usually available from CT imaging. Conversely, using 'one-size-fits-all' *S* values, without mass adjustment, should no longer be accepted in the context of patient-specific dosimetry (e.g. in therapy). This mass adjustment is proposed as an option in OLINDA (V1 and V2) and IDAC (V2.1).

Strictly speaking, patient-specific dosimetry requires that all steps implemented to derive the absorbed dose are specific, from pharmacokinetics (Ã) assessment to absorbed dose calculation itself. Ideally, this means that the geometry (density) of the organs/tissues of interest should be perfectly defined.

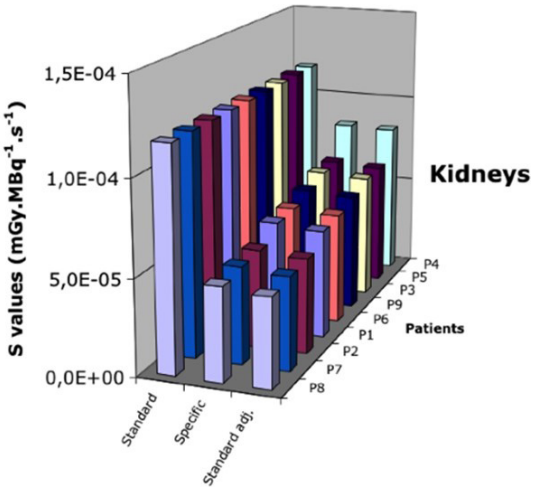

FIG. 7.9. Standard, specific and adjusted S values for the kidneys (mGy·MBq^{-1}) for ^{131}I in the nine patient models (P1 to P9). Reproduced with permission from Journal of Nuclear Medicine publishing.

In this situation, the explicit calculation of *S* values is no longer relevant and the absorbed dose or absorbed dose rate can be calculated directly for the patient. Results can be displayed as the average absorbed dose for volumes of interest, but absorbed dose volume histograms can also be computed, if needed. Obviously, as for any voxel based dosimetry approach, this raises the question of the feasibility of voxel based activity (or time-integrated activity) determination.

Several examples of absorbed dose calculation codes can be found in the literature. The oldest usually consider convolution based calculations (and therefore homogeneous media) [7.15, 7.16, 7.42], but most of the recently proposed codes include explicit modelling of radiation transport and energy deposition (i.e. Monte Carlo modelling). For example, Raydose [7.43] is a Geant4 based code that allows computing absorbed dose rates in a context of clinical dosimetry. Patient geometry is obtained from DICOM CT images, and the activity is obtained at the voxel level on scintigraphy images (PET or SPECT). Three dimensional absorbed dose maps can be calculated by integrating absorbed dose rate maps and generating absorbed dose volume histograms (Fig. 7.10). VIDA, proposed by Kost et al. in 2015 [7.44], is another Geant4 based dosimetry code for use in reference dosimetry (*S* value calculation) or in a clinical context.

A summary of the different global approaches of radiopharmaceutical dosimetry is presented in Table 7.3.

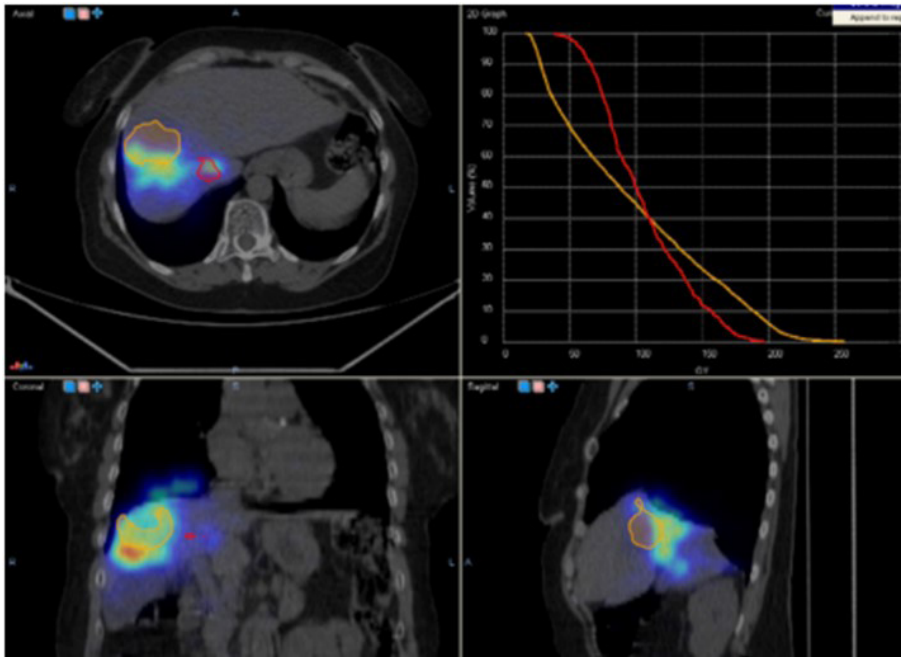

FIG. 7.10. Illustration of absorbed dose volume histogram obtained from Raydose [7.43]. Courtesy of E. Spezi.

TABLE 7.3. SUMMARY OF RADIOPHARMACEUTICAL DOSIMETRY APPROACHES

(courtesy of M. Bardiès)

Context	Pharmacokinetics assessment ($\tilde{A}$)	Absorbed dose calculation (S)	Purpose
Diagnostics	Group representing a population	Model based	Model based reference dosimetry: ICRP or MIRD dose estimate reports
Therapy (1)	Patient-specific	Model based ± adjusted for organ mass	'Adjusted' model based dosimetry
Therapy (2)	Patient-specific	Patient-specific	Fully patient-specific dosimetry

Absorbed dose calculation is a step of the dosimetry chain. As such, it cannot be dissociated from the context/purpose of the calculation (diagnostics or therapy). The other relevant steps, like activity determination, must also be considered as they condition the degree of refinement that can/must be implemented for absorbed dose calculation, and the uncertainties associated with the process. Once the frame of the calculation has been set, the choice of the relevant absorbed dose calculation algorithm can be made.

7.5. SUMMARY OF ABSORBED DOSE CALCULATION APPROACHES

The absorbed dose calculation is only one part of the dosimetry process. Advances in this field in the past decades have been striking. It is now possible to compute the absorbed dose for any geometry, for various densities, and to present results not only as mean absorbed doses in macroscopic volumes/organs/tissues, but as absorbed dose volume histograms, for user-defined volumes of interest.

The relationship between radiation range and geometry spatial sampling needs to be studied. Voxel based determination of the geometry is not necessarily a guarantee of accuracy [7.45]. Geometry description may have to be refined to be adapted to the context: a rough description of the geometry [7.46], even voxel based, will probably not lead to satisfying dosimetry results.

Yet, the accuracy associated with absorbed dose calculation (regardless of uncertainties in the activity quantification) has markedly improved, notably due to the increasing availability of Monte Carlo codes adapted to nuclear medicine dosimetry. This apparent gain in accuracy must not hide the fact that the absorbed dose calculation process is dependent on the other steps of the dosimetry chain: the uncertainties associated with the determination of the amount and location of radioactive sources are probably limiting the overall accuracy of clinical dosimetry.

In addition, the dosimetry procedure to implement depends on the clinical/scientific objective: the generation of **reference** dosimetry values probably requires a higher degree of refinement and aims for the best possible accuracy.

That being said, absorbed dose calculation algorithms are available and can be used in the various contexts encountered in nuclear medicine dosimetry. Resources for performing absorbed dose calculations are also available [7.47, 7.48]. Comparison of the various approaches available has been a field of interest over the past years [7.49, 7.50]. Since a growing number of commercial packages are available, the study of the algorithms incorporated into each set of software is relevant and must be seen in the context of other aspects of the

clinical dosimetry procedure. The absorbed dose calculation is just one step in the clinical dosimetry procedure, and its associated uncertainty must be considered in the context of the other contributors to the overall uncertainty, as discussed in Chapter 9.

REFERENCES

[7.1] BOLCH, W.E., et al., MIRD Pamphlet No. 17: The dosimetry of nonuniform activity distributions — radionuclide S values at the voxel level, J. Nucl. Med. **40** 1 (1999) 11S–36S.

[7.2] LANCONELLI, N., et al., A free database of radionuclide voxel S values for the dosimetry of nonuniform activity distributions, Phys. Med. Biol. **57** 2 (2012) 517–533, https://doi.org/10.1088/0031-9155/57/2/517

[7.3] ANDERSSON, M., JOHANSSON, L., ECKERMAN, K., MATTSSON, S., IDAC-Dose 2.1, an internal dosimetry program for diagnostic nuclear medicine based on the ICRP adult reference voxel phantoms, EJNMMI Res. **7** 1 (2017) 88, https://doi.org/10.1186/s13550-017-0339-3

[7.4] STABIN, M.G., SPARKS, R.B., CROWE, E., OLINDA/EXM: The second-generation personal computer software for internal dose assessment in nuclear medicine, J. Nucl. Med. **46** 6 (2005) 1023–1027.

[7.5] LOEVINGER, R., BUDINGER, T., WATSON, E., MIRD Primer for Absorbed Dose Calculations, The Society of Nuclear Medicine, New York (1991).

[7.6] BARDIÈS, M., "Small-scale dosimetry and microdosimetry", Dosimetry for Radionuclide Therapy, Report 104, IPEM, York, UK (2011).

[7.7] BARDIÈS, M., KWOK, C., SGOUROS, G., "Dose point-kernels for radionuclide dosimetry", Therapeutic Applications of Monte Carlo Calculations in Nuclear Medicine (ZAIDI, H., SGOUROS, G., Eds), CRC Press, Boca Raton, FL (2002), https://doi.org/10.1201/9781420033250-7

[7.8] FERRER, L., CHOUIN, N., BITAR, A., LISBONA, A., BARDIÈS, M., Implementing dosimetry in GATE: Dose-point kernel validation with GEANT4 4.8. 1, Cancer Biother. Radiopharm. **22** 1 (2007) 125–129, https://doi.org/10.1089/cbr.2007.304

[7.9] BOTTA, F., et al., Calculation of electron and isotopes dose point kernels with FLUKA Monte Carlo code for dosimetry in nuclear medicine therapy, Med. Phys. **38** 7 (2011) 3944–3954, https://doi.org/10.1118/1.3586038

[7.10] GIAP, H.B., MACEY, D.J., BAYOUTH, J.E., BOYER, A.L., Validation of a dose-point kernel convolution technique for internal dosimetry, Phys. Med. Biol. **40** 3 (1995) 365–381, https://doi.org/10.1088/0031-9155/40/3/003

[7.11] DIEUDONNÉ, A., HOBBS, R.F., BOLCH, W.E., SGOUROS, G., GARDIN, I., Fine-resolution voxel S values for constructing absorbed dose distributions at variable voxel size, J. Nucl. Med. **51** 10 (2010) 1600–1607, https://doi.org/10.2967/jnumed.110.077149

[7.12] FERNÁNDEZ, M., et al., A fast method for rescaling voxel S values for arbitrary voxel sizes in targeted radionuclide therapy from a single Monte Carlo calculation, Med. Phys. **40** 8 (2013) 082502, https://doi.org/10.1118/1.4812684

[7.13] SANCHEZ-GARCIA, M., GARDIN, I., LEBTAHI, R., DIEUDONNÉ, A., A new approach for dose calculation in targeted radionuclide therapy (TRT) based on collapsed cone superposition: Validation with (90)Y, Phys. Med. Biol. **59** 17 (2014) 4769–4784, https://doi.org/10.1088/0031-9155/59/17/4769

[7.14] KOLBERT, K.S., et al., Implementation and evaluation of patient-specific three-dimensional internal dosimetry, J. Nucl. Med. **38** 2 (1997) 301–308.

[7.15] GUY, M.J., FLUX, G.D., PAPAVASILEIOU, P., FLOWER, M.A., OTT, R.J., RMDP: A dedicated package for 131I SPECT quantification, registration and patient-specific dosimetry, Cancer Biother. Radiopharm. **18** 1 (2003) 61–69, https://doi.org/10.1089/108497803321269331

[7.16] GARDIN, I., et al., Voxeldose: A computer program for 3-D dose calculation in therapeutic nuclear medicine, Cancer Biother. Radiopharm. **18** 1 (2003) 109–115, https://doi.org/10.1089/108497803321269386

[7.17] BARDIÈS, M., LJUNGBERG, M., "Monte Carlo codes in radionuclide dosimetry", Dosimetry for Radionuclide Therapy, Report 104, IPEM, York, UK (2011).

[7.18] BERGER, M.J., "Monte Carlo calculation of the penetration and diffusion of fast charged particles", Methods in Computational Physics, Vol. 1 (ALDER, B., FERNBACH, S., ROTENBERG, M., Eds), Academic Press, New York (1963).

[7.19] SNYDER, W., FORD, M., WARNER, G., WATSON, S., MIRD Pamphlet No. 11: S, absorbed dose per unit cumulated activity for selected radionuclides and organs, Society of Nuclear Medicine, New York (1975).

[7.20] CRISTY, M., ECKERMAN, K.F., Specific Absorbed Fractions of Energy at Various Ages from Internal Photon Sources: 1, Methods, Rep. ORNL/TM-8381/V1, Oak Ridge Natl Lab., Oak Ridge, TN (1987), https://doi.org/10.2172/6233735

[7.21] CRISTY, M., ECKERMAN, K.F., Specific Absorbed Fractions of Energy at Various Ages from Internal Photon Sources: 2, One-year-old, Rep. ORNL/TM-8381/V2, Oak Ridge Natl Lab., Oak Ridge, TN (1987), https://doi.org/10.2172/6203023

[7.22] CRISTY, M., ECKERMAN, K.F., Specific Absorbed Fractions of Energy at Various Ages from Internal Photon Sources: 3, Five-year-old, Rep. ORNL/TM-8381/V3, Oak Ridge Natl Lab., Oak Ridge, TN (1987), https://doi.org/10.2172/6263443

[7.23] CRISTY, M., ECKERMAN, K.F., Specific Absorbed Fractions of Energy at Various Ages from Internal Photon Sources: 4, Ten-year-old, Rep. ORNL/TM-8381/V4, Oak Ridge Natl Lab., Oak Ridge, TN (1987), https://doi.org/10.2172/6233673

[7.24] CRISTY, M., ECKERMAN, K.F., Specific Absorbed Fractions of Energy at Various Ages from Internal Photon Sources: 5, Fifteen-year-old Male and Adult Female, Rep. ORNL/TM-8381/V5, Oak Ridge Natl Lab., Oak Ridge, TN (1987), https://doi.org/10.2172/6263426

[7.25] CRISTY, M., ECKERMAN, K.K., Specific Absorbed Fractions of Energy at Various Ages from Internal Photon Sources: 6, Newborn, Rep. ORNL/TM-8381/V6, Oak Ridge Natl Lab., Oak Ridge, TN (1987), https://doi.org/10.2172/6202949

[7.26] CRISTY, M., ECKERMAN, K.F., Specific Absorbed Fractions of Energy at Various Ages from Internal Photon Sources: 7, Adult Male, Rep. ORNL/TM-8381/V7, Oak Ridge Natl Lab., Oak Ridge, TN (1987), https://doi.org/10.2172/6233638

[7.27] ZAIDI, H., SGOUROS, G., Therapeutic Applications of Monte Carlo Calculations in Nuclear Medicine, CRC Press, Boca Raton, FL (2002), https://doi.org/10.1201/9781420033250

[7.28] BROWN, F., MCNP — A General Monte-Carlo N-Particle Transport Code, Los Alamos National Laboratory, Los Alamos, NM (2003).

[7.29] HIRAYAMA, H., NAMITO, Y., NELSON, W.R., BIELAJEW, A.F., WILDERMAN, S.J., The EGS5 Code System, Technical Report, SLAC Natl Accelerator Lab., Menlo Park, CA (2005), https://doi.org/10.2172/877459

[7.30] KAWRAKOW, I., ROGERS, D., The EGSnrc Code System: Monte Carlo Simulation of Electron and Photon Transport, NRC Report PIRS-701, NRC, Ottawa (2000).

[7.31] GEANT4 COLLABORATION, Book for Application Developers (2017).

[7.32] JAN, S., et al., GATE: A simulation toolkit for PET and SPECT, Phys. Med. Biol. **49** 19 (2004) 4543–4561.

[7.33] FERRARI, A., SALA, P.R., FASSO, A., RANFT, J., FLUKA: A Multi-Particle Transport Code, CERN-2005-010, SLAC, Stanford, CA (2005), https://doi.org/10.2172/877507

[7.34] ORGANISATION FOR ECONOMIC CO-OPERATION AND DEVELOPMENT, PENELOPE: A Code System for Monte Carlo Simulation of Electron and Photon Transport, Workshop Proc. Issy-les-Moulineaux, NEA/OECD, Paris (2003).

[7.35] SARRUT, D., et al., A review of the use and potential of the GATE Monte Carlo simulation code for radiation therapy and dosimetry applications, Med. Phys. **41** 6 Part 1 (2014) 064301, https://doi.org/10.1118/1.4871617

[7.36] MENZEL, H.-G., CLEMENT, C., DeLUCA, P., Realistic reference phantoms: An ICRP/ICRU joint effort. A report of adult reference computational phantoms, ICRP Publication 110, Ann. ICRP **39** 2 (2009) 1–64, https://doi.org/10.1016/j.icrp.2009.09.001

[7.37] STABIN, M.G., MIRDOSE: Personal computer software for internal dose assessment in nuclear medicine, J. Nucl. Med. **37** 3 (1996) 538–546.

[7.38] VILLOING, D., MARCATILI, S., GARCIA, M.-P., BARDIÈS, M., Internal dosimetry with the Monte Carlo code GATE: Validation using the ICRP/ICRU female reference computational model, Phys. Med. Biol. **62** 5 (2017) 1885–1904, https://doi.org/10.1088/1361-6560/62/5/1885

[7.39] EBERLEIN, U., et al., Biokinetics and dosimetry of commonly used radiopharmaceuticals in diagnostic nuclear medicine — a review, Eur. J. Nucl. Med. Mol. Imaging **38** 12 (2011) 2269–2281, https://doi.org/10.1007/s00259-011-1904-z

[7.40] PedDose.net, Dosimetry and Health Effects of Diagnostic Applications of Radiopharmaceuticals with particular emphasis on the use in children and adolescents | PEDDOSE.NET | Project | News & Multimedia | FP7 | CORDIS | European Commission (europa.eu)

[7.41] DIVOLI, A., et al., Effect of patient morphology on dosimetric calculations for internal irradiation as assessed by comparisons of Monte Carlo versus conventional methodologies, J. Nucl. Med. **50** 2 (2009) 316–323, https://doi.org/10.2967/jnumed.108.056705

[7.42] SGOUROS, G., KOLBERT, K.S., "The three-dimensional internal dosimetry software package, 3D-ID", Therapeutic Applications of Monte Carlo Calculations in Nuclear Medicine (ZAIDI, H., SGOUROS, G., Eds), CRC Press, Boca Raton, FL (2002), https://doi.org/10.1201/9781420033250-11

[7.43] MARCATILI, S., et al., Development and validation of RAYDOSE: A Geant4-based application for molecular radiotherapy, Phys. Med. Biol. **58** 8 (2013) 2491–2508, https://doi.org/10.1088/0031-9155/58/8/2491

[7.44] KOST, S.D., DEWARAJA, Y.K., ABRAMSON, R.G., STABIN, M.G., VIDA: A voxel-based dosimetry method for targeted radionuclide therapy using Geant4, Cancer Biother. Radiopharm. **30** 1 (2015) 16–26, https://doi.org/10.1089/cbr.2014.1713

[7.45] PETER, J., TORNAI, M.P., JASZCZEK, R.J., Analytical versus voxelized phantom representation for Monte Carlo simulation in radiological imaging, IEEE Trans. Med. Imaging **19** 5 (2000) 556–564, https://doi.org/10.1109/42.870266

[7.46] MARCATILI, S., VILLOING, D., GARCIA, M.P., BARDIÈS, M., Multi-scale hybrid models for radiopharmaceutical dosimetry with Geant4, Phys. Med. Biol. **59** 24 (2014) 7625–7641, https://doi.org/10.1088/0031-9155/59/24/7625

[7.47] OpenDose,
https://opendose.org

[7.48] S values for voxel dosimetry,
http://www.medphys.it/down_svoxel.htm

[7.49] GRIMES, J., CELLER, A., Comparison of internal dose estimates obtained using organ-level, voxel S value, and Monte Carlo techniques, Med. Phys. **41** 9 (2014) 092501,
https://doi.org/10.1118/1.4892606

[7.50] MARCATILI, S., VILLOING, D., MAUXION, T., McPARLAND, B.J., BARDIÈS, M., Model-based versus specific dosimetry in diagnostic context: Comparison of three dosimetric approaches, Med. Phys. **42** 3 (2015) 1288–1296,
https://doi.org/10.1118/1.4907957

Chapter 8

CLINICAL RADIOBIOLOGICAL MODELLING FOR RADIOPHARMACEUTICAL THERAPY

G. SGOUROS, M. KONIJNENBERG

8.1. INTRODUCTION

The objective of dosimetry in radiopharmaceutical therapy (RPT) is to understand or predict the likely biological consequences of administering a radiopharmaceutical to a patient. In diagnostic nuclear medicine the biological consequence of interest is risk of radiation detriment, which at the absorbed dose levels involved is primarily the risk of developing late occurring effects, like cancer. In RPT the relevant biological end points are toxicity and efficacy. In both cases, radiobiological models are invoked to convert the physical quantity, absorbed dose, into a biological response probability. The radiobiological model used in risk assessment for late stochastic effects (cancer induction) includes radiation and tissue weighting factors, w_R and w_T, respectively [8.1, 8.2]. These are associated with a 'reference person' and are used in conjunction with organ absorbed doses to calculate the effective dose, E. This quantity may be used to compare the cancer risk associated with diagnostic radiopharmaceuticals using lifetime attributable risk tables [8.3]. The weighting factors and lifetime attributable risk values may be thought of as parameters in a model by which absorbed dose, in Gy, is converted to cancer risk. The radiobiological 'model' in the diagnostic scenario has been standardized by international regulatory and professional bodies and is, in general, consistently applied throughout the world for radiation protection [8.4]. In RPT, such standardization of dose-response modelling has not taken place yet. RPT is becoming more widely implemented and efforts to optimize such treatment using dosimetry based treatment planning [8.5] will require standardized dosimetry methods and standardized or 'reference' radiobiological models that are, in a sense, analogous to the 'reference person' concept applied in cancer risk evaluation. Continuing the analogy, reference radiobiological models will not predict efficacy and toxicity in an individual patient but would allow biologically based treatment optimization and comparison of therapeutic agents and treatment strategies. The combination of reference radiobiological models and corresponding reference parameter values for different organs and tumour types may be thought of as a

'reference radiobiological human' analogous to the International Commission on Radiological Protection (ICRP) 'reference human' [8.6, 8.7]. Patient-specific prediction of possible successful therapy without overt toxicity can be obtained by combining individualized dosimetry and radiobiology models.

Recognizing that this is a rapidly evolving area of active research and that the radiobiological models discussed in this chapter are a snapshot of the current state of the field, we identify several basic radiobiological models applicable to RPT. For each model, the purpose, the conditions under which it may be applied and its limitations are briefly discussed. Within the field of external beam radiotherapy (EBRT) and brachytherapy vast knowledge on the dose–volume response of normal tissues to radiation has been reported in the Quantitative Analysis of Normal Tissue Effects in the Clinic (QUANTEC) reports [8.8, 8.9]. Both the absorbed dose rates and the absorbed dose distributions in the radiation fields of EBRT and brachytherapy differ strongly from the situation in RPT. Maximal dose rates obtained with EBRT, low-dose rate brachytherapy and RPT are typically in the order 1 to 10 Gy/min, 1 to 30 mGy/min and 1 to 10 mGy/min, respectively. For alpha RPT these values can be significantly lower. This indicates an almost 10 000-fold ratio between the highest and the lowest dose rates.

8.2. LINEAR–QUADRATIC MODEL

To use the dose-response relations from EBRT and brachytherapy within the field of RPT a model is needed to correct for the strong difference in dose rates. The most commonly used models for this purpose are based upon the linear–quadratic (LQ) formulation for the cell survival fraction *SF* as a function of the absorbed dose *D* [8.10, 8.11]:

$$SF = \mathrm{e}^{-\left(\alpha D + G\beta D^2\right)} \tag{8.1}$$

where α and β are tissue and end point specific LQ model parameters that reflect the shape of the cell survival curve, and the parameter *G* is discussed below. Equation (8.1) describes the fraction of cells surviving after an absorbed dose, *D*, is delivered. Figure 8.1 shows typical cell survival curves for EBRT for high and low linear energy transfer (LET) radiation.

The factor, *G*, is the Lea–Catcheside time factor given by:

$$G(T) = \frac{2}{D^2}\int_0^T \dot{D}(t)\left[\int_0^t \dot{D}(w)\mathrm{e}^{-\mu(t-w)}\mathrm{d}w\right]\mathrm{d}t \tag{8.2}$$

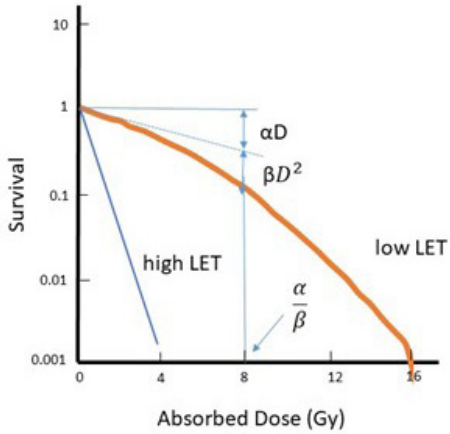

FIG. 8.1. Schematic illustration of the cell survival curves for high LET (densely ionizing) radiation and low LET (sparsely ionizing) radiation. The components of the cell-survival curve that are described by the LQ model parameters α and β are indicated, as well as α / β that represents the absorbed dose when the cell survival due to two components is equal.

This factor is traditionally used to account for repair of deoxyribonucleic acid (DNA) damage during protracted delivery of radiation for an irradiation time T with an absorbed dose rate $\dot{D}(t)$. Equation (8.1) can be interpreted as representing cell killing arising due to either a single event (log-linear term, $(e^{-\alpha D})$) or two events in close temporal and spatial proximity relative to DNA damage repair processes ($e^{-\beta \bar{D}^2}$). Equation (8.2) is derived assuming mono-exponential repair kinetics with μ as the repair rate constant. Complete faithful repair of lethal lesions occurs when $G = 0$. When $0 < G < 1$ an increase in cell killing due to double strand break misrepair during protracted radiation occurs. When $G = 1$, radiation is delivered in a single acute dose.

The biologically effective dose (BED) is a concept used to calculate the different absorbed doses required to produce the same probability of a specified biological end point when the absorbed doses are delivered with different fractionation schemes or absorbed dose rates. Using Eqs (8.1) and (8.2) and following the derivations by Barendsen, Fowler and Dale [8.12–8.14], the following BED expression may be obtained when integrating to infinity:

$$BED = D\left(1 + \frac{G(\infty)D}{\alpha/\beta}\right) \tag{8.3}$$

Assuming an exponentially decreasing time dependent dose rate with rate constant λ, such as the one encountered for ^{90}Y microsphere therapies:

$$\dot{D}(t) = \dot{D}_0 e^{-\lambda t} \tag{8.4}$$

and solving Eq. (8.2), then the expression for the BED is obtained [8.15]:

$$BED = D\left(1 + \frac{D}{\alpha/\beta} \cdot \frac{\lambda}{\lambda + \mu}\right) \tag{8.5}$$

The sublethal damage repair process sets in with the repair constant μ and proceeds during the actual delivery of the absorbed dose by RPT. Absorbed doses expressed in terms of BED make it easier to account for the biological effects of different dose delivery time patterns (i.e. dose rates). Accounting for differences in dose rate is particularly important in RPT [8.16, 8.17], especially when comparing absorbed doses from low versus high molecular weight radiopharmaceuticals [8.18], long versus short lived radiopharmaceuticals [8.19–8.21] or in devising fractionation schemes for radiopharmaceutical therapy [8.22].

BED formulations that allow for more general dose rate profiles than that represented by Eq. (8.4) have been published [8.20, 8.23]. The general convolution method can be used to allow more complex sublethal damage repair and dose rate over time processes [8.24].

As is evident from Eq. (8.5), the difference between BED and the absorbed dose depends on the absorbed dose, the pharmacokinetics and the repair half time. For example, for renal dosimetry in ^{177}Lu peptide receptor radionuclide therapy the difference between BED and the absorbed dose has been found to be only approximately +10% [8.25, 8.26], while in ^{90}Y microsphere therapies the difference is considerably higher [8.27].

The International Commission on Radiological Units and Measurements (ICRU) has published an initial report on a comprehensive framework for bioeffect modelling and equieffective dose (EQD) concepts in radiation oncology. This document recommends a general formulation that relates different dose delivery schedules to a reference dose delivery schedule [8.28]. Accordingly, the equieffective dose was adopted as the recommended quantity with the unit Gy. To relate this quantity to clinical practice in EBRT wherein the total absorbed dose, D, is often delivered over time in 2 Gy fractions, while retaining the flexibility to accommodate other fractionation schedules, the ICRU has recommended that nomenclature and symbol for equieffective dose include reference to the dose fraction and also the α/β ratio. With these considerations in mind, the recommended quantity is EQD$X_{\alpha/\beta}$, where X represents the absorbed dose per fraction. When $X = 0$ this is equivalent to BED as defined in Eqs (8.3) and (8.5) (for the case of dose rate decreasing exponentially) for RPT. For fractionated uniform external beam radiation, $BED = nd\left(1 + \frac{d}{\alpha/\beta}\right)$, with d the dose per fraction

(commonly d = 2 Gy) and the total number of fractions. For a single cycle in RPT (n = 1, $d = D$) then following Eq. (8.5):

$$EQD2_{\alpha/\beta} = \frac{D\left(\alpha/\beta + D\dfrac{\lambda}{\lambda+\mu}\right)}{\left(\alpha/\beta + 2\right)} \tag{8.6}$$

Equations (8.5) and (8.6) account for differences in dose rate assuming that the dose rate across the selected tissue volume is uniform. If, for example, different portions of an organ clear faster than other regions then BED over the whole volume will not reflect the biological impact of differences in dose rate. A voxel or sub-region formulation of Eq. (8.5) may be obtained by indexing the dose in each parameter according to its variation on a voxel or sub-region basis.

Depending upon the radiopharmaceutical molecular weight and tissue penetration properties and particle emission range in tissue and the tumour size and its vascular characteristics and binding affinity, the spatial absorbed dose distribution within a tumour is likely to be non-uniform. In such a situation, the average absorbed dose to a tumour volume is unlikely to reflect tumour response. For example, if half the tumour receives an absorbed dose of 100 Gy, but the other half receives a very low (close to zero) absorbed dose, then the average over the volume is approximately 50 Gy but the tumour portion receiving zero or very low absorbed dose will lead to a failure in tumour control even though the average absorbed dose is high. The equivalent uniform dose (EUD) provides a single value that is weighted in a way that accounts for the tumour control probability given the spatial distribution of absorbed dose within the tumour volume. EUD is defined as the spatial distribution of absorbed doses (or BED values) which, if delivered uniformly to the tumour, would yield a surviving fraction equal to that obtained from the actual distribution. Following the derivations by Hobbs, Niemierko and O'Donoghue [8.23, 8.29, 8.30], the equation for EUD is:

$$EUD = -\frac{1}{\alpha} ln\left(\frac{\sum_{i=1}^{N} \mathrm{e}^{-\alpha BED_i}}{N}\right) \tag{8.7}$$

Equation (8.7) provides the EUD for a single tumour with a given distribution of N values of BED_i; each BED_i could correspond to one of N sub-regions of a tumour or to voxelized BED (or absorbed dose values). Since the formalism assumes that all cells receiving a particular BED value are clonogenic with a radiosensitivity given by the parameter α, the EUD concept does not

apply to normal organs and large heterogeneous tumours [8.31]. Sub-voxel size heterogeneity is also not well described in this concept.

The radiation sensitivity parameter α is not always well known and a more pragmatic way of defining the generalized uniform BED dose which is applicable for both tumour and normal organ dosimetry is:

$$gEUD = \left(\frac{\sum_{i=1}^{N} BED_i^a}{N} \right)^{1/a} \tag{8.8}$$

where a indicates an empirically determined parameter for the tissue's sensitivity in response to non-uniform doses. For large values of the parameter a, the highest values of BED_i are those contributing the most to gEUD. In contrast, low values of a lead only to effects on gEUD when a critical volume has been exceeded [8.32]. The type of response depends on the damage end point and the functional architecture of the organ. For organs with serially organized functional sub-units, an absorbed dose exceeding the threshold in only a small part of the organ will lead to complications, corresponding to a situation with a large value of a. Examples of serial organs are spinal cord and rectum. Parallel organized functional sub-units within an organ lead to sub-volumes that can contribute relatively independently to the total organ's functionality, corresponding to small values of a. When a = 1, gEUD corresponds to the mean BED. Examples of parallel organs are lungs, liver and kidneys, although the nephrons themselves are in part serially organized [8.33].

The dose-response relation for radiation events in both normal and tumour tissue is usually described by Poisson statistics. For example, after an absorbed dose, D (or EUD in the case of non-uniform dose distribution), the tumour control probability (TCP) for a tumour consisting of an initial number N_0 of clonogenic cells with radiation sensitivity α is given by:

$$TCP = \exp\left(-N_0 SF\right) = \exp\left(-N_0 \exp\left(-\alpha D\right)\right) \tag{8.9}$$

To attain a successful therapy an absorbed dose or EUD is needed that is able to kill enough clonogenic cells to reach high TCP. In fast growing tumours the TCP has to be adjusted to incorporate tumour volume growth over time with doubling time T_{doubling}:

$$TCP = \exp\left(-N_0 \left[\exp(-\alpha D) + \ln 2 \frac{t}{T_{\text{doubling}}} \right] \right) \tag{8.10}$$

Below a critical absorbed dose rate, the proliferation of the remaining tumour cells will outpace the radiation induced cell kill.

The incidence of toxicity in normal organs is described by the normal tissue complication probability (NTCP) curves, which have been derived for various organs and toxicity end points. The most commonly used NTCP model is the Lyman–Kutcher–Berman model [8.34, 8.35]:

$$NTCP(D, D_{50}, m) = \frac{1}{\sqrt{2\pi}} \int_{-\infty}^{t} \exp\left(-\frac{u^2}{2} \right) \mathrm{d}u, \text{with } t = \frac{D - D_{50}}{m D_{50}} \tag{8.11}$$

where D_{50} is the absorbed dose corresponding to a 50% probability of the complication end point and m is a tissue and end point specific model parameter. The exact values for radiobiology parameters in various organs and tumours are not well known for most RPT situations. Table 8.1. provides ranges and recommended values based on literature reviews in QUANTEC [8.8].

TABLE 8.1. SUMMARY OF RADIOBIOLOGY PARAMETER VALUES RELATED TO DOSE RATE EFFECTS [8.8]

Organ	Toxicity end point	Mean AD or dose/volume parameters	α/β (Gy)	Repair half-life (h)
Kidneys	Late occurring nephritis	D_5: 15–18 Gy D_{50}: 28 Gy V_{23} <30%	2.6	2.8 [8.36] (1.3–5.0) [a]
Liver	Classic RILD	D_5: 30 Gy D_{50}: 42 Gy	(2.5–12.5)	2.5 [8.37]
Salivary (parotid) glands	Salivary function reduced to <25%	D_{20}: 25 Gy D_{50}: 39 Gy	Late effects: 0.8 (0.6–2.5) Early effects: 20	0.3–4
Bladder	Grade ≥3 late RTOG	D_{max} <65 Gy V_{65} <50% V_{80} <15%	(5–10)	

TABLE 8.1. SUMMARY OF RADIOBIOLOGY PARAMETER VALUES RELATED TO DOSE RATE EFFECTS [8.8] (cont.)

Organ	Toxicity end point	Mean AD or dose/volume parameters	α/β (Gy)	Repair half-life (h)
Lung	Symptomatic pneumonitis	D_5: 7 Gy D_{40}: 27 Gy V_{20} <30%	4.0 (2.2–5.8)	0.4 + 4.0 [b]
Bone marrow	Platelet reduction	2 Gy [8.38]	10	0.3

Notes: D_x signifies the absorbed dose that leads to an x% risk of the toxicity end point. V_y is the percentage of the organ volume that when irradiated to y Gy leads to a specified risk of inducing the toxicity end point [8.8]. AD: absorbed dose; RILD: radiation induced liver disease; RTOG: Radiation Oncology Therapy Group.

[a] Indicates values from laboratory animals [8.39].

[b] Two components of repair with different half-times.

The quantities, BED and EUD, account for differences in the dose rate and dose uniformity, respectively. The pattern of energy deposition in tissue also impacts the biological outcome for a given absorbed dose. In RPT, alpha particle and Auger electron emitters are two examples of radiation types that deliver a substantially higher energy deposition density than photon and beta particle emitters. These high LET emissions are associated with enhanced biological effects. The quantity, relative biological effectiveness (RBE), has been used to account for the increased biological effect of high LET emissions. The RBE is defined as:

$$RBE(X) = \left.\frac{D_{\text{ref}}}{D_{\text{test}}}\right|_X \tag{8.12}$$

As shown in Eq. (8.12), RBE depends on the biological end point, X, and the reference and test radiations selected. To obtain a reliable RBE value, the dosimetry approach used must accurately provide the absorbed dose to the tissue subregion or cell population which determines the chosen biological end point. Typically, photons originating from an external beam source are the low LET reference radiation. Published reports of RBE values, however, have used a variety of different reference radiations and absorbed dose calculation methods (summarized in the medical internal radiation dose (MIRD) alpha emitter

dosimetry monograph [8.40]), which have resulted in a very wide range of RBE values for different alpha emitting agents and tissue types.

8.3. DISCUSSION

In radiation protection the effective dose, *E*, has been defined as the quantity most pertinent to understanding the biological consequences (i.e. risk of radiation induced detriment) of a low (i.e. diagnostic) radiation exposure. This quantity is calculated using an implicit model that is defined by the anatomical dimensions and characteristics of a reference individual, along with radiation and tissue weighting factors. The quantity and associated (internationally agreed upon) model and parameter values have made it possible to compare different radiopharmaceuticals and diagnostic imaging procedures. Regulatory bodies have also used this framework to define radiation exposure thresholds applicable to diagnostic imaging.

In this chapter, we summarize radiobiological models applicable to RPT. The models described are based on the well established LQ formalism. We have identified previously developed extensions of the LQ model that account for differences in dose rate, spatial distribution and radiation type. These differences in RPT absorbed dose delivery are widely recognized to have the greatest impact on efficacy and toxicity. The models that are described do not necessarily represent the latest advances in radiobiological modelling but are widely accepted and considered appropriate in providing guidance on how to transform absorbed dose, dose rate and spatial distribution information so as to compare different agents and treatment regimens in terms of their potential toxicity and efficacy.

REFERENCES

[8.1] INTERNATIONAL COMMISSION ON RADIOLOGICAL PROTECTION, 1990 Recommendations of the ICRP, ICRP Publication 60, Ann. ICRP 21 1–3, Pergamon, Oxford (1991), https://doi.org/10.1016/0146-6453(91)90066-P

[8.2] INTERNATIONAL COMMISSION ON RADIOLOGICAL PROTECTION, The 2007 Recommendations of the International Commission on Radiological Protection, ICRP Publication 103, Ann. ICRP 37 2–4 (2007).

[8.3] NATIONAL RESEARCH COUNCIL, Health risks from exposure to low levels of ionizing radiation: BEIR VII Phase 2, The National Academies Press, Washington, DC (2005).

[8.4] BOLCH, W.E., ECKERMAN, K.F., SGOUROS, G., THOMAS, S.R., MIRD Pamphlet No. 21: A generalized schema for radiopharmaceutical dosimetry — standardization of nomenclature, J. Nucl. Med. **50** 3 (2009) 477–484, https://doi.org/10.2967/jnumed.108.056036

[8.5] SGOUROS, G., GOLDENBERG, D.M., Radiopharmaceutical therapy in the era of precision medicine, Eur. J. Cancer **50** 13 (2014) 2360–2363, https://doi.org/10.1016/j.ejca.2014.04.025

[8.6] INTERNATIONAL COMMISSION ON RADIOLOGICAL PROTECTION, Report of the Task Group on Reference Man, ICRP23, Pergamon, Oxford (1975).

[8.7] INTERNATIONAL COMMISSION ON RADIOLOGICAL PROTECTION, Basic anatomical and physiological data for use in radiological protection: Reference values, ICRP Publication 89, Ann. ICRP **32** 3–4 (2002) 5–265, https://doi.org/10.1016/S0146-6453(03)00002-2

[8.8] BENTZEN, S.M., et al., Quantitative analyses of normal tissue effects in the clinic (QUANTEC): An introduction to the scientific issues, Int. J. Radiat. Oncol. Biol. Phys. **76** 3 Suppl. (2010) S3–S9, https://doi.org/10.1016/j.ijrobp.2009.09.040

[8.9] DEASY, J.O., et al., Improving normal tissue complication probability models: The need to adopt a "data-pooling" culture, Int. J. Radiat. Oncol. Biol. Phys. **76** 3 Suppl. (2010) S151–154, https://doi.org/10.1016/j.ijrobp.2009.06.094

[8.10] BRENNER, D.J., HLATKY, L.R., HAHNFELDT, P.J., HUANG, Y., SACHS, R.K., The linear-quadratic model and most other common radiobiological models result in similar predictions of time-dose relationships, Radiat. Res. **150** 1 (1998) 83–91, https://doi.org/10.2307/3579648

[8.11] BROWN, J.M., CARLSON, D.J., BRENNER, D.J., The tumor radiobiology of SRS and SBRT: Are more than the 5 Rs involved? Int. J. Radiat. Oncol. Biol. Phys. **88** 2 (2014) 254–262, https://doi.org/10.1016/j.ijrobp.2013.07.022

[8.12] BARENDSEN, G.W., Dose fractionation, dose rate and iso-effect relationships for normal tissue responses, Int. J. Radiat. Oncol. Biol. Phys. **8** 11 (1982) 1981–1997, https://doi.org/10.1016/0360-3016(82)90459-X

[8.13] FOWLER, J.F., Radiobiological aspects of low dose rates in radioimmunotherapy, Int. J. Radiat. Oncol. Biol. Phys. **18** 5 (1990) 1261–1269, https://doi.org/10.1016/0360-3016(90)90467-X

[8.14] DALE, R.G., Dose-rate effects in targeted radiotherapy, Phys. Med. Biol. **41** 10 (1996) 1871–1884, https://doi.org/10.1088/0031-9155/41/10/001

[8.15] DALE, R.G., The application of the linear-quadratic dose-effect equation to fractionated and protracted radiotherapy, Br. J. Radiol. **58** 690 (1985) 515–528, https://doi.org/10.1259/0007-1285-58-690-515

[8.16] O'DONOGHUE, J., Relevance of external beam dose-response relationships to kidney toxicity associated with radionuclide therapy, Cancer Biother. Radiopharm. **19** 3 (2004) 378–387, https://doi.org/10.1089/1084978041425025

[8.17] WHELDON, T.E., O'DONOGHUE, J.A., The radiobiology of targeted radiotherapy, Int. J. Radiat. Biol. **58** 1 (1990) 1–21, https://doi.org/10.1080/09553009014551401

[8.18] SGOUROS, G., Introduction to kidney dose-response for radionuclide therapy, Cancer Biother. Radiopharm. **19** 3 (2004) 357–358, https://doi.org/10.1089/1084978041425061

[8.19] RAO, D.V., HOWELL, R.W., Time-dose-fractionation in radioimmunotherapy: Implications for selecting radionuclides, J. Nucl. Med. **34** 10 (1993) 1801–1810.

[8.20] HOWELL, R.W., GODDU, S.M., RAO, D.V., Application of the linear-quadratic model to radioimmunotherapy: Further support for the advantage of longer-lived radionuclides, J. Nucl. Med. **35** 11 (1994) 1861–1869.

[8.21] HOWELL, R.W., GODDU, S.M., RAO, D.V., Proliferation and the advantage of longer-lived radionuclides in radioimmunotherapy, Med. Phys. **25** 1 (1998) 37–42, https://doi.org/10.1118/1.598171

[8.22] BAECHLER, S., et al., Three-dimensional radiobiological dosimetry of kidneys for treatment planning in peptide receptor radionuclide therapy, Med. Phys. **39** 10 (2012) 6118–6128, https://doi.org/10.1118/1.4752213

[8.23] HOBBS, R.F., SGOUROS, G., Calculation of the biological effective dose for piecewise defined dose-rate fits, Med. Phys. **36** 3 (2009) 904–907, https://doi.org/10.1118/1.3070587

[8.24] GUSTAFSSON, J., NILSSON, P., SJÖGREEN-GLEISNER, K.S., On the biologically effective dose (BED) — using convolution for calculating the effects of repair: I. Analytical considerations, Phys. Med. Biol. **58** 5 (2013) 1507–1527, https://doi.org/10.1088/0031-9155/58/5/1507

[8.25] SUNDLÖV, A., et al., Individualised ^{177}Lu-DOTATATE treatment of neuroendocrine tumours based on kidney dosimetry, Eur. J. Nucl. Med. Mol. Imaging **44** 9 (2017) 1480–1489, https://doi.org/10.1007/s00259-017-3678-4

[8.26] SANDSTROM, M., et al., Kidney dosimetry during ^{177}Lu-DOTATATE therapy in patients with neuroendocrine tumors: Aspects on calculation and tolerance, Acta Oncol. **57** 4 (2018) 516–521, https://doi.org/10.1080/0284186X.2017.1378431

[8.27] DEWARAJA, Y.K., et al., Prediction of tumor control in ^{90}Y radioembolization by logit models with PET/CT-based dose metrics, J. Nucl. Med. **61** 1 (2020) 104–111, https://doi.org/10.2967/jnumed.119.226472

[8.28] BENTZEN, S.M., et al., Bioeffect modeling and equieffective dose concepts in radiation oncology — terminology, quantities and units, Radiother. Oncol. **105** 2 (2012) 266–268, https://doi.org/10.1016/j.radonc.2012.10.006

[8.29] NIEMIERKO, A., Reporting and analyzing dose distributions: A concept of equivalent uniform dose, Med. Phys. **24** 1 (1997) 103–110, https://doi.org/10.1118/1.598063

[8.30] O'DONOGHUE, J.A., Implications of nonuniform tumor doses for radioimmunotherapy, J. Nucl. Med. **40** 8 (1999) 1337–1341.

[8.31] JONES, L.C., HOBAN, P.W., Treatment plan comparison using equivalent uniform biologically effective dose (EUBED), Phys. Med. Biol. **45** 1 (2000) 159–170, https://doi.org/10.1088/0031-9155/45/1/311

[8.32] MARKS, L.B., et al., Radiation dose–volume effects in the lung, Int. J. Radiat. Oncol. Biol. Phys. **76** 3 Suppl. (2010) S70–S76.

[8.33] KÄLLMAN, P., ÅGREN, A., BRAHME, A., Tumour and normal tissue responses to fractionated non-uniform dose delivery, Int. J. Radiat. Biol. **62** 2 (1992) 249–262, https://doi.org/10.1080/09553009214552071

[8.34] LYMAN, J.T., Complication probability as assessed from dose-volume histograms, Radiat. Res. Suppl. **8** (1985) S13–19, https://doi.org/10.2307/3583506

[8.35] KUTCHER, G.J., BURMAN, C., Calculation of complication probability factors for non-uniform normal tissue irradiation: The effective volume method, Int. J. Radiat. Oncol. Biol. Phys. **16** 6 (1989) 1623–1630, https://doi.org/10.1016/0360-3016(89)90972-3

[8.36] THAMES, H.D., ANG, K.K., STEWART, F.A., VAN DER SCHUEREN, E., Does incomplete repair explain the apparent failure of the basic LQ model to predict spinal cord and kidney responses to low doses per fraction? Int. J. Radiat. Biol. **54** 1 (1988) 13–19, https://doi.org/10.1080/09553008814551461

[8.37] STRIGARI, L., et al., Dosimetry in nuclear medicine therapy: Radiobiology application and results, Q. J. Nucl. Med. Mol. Imaging **55** 2 (2011) 205–221.

[8.38] O'DONOGHUE, J.A., et al., Hematologic toxicity in radioimmunotherapy: Dose-response relationships for I-131 labeled antibody therapy, Cancer Biother. Radiopharm. **17** 4 (2002) 435–443, https://doi.org/10.1089/108497802760363222

[8.39] JOINER, M.C., VAN DER KOGEL, A.J. (Eds), Basic Clinical Radiobiology, CRC Press, Boca Raton, FL (2018), https://doi.org/10.1201/9780429490606

[8.40] SGOUROS, G. (Ed.), MIRD Monograph: Radiobiology and Dosimetry for Radiopharmaceutical Therapy with Alpha-Particle Emitters, SNMMI, Reston, VA (2015).

Chapter 9

UNCERTAINTY ANALYSIS

K. SJÖGREEN-GLEISNER, Y. DEWARAJA, J. GEAR, M. COX

9.1. INTRODUCTION

In order to estimate the risks or probabilities of radiobiological effects that are associated with a delivered absorbed dose, it is important to understand the reliability of the calculated absorbed dose value (i.e. to quantify the uncertainty associated with the absorbed dose estimate). Knowledge of this uncertainty is also essential for communication, both in the clinical context for the medical practitioner who makes decisions about patient treatment, and in the scientific context to be able to compare dosimetry results from different centres.

Uncertainty in measurement is closely related to metrological traceability, which, according to the International Vocabulary of Metrology (VIM), is defined as [9.1, 9.2]: "property of a measurement result whereby the result can be related to a reference through a documented unbroken chain of calibrations, each contributing to the measurement uncertainty".

There are yet few studies focusing on uncertainty analysis in radiopharmaceutical therapy (RPT) dosimetry, although the emphasis and interest have increased during recent years. Uncertainties deriving from the calibration of single photon emission computed tomography (SPECT) systems for image based dosimetry were addressed in a number of studies studies [9.3–9.7]. He et al. used Monte Carlo simulation studies to investigate the impact of the uncertainty associated with the definition of the volume of interest (VOI) [9.8] and with image based estimates of the residence time for a population of anthropomorphic computer phantoms [9.9]. Flux et al. focused on the propagation of random errors in whole body dosimetry using an analytic approach [9.10]. Gustafsson et al. used a Monte Carlo approach to propagate the uncertainty in image based renal absorbed dose estimates through the entire dosimetry chain [9.11]. In 2018, the European Association of Nuclear Medicine (EANM) guidance on RPT uncertainty analysis, including propagation through the dosimetry chain, was published [9.12].

The aim of this chapter is to give an overview of the methods available for uncertainty propagation through the dosimetry chain and to outline the sources of uncertainty that could be addressed for dosimetry methods used in different kinds

of RPT. This overview uses internationally recognized principles and procedures for uncertainty evaluation given in the Guide to the Expression of Uncertainty in Measurement (GUM) [9.13, 9.14]. The GUM and its related documents are endorsed by the Joint Committee for Guides in Metrology (JCGM) and its member organizations Bureau International des Poids et Mesures (BIPM), IEC, IFCC, ILAC, ISO, IUPAC, IUPAP and OIML. The mathematics of uncertainty propagation is not addressed in detail in this chapter; the reader is instead referred to Refs [9.12, 9.13].

9.2. TERMINOLOGY

According to the VIM, **measurement** is the process by which a quantity is determined experimentally. The quantity that we intend to measure is called the **measurand** and, in principle, the aim of any measurement is to determine the true value of the measurand. In RPT, the measurand may, for instance, be the absorbed dose delivered to an organ or tumour. The VIM also defines a **measurement procedure**, which, in addition to providing a detailed description of a measurement, also includes any calculation needed to obtain a measurement result. Dosimetry in RPT is thus best classified as a measurement procedure, since it involves a whole chain of events, from measurements of the administered activity, measurements performed on patients, via calculations to an estimate of the absorbed dose in an organ or tissue (the measurand).

Generally, a determination of the absorbed dose is not perfect, being subject to several sources of **error**. The error generally comprises random (imprecision) and systematic (bias) components, where random errors are those that arise due to unpredictable or stochastic variations. Systematic errors should as far as possible be corrected for, but in any case, contribute to the overall error. Even if efforts are made to minimize the magnitude of these errors by optimization of the measurement and calculation procedures, the result will just be an **estimate** of the true value of the measurand, and the true value will still be unknown. The **error** is the difference between the measured value and the true value. As for the true value, the error is an idealized concept and its value is in practice unknown. Uncertainty analysis aims to define an interval around the measured value within which the true value of the measurand lies with some probability. The uncertainty can be accompanied by a so-called **coverage factor** k, which then reflects the chosen level of probability with which the coverage interval covers the true value. When the coverage factor is unity, the half width of this interval is known as the **standard uncertainty**, akin to standard deviations in classical statistics [9.13]. The choice $k = 2$ delivers a coverage probability of 95% when the underlying probability distribution is normal. Figure 9.1 illustrates some of these concepts.

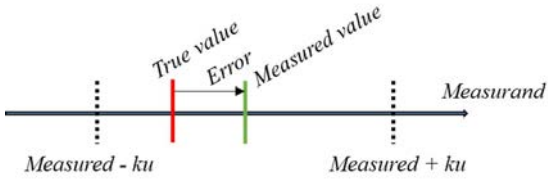

FIG. 9.1. The relationship between the measured value (i.e. the estimate of the measurand) and the true value. The coverage interval is defined by the measured value ± ku and indicates the interval in which the true value is enclosed according to a stipulated probability. Courtesy of K. Sjögreen-Gleisner.

9.3. PROPAGATION OF UNCERTAINTY

Uncertainty propagation is described in detail in the GUM and its supplements and is briefly outlined below.

For an output quantity, $y = f(x_1, x_2, \ldots, x_n)$, which thus depends on a number of input quantities, $(x_1, x_2, \ldots, x_n)$, the combined standard uncertainty in y depends on the standard uncertainties in each of $(x_1, x_2, \ldots, x_n)$. For instance, when the absorbed dose is the output quantity, y, its uncertainty depends on uncertainties in the time-integrated activity (corresponding to x_1), the S value (x_2), and the mass of the tissue in which the radiation energy is absorbed (corresponding to x_3); see Chapter 2, Section 2.5. The main GUM mechanism for propagating uncertainties is known as the law of propagation of uncertainty (LPU). In its simplest form the LPU is expressed according to:

$$u_c^2(y) = \sum_{i=1}^{n} \left(\frac{\partial f}{\partial x_i} \right)^2 u^2(x_i) \tag{9.1}$$

where $u_c(y)$ is the resulting combined standard uncertainty in y, and $u(x_i)$ is the standard uncertainty in x_i. The partial derivatives $\partial f / \partial x_i$ of the function f with respect to the x_i are called the sensitivity coefficients.

Thus, in the chain of calculations that RPT dosimetry comprises, when knowing the uncertainties in previous links (input quantities), the GUM mechanisms can be used to propagate these uncertainties to the next link in the chain (output quantities), whilst taking account of any further uncertainties introduced in the current link. In order to propagate uncertainties, the measurement function f, which relates the input quantities to one link in the chain to the output quantities from that link, must be established. This model may be mathematical or algorithmic.

Output quantities from a link may be correlated because they depend on the same input quantities. In this case the correlations must be considered, and the following form of the LPU that includes provision for correlations [9.13] should be used:

$$u_c^2(y) = \sum_{i=1}^{n}\sum_{j=1}^{n}\frac{\partial f}{\partial x_i}\frac{\partial f}{\partial x_j}u(x_i,x_j) \equiv \sum_{i=1}^{n}\left(\frac{\partial f}{\partial x_i}\right)^2 u^2(x_i) + 2\sum_{i=1}^{n-1}\sum_{j=i+1}^{n}\frac{\partial f}{\partial x_i}\frac{\partial f}{\partial x_j}u(x_i,x_j) \quad (9.2)$$

The functions encountered in activity quantification and conversion of activity to an absorbed dose typically have a multiplicative form. In this case it is convenient to use the relative standard uncertainty instead of the absolute standard uncertainty. For the case when *f* is a multiplicative function with respect to two input quantities (x_1, x_2), the uncertainties in x_1 and x_2 will propagate according to:

$$y = x_1x_2 \Rightarrow \left(\frac{u_c(y)}{y}\right)^2 = \left(\frac{u(x_1)}{x_1}\right)^2 + \left(\frac{u(x_2)}{x_2}\right)^2 + 2\frac{u(x_1,x_2)}{x_1x_2} \quad (9.3)$$

Likewise, when *f* is represented by a quotient of the two input quantities (x_1, x_2), the combined uncertainty is given by:

$$y = \frac{x_1}{x_2} \Rightarrow \left(\frac{u_c(y)}{y}\right)^2 = \left(\frac{u(x_1)}{x_1}\right)^2 + \left(\frac{u(x_2)}{x_2}\right)^2 - 2\frac{u(x_1,x_2)}{x_1x_2} \quad (9.4)$$

The right-most term in Eqs (9.3) and (9.4) designates the contribution from the relative covariance or correlation between x_1 and x_2. It is thus zero if x_1 and x_2 are considered to be independent (uncorrelated) measurements and the LPU reverts to its simpler form (Eq. (9.1)). Examples of expressions for the standard uncertainty and relative standard uncertainty for some other common functions are given by Farrance and Frenkel [9.15].

The simplest and first approach is to use the LPU while disregarding any correlation but doing so can lead to optimistically low statements of uncertainty, or overly large estimates if input quantities are negatively correlated or when *f* is a quotient of the two input quantities. The LPU tends to work well when correlation is taken into account, but when the measurement model is non-linear the LPU works less well. In such circumstances, a Monte Carlo method, which propagates probability distributions rather than uncertainties, may be more suitable [9.16].

9.4. SOURCES OF UNCERTAINTY IN RPT DOSIMETRY

The measurement technique used for obtaining dosimetry estimates depends on the kind of RPT. The choice of technique then largely depends on which organs are at risk of deterministic tissue reactions, and on the feasibility of performing imaging. However, irrespective of the measurement technique used, the principal steps and the quantities that need to be estimated remain the same. Figure 9.2 illustrates the quantities that need to be determined in order to estimate the mean absorbed dose from an internally distributed radioactive source and the major factors that may influence the uncertainty in this estimate.

An activity meter with validated dial settings is used to determine the activity of a source (a). The calibration factor (b) for the detector system used for patient measurement is applied to convert the detector output to activity and is determined by measuring a source with well specified activity. The output (usually acquired in counts) is normalized to the acquisition time and the calibration factor is then in unit counts/second/MBq. Patient imaging or detector measurements are then performed at various time points after administration, and the activity in the anatomical regions that exhibit radionuclide uptake (c) is then quantified in this set of images. The steps required to convert the number of detected counts to activity in a source region depend on the detector technique used (see Chapter 4). The obtained time activity data are integrated over time (d) to obtain an estimate of the time-integrated activity (or cumulated activity). Masses of tissues of dosimetry interest are then quantified (e), and lastly, the absorbed dose is calculated (f) by means of one of the methods given in

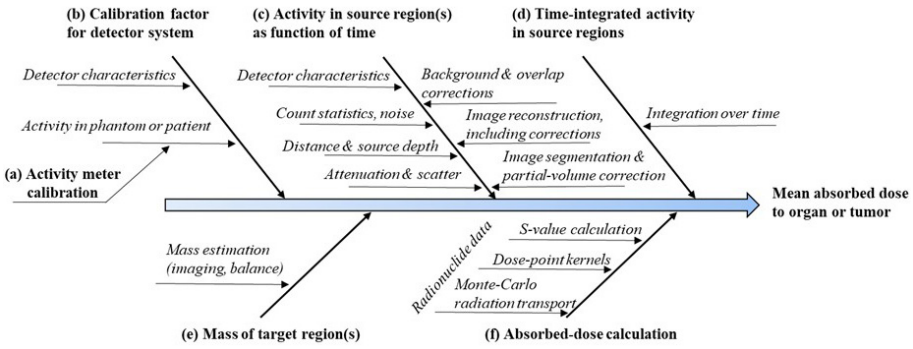

FIG. 9.2. The principal quantities that need to be determined when estimating the mean absorbed dose to the whole body, an organ or a tumour, in bold characters (a)–(f). Italicized text indicates factors that may contribute to the uncertainty in the estimate of the particular quantity, depending on the dosimetry technique used. Courtesy of K. Sjögreen-Gleisner.

Chapter 7. The order of the application of steps (a)–(f) may vary depending on the measurement techniques used and the dosimetry methods available.

We outline below the inherent sources of error in the most commonly used dosimetry techniques and suggest how the associated uncertainty contributions can be estimated. These uncertainties should then be propagated to quantify the uncertainty associated with the estimated absorbed dose using some of the equations indicated above. Some of the steps in Fig. 9.2 are similar for all the measurement techniques discussed, while others are closely related to the particular technique. The common steps are described first (Sections 4.1 and 4.2), followed by examples of dosimetry based on probe detector measurements (Section 4.3) and image based dosimetry (Section 4.4).

9.5. THE ACTIVITY METER

A basic requirement in any kind of dosimetry is the capability to accurately measure the activity of the radionuclide used, both before patient administration and, when applicable, the source used to calibrate the detector system for patient measurements. Measurement of the activity is commonly made by use of an activity meter. Thus, in principle, the activity meter is the instrument that forms the basis for the whole dosimetry chain.

The response of activity meters (i.e. the induced current in the ionization chamber per unit of activity of the source)) depends on a number of factors such as the emissions from the radionuclide, the detector linearity, the container for the active solution (e.g. a vial or a syringe) and the volume of the activity in this container [9.17]. Notably, the dial settings of activity meters provided by the manufacturer for radionuclides used in RPT are often not as well established as for ^{99m}Tc, for example, and thus need to be carefully validated, and sometimes readjusted at the local hospital. For instance, for ^{223}Ra an offset in the dial settings was reported yielding activity errors of 10% [9.18]. For resin ^{90}Y-microspheres activity deviations of 20% were obtained when measured in a particular geometry before patient administrations (polycarbonate V-vial) [9.19].

In order to determine the appropriate dial settings for the activity meter, a radioactive solution of the particular radionuclide, accompanied by a certificate stating the source activity and the traceability of the statement are needed [9.20]. By measurement of such a reference source solution under the same conditions (e.g. container and volume) that will later be used for activity measurements, the dial settings can be adjusted so that the activity meter reading correctly reflects the activity of the reference source. Then, by repeated measurements over time of the same radionuclide and under the same conditions, the standard uncertainty associated with the activity meter reading can be determined. Once

the appropriate dial settings have been established, these uncertainties are, for most radionuclides, small (approximately 1–2%) [9.21].

Quantification of the activity in different organs and tissues relies on the determination of a calibration factor for the patient detector system, which, depending on the dosimetry technique applied, may be determined (i) prior to patient administration by separate calibration measurements, or (ii) after patient administration by knowledge of the total amount of activity that is in the patient, as determined from the activity administered. In either of these methods, the uncertainty in the activity meter reading propagates to an uncertainty in the estimated activity in the patient, and can be propagated using the basic form of the LPU (Eq. (9.1)).

9.6. TIME-INTEGRATED ACTIVITY

Common to most dosimetry techniques is the calculation of the time-integrated activity (or cumulated activity) in the tissue of interest from multi-time point measurements and quantification of the activity. For some dosimetry techniques a different order of calculations than those illustrated in Fig. 9.2 is applied, by first calculating the absorbed dose rate for each time point, and then performing the integration over time. Whichever is the order of the calculation, the integration is a necessary step to move from quantitative temporal data to an estimate of the area under the curve. Approaches for this integration are described in Chapter 6.

The uncertainty in the time-integrated activity is governed by the uncertainty associated with the individual data points, the number of time points measured and how these time points are distributed in relation to the underlying pharmacokinetics for the organs and tissues. In addition, the method used for integration, possibly including curve fitting, may be of importance. For image based dosimetry the practical and logistical workflow often puts a limit on the number of time points that can be acquired, which restricts how well the actual uptake and washout phases of the radiopharmaceutical can be resolved. In this regard, probe detectors (Section 4.2.2) present the advantage that more time points can be acquired (i.e. the time sampling can be made with a higher frequency).

Errors in the measured time activity data may be both random and systematic in nature. Generally, the systematic errors are considered to yield a higher contribution to the uncertainty in time integrated activity, since these errors essentially affect the amplitude of the entire curve. The impact of random errors is intimately connected to the number of data points available. When there are many data points, the contribution from random errors tends to be reduced and the relative uncertainty in time-integrated activity may become considerably smaller

than the relative uncertainty in each data point. Integration can thus be seen as a smoothing operation. Table 9.1 summarizes possible approaches for evaluation of the uncertainty in the time-integrated activity. However, it should be noted that the applicability of these approaches for the particular RPT is intimately tied to the dosimetry method used and the number of data points available.

TABLE 9.1. EVALUATION OF UNCERTAINTY IN THE TIME-INTEGRATED ACTIVITY ($\tilde{A}$)

(courtesy of K. Sjögreen-Gleisner and Y. Dewaraja)

(i)	A first credibility check of the values calculated at the individual centre of the effective half-life, time-integrated activity coefficient and absorbed doses per unit of administered activity, can be made by comparison to data reported in the literature. For the same radiopharmaceutical and a similar cohort of patients, the calculated values are expected to be in the same range.
(ii)	An analytical method for determining the uncertainty in time-integrated activity for methods, including curve-fitting, was presented by Gear et al. [9.12]. In this method the residuals of the time activity data around the fitted curve were used to estimate the random uncertainty in the time-integrated activity from the chi-squared metric. The systematic component of the uncertainty was estimated by the assumption that the relative uncertainty time-integrated activity was equal to the relative uncertainty in the activity data. The random and systematic components were then added in quadrature to obtain an estimate of the combined variance.
(iii)	An alternative approach for curve fitting is to use literature data to construct hypothetical sets of densely sampled time activity curves (TACs) for which corresponding time-integrated activities can be calculated and used as reference ($\tilde{A}_{ref}$). In order to test the ability to reproduce $\tilde{A}_{ref}$, data can be extracted from these curves at the time points that correspond to those used for patient acquisition. From these sparsely sampled data sets, the integration is performed according to the routinely used integration method giving $\tilde{A}_{test}$. The absolute difference between $\tilde{A}_{test}$ and $\tilde{A}_{ref}$ will then give an indication of the uncertainty in the estimated time-integrated activity.
(iv)	A further step can be taken by adding errors to each of the data points in the sparsely sampled time activity data set. Preferably, the magnitude of these errors should be consistent with the uncertainties in the time activity data and include both systematic and random components. When repeating the above procedure (i.e. calculating many instances of $\tilde{A}_{test}$ for different realizations of the random errors), additional evaluations of the uncertainty are obtained. Indeed, when this procedure is repeated a large number of times and errors are drawn from probability distributions valid for the time activity data points; this becomes a Monte Carlo based approach to uncertainty propagation [9.16].

TABLE 9.1. EVALUATION OF UNCERTAINTY IN THE TIME-INTEGRATED ACTIVITY ($\tilde{A}$)

(courtesy of K. Sjögreen-Gleisner and Y. Dewaraja) (cont.)

(v)	Of particular importance are the time intervals within which data are **not** acquired and for which some method for extrapolation needs to be adopted. These intervals correspond to the very beginning of the curve (from administration to the first acquisition) during the radiopharmaceutical uptake phase, and the (infinite) time period beyond the last acquisition time point. Since the time-integrated activity for these time intervals needs to be estimated by extrapolation, there is reason to investigate thoroughly the possible uncertainties introduced. One way is to make extrapolations based on different assumptions. The uncertainty can then be expressed based on reasoning of which curve shapes are considered to be realistic. It is also of importance to investigate the proportion of the total time-integrated activity associated with the extrapolated time interval, and if this proportion is high, the consequential uncertainty in the time-integrated activity may give reason to consider a modification of the acquisition time points.

9.7. DOSIMETRY BASED ON PROBE DETECTOR MEASUREMENTS

9.7.1. Whole body dosimetry

The mean absorbed dose to the total body is often used as a surrogate for the bone marrow absorbed dose in treatments of neuroblastoma using ^{131}I-m-iodobenzylguanidine (mIBG) [9.22, 9.23]. The time-integrated activity in whole body is derived from measurements of the activity using a probe detector placed at some predefined distance from the patient (e.g. 1 m). Commonly, the detector calibration factor ε (i.e. the factor required to convert the detector output to activity) is determined by performing the first measurement close to the time of activity administration, before the patient has voided. The calibration factor is then determined according to:

$$\varepsilon = \frac{C(t_1)}{A_{\text{inj}}} \tag{9.5}$$

where A_{inj} is the administered activity as measured in the activity meter, and $C(t_1)$ is the detected count rate (or other detector output) at a time t_1 close to administration. This calibration factor is thus specific to the patient and the activity at times other than t_1 is determined by dividing the detected count rate by the same calibration factor. It is thus implicitly assumed that the effective source

depth and the attenuation and scatter conditions remain constant from the first measurement to all time points after patient administration. After integration of the time activity curve, the absorbed dose is estimated by multiplication of the time-integrated activity by the *S* value valid for the patient weight. As the weight is usually determined by use of a scale, for which the uncertainty is regarded as negligible in this context, the major part of the uncertainty from this latter part of the calculation is how well the *S* value, obtained from a reference phantom, applies to the individual patient. This uncertainty contribution is related to the particular geometry and Monte Carlo code used for radiation energy transport calculation, as addressed in Chapter 7. Table 9.2 lists the sources of error that can be addressed and suggestions of how to investigate their uncertainty contribution. These sources all relate to the quantification of the total body activity and should be combined with uncertainty contributions in A_{inj} measured in the activity meter (Section 9.5), and in the time-integrated activity (Section 9.6), to obtain an estimate of the combined uncertainty associated with total body absorbed dose.

TABLE 9.2. WHOLE BODY DOSIMETRY BASED ON PROBE DETECTOR MEASUREMENTS: SOURCES OF ERROR IN THE ACTIVITY QUANTIFICATION STEP AND SUGGESTIONS OF HOW TO EVALUATE THEIR CONTRIBUTION TO THE UNCERTAINTY IN THE TOTAL BODY ABSORBED DOSE

(courtesy of K. Sjögreen-Gleisner and Y. Dewaraja)

Source of error	Underlying assumption	Approach to evaluate the standard uncertainty that results from deviations from the assumption
Detector characteristics	The calibration factor for the detector system is exactly characterized (i.e. the detector response is constant over time and possible effects of dead time that differ between the acquisition time points can be taken into consideration).	Examine the constancy in the detector response over time, and possible effects of dead time and pulse pile-up, according to established procedures. Deduce uncertainty associated with the calibration factor from possible variations in these characteristics for the range of count rates that may be measured for patients.

TABLE 9.2. WHOLE BODY DOSIMETRY BASED ON PROBE DETECTOR MEASUREMENTS: SOURCES OF ERROR IN THE ACTIVITY QUANTIFICATION STEP AND SUGGESTIONS OF HOW TO EVALUATE THEIR CONTRIBUTION TO THE UNCERTAINTY IN THE TOTAL BODY ABSORBED DOSE

(courtesy of K. Sjögreen-Gleisner and Y. Dewaraja) (cont.)

Source of error	Underlying assumption	Approach to evaluate the standard uncertainty that results from deviations from the assumption
Counting statistics	The acquisition time is sufficiently long so that influence from noise becomes negligible.	Examine the detector response and the noise characteristics for typical acquisition times and typical ranges of activity in patients, using multiple acquisitions of a phantom under the same conditions. Deduce uncertainty in the detected counts due to noise (standard deviation over the acquisitions), which usually follows Poisson statistics.
Patient–detector distance	The patient–detector distance is perfectly specified for all measurements.	Investigate the count rate sensitivity to the range of distances that may occur in practice, to a first approximation by use of the inverse square law.
Source depth	The source depth is exactly the same for all time points.	These contributions are difficult to assess simply since the radiopharmaceutical redistributes from circulating plasma (i.e. the whole body) to a few uptake regions. However, as a starting point, the range of source depths that can be encountered in patients can be estimated. The uncertainty in count rate due to variable source depths between time points can be investigated by use of the inverse square law. The uncertainty contribution from variable attenuation and scatter conditions can be evaluated (e.g. by means of experimental measurements of a source placed below different thicknesses of Perspex).
Photon attenuation and scatter	The attenuation and scatter conditions are exactly the same for all time points and are not affected by the redistribution of activity in the body.	
Contamination in the room	There is no contamination in the room where the measurement takes place, for any of the measurements.	Estimate the possibility that contamination may occur for some of the measurement time points, based on previous experience from room monitoring.

9.7.2. Thyroid dosimetry

The absorbed dose to the thyroid is performed for ^{131}I NaI treatment of benign thyroid disease [9.24]. In some countries dosimetry is performed prospectively and is used as the basis for calculating the activity to administer the subsequent therapy [9.25]. The time-integrated activity in the thyroid is derived from measurements of the activity using a spectrometric probe detector placed at some predefined distance from the patient's neck. The detector calibration factor, ε, is determined from acquisition of a small bottle containing a solution of ^{131}I placed in a phantom designed to mimic a patient's neck. The calibration factor is then determined as the ratio of the detected count rate and the known ^{131}I activity in the bottle. Patient acquisitions are performed at a number of time points (typically 1 or 2), using the same detector distance as for the phantom acquisition, and the thyroid activity is determined by dividing the detected count rate by the calibration factor. It is thus implicitly assumed that the thickness, shape and depth of the thyroid are well represented by the phantom geometry. The time-integrated activity is calculated based on the resulting time activity data. The thyroid mass is usually estimated based on either ultrasound imaging, ^{99m}Tc-scintigraphy and/or palpation. The absorbed dose is calculated from these estimated quantities following expressions given in Ref. [9.24].

In Table 9.3, sources of error that have an impact on the estimated thyroid absorbed dose are listed. Again, these should be combined with uncertainty contributions from the ^{131}I activity in the bottle measured in the activity meter (Section 9.5) and in the time-integrated activity (Section 9.6), to obtain an estimate of the combined uncertainty in thyroid absorbed dose.

TABLE 9.3. THYROID DOSIMETRY BASED ON PROBE DETECTOR MEASUREMENTS: SOURCES OF ERROR AND SUGGESTIONS OF HOW TO EVALUATE THEIR UNCERTAINTY CONTRIBUTION TO THE ESTIMATED THYROID ABSORBED DOSE

(courtesy of K. Sjögreen-Gleisner and Y. Dewaraja)

Source of error	Underlying assumption	Approach to evaluate the standard uncertainty that results from deviations from the assumption
Detector characteristics	As in Table 9.2	As in Table 9.2
Counting statistics	As in Table 9.2	As in Table 9.2

TABLE 9.3. THYROID DOSIMETRY BASED ON PROBE DETECTOR MEASUREMENTS: SOURCES OF ERROR AND SUGGESTIONS OF HOW TO EVALUATE THEIR UNCERTAINTY CONTRIBUTION TO THE ESTIMATED THYROID ABSORBED DOSE

(courtesy of K. Sjögreen-Gleisner and Y. Dewaraja) (cont.)

Source of error	Underlying assumption	Approach to evaluate the standard uncertainty that results from deviations from the assumption
Phantom/ patient–detector distance	The patient–detector distance is identical to the phantom–detector distance.	Investigate the count rate sensitivity to the range of distances that may occur in practice, by use of the inverse square law.
Thyroid depth	The effective depth of the thyroid is identical to the depth of the bottle in the phantom.	The uncertainty in count rate due to the range of thyroid depths encountered in practice can be investigated by use of the inverse square law.
Photon attenuation and scatter	The phantom geometry yields the same attenuation and scatter conditions as the patient geometry, irrespective of the thyroid shape, thickness and depth.	The uncertainty contribution from variable attenuation and scatter conditions can be evaluated by means of experimental measurement of the count rate from a source placed below different thicknesses of Perspex. To a first approximation, the differences in attenuation between the phantom and patient can be estimated from reference data on linear attenuation coefficients.
Thyroid mass	The thyroid mass can be exactly quantified by volumetry.	If imaging is used for volume estimation, the uncertainty can be investigated by imaging different thyroid shaped phantoms and comparing the actual phantom volumes to those estimated using the same procedure as for patients. If this procedure involves operator dependent steps, such as region drawing, then the operator dependency can be investigated by letting several operators perform region drawing on the same set of data.

9.8. IMAGE BASED DOSIMETRY

Analytical expressions needed to propagate the uncertainty from image based serial SPECT/computed tomography (CT)–based estimates of the activity to an uncertainty in absorbed dose were presented in [9.12]. The paragraphs below are intended to complement that uncertainty analysis with two particular examples: dosimetry based on a hybrid planar–SPECT/CT method in peptide receptor radionuclide therapy (PRRT) and SPECT/CT based ^{90}Y-microsphere therapy of lesions in the liver. Common to those applications is the need to evaluate the uncertainty in the activity quantified from tomographic images.

9.8.1. Activity quantification from tomographic images

As described in Chapter 4, the basic equation for estimation of the activity in a source region from tomographic images is given by:

$$A = \frac{1}{RC(v)} \frac{C_{\mathrm{VOI}}}{CF} \tag{9.6}$$

where $RC(v)$ is the volume dependent recovery coefficient, C_{VOI} is the total count rate determined in the VOI delineated around the source region in the reconstructed image and CF is the calibration factor used to convert from count rate to activity (the correspondence to the factor, ε, for probe based detectors above).

In an ideal case, the count rate in each voxel of a reconstructed SPECT or positron emission tomography (PET) image is perfectly linear with the source activity, independent of the amount of activity in the imaged source distribution, its shape and position, and the physical characteristics of the medium in which the source is situated. Likewise, in an ideal imaging system, the positioning of counts is exact in the sense that the counts in each voxel are a true reflection of the activity located at the corresponding position in the patient.

In practice there are a number of physical processes that affect the acquired projection data, which need to be modelled and compensated for in the tomographic reconstruction, in order to obtain a quantitative SPECT or PET image (see Chapter 4). Even when such corrections are applied, these are never perfect as they rely on input in the form of models or experimentally measured data. Consequently, the overall count level and count distribution, and thus C_{VOI} and CF, are affected by imperfect corrections for attenuation, scatter and septal penetration. Other sources of error are related to the count rate during image acquisition that could be low, yielding noise in the reconstructed images, or high, yielding pile-up and dead time effects resulting in a non-linear relationship

between the activity and the detected count rate. Imperfect compensation for the collimator response (so-called resolution recovery) and insufficient or non-uniform convergence of the iterative reconstruction are additional sources of error which together affect the spatial resolution, possibly in a non-uniform manner over the reconstructed SPECT image field of view. In turn, the resolution effects produce so-called spill-in and spill-out of counts with respect to a VOI, which affect both C_{VOI} and $RC(v)$.

9.8.1.1. Calibration factor

The calibration factor *CF* is used to scale the overall level of the voxel values in the reconstructed image into activity. The calibration factor generally is related to the camera system sensitivity and is thus specific for the particular camera system (including the collimator in the case of SPECT). Ideally, the *CF* should be constant across patients, across the SPECT or PET image FOV, and across different objects, including different sizes, shapes, activity levels, background activity concentrations, and the physical characteristics of the object itself and of surrounding tissues. When the uncertainty in the *CF* is low, it provides an accurate estimate of the total activity $A_{tot,pat}$ contained in the imaged part of the patient, determined according to:

$$A_{tot,pat} = \frac{C_{tot,pat}}{CF} \tag{9.7}$$

where $C_{tot,pat}$ is the total count rate in an expanded VOI delineated over all axial slices and along the patient boundary, possibly with a margin so as to also include counts that are spilled out due to spatial resolution effects.

Generally, the calibration factor is determined by imaging a source of known activity in a phantom and taking the ratio of the detected count rate and the activity ($CF = C_{tot,ph}/A_{tot,ph}$). As noted in Chapter 4, a variety of calibration geometries and methods currently exist, and include planar imaging of a point source or a flat uniform source (Petri dish), tomographic imaging of a large object (such as a cylinder phantom) with uniform activity concentration [9.26], or the 'known' activity in the patient liver such as for ^{90}Y microsphere dosimetry. Irrespective of the method used, it is important that partial volume effects are avoided in the determination of the count rate $C_{tot,ph}$. Thus, the VOI applied in the image of the calibration phantom needs to be sufficiently large so as to include all counts caused by the radioactive source. Alternatively, for an extended uniform phantom, several, equally sized, smaller VOIs can be applied to determine the count rate concentration (cps/voxel or cps/mL), followed by normalization to the activity concentration (MBq/voxel or MBq/mL). It is also important that the

calibration measurement is made with a sufficient number of counts so that the uncertainty contribution from noise becomes negligible.

The choice of calibration geometry largely depends on the method at hand for reconstruction of tomographic images for patients. Planar image calibration methods work by the assumption that when the reconstruction is properly normalized by the number of projection angles and time per projection, and includes accurate corrections for attenuation, scatter and septal penetration, then either the projection data (i.e. planar images) or the reconstructed image can be normalized by a *CF* determined in air. Calibration methods based on reconstructed images work by the assumption that possible errors in the above mentioned corrections will cancel when the calibration measurement is performed under similar conditions as the patient image acquisition (i.e. $C_{\text{tot,ph}}$ is determined under equivalent conditions as C_{VOI} in Eq. (9.6)). Thus, both calibration approaches rely on assumptions (accurate corrections for planar based, patient-equivalent conditions for reconstructed image based).

Uncertainty $u(CF)$ in CF arises due to uncertainty in the reading of $A_{\text{tot,ph}}$ from the activity meter (Section 9.5), and in the determination of $C_{\text{tot,ph}}$. For the latter, uncertainty may arise due to variability of the scanner, noise in the detected counts and uncertainty in the delineated ROI (planar calibration methods) or VOI (tomographic imaging methods) used for determination of $C_{\text{tot,ph}}$. To quantify these contributions to $u(CF)$ a number of calibration measurements can be undertaken at the range of count rates observed clinically, including effects of dead time and pile-up on the calibration factor. In addition, the value of CF should not vary for different source geometries or scatter and attenuation conditions. To examine these contributions to $u(CF)$ a range of differently shaped phantoms may be used. The average of all the performed measurements is determined, and the standard deviation is used as an estimate of $u(CF)$ that could occur clinically.

In general, as discussed in Chapter 4, the gamma camera calibration factor of Eqs (9.6) and (9.7) can be determined with high precision because the phantom/source acquisition can be performed over a relatively long period to achieve high counting statistics and the VOIs can be well defined using high quality CT. Furthermore, the variability associated with modern scanners and activity meters is low [9.4].

9.8.1.2. Count rate in a VOI

The factor C_{VOI} in Eq. (9.6) is intended to represent the total count rate caused by activity located in a particular source region, such as an organ or tumour, and uncertainty in activity A will arise from the inability to enclose this count rate perfectly in the delineated VOI. In addition, it is assumed that the **distribution** of counts in the reconstructed image truly reflects the underlying

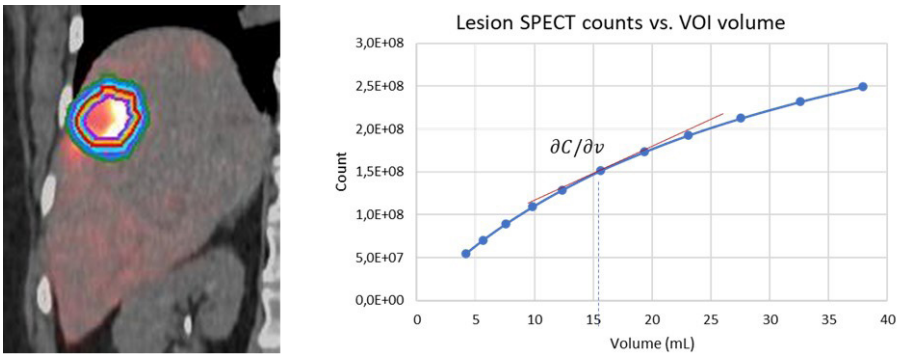

FIG. 9.3. Example showing a graphical approach for determining the effect of VOI delineation on total counts in a VOI. The radiologist-defined contour (15.7 mL) for the liver lesion is indicated by the red outline on the SPECT/CT image. This contour was expanded/reduced in all directions as indicated in the image to generate the curve. Courtesy of Y. Dewaraja.

activity distribution, and that the tomographic reconstruction, including corrections (attenuation, scatter, etc.) and with the chosen number of iterations, manages to position the counts appropriately. Thus, additional contributions to the uncertainty in C_{VOI} arise from imperfect corrections or insufficient convergence during the tomographic reconstruction.

The effects of VOI delineation on C_{VOI} can be determined using the analytical expression given by Gear et al. [9.12]. By this approach the change in total count rate within a VOI is modelled as a function of VOI volume. However, this model assumes that the count rate distribution can be adequately expressed as a uniform spherical distribution convolved with a Gaussian function. An alternative practical approach is to perform a sensitivity analysis for the dataset in question. In this approach the outlined VOI is incrementally modified, increased and decreased in all dimensions (Fig. 9.3).

The C_{VOI} is then computed and plotted as a function of VOI volume, and the slope of the curve at the appropriate volume gives the sensitivity coefficient, which is used alongside the VOI uncertainty to propagate an estimated standard uncertainty $u(C_{VOI})$.

To examine the uncertainty in C_{VOI} from imperfect corrections or insufficient convergence during the tomographic reconstruction, a range of differently shaped objects and phantoms may be used, and reconstruction performed with different numbers of iterations. By determining C_{VOI} for the above examinations the observed standard deviation can be used as an estimate of these contributions to $u(C_{VOI})$.

9.8.1.3. Recovery coefficient

The recovery coefficient (*RC*) is defined as the ratio of the measured to true activity, or measured to true activity concentration in an object and is ideally estimated from measurement of objects that are considered to represent the organ or tissue for which the activity is to be quantified. The value of the recovery coefficient is intimately tied to the strategy used for image segmentation for determination of C_{VOI} in Eq. (9.6); for instance, a strategy may be to segment the image according to the physical object boundary.

Recovery coefficients are generally measured experimentally. For simplicity, spherical inserts with uniform activity concentration are often used and *RC* is parametrized in terms of sphere volume, thus generating a recovery-coefficient curve. When used in Eq. (9.6), the source-region volume v may be determined from a VOI delineated in anatomical images such as CT or magnetic resonance (MR), or from the VOI delineated in the nuclear medicine image used for activity determination. The standard uncertainty $u(RC)$ in *RC* is thus related to the uncertainty in the estimated volume. Other uncertainties arise when the geometry used for determining the recovery-coefficient curve is different from the geometry of the source region to be quantified, including the effects of differing object shape, object-to-background activity concentrations producing spill-out and spill-in of counts and any activity concentration variations within the source region to be quantified. In an ideal case the value of *RC* will exactly specify the ratio of the true and measured activity and will not be affected by any of the sources of error above. In order to examine the related uncertainty in a clinical patient image, imaging of objects that have a different shape and with different image contrasts than those used for determination of the recovery coefficient curve can be made, and the observed standard deviation used as an estimate of the $u(RC)$ that could occur clinically.

9.8.1.4. VOI delineation and volume

The uncertainty in the volume estimated by VOI delineation affects the uncertainties associated with the count rate and the recovery coefficient. The VOI delineation is typically either manual or semi-automatic with some operator dependence. The operator dependence can be estimated by asking several operators to perform the same segmentation. However, such an exercise is impractical for each patient. An alternative is to estimate the volume uncertainty from a multi-operator study previously performed on a similar cohort. The uncertainty in the volume definition can also be estimated by analytical approaches, as described by Gear et al. [9.12].

9.8.1.5. Uncertainty propagation

To a first approximation, the factor *CF* in Eq. (9.6) can be considered to be independent of both C_{VOI} and *RC*. One may object that the definition of *RC* includes the calibration factor *CF*, such that:

$$RC(v) = \frac{C_{obj,ph} / CF}{A_{obj,ph}} \tag{9.8}$$

where $C_{obj,ph}$ is the reconstructed count rate in a VOI delineated along the physical object boundary, and $A_{obj,ph}$ is the contained activity in the object. However, if using a single object located in a cold background, *RC* can alternatively be expressed according to:

$$RC(v) = \frac{C_{obj,ph} / CF}{C_{tot,ph} / CF} = \frac{C_{obj,ph}}{C_{tot,ph}} \tag{9.9}$$

In this geometry the *CF* thus cancels, and *RC* is given by the ratio of the count rate from the object and the total recorded counts in the whole phantom. For convenience, in uncertainty propagation *RC* is thus assumed to be independent of *CF*, and propagation from $u(CF)$ to $u(A)$ can then be made by use of Eq. (9.1). When there are multiple objects in the phantom used for determination of *RC*, or when there is background activity in the phantom, Eq. (9.9) is no longer valid, and covariance between *CF* and *RC* enters the calculation; however, this description is beyond the scope of this chapter. The factors C_{VOI} and *RC* are correlated because they both depend on the VOI volume and thus the VOI delineation. In terms of propagation of the uncertainties $u(C_{VOI})$ and $u(RC)$ to $u(A)$, a covariance term, $u(C_{VOI},RC)$, between C_{VOI} and *RC* needs to be included in addition to the individually propagated uncertainties, following Eq. (9.4) [9.12].

9.8.2. Dosimetry for kidneys and lesions in ^{177}Lu-DOTATATE treatments of neuroendocrine tumours based on hybrid SPECT/CT and planar imaging

The absorbed dose to lesions and normal organs following ^{177}Lu-DOTATATE treatments can be performed using a combination of quantitative SPECT imaging and serial non-quantitative planar imaging [9.27, 9.28]. In this case, a region of interest (ROI) is drawn over the organ of interest in the serial planar images and the ROI count rate is used to derive a time-count rate curve. The SPECT scan provides the quantitative information at a single time point to convert the serial count rate data into activity (see Fig. 6.1). Potential errors in the time activity

curve data can be both random (from the planar data) and systematic (from the SPECT data).

The uncertainty in the count rate data derived from the planar imaging will largely depend on the ability to delineate and replicate the ROI within the organ on each planar image. For a uniform source, the distribution of counts within the pixels of an ROI can be described by a Poisson distribution. Therefore, a standard uncertainty in total ROI counts can be described as $u\left(N_i\right)=\sqrt{N_i}$, where N_i is the total counts within a ROI drawn at the *i*th time point. The standard uncertainty $u(C_i)$ in count rate C_i is therefore:

$$u\left(C_i\right)=\sqrt{N_i}/T_i \tag{9.10}$$

where T_i is the acquisition time interval at the *i*th time point. It follows that the relative uncertainty in count rate due to the counting statistics can be reduced by increasing the acquisition period.

A secondary source of random error can arise due to misplacement of the ROI on subsequent images. The magnitude of this error will depend largely on the heterogeneous distribution of activity in the ROI and can be explored by using multiple ROIs within the organ and recording the standard deviation of total counts across all ROIs (Fig. 9.4).

Counts within ROIs placed on static images can also be influenced by the counts originating from overlying structures, other than that of interest. In principle, if the effective half-lives of the activity within the two organs are similar, the influence of the overlying organ (or background) is negligible (as

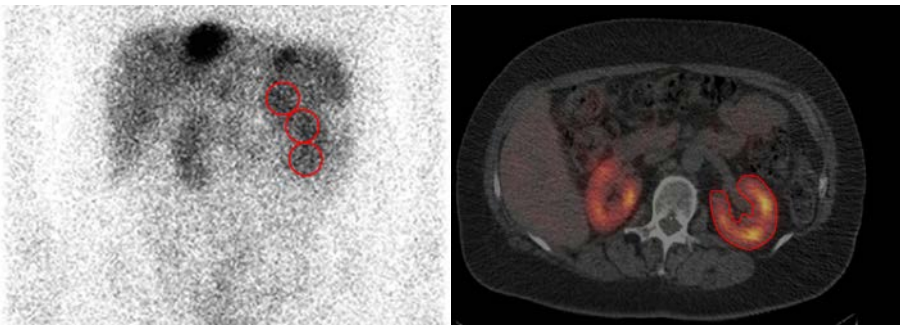

FIG. 9.4. Images acquired during ^{177}Lu-DOTATATE therapy of neuroendocrine tumours. Left: planar image with circles indicating ROIs placed at different positions over the left kidney. Right: reconstructed SPECT/CT image with VOI delineated over the same kidney. Courtesy of K. Sjögreen-Gleisner.

the relative change in count rate remains unaffected). However, if there are large differences and the overlying structure contributes a significant proportion of counts within the ROI, then a background correction should be applied. A secondary ROI adjacent to the organ of interest, with the same size as the object ROI and within the overlying structure should then be used for subtraction. The standard uncertainty $u(C_{\text{corr},i})$ in the background subtracted count rate $C_{\text{corr},i}$ will then be obtained from:

$$u^2\left(C_{\text{corr},i}\right) = C_i + C_{\text{BG},i} \tag{9.11}$$

where $C_{\text{BG},i}$ is the count rate in the background ROI. Equally as above, both organ and background ROI may additionally be sensitive to placement and a similar procedure with multiple ROIs may be necessary.

Conversion of the background corrected count rate $C_{\text{corr},i}$ to activity is performed by scaling by a conversion factor determined using a quantitative SPECT image acquired a short time before or after the static acquisition (Fig. 6.1). In this case, it is often convenient to assume a negligible time difference and hence equivalent activities in the source region at both the time of the SPECT and static time points. The activity A_j can thus be estimated as:

$$A_j = A_i . \frac{C_{\text{corr},j}}{C_{\text{corr},i}} \tag{9.12}$$

where A_j is the activity in the organ of interest measured using the SPECT dataset at the time point i that corresponds to the time of the planar $C_{\text{corr},i}$ and $C_{\text{corr},j}$ is the background corrected count rate from another time point j. If there is significant difference in time between the SPECT and planar image, then a correction for the effective half-life should be made. The relative uncertainty in A_j when $i \neq j$ is expressed as:

$$\left(\frac{u\left(A_j\right)}{A_j}\right)^2 = \left(\frac{u\left(A_i\right)}{A_i}\right)^2 + \left(\frac{u\left(C_{\text{corr},i}\right)}{C_{\text{corr},i}}\right)^2 + \left(\frac{u\left(C_{\text{corr},j}\right)}{C_{\text{corr},j}}\right)^2 \tag{9.13}$$

while when $i = j$ then $u\left(A_j\right) = u\left(A_i\right)$.

As discussed in Section 9.6 and [9.12], the uncertainty in time-integrated activity can be expressed as a combination of random, *r*, and systematic, *s*, effects, following:

$$u^2\left(\tilde{A}\right)=u_r^2\left(\tilde{A}\right)+u_s^2\left(\tilde{A}\right) \tag{9.14}$$

As $u(A_i)$ and $u(C_{\text{corr},i})$ are common to all A_j, they can be considered systematic uncertainties and be added to the final uncertainty in time-integrated activity. Methods for determining the uncertainty in A_{SPECT} are summarized in Section 9.8.1 and discussed in detail in [9.12]. As $u(C_{\text{corr},j})$ will vary at different time points it can be treated as a random effect. Propagation of $u(C_{\text{corr},j})$ into time-integrated activity will require the construction of a covariance matrix used to determine the standard uncertainty in the fitting parameters. For a single exponential function this will take the form:

$$\begin{bmatrix} u^2\left(A_0\right) & u\left(A_0,\lambda\right) \\ u\left(A_0,\lambda\right) & u^2\left(\lambda\right) \end{bmatrix} = \boldsymbol{J}_{\boldsymbol{p}}^{\top}\left[\frac{A_{\text{SPECT}}}{C_{\text{SPECT}}}\right]^2\begin{bmatrix} u^2\left(C_{\text{corr},1}\right) & 0 & 0 \\ 0 & \ddots & 0 \\ 0 & 0 & u^2\left(C_{\text{corr},i}\right) \end{bmatrix}\boldsymbol{J}_{\boldsymbol{p}} \tag{9.15}$$

where $\boldsymbol{J}_{\boldsymbol{p}}$ is the matrix of first-order partial derivatives of the TAC model with respect to the fit parameters, evaluated at each activity measurement:

$$\boldsymbol{J}_{\boldsymbol{p}}=\begin{bmatrix} \frac{\partial A_1}{\partial A_0} & \frac{\partial A_1}{\partial \lambda} \\ \vdots & \vdots \\ \frac{\partial A_n}{\partial A_0} & \frac{\partial A_n}{\partial \lambda} \end{bmatrix}=\begin{bmatrix} \mathrm{e}^{-\lambda t_1} & -A_0 t_1 \mathrm{e}^{-\lambda t_1} \\ \vdots & \vdots \\ \mathrm{e}^{-\lambda t_n} & -A_0 t_n \mathrm{e}^{-\lambda t_n} \end{bmatrix} \tag{9.16}$$

Uncertainty in time-integrated activity is then given by:

$$\left(\frac{u\left(\tilde{A}\right)}{\tilde{A}}\right)^2=\left(\frac{u\left(A_0\right)}{A_0}\right)^2+\left(\frac{u\left(\lambda\right)}{\lambda}\right)^2-2\frac{u\left(A_0,\lambda\right)}{A_0\lambda}+\left(\frac{u\left(C_{\text{SPECT}}\right)}{C_{\text{SPECT}}}\right)^2+\left(\frac{u\left(A_{\text{SPECT}}\right)}{A_{\text{SPECT}}}\right)^2 \tag{9.17}$$

Table 9.4 lists the sources of error that may affect the estimated absorbed doses based on a hybrid planar–SPECT/CT method.

TABLE 9.4. DOSIMETRY FOR KIDNEYS AND LESIONS IN ^{177}Lu-DOTATATE TREATMENTS OF NEUROENDOCRINE TUMOURS BASED ON HYBRID SPECT/CT AND PLANAR IMAGING: SOURCES OF ERROR AND SUGGESTIONS OF HOW TO EVALUATE THEIR UNCERTAINTY CONTRIBUTION TO THE ESTIMATED ORGAN ABSORBED DOSE

(courtesy of K. Sjögreen-Gleisner and Y. Dewaraja)

Source of error	Underlying assumption	Approach to evaluate the standard uncertainty that results from deviations from the assumption
Counts within ROI delineated in planar images	Change in count rate in ROI observed over sequential images is solely due to change in organ activity.	Assume Poisson distribution of counts. Determine sensitivity in ROI placement by drawing multiple ROIs in each organ.
Curve parameters for time-count rate curve	The fitted curve exactly represents the pharmacokinetic pattern of the organ/lesion.	See Section 9.6.
Organ mass	The organ/lesion mass can be exactly quantified by VOI delineation and volumetric measurement on SPECT or CT.	If this procedure involves operator-dependent steps, such as region drawing or segmentation initialization, then the operator dependence can be investigated by letting several operators perform VOI delineation on the same set of data. Carefully designed phantom studies can be used to complement the approach.
Camera characteristics	The calibration factor for the detector system is exactly characterized (i.e. the detector response is constant over time and possible effects that differ between the calibration acquisition and patient scan can be taken into consideration).	Repeat calibration measurements on a regular basis as part of quality control and use their standard deviation as an estimate of calibration uncertainty. See Section 9.8.1.

TABLE 9.4. DOSIMETRY FOR KIDNEYS AND LESIONS IN ^{177}Lu-DOTATATE TREATMENTS OF NEUROENDOCRINE TUMOURS BASED ON HYBRID SPECT/CT AND PLANAR IMAGING: SOURCES OF ERROR AND SUGGESTIONS OF HOW TO EVALUATE THEIR UNCERTAINTY CONTRIBUTION TO THE ESTIMATED ORGAN ABSORBED DOSE

(courtesy of K. Sjögreen-Gleisner and Y. Dewaraja) (cont.)

Source of error	Underlying assumption	Approach to evaluate the standard uncertainty that results from deviations from the assumption
Activity measurement within the VOI	The activity measured within the VOI delineated on the SPECT/CT is a true reflection of the total organ/lesion activity.	Propagate uncertainty using the methodology in [9.12], or estimate organ activities based on different VOI outlines and make a sensitivity analysis of activity to VOI volume. See Section 9.8.1.
Photon attenuation and scatter	The attenuation and scatter estimates built into the reconstruction algorithm are correct for the influence of these effects.	The uncertainty contribution from variable attenuation and scatter conditions can be evaluated by means of experimental measurement of the reconstructed count rate from a source placed within different sized phantoms of water. See Section 9.8.1.
S value	The mass of the organ or lesion is perfectly known and the geometry difference between the model and patient anatomy is negligible.	The relative standard uncertainty in the *S* value is equal to the relative standard uncertainty in the source volume [9.12]. When capabilities exist, *S* values can be calculated for a range of organ phantoms by Monte Carlo methods, to make a sensitivity analysis of *S* value to organ shape/volume.

Assuming that the geometry difference between model and patient anatomy is negligible, the relative standard uncertainty in the *S* value is equal to the relative standard uncertainty in the source volume [9.12]. From Eq. (9.4), the uncertainty in absorbed dose can then be expressed as:

$$\left(\frac{u(\bar{D})}{\bar{D}}\right)^2 = \left(\frac{u(\tilde{A})}{\tilde{A}}\right)^2 + \left(\frac{u(M)}{M}\right)^2 - 2\frac{u(A_{\mathrm{SPECT}}, M)}{A_{\mathrm{SPECT}} M} \tag{9.18}$$

The covariate term $u(A_{SPECT}, M)$ exists as both the S value and activity derived from SPECT are influenced by the volume estimate. Methods for estimating this term are described in [9.12] and Section 9.8.3, below.

9.8.3. Technetiumechnetium-99m-MAA SPECT/CT image based predictive dosimetry in ^{90}Y microsphere radioembolization

Pre-therapy prediction of the absorbed dose to the non-tumoural liver and lesions is of interest for dosimetry guided treatment planning to improve the efficacy and safety of radioembolization. Predictive dosimetry using ^{99m}Tc-macro-aggregated albumin (MAA) imaging is typically performed under the following assumptions:

(1) The microspheres and MAA particles are permanently trapped in the micro-capillaries and do not redistribute.
(2) The ^{90}Y microspheres and ^{99m}Tc-MAA particles have an identical distribution in the body; hence a (patient) relative calibration is used to convert counts to activity (without using camera sensitivity or calibration factor from external measurements).
(3) Dosimetry is performed assuming that a beta particle originating in a source VOI/voxel deposits its full energy in that VOI/voxel (local energy deposition).

The first assumption is reasonable for microspheres and for MAA particles if imaged early before ^{99m}Tc disassociation becomes significant [9.29]. Time-integrated activity is determined with a single imaging time point accounting for physical decay only. Although using one single time point makes dosimetry considerably simpler, the calculated activity and absorbed dose become very sensitive to random effects, such as those induced by misregistration.

The second assumption also simplifies the dosimetry process because it enables the conversion of ^{99m}Tc image based counts in a VOI to ^{90}Y activity using a patient (liver) relative calibration approach. Thus, the activity and corresponding absorbed dose can be estimated without consideration of uncertainties associated with the camera sensitivity measurement. However, with self-calibration the ^{90}Y activity administered to the patient enters the calculation. Thus, the uncertainty associated with the assay of the vial by the activity meter before administration and the measurement of the residual after administration become important. For ^{90}Y, because of the geometry dependence of bremsstrahlung photon generation, careful measurement of activity (and subsequent determination of the associated uncertainties) must be made using recommended settings for the activity meter [9.30, 9.31]. Small variations in the delivery vial geometry and microsphere

volume can potentially make a substantial contribution to the uncertainty when using manufacturer recommended settings of the activity meter. Furthermore, the residual measurement in radioembolization can have large uncertainty because of potential leftover activity in the tubing that cannot be easily measured with an activity meter and is sometimes estimated using a reading from a survey meter.

The third assumption implies that cross-absorbed dose contributions are negligible, which is reasonable for ^{90}Y considering the spatial resolution of the imaging systems and the ^{90}Y beta particle range of this almost pure beta emitter. Hence, the absorbed dose calculated for a VOI or a voxel can be estimated simply based on the activity and mass calculated for the same VOI or voxel, and a scale factor that accounts for physical constants. The physical constants, half-life and mean beta energy per disintegration, have small uncertainties that can be obtained from publications [9.32, 9.33]. For example, in a report by the BIPM [9.32] the ^{90}Y physical half-life is reported as 2.6684 d and the associated relative standard uncertainty as 0.049%.

The uncertainties associated with activity and mass both depend on the uncertainty in VOI definition, which can be substantial. The lesion/liver definition is performed directly on (1) ^{99m}Tc SPECT, (2) diagnostic quality baseline CT or MRI or (3) CT of ^{99m}Tc SPECT/CT (Fig. 9.5).

The non-tumoural liver is typically defined by subtracting lesion VOIs from the liver VOI. While VOI definition on high quality anatomical images potentially reduces the uncertainty in the segmentation process itself, there is uncertainty associated with mis-registration between the baseline image and the SPECT/CT. Even when the segmentation is performed on the CT of SPECT/CT there will be uncertainty associated with mis-registration between SPECT and CT. The uncertainty in VOI counts due to mis-registration of SPECT

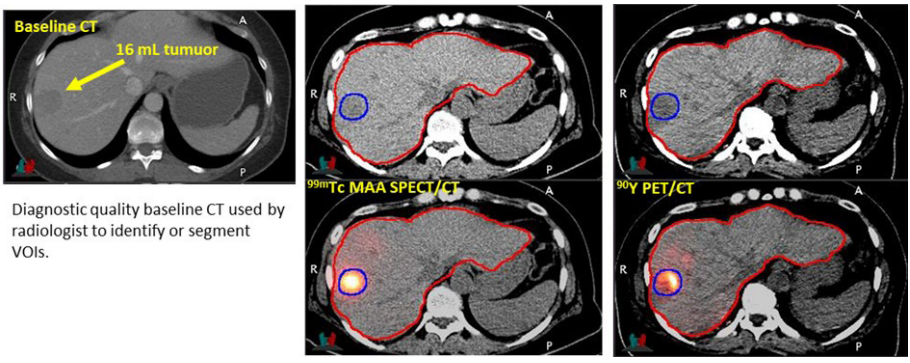

FIG. 9.5. Images corresponding to a patient who underwent ^{90}Y radioembolization with glass microspheres. In this example lesion and liver segmentation was performed directly on the CT of the SPECT/CT and PET/CT. Courtesy of Y. Dewaraja.

and CT images, particularly due to respiratory motion, is especially significant in radioembolization because of the close proximity of the liver dome to the lungs. Reported descriptive statistics on liver dome motion determined from a large 4-D CT dataset show the mean displacement to be 1.56 cm with an interquartile interval of 1.17–1.85 cm [9.34]. The sensitivity of liver and lesion counts to mis-registration can be estimated by introducing realistic displacements to the segmented contour.

9.8.3.1. Absorbed dose

Based on the medical internal radiation dose (MIRD) schema (Chapter 2), under the assumptions (1) and (3), above, the mean absorbed dose, D, from ^{90}Y that is internally deposited in tissue of mass M can be generally expressed as:

$$D = k\frac{A}{M} \tag{9.19}$$

where A is the initial ^{90}Y activity in the tissue and k is a constant that accounts for the physical half-life and the emitted beta particle energy. When D is expressed in Gy, A in GBq and M in kg, then k = 49.38 J/GBq [9.30]. It is reasonable to assume that k is known exactly. The factors A and M are correlated because they both depend on VOI delineation. Then, based on Eq. (9.4), the relative standard uncertainty in the absorbed dose is:

$$\left(\frac{u(D)}{D}\right)^2 = \left(\frac{u(A)}{A}\right)^2 + \left(\frac{u(M)}{M}\right)^2 - 2\left(\frac{u(A,M)}{AM}\right) \tag{9.20}$$

Determination of each of the terms that go into the above equation to estimate uncertainty in lesion and normal liver absorbed doses is described below.

9.8.3.2. Activity and image calibration factor

Predictive dosimetry is typically performed assuming an identical distribution for the ^{90}Y microspheres and the ^{99m}Tc-MAA particles. Then, ignoring partial volume effects (valid for a large region):

$$A = \frac{C_{\mathrm{VOI}}}{CF} = C_{\mathrm{VOI}}\frac{A_{\mathrm{L}}}{C_{\mathrm{L}}} \tag{9.21}$$

where A_{L} is the ^{90}Y activity in the liver and C_{VOI} and C_{L} are the reconstructed ^{99m}Tc SPECT counts or count rate in VOIs over the particular tissue region and the

whole liver, respectively. The conversion factor of counts to activity, $CF = C_L/A_L$, is considered as a patient- or liver-relative calibration since quantification is achieved without a calibration factor from external measurements and thus follows from assumption (2), above.

The activity in the liver is the administered activity A_{admin} minus any extra-hepatic deposition of the microspheres, which is typically small and limited to the lung. For the uncertainty calculation, ignoring extra-hepatic deposition, the activity in the liver can be assumed to be the difference between the assay of the activity vial measured in the activity meter, A_{assay}, and the residual activity $A_{residual}$ in the vial and tubing after administration. The standard uncertainty in the administered activity (also, the activity in the liver) can then be obtained as:

$$u^2(A_L) = u^2\left(A_{admin}\right) = u^2(A_{assay}) + u^2(A_{residual}) \tag{9.22}$$

The standard uncertainty in the assayed activity can be determined by repeated measurements of the dose vial over several days between delivery and treatment. The residual activity is not always measured or is measured using a survey meter as the tubing does not fit into the source holder of the activity meter. Repeated measurements of the residual with the survey meter can be performed to estimate the standard uncertainty.

When the tissue region is a tumour (T), then since C_T, C_L and A_L are independent measurements, the relative standard uncertainty in the VOI activity can be calculated using Eq. (9.4), setting the covariance terms to zero, according to:

$$\left(\frac{u\left(A_T\right)}{A_T}\right)^2 = \left(\frac{u\left(A_L\right)}{A_L}\right)^2 + \left(\frac{u\left(C_T\right)}{C_T}\right)^2 + \left(\frac{u\left(C_L\right)}{C_L}\right)^2 \tag{9.23}$$

The non-tumoural liver outline is typically determined by subtracting the lesion VOI from the liver VOI. In this case, according to Eq. (9.21), the activity in the non-tumoural liver can be written as:

$$A_{NL} = \left(C_L - C_T\right) \cdot \frac{A_L}{C_L} \tag{9.24}$$

Then, since C_T, C_L and A_L are independent, the standard uncertainty in the non-tumoural liver activity can be calculated using Eq. (9.1), according to:

$$u^2(A_{NL}) = \left(\frac{\partial A_{NL}}{\partial A_L}\right)^2 u^2(A_L) + \left(\frac{\partial A_{NL}}{\partial C_L}\right)^2 u^2(C_L) + \left(\frac{\partial A_{NL}}{\partial C_T}\right)^2 u^2(C_T) \quad (9.25)$$

where the partial derivatives can be obtained from the previous definition of A_{NL}. Note that the above equations assume that no partial volume correction is performed to recover counts, which is a reasonable assumption for large VOIs such as the liver and some lesions. If a recovery coefficient is used, then procedures outlined in Section 9.8.1 should be applied.

9.8.3.3. Volume and mass

Typically, lesion and liver segmentation for predictive dosimetry is performed on baseline anatomical (CT or MR) images, CT of the ^{99m}Tc-MAA SPECT/CT or on the SPECT image, and their volumes are determined from the resulting VOIs. The uncertainty in tumour and liver volume due to uncertainty in VOI delineation can be determined from historical multi-operator studies. With PET or SPECT thresholding based VOI delineation, volume uncertainty can also be determined from analytical approaches that consider the spatial resolution of the imaging system (full width at half-maximum, FWHM) and the voxel size, as detailed in Gear et al. [9.12]. Application of this analytical approach with CT or MR based manual VOI delineation can substantially underestimate the volume uncertainty because of the superior spatial resolution, while other factors that do not enter into this calculation, such as mis-registration and impact of contrast, can dominate the uncertainty.

Particular to microsphere dosimetry is that the volume of non-tumoural liver, V_{NL}, is obtained by subtracting the tumour volume, V_T, from the total liver volume, V_L, and the standard uncertainty is thus given by:

$$u^2(V_{NL}) = u^2(V_L) + u^2(V_T) \quad (9.26)$$

If multiple tumours are present, the standard uncertainties associated with each of their volumes should be included above. The mass of the respective compartment is determined by multiplying the volume by the mass density of the tissue. Assuming the density is known exactly, the relative standard uncertainty in mass M and volume V are equal (i.e. $u(M) / M = u(V)/V$).

9.8.3.4. Counts

Technetium-99m-MAA SPECT/CT performed with the standard 185 MBq administration and a 10–30 min acquisition time results in high counting statistics;

hence the uncertainty in the tumour and liver VOI counts primarily depends on the uncertainty in the VOI definition. Methods for estimating the uncertainty in counts using either an analytical expression of counts as a function of volume or a graphical approach using a sensitivity analysis of counts on volume, were discussed in Section 9.8.1 and are detailed by Gear et al. [9.12]. For the counts in the normal liver, C_{NL}, the standard uncertainty can be estimated as:

$$u^2(C_{NL}) = u^2(C_L) + u^2(C_T) \tag{9.27}$$

9.8.3.5. Covariance between activity and mass

Since in Eq. (9.9) both A and M, denoted as general terms for all the regions addressed (whole liver, normal liver and tumour), depend on the VOI delineation, the covariance term in Eq. (9.20) is expressed as:

$$u(A,M) = \frac{\partial A}{\partial V}\frac{\partial M}{\partial V}u^2(V) \tag{9.28}$$

From Eq. (9.21), the gradient term associated with activity is:

$$\frac{\partial A}{\partial V} = \frac{\partial C_{VOI}}{\partial V}\frac{A_L}{C_L} \tag{9.29}$$

where the partial derivative of counts with respect to volume can be determined by the previously discussed graphical approach or the analytical expression in [9.12].

The gradient term associated with mass is equal to density of the tissue, ρ:

$$\frac{\partial M}{\partial V} = \rho \tag{9.30}$$

Table 9.5 indicates sources of error and how their contributions to the combined uncertainty in the absorbed dose may be estimated.

TABLE 9.5. PREDICTIVE DOSIMETRY OF LIVER AND LESIONS IN ^{90}Y MICROSPHERE TREATMENTS BASED ON ^{99m}TC-MAA SPECT/CT IMAGING: SOURCES OF ERROR AND SUGGESTIONS OF HOW TO EVALUATE THEIR UNCERTAINTY CONTRIBUTION TO THE ESTIMATED ORGAN/LESION ABSORBED DOSE

(courtesy of K. Sjögreen-Gleisner and Y. Dewaraja)

Source of error	Underlying assumption	Approach to evaluate the standard uncertainty that results from deviations from the assumption
Counting statistics	The acquisition is sufficiently long that noise associated with Poisson counting statistics is negligible.	Perform multiple acquisitions of a phantom with clinically relevant Tc-99m activities and acquisition time. Determine the uncertainty in counts due to noise from the multiple acquisitions. Multiple realizations from Monte Carlo simulations can also be used if a well-validated code is available.
Counts within VOI	The number of counts measured within the VOI delineated on the SPECT/CT is a true reflection of the total organ/lesion activity.	Perform a sensitivity analysis by repeating the counts measurement for different VOI contours segmented by multiple observers or generated for different SPECT threshold levels. Perform a sensitivity analysis to assess the impact of motion/mis-registration by repeating the counts measurement with the contoured liver/lesion VOI displaced in all directions by a range of values that mimic realistic motion effects and estimates of mis-registration.
Organ mass	The organ mass can be exactly quantified by multiplying volumetric measurements on SPECT or CT by a constant liver tissue density of 1.03 g/cm^3.	Investigate CT derived density values for liver voxels in different patients.

TABLE 9.5. PREDICTIVE DOSIMETRY OF LIVER AND LESIONS IN ^{90}Y MICROSPHERE TREATMENTS BASED ON ^{99m}TC-MAA SPECT/CT IMAGING: SOURCES OF ERROR AND SUGGESTIONS OF HOW TO EVALUATE THEIR UNCERTAINTY CONTRIBUTION TO THE ESTIMATED ORGAN/LESION ABSORBED DOSE

(courtesy of K. Sjögreen-Gleisner and Y. Dewaraja) (cont.)

Source of error	Underlying assumption	Approach to evaluate the standard uncertainty that results from deviations from the assumption
Activity measurement within the VOI	The activity measured within the VOI delineated on the SPECT/CT is a true reflection of the total organ/lesion activity. The activity in the liver is equal to the administered activity minus activity in the lung. The activity in the liver is known exactly from the lung shunt measurement, the activity in the vial and the residual assay.	Estimate fraction of extra-hepatic (other than lung) activity by examining counts in the image. Determine the uncertainty associated with the lung shunt calculation by using different liver/lung VOIs or ROIs on the Tc-99m-MAA image. Determine the uncertainty associated with the vial activity by repeating the measurement several times between time of delivery and the radioembolization procedure. Also determine uncertainty associated with residual measurement by repeating the measurement.
Photon attenuation and scatter	The attenuation and scatter estimates built into the reconstruction algorithm are perfectly correct for the influence of these effects.	As in Table 9.3.
Dosimetry: local energy deposition	The beta particle energy is completely deposited within the VOI (or voxel for voxel-level dosimetry). The mean Y-90 beta particle energy per disintegration and the physical Y-90 half-life used to determine the factor in Eq. (9.18) are known exactly.	Perform the calculation for different geometries using dose point kernel convolution or Monte Carlo radiation transport and compare with results for local energy deposition assumption. Consider published statistical uncertainties in the physical constants.

9.8.4. Post-therapy ^{90}Y PET/CT or bremsstrahlung SPECT/CT imaging based dosimetry in radioembolization

For post-therapy imaging in radioembolization absolute quantification is achieved either using the (liver) relative image calibration, as discussed for pre-therapy imaging with ^{99m}Tc-MAA SPECT, or from an independent measurement of the calibration factor. In the latter case, activity is determined using Eq. (9.6) instead of Eq. (9.21) with related uncertainties and their propagation as described in Section 9.8.1. Although for PET the calibration factor measurement is performed by the manufacturer and built into the system software, this measurement is typically performed with ^{18}F. Hence, for ^{90}Y, the corresponding calibration factor is determined by multiplying the calibration factor for ^{18}F by a scaling factor that is equal to the ^{90}Y positron branching ratio divided by the ^{18}F positron branching ratio. In most state of the art PET systems ^{90}Y is a viable PET radionuclide option that is selected at the time of acquisition and this scaling is performed internally. However, because the measurement precision reported for the very low ^{90}Y positron branching ratio ($(3.186 \pm 0.047)\ 10^{-5}$ per beta decay [9.35]) is relatively low, this scaling is an additional source of uncertainty in quantitative ^{90}Y PET when the image Bq/mL values are directly used. The uncertainty in the calibration factor due to camera variability can be estimated based on the daily quality control records since the variation in the scanner efficiency is typically performed as part of the daily quality control using a long lived source such as ^{68}Ge solid phantom. Additionally, for ^{90}Y, uncertainty associated with Poisson counting statistics can be substantial in PET due to the very low count rates, and uncertainty associated with scatter correction in bremsstrahlung SPECT can be higher than for typical gamma ray emitters because the scatter fraction is substantially higher.

Regardless of the calibration procedure, the expression for absorbed dose is given by Eq. (9.19), and the related uncertainties and their propagation thus follow the same calculation schema as for pre-therapeutic dosimetry described above.

REFERENCES

[9.1] JOINT COMMITTEE FOR GUIDES IN METROLOGY, International vocabulary of metrology – Basic and general concepts and associated terms (VIM), Bureau International des Poids et Mesures, Sèvres (2012).

[9.2] International Vocabulary on Metrology, https://www.bipm.org/en/publications/guides/vim.html

[9.3] D'ARIENZO, M., COX, M., Uncertainty analysis in the calibration of an emission tomography system for quantitative imaging, Comput. Math Methods Med. **2017** (2017) 9830386, https://doi.org/10.1155/2017/9830386

[9.4] ANIZAN, N., et al., Factors affecting the stability and repeatability of gamma camera calibration for quantitative imaging applications based on a retrospective review of clinical data, EJNMMI Res. **4** 1 (2014) 67, https://doi.org/10.1186/s13550-014-0067-x

[9.5] ANIZAN, N., WANG, H., ZHOU, X.C., WAHL, R.L., FREY, E.C., Factors affecting the repeatability of gamma camera calibration for quantitative imaging applications using a sealed source, Phys. Med. Biol. **60** 3 (2015) 1325–1337, https://doi.org/10.1088/0031-9155/60/3/1325

[9.6] ZHAO, W., et al., Determination of gamma camera calibration factors for quantitation of therapeutic radioisotopes, EJNMMI Phys. **5** 1 (2018) 8, https://doi.org/10.1186/s40658-018-0208-9

[9.7] MARIN, G., et al., Accuracy and precision assessment for activity quantification in individualized dosimetry of ^{177}Lu-DOTATATE therapy, EJNMMI Phys. **4** 1 (2017) 7, https://doi.org/10.1186/s40658-017-0174-7

[9.8] HE, B., FREY, E.C., The impact of 3D volume of interest definition on accuracy and precision of activity estimation in quantitative SPECT and planar processing methods, Phys. Med. Biol. **55** 12 (2010) 3535–3544, https://doi.org/10.1088/0031-9155/55/12/017

[9.9] HE, B., et al., Evaluation of quantitative imaging methods for organ activity and residence time estimation using a population of phantoms having realistic variations in anatomy and uptake, Med. Phys. **36** 2 (2009) 612–619, https://doi.org/10.1118/1.3063156

[9.10] FLUX, G.D., GUY, M.J., BEDDOWS, R., PRYOR, M., FLOWER, M.A., Estimation and implications of random errors in whole-body dosimetry for targeted radionuclide therapy, Phys. Med. Biol. **47** 17 (2002) 3211–3223, https://doi.org/10.1088/0031-9155/47/17/311

[9.11] GUSTAFSSON, J., et al., Uncertainty propagation for SPECT/CT-based renal dosimetry in (177)Lu peptide receptor radionuclide therapy, Phys. Med. Biol. **60** 21 (2015) 8329–8346, https://doi.org/10.1088/0031-9155/60/21/8329

[9.12] GEAR, J.I., et al., EANM practical guidance on uncertainty analysis for molecular radiotherapy absorbed dose calculations, Eur. J. Nucl. Med. Mol. Imaging **45** 13 (2018) 2456–2474, https://doi.org/10.1007/s00259-018-4136-7

[9.13] JOINT COMMITTEE ON GUIDES IN METROLOGY, Evaluation of measurement data — guide to the expression of uncertainty in measurement, Bureau International des Poids et Mesures, Sèvres (2008).

[9.14] Guide to the expression of uncertainty in measurement, https://www.bipm.org/en/publications/guides/#gum

[9.15] FARRANCE, I., FRENKEL, R., Uncertainty of measurement: A review of the rules for calculating uncertainty components through functional relationships, Clin. Biochem. Rev. **33** 2 (2012) 49–75.

[9.16] JOINT COMMITTEE ON GUIDES IN METROLOGY, Evaluation of measurement data — supplement 1 to the "Guide to the expression of uncertainty in measurement" — propagation of distributions using a Monte Carlo method, Bureau International des Poids et Mesures, Sèvres (2008).

[9.17] GADD, R., et al., Measurement Good Practice Guide No. 93: Protocol for Establishing and Maintaining the Calibration of Medical Radionuclide Calibrators and Their Quality Control, National Physical Laboratory, Teddington, UK (2006).

[9.18] BERGERON, D.E., CESSNA, J.T., ZIMMERMAN, B.E., Secondary standards for ^{223}Ra revised, Appl. Radiat. Isot. **101** (2015) 10–14, https://doi.org/10.1016/j.apradiso.2015.03.008

[9.19] DEZARN, W.A., KENNEDY, A.S., Resin ^{90}Y microsphere activity measurements for liver brachytherapy, Med. Phys. **34** 6 (2007) 1896–1900, https://doi.org/10.1118/1.2731034

[9.20] ZIMMERMAN, B.E., CESSNA, J.T., Experimental determinations of commercial 'dose calibrator' settings for nuclides used in nuclear medicine, Appl. Radiat. Isot. **52** 3 (2000) 615–619, https://doi.org/10.1016/S0969-8043(99)00219-5

[9.21] AMERICAN ASSOCIATION OF PHYSICISTS IN MEDICINE, The Selection, Use, Calibration, and Quality Assurance of Radionuclide Calibrators Used in Nuclear Medicine, AAPM Report No. 181, AAPM, College Park, MD (2012).

[9.22] BUCKLEY, S.E., CHITTENDEN, S.J., SARAN, F.H., MELLER, S.T., FLUX, G.D., Whole-body dosimetry for individualized treatment planning of 131I-MIBG radionuclide therapy for neuroblastoma, J. Nucl. Med. **50** 9 (2009) 1518–1524, https://doi.org/10.2967/jnumed.109.064469

[9.23] MINGUEZ, P., et al., Dosimetric results in treatments of neuroblastoma and neuroendocrine tumors with ^{131}I-metaiodobenzylguanidine with implications for the activity to administer, Med. Phys. **42** 7 (2015) 3969–3978, https://doi.org/10.1118/1.4921807

[9.24] HÄNSCHEID, H., et al., EANM Dosimetry Committee series on standard operational procedures for pre-therapeutic dosimetry II. Dosimetry prior to radioiodine therapy of benign thyroid diseases, Eur. J. Nucl. Med. Mol. Imaging **40** 7 (2013) 1126–1134, https://doi.org/10.1007/s00259-013-2387-x

[9.25] SJÖGREEN-GLEISNER, K., et al., Variations in the practice of molecular radiotherapy and implementation of dosimetry: Results from a European survey, EJNMMI Phys. **4** 1 (2017) 28, https://doi.org/10.1186/s40658-017-0193-4

[9.26] DEWARAJA, Y.K., et al., MIRD Pamphlet No. 23: Quantitative SPECT for patient-specific 3-dimensional dosimetry in internal radionuclide therapy, J. Nucl. Med. **53** 8 (2012) 1310–1325, https://doi.org/10.2967/jnumed.111.100123

[9.27] SUNDLÖV, A., et al., Individualised ^{177}Lu-DOTATATE treatment of neuroendocrine tumours based on kidney dosimetry, Eur. J. Nucl. Med. Mol. Imaging **44** 9 (2017) 1480–1489, https://doi.org/10.1007/s00259-017-3678-4

[9.28] ROTH, D., GUSTAFSSON, J., SUNDLÖV, A., SJÖGREEN-GLEISNER, K., A method for tumor dosimetry based on hybrid planar-SPECT/CT images and semiautomatic segmentation, Med. Phys. **45** 11 (2018) 5004–5018, https://doi.org/10.1002/mp.13178

[9.29] BAILEY, J.J., DEWARAJA, Y., HUBERS, D., SRINIVASA, R.N., FREY, K.A., Biodistribution of ^{99m}Tc-MAA on SPECT/CT performed for 90Y radioembolization therapy planning: A pictorial review, Clin. Transl. Imaging **5** 5 (2017) 473–485, https://doi.org/10.1007/s40336-017-0245-8

[9.30] DEZARN, W.A., et al., Recommendations of the American Association of Physicists in Medicine on dosimetry, imaging, and quality assurance procedures for ^{90}Y microsphere brachytherapy in the treatment of hepatic malignancies, Med. Phys. **38** 8 (2011) 4824–4845, https://doi.org/10.1118/1.3608909

[9.31] COURSEY, B.M., CALHOUN, J.M., CESSNA, J.T., Radioassays of yttrium-90 used in nuclear medicine, Nucl. Med. Biol. **20** 5 (1993) 693–699, https://doi.org/10.1016/0969-8051(93)90040-2

[9.32] BÉ, M.M., et al., Table of Radionuclides, Bureau International des Poids et Mesures, Sèvres (2006).

[9.33] NATIONAL NUCLEAR DATA CENTER (NNDC), The National Nuclear Data Center, https://www.nndc.bnl.gov/

[9.34] SIVA, S., et al., An analysis of respiratory induced kidney motion on four-dimensional computed tomography and its implications for stereotactic kidney radiotherapy, Radiat. Oncol. **8** (2013) 248, https://doi.org/10.1186/1748-717X-8-248

[9.35] SELWYN, R.G., NICKLES, R.J., THOMADSEN, B.R., DeWERD, L.A., MICKA, J.A., A new internal pair production branching ratio of ^{90}Y: The development of a non-destructive assay for ^{90}Y and ^{90}Sr, Appl. Radiat. Isot. **65** 3 (2007) 318–327, https://doi.org/10.1016/j.apradiso.2006.08.009

Chapter 10

RADIOPHARMACEUTICAL TREATMENT MODALITIES

F.A. VERBURG, Y.K. DEWARAJA, M. LASSMANN

10.1. OVERVIEW

Since the first application of radiopharmaceutical therapy (RPT) in the late 1930s and early 1940s, a number of radionuclide therapeutic modalities have been introduced, whereas others have fallen out of use. An overview of commonly

TABLE 10.1. AN OVERVIEW OF RADIONUCLIDES USED FOR RPT, THE ASSOCIATED TRACER, THE TARGET INVOLVED AND THE CLINICAL INDICATION(S)

(courtesy of E. Verburg and M. Lassmann)

Radionuclide	Radiopharmaceutical	Target	Clinical indication
I-131	I-131 sodium iodide	Sodium-iodine-symporter	Benign and malignant thyroid disease
	I-131 mIBG	Active transport into cells of neuroendocrine lineage	Malignant pheochromocytoma, carcinoid, paraganglioma, neuroblastoma
Lu-177	Lu-177 labelled somatostatin analogues	Somatostatin receptor	Neuroendocrine tumours
	Lu-177 PSMA	Prostate-specific membrane antigen	Metastatic, castration resistant prostate cancer
Ra-223	Ra-223 dichloride	Osteoblastic activity: calcium metabolism	Metastatic, castration resistant prostate cancer
Y-90	Y-90 microspheres	Liver tumours	Primary and secondary liver malignancies

used therapeutic radionuclides for targeted radionuclide therapy with marketing authorization in North America and Europe at the time of writing (except ^{177}Lu prostate-specific membrane antigen (PSMA)) is given in Table 10.1; the different radionuclides and their applications will be discussed separately. This list is by no means complete: there are many more therapies with different ligands and radionuclides in use worldwide.

10.2. IODINE-131

10.2.1. Iodine-131 sodium iodide

For thyroid disease, ^{131}I is given in the form of sodium iodide. Iodine-131 is chemically identical to stable ^{127}I and is physiologically taken up by the sodium iodine symporter and incorporated in the thyroid hormone production process. Details on the radionuclide decay scheme, the photon energies and the range of the charged particles are given in Chapter 2.

10.2.2. Iodine-131 in benign thyroid disease

After using ^{128}I to investigate rabbit thyroid function in 1937, Hertz, Roberts and Evans had treated Graves' disease, among other thyroid disorders, using ^{130}I. The investigators administered ^{130}I activities that would have been merely diagnostic were it not for a probable 10% contamination with ^{131}I. In 1938 though, Livingood and Seaborg synthesized ^{131}I as a separate isotope. A mere few years later, in in 1941, radioiodine therapy with ^{131}I was first introduced for treatment of benign thyroid disease at Massachusetts General Hospital in Boston [10.1], although it took until after the Second World War for this therapy to become widely available.

Iodine-131 therapy is one of the many therapeutic options available for benign thyroid diseases. Alternatives to radioiodine therapy are surgical resection in the form of hemi- or total thyroidectomy and anti-thyroid drugs (ATDs) such as methimazole or propylthiouracil [10.2].

The exact goals and therefore the therapeutic procedures vary depending on the particular disorder for which radioiodine therapy is prescribed and the attending physicians' ideas and experiences (e.g. euthyroidism versus hypothyroidism as a therapy goal in radioiodine therapy for Graves' disease).

10.2.2.1. Indications and contraindications

Indications for ^{131}I therapy include:

(a) Subclinical or clinically overt hyperthyroidism caused by:
    (i) Graves' disease;
    (ii) Diffuse toxic goitre;
    (iii) Toxic uni- or multi-nodular thyroid disease.
(b) Symptomatic non-toxic goitre with sufficient uptake on pertechnetate scintigraphy.

In all forms of nodular thyroid disease, malignancy should be excluded before radioiodine therapy takes place. Furthermore, in obstructive goitre with severe symptoms of dyspnoea, either toxic or non-toxic, surgery must be considered the preferred therapeutic modality as it is effective immediately.

10.2.2.2. Procedure

Patient preparation

Before radioiodine therapy, any excess of iodine intake should be avoided or eliminated. In practice this means that within three months prior to radioiodine therapy no iodinated X ray contrast enhancing agents should be given. In addition, iodinated drugs such as amiodarone should be avoided. If in doubt, patients' iodine status should be checked by measuring the urinary iodine excretion.

If a patient is on ATDs before radioiodine therapy, these drugs should preferably be stopped at least three days prior to radioiodine therapy as they interfere with the organification of iodine and thus potentially with the efficacy of radioiodine therapy [10.2–10.4]. When pre-therapeutic dosimetry is performed, ATDs should be stopped three days prior to dosimetry. If it is not medically feasible to stop ATDs for a longer period (e.g. in case of concomitant cardiac disease), they should be taken during both dosimetry and therapy in order to provide similar iodine pharmacokinetics uptake and washout rates during both procedures.

Therapy activity prescription

The optimal dosing strategy for ^{131}I therapy of benign thyroid disease has been a subject of debate since the early days of ^{131}I therapy in the 1940s. For toxic goitre and Graves' disease, various strategies have been proposed, including those administering fixed activities of various amounts, an activity range from which

the physician can choose at their discretion as well as various strategies which take account of the thyroid size, ^{131}I uptake, ^{131}I pharmacokinetics or a combination of these factors [10.2, 10.3, 10.5–10.14]. Still, there is yet no consensus in the literature on the target variable to employ when dosing ^{131}I for radioiodine therapy of benign thyroid diseases. Current guideline recommendations regarding activity prescriptions are inconsistent. While the European Association of Nuclear Medicine (EANM) [10.3] recommends targeting at a total radiation absorbed dose) to the thyroid of 100–150 Gy for toxic goitre or 200–300 Gy when striving for functional ablation such as in Graves' disease, giving fixed activities of 200–800 MBq is also suggested. American guidelines [10.2, 10.7] suggest using either fixed activities or prescription based on the thyroid mass and the results of a 24 h uptake measurement to calculate the amount of ^{131}I to administer in order to achieve a radioiodine concentration in the thyroid gland of 3–8 MBq/g. The latter concept is equivalent to targeting at a maximum absorbed dose rate instead of a total absorbed dose — which may be more effective [10.15] — as the absorbed dose rate is proportional to the activity per unit of mass multiplied by a factor that represents the absorbed dose per decay per unit mass (0.1177 Gy·g·MBq^{-1}·h^{-1} in a thyroid of 30 g mass).

Role of dosimetry

The maximum extent of individualization, which is required by radiation protection regulations in some countries, is a full pre-therapeutic dosimetry in which thyroid and/or nodule size, uptake and effective half-life are all measured in order to be able to calculate the activity necessary to achieve a desired absorbed dose to the target tissue [10.4].

The goal of pre-therapeutic dosimetry is to provide a therapy that is both effective and uses the lowest possible ^{131}I activity and that still delivers a therapeutically effective absorbed dose to the thyroid, thus minimizing unnecessary radiation exposure. Usually, 100–150 Gy to the target volume is recommended in order to treat hyperthyroidism when aiming at euthyroidism, whereas 200–300 Gy is recommended when aiming at the functional ablation of the target volume (resulting e.g. in post-therapeutic hypothyroidism in Graves' disease or making a toxic nodule hypofunctional).

The procedure is relatively straightforward [10.4]: a small, non-therapeutic ^{131}I activity is administered and the uptake in the thyroid of this activity is then measured at one or more time points after administration. According to the EANM standard operating procedures the activity A_a necessary to achieve a specified absorbed dose D in the target mass M is:

$$A_a = \frac{1}{\bar{E}} \cdot \frac{M \cdot D}{\int_0^\infty RIU(t)\,\mathrm{d}t} \tag{10.1}$$

The radioiodine uptake $RIU(t)$ is the residual fraction of the administered activity A_a in the uptake region of the thyroid with mass M, at time t after the administration:

$$RIU(t) = \frac{A_T(t)}{A_a} \tag{10.2}$$

The constant value for the mean energy $\bar{E}$ deposited in the target tissue per decay of ^{131}I, is $\bar{E}$ = 2.808 Gy·g·MBq^{-1}·d^{-1} for a thyroid with M = 20 g [10.4]. A simple mass dependent expression for the factor $1/\bar{E}$ that might be used for an improved estimate in large goitres is given in the supplement of the EANM standard operating procedures [10.4]. Details on the different data acquisition schedules suggested are explained in the EANM standard operating procedures [10.4].

Intuitively, a dosimetry approach for calculating the activity to administer should produce the best treatment outcome. However, thus far, no conclusive evidence exists on the superiority of dosimetry over empiric, fixed activity approaches, or semi-dosimetry approaches based on volume or an uptake percentage alone.

10.2.2.3. Side effects and complications

Immediate side effects

The immediate side effects of radioiodine therapy are comparatively rare and usually confined to the thyroid. It is possible that in the first few days after ^{131}I administration patients may develop radiation thyroiditis, which can cause local symptoms such as increased pressure or thyroidal pain. These symptoms are usually mild and can be alleviated adequately with ice packs and/or pain medication such as paracetamol or ibuprofen. Only in patients with massive goitre and tracheal compression, symptomatic radiation thyroiditis, especially swelling of the thyroid, should be prevented in order to avoid an acute medical emergency due to complete tracheal obstruction. In such patients, a brief pre-therapeutic course of corticosteroids usually provides ample prophylaxis.

Long term side effects

The most important side effect of ^{131}I therapy of benign thyroid disease is that in the long term patients can develop hypothyroidism even if initially the goal of euthyroidism was strived for and reached. The risk for developing hypothyroidism after ^{131}I therapy continues to exist long after treatment. It is therefore necessary to regularly (e.g. initially annually, later on bi-annually) check TSH levels after radioiodine therapy for ten years or more.

Although ^{131}I therapy has been employed to treat benign thyroid disease for well over 70 years now, an extensive review of the literature [10.16] was unable to find studies that meet the usual criteria for establishing the radiogenicity of an increased cancer incidence in patients after ^{131}I exposure for treatment of benign thyroid disease. Therefore, considering that millions of patients have been treated for benign thyroid disease over the past seven decades and still no elevated cancer risk due to ^{131}I therapy of benign thyroid disease has been proven conclusively, it is highly unlikely that radioiodine therapy of benign thyroid disease is associated with a long term elevated risk of malignancies.

10.2.3. Iodine-131 in malignant thyroid disease

Samuel M. Seidlin of the Montefiore Hospital in New York treated a patient in 1942 who had undergone a thyroidectomy for what had been histologically diagnosed as a ‘malignant adenoma’ of the thyroid two decades earlier. The patient was in poor condition with hyperthyroidism, underweight and in pain. The patient was given radioiodine, which had just become available and responded favourably to the treatment, going on to receive several more courses. Nowadays, treatment of differentiated thyroid cancer (DTC) usually consists of a combination of surgery, radioiodine therapy and thyroid hormone replacement aiming at, depending on the stage of disease, TSH levels in the low–normal range or at suppression of TSH [10.17–10.20].

The efficacy of radioiodine therapy

Mazzaferri and Jhiang published a study in 1994 of 1500 patients who were followed for several decades. The study clearly showed that DTC related recurrence and death rates were much lower in patients who received radioiodine treatment after surgery than in patients who did not receive this therapy [10.21]. Iodine-131 therapy now belongs to the standard treatment of DTC and in patients without extensive neck or distant metastases the life expectancy remains unchanged [10.22].

The good prognosis of DTC is associated with the use of ^{131}I in both an ablative and a therapeutic setting. Iodine-131 NaI is almost the ideal oncologic drug since the thyroid cells act as the body's main iodine reservoir and express the sodium iodide symporter [10.23]. Thus, radioiodine is largely specific for the cancer cells and has relatively limited side effects. Additionally, this isotope emits beta radiation (used for therapy) as well as gamma rays for imaging.

Iodine-131 thyroid remnant ablation

The majority of current guidelines recommend post-surgical application of a high ('ablative') ^{131}I activity as additional treatment of DTC in most (near) totally thyroidectomized patients [10.17–10.20].

In clinical practice, ^{131}I ablation has three goals [10.24]:

— To destroy occult small DTC foci to decrease the long term risk of recurrent disease [10.21, 10.25–10.28].
— To eliminate any remaining healthy thyroid tissue to increase the specificity of detectable serum thyroglobulin (Tg) and positive whole body scans as markers for persistent or recurrent DTC [10.24, 10.26, 10.29]. Additionally, ablation may remove a locus for new neoplastic transformation [10.30], given the multiclonal nature of many DTC cases [10.31].
— A few days after administration of high activities of ^{131}I for ablation, sensitive post-ablation whole body scans can be performed to detect previously unknown persistent locoregional disease or metastases [10.32, 10.33]. In selected cases, post-ablation scintigraphy also allows precise surgical or even probe guided removal of the newly detected disease foci [10.34].

Achieving these goals should lead to decreased rates and to more timely diagnosis of persistent or recurrent disease, and, more importantly, to improved tumour specific survival in thyroidectomized patients with DTC [10.21, 10.28, 10.35]. However, these effects of ^{131}I ablation may partly depend on surgical technique in the particular case: DTC excision by the most highly skilled surgeons may obviate the need for ablation at least in low risk cases [10.36].

Survival benefits of ablation have not been established for low risk patients (TNM stage T1-2N0M0), and the measured results on the prevention of recurrent disease differ between reports [10.37, 10.38]. In patients with a non-invasive primary tumour less than 2 cm in diameter, studies have not shown a significant difference in remission or death rates between patients who were or were not given ^{131}I ablation [10.39]. However, it appears that studies with a longer follow-up time are more likely to show a significant benefit of ^{131}I ablation [10.37, 10.40]. In a meta-analysis Sawka et al. (2008) found that the risk of developing distant

metastases was significantly lower after ^{131}I ablation in patients with a tumour diameter >1 cm [10.40]. This indicates a significant benefit from ^{131}I ablation even in patients who are traditionally considered to be at low risk. Beneficial effects of initial ^{131}I therapy have been demonstrated in high risk patients or in cases of non-radical surgery [10.21, 10.41–10.43].

Iodine-131 therapy of advanced disease

This is an effective therapy not only in the initial post-operative situation, but also in further treatment of patients with metastasized or recurrent DTC. Patients in whom the metastases accumulate radioiodine therefore have a much better prognosis than those in whom the capacity for ^{131}I uptake has been lost [10.44]. On the other hand, especially in younger patients, ^{131}I can achieve a lasting full remission in patients with extensive metastases [10.45–10.48], even years after the ^{131}I therapy itself has ceased [10.49]. However, and amazingly for a therapy modality that has been used without alternative for almost 70 years, most therapeutic interventions are entirely empiric in nature — no consensus exists on the exact timing of ^{131}I therapy courses, how much activity to use in which patients, whether to use dosimetry or not [10.50, 10.51] and when to cease ^{131}I therapy. Most recommendations are based solely on expert opinion and no prospective randomized trials on the use of ^{131}I in patients with advanced disease have thus far been published [10.17].

Standard activities versus patient-specific dosimetry

Sixty-five years [10.52] after the of treatment of DTC by systemic administration of radioiodine was introduced there is still no generally accepted dosage regimen to ensure an individually optimized therapy. There is consensus that the primary goal of radioiodine therapy — ablation of thyroid remnants as adjuvant modality after thyroidectomy on the one hand and curative or palliative therapy of local tumour and distant metastases on the other — should have an influence on the therapeutic activity [10.18, 10.20, 10.53, 10.54].

The most common method of radioiodine therapy is administration of a standard activity of ^{131}I and the simplest approach to optimize therapy is empirical variation of this fixed activity dosage. Doi et al. [10.55] reported on 19 studies comparing the efficacy of high vs low ablation activities and pooled data of 11 of these in a meta-analysis together with their own cohort study data. They concluded that treatment with the higher activity of ^{131}I is significantly more efficient for remnant ablation particularly after less than total thyroidectomy. A more recent systematic review by Hackshaw et al. [10.56] with a meta-analysis including data from 41 patient case reviews, 12 prospective studies and

6 randomized trials published in the years from 1966 to 2006 concludes that the current evidence is not conclusive and published data are insufficient to reliably determine whether ablation success rates are similar with ablation activities of 1.1 vs 3.7 GBq. However, after re-analysing the same data as those used in [10.56], Doi et al. [10.55] came to the opposite result, finding a significant difference in the efficacy of both regimens.

For remnant ablation alone, which is no longer generally recommended, randomized trials have shown that a dosage of 1.1 GBq is likely as effective as 3.7 GBq. However, these studies have merely focused on the short term efficacy of therapy. Long term results of these patient cohorts, which might serve to compare low and high activities in terms of adjuvant therapy, are still lacking. However, retrospective data seem to indicate that in the long term higher activities may be superior in terms of DTC specific survival [10.57].

The subject remains controversial and current guidelines leave it up to the responsible physician, selecting radioiodine activities in a range between 1.1 and 3.7 GBq for post-surgical ablation of thyroid residues, or up to 5.5 GBq for adjuvant therapy [10.53].

Dosimetry in advanced disease

Many regimens with repeated administration of fixed activities ranging from 3.7 GBq [10.58] to 11.1 GBq [10.59] have been reported for the treatment of locoregional or metastatic disease. A good compilation of the observed outcomes was given by Van Nostrand [10.60]. No prospective randomized trials are available to demonstrate superior effectiveness for any of these strategies. The guidelines recommend repeatedly administering 3.7–7.4 GBq of ^{131}I without dosimetry, activities that have empirically found to be safe and have not been shown to induce severe adverse effects in affected patients, or performing personalized dosimetry in selected cases where higher activities are deemed beneficial.

Multiple administrations of lower activities in a ‘fractionated’ therapy could lead to changes in tumour/lesion biokinetics as has been reported [10.61, 10.62]. These studies suggest that the repetition of treatment substantially reduces lesion uptake, with a loss of therapeutic efficacy in subsequent administrations. There is also clinical evidence that prognosis progressively worsens as the number of therapy courses is increased, but not with increasing cumulative activities [10.63].

Biological variability: Personalizing ^{131}I therapy

In radioiodine therapy of DTC, several parameters are equally or even more important than the administered activity for the radiation absorbed dose to the target tissue. These include:

(a) Iodine avidity, which depends on stimulation and differentiation;
(b) The time-integrated activity coefficient of the radioiodine per volume of blood plasma representing the bioavailability of the ^{131}I;
(c) The effective half-life in the target volume;
(d) The mean energy deposited per decay determined mainly by the size and shape of the accumulating mass [10.64].

The high individual variability of the above parameters [10.64] questions the value and practicality of the quest for the 'best' fixed therapeutic activity.

To overcome the uncertainty of individual biokinetics, two dosimetry based approaches have been introduced by Benua and Maxon. As early as 1962, Benua et al. [10.65] used the easily measurable absorbed dose to the blood as a surrogate of the absorbed dose to the organ at risk, the red marrow.

They settled on a conservative limit of 2 Gy to the blood to determine the highest activity that is safely deliverable to the patient without severe damage to the haematopoietic system. This absorbed dose limitis based on only a few cases of severe bone marrow suppression [10.65] and evidence that the 2 Gy limit might be too conservative has been demonstrated [10.66–10.68].

The blood absorbed dose reflects the amount of ^{131}I available to the target tissue [10.69] and, in thyroid remnant ablation, appears to correlate better with therapeutic success than the administered activity [10.70, 10.71]. Further details on dosimetry based activity selection can be found in [10.51, 10.72].

Maxon et al. [10.73, 10.74] also aimed at a specified absorbed dose to the target tissue: 300 Gy to thyroid remnants and 80 Gy for cervical lymph node metastases. These values by Maxon, although quoted often and used widely, have not been verified by independent prospective trials. In Maxon's lesion dosimetry approach, the recommended values mainly suffer from uncertainties in the determination of the target mass and how much of the energy is imparted to surrounding tissue. A publication by Jentzen et al., based on measurements with ^{124}I PET/CT, supports the hypothesis that therapeutic outcome correlates with the absorbed dose delivered to the target tissue [10.75].

The main argument against Maxon's approach arises from the fact that absorbed doses may vary considerably between different lesions within the same patient and that the distribution of the absorbed dose in a tumour may be inhomogeneous [10.62, 10.76]. This may lead to undertreatment of lesions not

included in the dosimetric evaluation or with supposedly sufficient absorbed dose but inhomogeneous activity distribution. It remains for prospective studies to clarify whether or not improved techniques for dosimetry and the introduction of formalisms for calculating the biologically effective dose (BED) or the equivalent uniform dose (EUD) [10.77, 10.78] will result in unique and reliable recommendations for lesion dosimetry in DTC.

Side effects and complications

The risk of malignancy associated with ^{131}I therapy in DTC patients has not been established. Furthermore, side effects such as xerostomia (prevalence range 16–54%), lacrimal gland dysfunction (prevalence 11%), transient male gonadal dysfunction or transient female gonadal dysfunction may occur [10.79]. The severity and prevalence of adverse effects appear to be correlated to the cumulative ^{131}I activity, which can severely impact quality of life [10.79].

As already observed in some of the first DTC patients treated with ^{131}I therapy [10.80], high ^{131}I activities can induce acute myeloid leukaemia. This finding has been confirmed in multiple subsequent case reports. These reports included patients treated with low activities or multiple treatments within a short duration. A more frequent radiation exposure or an exposure to higher cumulative activities will lead to a higher risk of complications. Furthermore, it was reported that the risk of second primary solid tumours could be elevated after therapy [10.81], but also before [10.82]. Hay et al. [10.48] reported a statistically significant excess mortality due to non-thyroid malignancies in survivors of paediatric papillary thyroid cancer first occurring three to five decades after the initial diagnosis. However, the excess mortality can also be due to other (e.g. genetic) causes.

In contrast with these negative results, Reiners et al. [10.83] reported on the findings of treatment from children with radiation-induced high risk papillary thyroid cancer after the reactor meltdown at Chornobyl. These children mostly received multiple courses of 100 MBq/kg treatments. Secondary malignancies during a median 11.3 year follow-up after the last radioiodine therapy were not observed.

The risk of developing secondary tumours over the course of a lifetime is non-negligible in paediatric papillary thyroid cancer patients who have a long remaining life expectancy. This is related to the cumulative ^{131}I activity administered over the patient's lifetime as well as to other, potentially predisposing, factors. A rare, but potentially lethal complication is the risk of pulmonary fibrosis in patients with extensive lung metastasis, which is also related to the cumulative radiation exposure. Considering evidence [10.49] that long term prognosis in patients who do eventually become disease free does not

substantially improve after more than four courses of ^{131}I therapy or a lifetime cumulative administered ^{131}I activity of 22 GBq compared to those who never become disease free, the long term side effects may outweigh the benefits. Thus, for the future it may be advisable in paediatric papillary thyroid cancer patients to consider cessation of further ^{131}I therapy courses if a complete remission of disease is not achieved with 3–4 courses of ^{131}I therapy.

10.2.4. Iodine-131 mIBG

10.2.4.1. Background

Metaiodobenzylguanidine (mIBG) is a noradrenaline analogue which is taken up by cells derived from the primitive neural crest as well as cells in other tissue with a rich adrenergic innervation. It is taken up both by passive diffusion and the neuronal uptake-I mechanism and is subsequently stored in neurosecretory granules in analogy to adrenalin. In contrast to adrenalin, however, mIBG is not metabolized and will be excreted in unchanged form [10.84]. When labelled with ^{131}I, this pharmaceutical can be used for radionuclide therapy of tumours originating from the primitive neural crest. Currently, however, most of these tumours are preferentially treated by means of ^{177}Lu labelled somatostatin analogues (see Section 10.3).

10.2.4.2. Indications and contraindications

Tumours for which ^{131}I mIBG therapy can be considered include any inoperable tumour derived from the primitive neural crest. These include phaeochromocytoma, paraganglioma, carcinoid tumours, neuroblastoma and, rarely, medullary thyroid cancer [10.85]. A necessary condition is that a sufficient tracer uptake in the target lesions be present in a pre-therapeutic I-123-mIBG imaging procedure.

(a) Absolute contraindications [10.85]:
    (i) Pregnancy/breastfeeding.
(b) Relative contraindications:
    (i) Life expectancy <3 months; in this case therapy should only be considered for palliative purposes;
    (ii) Glomerular filtration rate <30 mL/min;
    (iii) White blood cell count <3.0 10^9/L;
    (iv) Platelet count <100 10^9/L.

For contraindications (ii–iv) a reduction of the administered activity should be considered.

10.2.4.3. Administered activity

The activity to administer for ^{131}I therapy is not standardized. EANM guidelines [10.85] report a range between 3.7 and 11.2 GBq for single therapy courses (for paediatric patients this corresponds to approximately 50–150 MBq/kg of body weight). Courses can be repeated, but generally accepted regular intervals at which to give further cycles are not established, nor is the number of cycles limited. Clinical parameters such as blood cell counts, clinical conditions and response to therapy will lead to personalization of therapy.

10.2.4.4. Dosimetry

Like in ^{131}I NaI therapy, in ^{131}I mIBG therapy the bone marrow is the absorbed dose limiting organ. Whole body absorbed dose proved to be a good surrogate measure for bone marrow absorbed dose and significant correlations between whole body absorbed dose and myelotoxicity have been demonstrated [10.86–10.88]. In general, a whole body absorbed dose of 2 Gy is recommended in order to avoid myelotoxicity. The methodology on how to perform whole body dosimetry is described in detail by Buckley et al. [10.87].

10.2.4.5. Side effects

Like most radionuclide therapies, ^{131}I mIBG therapy can cause nausea and vomiting, which can be suppressed by antiemetic medication.

Iodine-131 mIBG therapy will also cause free ^{131}I in the blood, which may damage the thyroid. Therefore, patients should be given adequate thyroidal protection in the form of stable iodine and/or perchlorate before therapy.

In the case of catecholamine secreting tumours, ^{131}I mIBG therapy may lead to a hypertensive crisis; in order to prevent this, short acting intravenous alpha and/or beta blockers should be available in the immediate vicinity of the patient.

Longer term side effects include myelosuppression, occurring 4–6 weeks after therapy. This is frequently observed in paediatric patients receiving ^{131}I mIBG for neuroblastoma. These patients are at greater risk of haematological complications if prior to ^{131}I mIBG, myelotoxic chemotherapy was given.

10.3. LUTETIUM-177

10.3.1. Lutetium-177

Details on the radionuclide decay scheme of ^{177}Lu, the corresponding photon energies and the ranges of the charged particles are given in Chapter 2. Like ^{131}I, the emission spectrum of ^{177}Lu makes it a radiopharmaceutical, which allows for both therapy and imaging of the distribution. Unlike ^{131}I, however, its metallic nature necessitates the use of a chelator to bind tracer and radioisotope.

10.3.2. Lutetium-177 labelled somatostatin analogues

In neuroendocrine tumours (NETs), the somatostatin receptors, especially the subtypes 2 and 5, are expressed in abundance on the membrane of tumour cells. Over the course of time various tracers were developed which targeted these receptors, all based on the hormone somatostatin. Originally, the somatostatin analogue octreotide, which was available as a pharmacological tumour therapy, was made radioactive by labelling it with ^{111}I. Later on, different analogues containing a chelator for labelling with different positron or beta emitting radionuclides were introduced. The two analogues most frequently used for this peptide receptor radionuclide therapy (PRRT), both of which have a very high affinity for the somatostatin receptor subtype 2a [10.89], are [DOTA0,Tyr3]-octreotide (DOTATOC) and [DOTA0,Tyr3,Thr8]-octreotate (DOTATATE). Although previously these substances were predominantly labelled with ^{90}Y for therapeutic purposes, ^{177}Lu is now the standard radionuclide because of its similar efficacy but better profile with regard to side effects [10.90].

10.3.2.1. Background information

Many tumours typically show an elevated expression of the somatostatin receptor. These tumours include mainly those grouped under the moniker of NETs (among others, gastroenteropancreatic neuroendocrine tumours (GEP-NETs) and carcinoids), but also pheochromocytomas/paragangliomas and neuroblastomas as well as medullary thyroid cancer or Merkel-cell carcinomas. The intensity of expression of the somatostatin receptor differs between these tumours and may vary with differentiation grade of the neoplasia. These well-differentiated tumours have to be considered separately from the much less differentiated and more aggressive neuroendocrine carcinomas, which mostly show little or no expression of the somatostatin receptor.

Currently, somatostatin receptor positive NETs are primarily treated by injection of the (non-radiolabelled) somatostatin analogue octreotide.

Often, patients have a stable disease for many years under this therapy. Once patients progress under octreotide therapy, their options are limited as the still not highly proliferative NETs mostly respond poorly to chemotherapy. In such patients,treatment with ^{177}Lu labelled somatostatin analogues is indicated.

10.3.2.2. Indications and contraindications

In 2018, ^{177}Lu DOTATATE (Lutathera) received Food and Drug Administration (FDA) approval and European Medicines Agency (EMA) marketing authorization for the treatment of somatostatin receptor positive (GEP-NETs), including foregut, midgut and hindgut NETs in adults. A randomized, controlled trial using ^{177}Lu DOTATATE was completed showing that it has a clear clinical effect in 50% of patients [10.91].

The usual indication for PRRT is the presence of an unresectable somatostatin receptor positive NET (as proven by scintigraphy with ^{111}In-octreotide or PET/CT with ^{68}Ga DOTATOC/DOTATATE), which is progressive under first line therapy. Other niche indications which have been reported with at least occasional therapeutic efficacy include meningioma, medullary and differentiated thyroid cancer.

(a) Absolute contraindications [10.92]:
    (i) Absence of somatostatin receptor overexpression in the tumour;
    (ii) Pregnancy.
(b) Relative contraindications [10.92]:
    (i) Highly proliferative tumours (Ki-67 index >20%);
    (ii) <6 weeks' time interval since the last myelotoxic chemotherapy course;
    (iii) Low performance status (i.e. Karnofsky index <50% or ECOG performance status >2);
    (iv) Estimated life expectancy <3 months;
    (v) Thrombocyte counts <80 10^9/L;
    (vi) Leukocyte count <2.0 10^9/L;
    (vii) Glomerular filtration rate as estimated by 24 h urine sampling <50 mL/min;
    (viii) Breastfeeding (must be stopped before therapy).

10.3.2.3. Therapeutic activity

PRRT is given in the form of a fractionated radionuclide therapy. Cycles are given in intervals of 10–12 weeks in order to allow for recuperation of the bone marrow. Currently, the standard therapy regimen for PRRT consists

of 3–5 cycles of 5.5–7.4 GBq ^{177}Lu DOTATOC/DOTATATE with possible individual variations.

10.3.2.4. Dosimetry

In PRRT, the critical organs are mainly the kidneys and, to a much lower extent, the bone marrow. A summaryof the values of absorbed doses to these critical organs, published by several groups, is provided by Eberlein et al. [10.93]. According to this review, the mean absorbed dose coefficients to the kidney ranged from 0.6 to 1.0 Gy/GBq, most likely caused by differences in the dosimetry methodology applied and whether renal protection by infusion of a lysine/arginine amino acid solution before and during infusion of the radionuclide therapy was applied or not [10.94]. However, the individual variation in kidney exposure is quite high and the kidney response to PRRT may vary as well, also depending on kidney function prior to PRRT [10.95]. Some patients may tolerate considerably higher cumulative activities whereas others will require a cessation of therapy after much lower ones.

Blood based dosimetry performed to evaluate red marrow absorbed doses and haematologic toxicity resulted in absorbed doses lower than 0.1 Gy/GBq [10.93]. Consequently, high grade haematologic toxicity has not been observed in patients; mostly grade 3 leukopenia and thrombocytopenia have been noted.

10.3.2.5. Side effects

The most common side effects of PRRT include nausea (up to 25% of patients) and vomiting, which are mostly related to the infusion of amino acids. Up to 15% of patients will show transient or permanent changes of blood counts, which occur within a time frame of 4–12 weeks after each PRRT cycle. Blood counts will normalize for most of the patients; however, less than 1% of patients develop a myelodysplastic syndrome. Furthermore, patients risk kidney damage despite nephroprotective measures; patients with decreased kidney function before therapy are especially at risk of this serious side effect.

Patients who have hormonally active tumours may develop an endocrine crisis during infusion of the PRRT, which may exacerbate to the point that intensive care treatment is warranted.

10.3.3. Lutetium-177 PSMA

In prostate cancer, prostate-specific membrane antigen (PSMA) targeted radionuclide therapy has been the subject of research for a number of years. Initial attempts using the radiolabelled antibody J591 did not provide a

convincing clinical breakthrough [10.96, 10.97]. However, PSMA targeted radionuclide therapy using functionally antagonistic ligands of PSMA has gone straight from bench to bedside in recent years. Although initial reports using ^{131}I labelled MIP-1095 looked promising [10.98], this compound was not developed further. In contrast, several functionally antagonistic PSMA ligands labelled with ^{177}Lu have seen a rapid evolution and are currently being used in several clinical trials. Data on the latter group of radiotherapeutic agents is rapidly increasing [10.99–10.103]. Currently, published data on PSMA targeted radionuclide therapy, including data on dosimetry, the objective clinical efficacy and potential side effects and long term complications, are still preliminary and no formal clinical trials have yet been completed.

Currently, two chemically distinct but similar compounds are available, which thus far appear to have a roughly similar clinical efficacy and toxicity profile:

— PSMA-DOTA (also known as PSMA-617) [10.102, 10.103];
— PSMA-DOTAGA (also known as PSMA imaging and therapy (I&T)) [10.101].

10.3.3.1. Background information

PSMA is expressed on the cell membrane of prostate cells. In prostate cancer, it is expressed much more strongly than in normal, healthy prostate cells, thus providing a comparatively specific target in patients with prostate cancer [10.104, 10.105].

However, it needs to be remembered that PSMA is in fact a misleading moniker. PSMA is also known as glutamate carboxypeptidase II or folate hydrolase I. It is in fact expressed in a variety of healthy tissues. Furthermore, PSMA is expressed strongly in various forms of neovascularization [10.106], including diabetic retinopathy [10.104] as well as the epithelium of the neovasculature of most solid neoplasms. Furthermore, there are indications that cells of other neoplasms may also endogenously express PSMA [10.107].

Lutetium-177 labelled small antagonists of PSMA have recently received nearly unprecedented interest, especially considering that randomized, controlled clinical trials have yet to start. This is due to the high response rates in patients with PSMA positive prostate cancer, in some of whom prostate cancer with extensive distant metastases completely disappeared both on imaging and biochemically [10.108]. However, it still needs to be determined whether this evident success improves tumor-specific and/or overall survival.

10.3.3.2. Indications and contraindications

At the time of writing, PSMA RPT has no formal, registered indication and has only been tried to a certain extent in histologically proven, progressive and/or symptomatic metastasized prostate cancer.

Lutetium-177 labelled PSMA RPT still needs to be considered a highly experimental procedure. Although the very promising results in metastasized prostate cancer certainly tempt physicians and patients alike to use this procedure in earlier stages of the treatment of metastasized prostate cancer, its precise clinical efficacy as well as the short and especially long term side tolerability have yet to be established. Therefore, outside of formal trials, this treatment is generally reserved for patients who have undergone all other available accepted or registered therapeutic options. For localized disease treatments such as surgery, radiation therapy or various forms of locally ablative treatment should be preferred. For disease which has spread beyond the reach of localized therapy systemic options, including multiple lines of conventional and novel anti-hormonal drugs, chemotherapy with docetaxel and/or cabazitaxel and RPT with ^{223}Ra dichloride should be considered before turning to PSMA RPT. Of course, there may be circumstances where PSMA RPT is given before all other medical options are exhausted. These include, but are not limited to, the refusal of a patient to undergo certain treatments such as chemotherapy or the clinical judgement of the attending urologist/oncologist that PSMA RPT for a particular patient is likely to be more effective than other systemic therapies.

As the literature describes that 10–15% of prostate cancer cases are PSMA negative [10.109], patients should only be treated with PSMA targeted radionuclide therapy once the in vivo expression of PSMA on prostate cancer cells is proven. This is best done by ^{68}Ga PSMA PET/CT; for optimal theragnostic results this is likely best performed using the same compound as is used for therapy. It is not possible to provide a quantitative criterion for patient selection, as the limited studies performed thus far have not yet been able to establish a relationship between the standardized uptake value in ^{68}Ga PSMA PET/CT and response to therapy.

As PSMA RPT is an experimental drug, the precise contraindications are yet to be established firmly.

The following contraindications modified from PRRT (see above) are currently employed in clinical practice:

(a) Absolute contraindications:
    (i) Life expectancy <3 months;

(ii) Potentially myelotoxic radionuclide therapy (e.g. ^{223}Ra) or chemotherapy (e.g. docetaxel) within 6 weeks prior to planned PSMA RPT.

(b) Relative contraindications:
   (i) Thrombocyte counts $<75 \times 10^9$/L;
   (ii) Leukocyte count $<2.0 \times 10^9$/L;
   (iii) Creatinine levels >1.8 mg/dL or more than twice the upper limit of the reference range;
   (iv) Pre-existent salivary gland damage (e.g. prior radiation therapy to the head/neck, Sjögren syndrome).

10.3.3.3. Therapeutic activity

PSMA RPT is given in fractions, similar to, for example, PRRT. Cycles are given in intervals of at least 8 weeks in order to allow for recovery of the bone marrow. Currently, the standard therapy regimen for PSMA RPT consists of 3 cycles. However, this can be varied individually. Theoretical considerations have shown that cumulative activities of about 37 GBq can be given in the majority of patients; however, practical experience is still lacking here.

PSMA-DKFZ-617, which is the more frequently used compound, is usually given in well-tolerated activities of 6 GBq/cycle. For the second available compound, PSMA I&T, safe administration of activities up to 7.4 GBq/cycle has been described. There are, however, insufficient data to prescribe a specific activity per cycle — the only established constraints here are the absorbed dose limits to the critical organs (see Section 10.3.3.4). Depending on the compound used and the activity given per cycle, 4 cycles of PSMA I&T of 7.4 GBq/cycle or 6 consecutive cycles of PSMA-DKFZ-617 of 6 GBq/cycle can be given before critical cumulative dose limits will be reached.

10.3.3.4. Dosimetry

In PSMA RPT, besides prostate cancer lesions, several organs will be exposed to a significant absorbed dose. These organs are the salivary and lacrimal glands, the liver, the spleen and the kidneys [10.103]. An overview of the current knowledge about specific absorbed doses for kidneys and salivary glands of ^{177}Lu PSMA-617 and ^{177}Lu PSMA I&T is provided in Table 10.2. This table shows only the results of publications which corrected for the individual patients' organ masses. No differences can be seen between the two ligands which are in clinical use.

TABLE 10.2. ABSORBED DOSE COEFFICIENTS FOR KIDNEYS AND SALIVARY GLANDS

(courtesy of E. Verburg and M. Lassmann)

Ligand	Kidneys	Salivary glands	Reference
	Gy/GBq ± SD	Gy/GBq ± SD	
Lu-177 PSMA-617	0.6 ± 0.2	1.0 ± 0.6	[10.103, 10.115]
Lu-177 PSMA-617	0.8 ± 0.3	1.9 ± 1.2	[10.116]
Lu-177 PSMA-617	0.6 ± 0.4	0.6 ± 0.3	[10.117]
Lu-177 PSMA I&T	0.7 ± 0.2	0.6 ± 0.4	[10.118]
Lu-177 PSMA-617	0.4 ± 0.2	0.6 ± 0.4	[10.119]

The published data for absorbed doses to bone marrow are inconclusive at the time of writing. Of course, the bone marrow dose is difficult to calculate in prostate cancer patients with extensive bone metastases as the red bone marrow will receive a dose not only from circulating activity, but also from the activity taken up in the metastases adjacent to or even within the red bone marrow. This effect is, however, highly locally variable between different bone marrow regions and challenging to quantify.

Established tolerance limits for red marrow are 2 Gy (single exposure) [10.110], kidneys 28–40 Gy (depending on risk factors; data for ^{177}Lu PRRT are considered more appropriate than literature data for external beam radiotherapy (EBRT)) [10.111, 10.112] and salivary glands 35 Gy [10.113, 10.114].

The lacrimal and salivary glands are at highest risk for radiation induced dysfunction, but no validated dose tolerability limits are available for setting a threshold. Furthermore, in the case of a potentially lethal disease the function of the salivary and lacrimal glands in contrast to the metastasized prostate cancer does not immediately impact mortality despite the obvious reduction in quality of life. Hence, the kidney appears to be the dose-limiting organ. Using the standard 3 cycle therapy regimen, critical absorbed doses to organs at risk should rarely if ever be reached. However, when considering giving more than 4 therapy cycles caution should be exercised, for instance, by implementing critical organ dosimetry.

10.3.3.5. Side effects

Considering that PSMA RPT is new and as yet has not undergone structured evaluation in a formal trial, the information on potential side effects has to be considered as preliminary. In the largest multicentre series published to date, the results and side effects of 248 cycles of ^{177}Lu PSMA-617 in 145 patients were evaluated with a follow-up after therapy of up to 30 weeks (median 16 weeks) [10.102]. In this series no patient suffered a death which was attributable to PSMA therapy.

The most frequently reported adverse events in terms of side effects of therapy in this series were fatigue (12% of patients) followed by clinically reported xerostomia with 8%. Other reported side effects occurring in more than 1 patient include nausea (6%), changes in taste (4%) as well as pain in response to therapy (3%), the occurrence of ascites (1%) or peripheral edema (1%). Myelotoxicity did not appear to be a major problem with grade 4 thrombocytopenia in accordance with CTCAE version 4.03 occurring in 2% of patients and no relevant changes occurring in white blood cell counts or haemoglobin levels. Major nephrotoxicity was not observed.

In the largest series reported using PSMA I&T, toxicity in 22 patients was mostly similar, although a dry mouth was reported more often (37%). No severe (grade 3/4) haematological toxicity reactions were observed.

10.3.3.6. Results of therapy

PSMA RPT has seen some impressive results, in isolated cases resulting in a complete response to therapy [10.99]. In most patients, however, PSMA RPT does not result in complete disappearance of disease. In the same series of patients as described under side effects, follow-up for the assessment of efficacy was available in 99/145 (68%) patients. Of these patients, 45% showed a prostate-specific antigen nadir during follow-up of less than 50% of the baseline level (two of whom showed a complete biochemical response). Overall, 60% of patients showed a decline in prostate-specific antigens after therapy. The presence of visceral metastases and a strongly elevated level of alkaline phosphatase are both adverse indicators for the chance of a response to therapy. An increasing number of administered therapy cycles was associated with a higher rate of response to therapy.

For PSMA I&T, in the series referenced under side effects, a maximum decrease of prostate-specific antigen level of 30% or greater, 50% or greater and 90% or greater was seen in 56%, 33% and 11%, respectively. In 5% of patients (one patient) a complete remission was seen on imaging. Furthermore, in this

series a reduction in symptoms was seen in 58% of men who reported bone pain prior to therapy.

10.4. RADIUM-223

Details on the radionuclide decay scheme of ^{223}Ra are given in Chapter 2.

10.4.1. Radium-223 dichloride

10.4.1.1. Background information

Prostate cancer (and other malignancies) frequently metastasizes to the bones. The metastases cause an increase in osteoblastic activity. These foci of pathologically increased osteoblastic activity can be visualized using radiopharmaceuticals that accumulate into the bone matrix in proportion to osteoblastic activity such as bisphosphonates, fluoride or a calcium analogue. In the past, various radiopharmaceuticals have been marketed for palliation caused by the bone metastases, which function by reducing osteoblastic activity. Among these pharmaceuticals were ^{89}Sr or ^{153}Sm ethylene diamine tetramethylene phosphonate (EDTMP). More recently, the alpha emitter ^{223}Ra, which acts like a calcium analogue, has come onto the market. This pharmaceutical has been shown to deliver pain palliation as well as a statistically significant increase in survival [10.120].

10.4.1.2. Indications and contraindications

Radium-223 dichloride is currently only registered for symptomatic, castration resistant prostate cancer with bone metastases but no visceral metastases.

10.4.1.3. Therapeutic activity

Radium-223 dichloride is usually administered in an activity of 55 kBq/kg body weight per cycle. It is given in 6 cycles with at least 4 weeks between cycles.

10.4.1.4. Dosimetry

Two studies reported the clearance of ^{223}Ra from the blood and the excretion pathways [10.121, 10.122]. Both studies showed a rapid blood clearance and confirmed that the major excretion pathway is faecal excretion, which is not

the case for most therapeutic radiopharmaceuticals labelled with beta emitters (mostly excreted via the kidneys and the urinary tract).

An assessment of the absorbed dose to normal organs and tissues, based on pharmacokinetic modelling, showed that the bone endosteum receives the highest absorbed doses at 7.5×10^{-7} Gy/Bq for alphas and 1.1×10^{-8} Gy/Bq for beta/gammas, and absorbed doses to the red marrow are 7.2×10^{-8} Gy/Bq and 5.5×10^{-8} Gy/Bq, respectively. A dosimetry calculation based on compartment modelling [10.123] results in an absorbed dose due to alpha particles of approximately 17 Gy to the bone endosteum after a series of six treatments for a 70 kg reference person with a total administered activity of 23 MBq of ^{223}Ra. The corresponding absorbed dose to the red bone marrow is estimated to 1.7 Gy. Pacilio et al. [10.124] reported that the mean absorbed dose in bone lesions after the first injection was 0.7 Gy (range 0.2–1.9 Gy).

10.4.1.5. Side effects

The major side effects of ^{223}Ra dichloride are changes in blood counts, even though it is not clear to what extent these changes are attributable to the radiopharmaceutical or to progression of bone/bone marrow infiltrating metastases. Another major side effect is related to the uptake in the digestive system leading to increased diarrhoea and nausea.

10.5. YTTRIUM-90

Details on the radionuclide decay scheme of ^{90}Y, the corresponding photon energies and the ranges of the charged particles are given in Chapter 2. Although ^{90}Y formerly was used quite frequently for PRRT (see also Section 10.3.1), the unfavourable side effects profile compared to ^{177}Lu has largely obviated the use of this nuclide for systemic therapy. The current main application for ^{90}Y is in the form of glass or resin microspheres loaded with ^{90}Y that are used in radioembolization of primary and secondary liver malignancies [10.125–10.127].

10.5.1. Yttrium-90 labelled microspheres

10.5.1.1. Background information

Hepatocellular carcinoma (HCC) is a leading cause of cancer mortality in the world. The liver is also a common site for metastases. Radioembolization is a well established treatment option for liver cancers that are chemoresistant and unresectable. In radioembolization, radioactive microspheres are preferentially

delivered and implanted into hepatic tumours by exploiting the unique dual vascular anatomy of the liver [10.128]. The procedure, typically performed by an interventional radiologist, involves transfemoral catheterization to release the microspheres into the hepatic arterial supply. The microspheres become permanently lodged in the terminal arterioles of the tumour and the ^{90}Y beta particles irradiate the tumour cells. Because of the relatively long range of the ^{90}Y beta particles (Table 2.2) tumour cells that are not directly targeted can be eradicated. However, crossfire effects to surrounding organs are minimal because ^{90}Y has negligible associated photon emission. Prior to treatment, lung shunting of the microspheres is evaluated by surrogate imaging with ^{99m}Tc MAA that are assumed to mimic the distribution of the microspheres. The ^{99m}Tc MAA SPECT/CT imaging based estimates are sometimes used to predict the absorbed doses delivered to the tumour and normal liver parenchyma by the ^{90}Y administration.

Currently, two different products are on the market: one based on glass and the other based on resin microspheres. Although the intra-arterial delivery process is similar, there are several differences between the two devices, the most relevant being the specific activity (activity per sphere), which is much higher in the case of glass (~2500 Bq) than in resin (~50 Bq), which lowers the number of glass microspheres required for treatment. The dosimetry consequences of these differences are discussed in a review article by Cremonesi et al. [10.129]. Thus far, no randomized controlled studies exist which unequivocally show the added benefit of radioembolization in terms of patients' survival compared to other therapeutic modalities [10.125–10.127].

10.5.1.2. Indications and contraindications

Delivering external radiation to multifocal HCC and liver metastases is challenging due to damage of normal liver parenchyma traversed by incoming beams, and the need to account for motion-induced uncertainties in the radiation delivery. While non-radioactive ablative therapies and stereotactic body radiation therapy can be considered for certain unresectable hepatic tumours, radioembolization is considered a standard therapy choice for patients with unresectable liver cancer with more than three tumours and/or challenging tumour locations [10.128]. Yttrium-90 resin microspheres are currently approved [10.130] for the treatment of unresectable metastatic liver tumours from primary colorectal cancer with adjuvant intrahepatic artery chemotherapy. Yttrium-90 glass microspheres are approved [10.131] for radiation treatment or as a neoadjuvant to surgery or transplantation in patients with unresectable HCC who can have placement of appropriately positioned hepatic arterial catheters.

The device is also indicated for HCC patients with partial or branch portal vein thrombosis/occlusion when clinical evaluation warrants the treatment.

Contraindications include abdominal ascites, severe portal hypertension, prior EBRT and lung shunt fraction >20%. Absolute contraindications include decompensated liver function, hepatic encephalopathy, functional liver reserve <700 cc, pregnancy and uncorrectable liver shunt to the gastro-intestinal tract or the lungs [10.128].

10.5.1.3. Therapeutic activity

For ^{90}Y RE, assuming that all of the beta particle energy is deposited in the target tissue, and that the microspheres are permanently implanted (i.e. no redistribution), the single compartment medical internal radiation dose (MIRD) formalism for organ level dosimetry reduces to [10.132]:

$$A = D \cdot M / 49.38 \tag{10.3}$$

where A is the activity to administer (GBq), M is the mass of interest (kg) and D is the planned absorbed dose to be delivered.

For glass microspheres, the above expression is used to calculate the activity to be administered to deliver 80–150 Gy to the perfused liver volume, at the discretion of the clinician, while staying within the constraint of <30 Gy to the lung. The lung shunt fraction (defined as lung counts divided by lung plus liver counts) is estimated from pre-therapy gamma camera planar or SPECT imaging with ^{99m}Tc MAA. Then, the absorbed dose to the lungs is calculated, typically assuming a lung mass of 1 kg and approximating the activity in the lungs as the lung shunt fraction multiplied by the administered activity. The absorbed dose to the tumour is not a consideration in this planning scheme.

In the case of resin microspheres, there are three different approaches to determining the activity to be administered [10.132]: (i) the empiric method, (ii) the body surface area (BSA) method and (iii) the partition model method. The empiric method uses three standard activity levels (2, 2.5 and 3 GBq), depending on whether the tumour involvement in the liver is <25%, between 25 and 50% or >50%. Further modifiers are included that depend on the lobe that is treated and the measured lung shunt fraction, with a recommendation not to proceed if >20%. This method is no longer recommended due to safety concerns as it does not account for the liver volume or the absorbed dose to the liver. A retrospective multi-institutional evaluation of toxicity following radioembolization with resin microspheres reported that using the BSA method instead of the empiric method enhanced patient safety [10.133]. In this study, radiation induced liver disease was diagnosed in 21 out of 28 cases from one centre that used the empiric method.

The BSA method also does not consider the absorbed doses when calculating the activity to be administered, but the tumour and liver volumes are considered, which makes the method more personalized. The activity A (GBq) to administer for therapy is determined as:

$$A = \text{BSA} - 0.2 + \left(\text{Tumour volume}\right) / \left(\text{Liver volume}\right) \quad (10.4)$$

and typically ranges from 1.0–2.5 GBq.

In the partition model method, the activity to be administered is determined based on limiting absorbed doses to non-tumoural liver and lungs estimated using the MIRD formalism for organ level dosimetry. While the absorbed dose based activity planning of the partition model is highly desirable, the required segmentation of tumour and non-tumoural liver volumes and estimation of tumour-to-normal liver uptake ratio can be challenging, especially with diffuse disease. Pretreatment ^{99m}Tc MAA SPECT imaging is typically used to determine the tumour-to-normal liver uptake and either SPECT or anatomical imaging based methods are used to segment the tumour and non-tumoural liver.

10.5.1.4. Dosimetry

As the microspheres are essentially captured in the liver capillary bed, the absorbed dose to other organs is negligible, at least in theory. However, in the case of shunting (i.e. blood flowing from the artery to the veins without passing through the capillary bed) this may vary individually and should be assessed pre-therapy. In certain cases, the absorbed dose to the non-tumoural liver parenchyma can be as high as to the malignancies treated, causing side effects, as discussed below.

Some studies have shown pretreatment ^{99m}Tc MAA imaging based absorbed dose estimates to be highly predictive of response/survival in HCC [10.134, 10.135], while others have shown it to be a less reliable surrogate of the microsphere distribution and the delivered absorbed doses [10.136, 10.137]. Because of the potential for different distributions of the MAA particles and the microspheres due to various factors, absorbed dose estimates from direct ^{90}Y imaging either by PET or by bremsstrahlung SPECT imaging (Chapter 5) is expected to be more reliable for absorbed dose outcome studies. Overall, there is substantial evidence of an absorbed dose–effect relationship in ^{90}Y radioembolization as summarized in review articles [10.129, 10.138]. However, in these studies there is a wide variation in the reported threshold absorbed doses that lead to liver complications (~50–100 Gy to parenchyma) and tumour control (~50–500 Gy to tumour), potentially due to variation in factors such

as microsphere type (resin vs glass), response assessment criteria and imaging modality/parameters used when estimating the absorbed dose.

10.5.1.5. Side effects

The side effects of ^{90}Y radioembolization [10.133] are typically mild gastro-intestinal issues limited to the first 7–14 days post-treatment. There are, however, multiple potential complications that occur infrequently. Grade 3/4 liver toxicity, evaluated by assessment of liver enzymes and metabolites, typically occur in less than 10% of treatments. The most serious complication is radiation induced liver disease, which means that the remaining functional liver parenchyma is damaged by the radiation to an extent that the liver cannot perform its vital physiological functions. Also, extrahepatic accumulation of activity in the stomach or duodenum can cause ulcers and perforations. These complications, though rare, are potentially fatal; therefore, any patient receiving radioembolization should receive proper and intensive aftercare to detect such complications in time.

REFERENCES

[10.1] HERTZ, S., ROBERTS, A., Application of radioactive iodine in Graves disease, J. Clin. Invest **21** 5 (1942) 624, https://doi.org/10.1172/JCI101275

[10.2] ROSS, D.S., et al., 2016 American Thyroid Association guidelines for diagnosis and management of hyperthyroidism and other causes of thyrotoxicosis, Thyroid **26** 10 (2016) 1343–1421, https://doi.org/10.1089/thy.2016.0229

[10.3] STOKKEL, M.P., HANDKIEWICZ JUNAK, D., LASSMANN, M., DIETLEIN, M., LUSTER, M., EANM procedure guidelines for therapy of benign thyroid disease, Eur. J. Nucl. Med. Mol. Imaging **37** 11 (2010) 2218–2228, https://doi.org/10.1007/s00259-010-1536-8

[10.4] HÄNSCHEID, H., et al., EANM Dosimetry Committee series on standard operational procedures for pre-therapeutic dosimetry II. Dosimetry prior to radioiodine therapy of benign thyroid diseases, Eur. J. Nucl. Med. Mol. Imaging **40** 7 (2013) 1126–1134, https://doi.org/10.1007/s00259-013-2387-x

[10.5] ORSINI, F., et al., Personalization of radioiodine treatment for Graves' disease: A prospective, randomized study with a novel method for calculating the optimal ^{131}I-iodide activity based on target reduction of thyroid mass, Q. J. Nucl. Med. Mol. Imaging **56** 6 (2012) 496–502.

[10.6] GOOLDEN, A.W., FRASER, T.R., Treatment of thyrotoxicosis with low doses of radioactive iodine, Br. Med. J. **3** 5668 (1969) 442–443, https://doi.org/10.1136/bmj.3.5668.442

[10.7] SILBERSTEIN, E.B., et al., The SNMMI practice guideline for therapy of thyroid disease with ^{131}I 3.0, J. Nucl. Med. **53** 10 (2012) 1633–1651, https://doi.org/10.2967/jnumed.112.105148

[10.8] ALEXANDER, E.K., LARSEN, P.R., High dose of ^{131}I therapy for the treatment of hyperthyroidism caused by Graves' disease, J. Clin. Endocrinol. Metab. **87** 3 (2002) 1073–1077, https://doi.org/10.1210/jc.87.3.1073

[10.9] PETERS, H., FISCHER, C., BOGNER, U., REINERS, C., SCHLEUSENER, H., Radioiodine therapy of Graves' hyperthyroidism: Standard vs. calculated ^{131}iodine activity. Results from a prospective, randomized, multicentre study, Eur. J. Clin. Invest. **25** 3 (1995) 186–193, https://doi.org/10.1111/j.1365-2362.1995.tb01547.x

[10.10] DE JONG, J.A., VERKOOIJEN, H.M., VALK, G.D., ZELISSEN, P.M., DE KEIZER, B., High failure rates after ^{131}I therapy in Graves hyperthyroidism patients with large thyroid volumes, high iodine uptake, and high iodine turnover, Clin. Nucl. Med. **38** 6 (2013) 401–406, https://doi.org/10.1097/RLU.0b013e3182817c78

[10.11] KOBE, C., et al., Graves' disease and radioiodine therapy. Is success of ablation dependent on the achieved dose above 200 Gy? Nuklearmed. **47** 1 (2008) 13–17, https://doi.org/10.3413/nukmed-0087

[10.12] VAN ISSELT, J.W., BROEKHUIZEN-DE GAST, H.S., The radioiodine turnover rate as a determinant of radioiodine treatment outcome in Graves' disease, Hell. J. Nucl. Med. **13** 1 (2010) 2–5.

[10.13] AKTAY, R., REZAI, K., SEABOLD, J.E., BAR, R.S., KIRCHNER, P.T., Four- to twenty-four-hour uptake ratio: An index of rapid iodine-131 turnover in hyperthyroidism, J. Nucl. Med. **37** 11 (1996) 1815–1819.

[10.14] LESLIE, W.D., et al., A randomized comparison of radioiodine doses in Graves' hyperthyroidism, J. Clin. Endocrinol. Metab. **88** 3 (2003) 978–983, https://doi.org/10.1210/jc.2002-020805

[10.15] KROHN, T., et al., Maximum dose rate is a determinant of hypothyroidism after ^{131}I therapy of Graves' disease but the total thyroid absorbed dose is not, J. Clin. Endocrinol. Metab. **99** 11 (2014) 4109–4115, https://doi.org/10.1210/jc.2014-1347

[10.16] VERBURG, F.A., LUSTER, M., LASSMANN, M., REINERS, C., ^{131}I therapy in patients with benign thyroid disease does not conclusively lead to a higher risk of subsequent malignancies, Nuklearmed. **50** 3 (2011) 93–99, https://doi.org/10.3413/Nukmed-0341-10-08

[10.17] COOPER, D.S., et al., Revised American Thyroid Association management guidelines for patients with thyroid nodules and differentiated thyroid cancer, Thyroid **19** 11 (2009) 1167–1214, https://doi.org/10.1089/thy.2009.0110

[10.18] PACINI, F., et al., European consensus for the management of patients with differentiated thyroid carcinoma of the follicular epithelium, Eur. J. Endocrinol. **154** 6 (2006) 787–803, https://doi.org/10.1530/eje.1.02158

[10.19] PACINI, F., CASTAGNA, M.G., BRILLI, L., PENTHEROUDAKIS, G., Thyroid cancer: ESMO Clinical Practice Guidelines for diagnosis, treatment and follow-up, Ann. Oncol. **21** Suppl. 5 (2010) v214–v219, https://doi.org/10.1093/annonc/mdq190

[10.20] LUSTER, M., et al., Guidelines for radioiodine therapy of differentiated thyroid cancer, Eur. J. Nucl. Med. Mol. Imaging **35** 10 (2008) 1941–1959, https://doi.org/10.1007/s00259-008-0883-1

[10.21] MAZZAFERRI, E.L., JHIANG, S.M., Long-term impact of initial surgical and medical therapy on papillary and follicular thyroid cancer, Am. J. Med. **97** 5 (1994) 418–428, https://doi.org/10.1016/0002-9343(94)90321-2

[10.22] VERBURG, F.A., et al., Life expectancy is reduced in differentiated thyroid cancer patients ≥ 45 years old with extensive local tumor invasion, lateral lymph node, or distant metastases at diagnosis and normal in all other DTC patients, J. Clin. Endocrinol. Metab. **98** 1 (2013) 172–180, https://doi.org/10.1210/jc.2012-2458

[10.23] ESKANDARI, S., et al., Thyroid Na+/I- symporter. Mechanism, stoichiometry, and specificity, J. Biol. Chem. **272** 43 (1997) 27230–27238, https://doi.org/10.1074/jbc.272.43.27230

[10.24] SCHLUMBERGER, M.J., Papillary and follicular thyroid carcinoma, N. Engl. J. Med. **338** 5 (1998) 297–306, https://doi.org/10.1056/NEJM199801293380506

[10.25] VERBURG, F.A., DE KEIZER, B., LIPS, C.J., ZELISSEN, P.M., DE KLERK, J.M., Prognostic significance of successful ablation with radioiodine of differentiated thyroid cancer patients, Eur. J. Endocrinol. **152** 1 (2005) 33–37, https://doi.org/10.1530/eje.1.01819

[10.26] MAZZAFERRI, E.L., KLOOS, R.T., Clinical review 128: Current approaches to primary therapy for papillary and follicular thyroid cancer, J. Clin. Endocrinol. Metab. **86** 4 (2001) 1447–1463, https://doi.org/10.1210/jcem.86.4.7407

[10.27] TUBIANA, M., et al., Long-term results and prognostic factors in patients with differentiated thyroid carcinoma, Cancer **55** 4 (1985) 794–804, https://doi.org/10.1002/1097-0142(19850215)55:4%3C794::AID-CNCR2820550418%3E3.0.CO;2-Z

[10.28] SIMPSON, W.J., PANZARELLA, T., CARRUTHERS, J.S., GOSPODAROWICZ, M.K., SUTCLIFFE, S.B., Papillary and follicular thyroid cancer: Impact of treatment in 1578 patients, Int. J. Radiat. Oncol. Biol. Phys. **14** 6 (1988) 1063–1075, https://doi.org/10.1016/0360-3016(88)90381-1

[10.29] UTIGER, R.D., Follow-up of patients with thyroid carcinoma, N. Engl. J. Med. **337** 13 (1997) 928–931, https://doi.org/10.1056/NEJM199709253371311

[10.30] VERBURG, F.A., DIETLEIN, M., LASSMANN, M., LUSTER, M., REINERS, C., Why radioiodine remnant ablation is right for most patients with differentiated thyroid carcinoma, Eur. J. Nucl. Med. Mol. Imaging **36** 3 (2009) 343–346, https://doi.org/10.1007/s00259-008-0997-5

[10.31] SHATTUCK, T.M., WESTRA, W.H., LADENSON, P.W., ARNOLD, A., Independent clonal origins of distinct tumor foci in multifocal papillary thyroid carcinoma, N. Engl. J. Med. **352** 23 (2005) 2406–2412, https://doi.org/10.1056/NEJMoa044190

[10.32] SHERMAN, S.I., TIELENS, E.T., SOSTRE, S., WHARAM, M.D., Jr., LADENSON, P.W., Clinical utility of posttreatment radioiodine scans in the management of patients with thyroid carcinoma, J. Clin. Endocrinol. Metab. **78** 3 (1994) 629–634, https://doi.org/10.1210/jcem.78.3.8126134

[10.33] TENENBAUM, F., CORONE, C., SCHLUMBERGER, M., PARMENTIER, C., Thyroglobulin measurement and postablative iodine-131 total body scan after total thyroidectomy for differentiated thyroid carcinoma in patients with no evidence of disease, Eur. J. Cancer **32A** 7 (1996) 1262, https://doi.org/10.1016/0959-8049(96)00020-2

[10.34] TRAVAGLI, J.P., et al., Combination of radioiodine (131)I and probe-guided surgery for persistent or recurrent thyroid carcinoma, J. Clin. Endocrinol. Metab. **83** 8 (1998) 2675–2680, https://doi.org/10.1210/jcem.83.8.5014

[10.35] TAYLOR, T., et al., Outcome after treatment of high-risk papillary and non-Hürthle-cell follicular thyroid carcinoma, Ann. Intern. Med. **129** 8 (1998) 622–627, https://doi.org/10.7326/0003-4819-129-8-199810150-00007

[10.36] HAY, I.D., et al., Papillary thyroid carcinoma managed at the Mayo Clinic during six decades (1940–1999): Temporal trends in initial therapy and long-term outcome in 2444 consecutively treated patients, World J. Surg. **26** 8 (2002) 879–885, https://doi.org/10.1007/s00268-002-6612-1

[10.37] SAWKA, A.M., et al., Clinical review 170: A systematic review and metaanalysis of the effectiveness of radioactive iodine remnant ablation for well-differentiated thyroid cancer, J. Clin. Endocrinol. Metab. **89** 3 (2004) 3668–3676, https://doi.org/10.1210/jc.2003-031167

[10.38] PACINI, F., et al., Post-surgical use of radioiodine ^{131}I in patients with papillary and follicular thyroid cancer and the issue of remnant ablation: A consensus report, Eur. J. Endocrinol. **153** 5 (2005) 651–659, https://doi.org/10.1530/eje.1.02014

[10.39] ROSÁRIO, P.W., et al., Is adjuvant therapy useful in patients with papillary carcinoma smaller than 2 cm? Thyroid **17** 12 (2007) 1225–1228, https://doi.org/10.1089/thy.2006.0254

[10.40] SAWKA, A.M., et al., An updated systematic review and commentary examining the effectiveness of radioactive iodine remnant ablation in well-differentiated thyroid cancer, Endocrinol. Metab. Clin. North Am. **37** 2 (2008) 457–480, https://doi.org/10.1016/j.ecl.2008.02.007

[10.41] DeGROOT, L.J., KAPLAN, E.L., SHUKLA, M.S., SALTI, G., STRAUS, F.H., Morbidity and mortality in follicular thyroid cancer, J. Clin. Endocrinol. Metab. **80** 10 (1995) 2946–2953, https://doi.org/10.1210/jcem.80.10.7559879

[10.42] MAZZAFERRI, E.L., Thyroid remnant ^{131}I ablation for papillary and follicular thyroid carcinoma, Thyroid **7** 2 (1997) 265–271, https://doi.org/10.1089/thy.1997.7.265

[10.43] SAMAAN, N.A., et al., The results of various modalities of treatment of well differentiated thyroid carcinomas: A retrospective review of 1599 patients, J. Clin. Endocrinol. Metab. **75** 3 (1992) 714–720, https://doi.org/10.1210/jc.75.3.714

[10.44] ROBBINS, R.J., et al., Real-time prognosis for metastatic thyroid carcinoma based on 2-[^{18}F]fluoro-2-deoxy-D-glucose-positron emission tomography scanning, J. Clin. Endocrinol. Metab. **91** 2 (2006) 498–505, https://doi.org/10.1210/jc.2005-1534

[10.45] DEMIDCHIK, Y.E., et al., Comprehensive clinical assessment of 740 cases of surgically treated thyroid cancer in children of Belarus, Ann. Surg. **243** 4 (2006) 525–532, https://doi.org/10.1097/01.sla.0000205977.74806.0b

[10.46] REINERS, C., DEMIDCHIK, Y.E., DROZD, V.M., BIKO, J., Thyroid cancer in infants and adolescents after Chernobyl, Minerva Endocrinol. **33** 4 (2008) 381–395.

[10.47] DOTTORINI, M.E., LOMUSCIO, G., MAZZUCCHELLI, L., VIGNATI, A., COLOMBO, L., Assessment of female fertility and carcinogenesis after iodine-131 therapy for differentiated thyroid carcinoma, J. Nucl. Med. **36** 1 (1995) 21–27.

[10.48] HAY, I.D., et al., Long-term outcome in 215 children and adolescents with papillary thyroid cancer treated during 1940 through 2008, World J. Surg. **34** 6 (2010) 1192–1202, https://doi.org/10.1007/s00268-009-0364-0

[10.49] BIKO, J., et al., Favourable course of disease after incomplete remission on ^{131}I therapy in children with pulmonary metastases of papillary thyroid carcinoma: 10 years follow-up, Eur. J. Nucl. Med. Mol. Imaging **38** 4 (2011) 651–655, https://doi.org/10.1007/s00259-010-1669-9

[10.50] VERBURG, F.A., et al., Dosimetry-guided high-activity ^{131}I therapy in patients with advanced differentiated thyroid carcinoma: Initial experience, Eur. J. Nucl. Med. Mol. Imaging **37** 5 (2010) 896–903, https://doi.org/10.1007/s00259-009-1303-x

[10.51] LASSMANN, M., REINERS, C., LUSTER, M., Dosimetry and thyroid cancer: The individual dosage of radioiodine, Endocr. Relat. Cancer **17** 3 (2010) R161–R172, https://doi.org/10.1677/ERC-10-0071

[10.52] SEIDLIN, S.M., MARINELLI, L.D., OSHRY, E., Radioactive iodine therapy: Effect on functioning metastases of adenocarcinoma of the thyroid, J. Am. Med. Assoc. **132** 14 (1946) 838–847, https://doi.org/10.1001/jama.1946.02870490016004

[10.53] HAUGEN, B.R., et al., 2015 American Thyroid Association management guidelines for adult patients with thyroid nodules and differentiated thyroid cancer: The American Thyroid Association guidelines task force on thyroid nodules and differentiated thyroid cancer, Thyroid **26** 1 (2016) 1–133, https://doi.org/10.1089/thy.2015.0020

[10.54] TUTTLE, R.M., et al., Thyroid carcinoma, J. Natl. Compr. Cancer Netw. **8** 11 (2010) 1228–1274, https://doi.org/10.6004/jnccn.2010.0093

[10.55] DOI, S.A., WOODHOUSE, N.J., THALIB, L., ONITILO, A., Ablation of the thyroid remnant and I-131 dose in differentiated thyroid cancer: A meta-analysis revisited, Clin. Med. Res. **5** 2 (2007) 87–90, https://doi.org/10.3121/cmr.2007.763

[10.56] HACKSHAW, A., HARMER, C., MALLICK, U., HAQ, M., FRANKLYN, J.A., ^{131}I activity for remnant ablation in patients with differentiated thyroid cancer: A systematic review, J. Clin. Endocrinol. Metab. **92** 1 (2007) 28–38, https://doi.org/10.1210/jc.2006-1345

[10.57] VERBURG, F.A., MÄDER, U., REINERS, C., HÄNSCHEID, H., Long-term survival in differentiated thyroid cancer is worse after low-activity initial post-surgical ^{131}I therapy in both high- and low-risk patients, J. Clin. Endocrinol. Metab. **99** 12 (2014) 4487–4496, https://doi.org/10.1210/jc.2014-1631

[10.58] SCHLUMBERGER, M., et al., Radioactive iodine treatment and external radiotherapy for lung and bone metastases from thyroid carcinoma, J. Nucl. Med. **37** 4 (1996) 598–605.

[10.59] MENZEL, C., et al., "High-dose" radioiodine therapy in advanced differentiated thyroid carcinoma, J. Nucl. Med. **37** 9 (1996) 1496–1503.

[10.60] VAN NOSTRAND, D., "Radioiodine treatment of distant metastases", Thyroid Cancer: A Comprehensive Guide to Clinical Management (WARTOFSKY, L., Ed.), Humana Press, Totowa, NJ (2006) 411–425, https://doi.org/10.1007/978-1-59259-995-0_47

[10.61] SAMUEL, A.M., RAJASHEKHARRAO, B., SHAH, D.H., Pulmonary metastases in children and adolescents with well-differentiated thyroid cancer, J. Nucl. Med. **39** 9 (1998) 1531–1536.

[10.62] CHIESA, C., et al., Individualized dosimetry in the management of metastatic differentiated thyroid cancer, Q. J. Nucl. Med. Mol. Imaging **53** 5 (2009) 546–561.

[10.63] THIES, E.-D., et al., The number of ^{131}I therapy courses needed to achieve complete remission is an indicator of prognosis in patients with differentiated thyroid carcinoma, Eur. J. Nucl. Med. Mol. Imaging **41** 12 (2014) 2281–2290, https://doi.org/10.1007/s00259-014-2851-2

[10.64] HÄNSCHEID, H., et al., Iodine biokinetics and dosimetry in radioiodine therapy of thyroid cancer: Procedures and results of a prospective international controlled study of ablation after rhTSH or hormone withdrawal, J. Nucl. Med. **47** 4 (2006) 648–654.

[10.65] BENUA, R.S., CICALE, N.R., SONENBERG, M., RAWSON, R.W., The relation of radioiodine dosimetry to results and complications in the treatment of metastatic thyroid cancer, Am. J. Roentgenol. Radium Ther. Nucl. Med. **87** (1962) 171–182.

[10.66] DORN, R., et al., Dosimetry-guided radioactive iodine treatment in patients with metastatic differentiated thyroid cancer: Largest safe dose using a risk-adapted approach, J. Nucl. Med. **44** 3 (2003) 451–456.

[10.67] TUTTLE, R.M., et al., Empiric radioactive iodine dosing regimens frequently exceed maximum tolerated activity levels in elderly patients with thyroid cancer, J. Nucl. Med. **47** 10 (2006) 1587–1591.

[10.68] KULKARNI, K., et al., The relative frequency in which empiric dosages of radioiodine would potentially overtreat or undertreat patients who have metastatic well-differentiated thyroid cancer, Thyroid **16** 10 (2006) 1019–1023, https://doi.org/10.1089/thy.2006.16.1019

[10.69] HÄNSCHEID, H., LASSMANN, M., LUSTER, M., KLOOS, R., REINERS, C., Blood dosimetry from a single measurement of the whole body radioiodine retention in patients with differentiated thyroid carcinoma, Endocr. Relat. Cancer **16** 4 (2009) 1283–1289, https://doi.org/10.1677/ERC-09-0076

[10.70] HÄNSCHEID, H., et al., Success of the postoperative ^{131}I therapy in young Belarusian patients with differentiated thyroid cancer after Chernobyl depends on the radiation absorbed dose to the blood and the thyroglobulin level, Eur. J. Nucl. Med. Mol. Imaging **38** 7 (2011) 1296–1302, https://doi.org/10.1007/s00259-011-1788-y

[10.71] VERBURG, F.A., et al., The absorbed dose to the blood is a better predictor of ablation success than the administered 131I activity in thyroid cancer patients, Eur. J. Nucl. Med. Mol. Imaging **38** 4 (2011) 673–680, https://doi.org/10.1007/s00259-010-1689-5

[10.72] VAN NOSTRAND, D., et al., Dosimetrically determined doses of radioiodine for the treatment of metastatic thyroid carcinoma, Thyroid **12** 2 (2002) 121–134, https://doi.org/10.1089/105072502753522356

[10.73] MAXON, H.R., et al., Relation between effective radiation dose and outcome of radioiodine therapy for thyroid cancer, N. Engl. J. Med. **309** 16 (1983) 937–941, https://doi.org/10.1056/NEJM198310203091601

[10.74] MAXON, H.R., III, et al., Radioiodine-131 therapy for well-differentiated thyroid cancer–a quantitative radiation dosimetric approach: Outcome and validation in 85 patients, J. Nucl. Med. **33** 6 (1992) 1132–1136.

[10.75] JENTZEN, W., et al., ^{124}I PET assessment of response of bone metastases to initial radioiodine treatment of differentiated thyroid cancer, J. Nucl. Med. **57** 10 (2016) 1499–1504, https://doi.org/10.2967/jnumed.115.170571

[10.76] SGOUROS, G., et al., Patient-specific dosimetry for ^{131}I thyroid cancer therapy using ^{124}I PET and 3-dimensional-internal dosimetry (3D-ID) software, J. Nucl. Med. **45** 8 (2004) 1366–1372.

[10.77] BOLCH, W.E., ECKERMAN, K.F., SGOUROS, G., THOMAS, S.R., MIRD Pamphlet No. 21: A generalized schema for radiopharmaceutical dosimetry — standardization of nomenclature, J. Nucl. Med. **50** 3 (2009) 477–484, https://doi.org/10.2967/jnumed.108.056036

[10.78] PRIDEAUX, A.R., et al., Three-dimensional radiobiologic dosimetry: Application of radiobiologic modeling to patient-specific 3-dimensional imaging-based internal dosimetry, J. Nucl. Med. **48** 6 (2007) 1008–1016, https://doi.org/10.2967/jnumed.106.038000

[10.79] CLEMENT, S.C., et al., Intermediate and long-term adverse effects of radioiodine therapy for differentiated thyroid carcinoma — a systematic review, Cancer Treat. Rev. **41** 10 (2015) 925–934, https://doi.org/10.1016/j.ctrv.2015.09.001

[10.80] SEIDLIN, S.M., SIEGAL, E., YALOW, A.A., MELAMED, S., Acute myeloid leukemia following prolonged iodine-131 therapy for metastatic thyroid carcinoma, Science **123** 3201 (1956) 800–801, https://doi.org/10.1126/science.123.3201.800

[10.81] IYER, N.G., MORRIS, L.G., TUTTLE, R.M., SHAHA, A.R., GANLY, I., Rising incidence of second cancers in patients with low-risk (T1N0) thyroid cancer who receive radioactive iodine therapy, Cancer **117** 19 (2011) 4439–4446, https://doi.org/10.1002/cncr.26070

[10.82] VERKOOIJEN, R.B., SMIT, J.W., ROMIJN, J.A., STOKKEL, M.P., The incidence of second primary tumors in thyroid cancer patients is increased, but not related to treatment of thyroid cancer, Eur. J. Endocrinol. **155** 6 (2006) 801–806, https://doi.org/10.1530/eje.1.02300

[10.83] REINERS, C., et al., Twenty-five years after Chernobyl: Outcome of radioiodine treatment in children and adolescents with very high-risk radiation-induced differentiated thyroid carcinoma, J. Clin. Endocrinol. Metab. **98** 7 (2013) 3039–3048, https://doi.org/10.1210/jc.2013-1059

[10.84] WAFELMAN, A.R., HOEFNAGEL, C.A., MAES, R.A., BEIJNEN, J.H., Radioiodinated metaiodobenzylguanidine: A review of its biodistribution and pharmacokinetics, drug interactions, cytotoxicity and dosimetry, Eur. J. Nucl. Med. **21** 6 (1994) 545–559, https://doi.org/10.1007/BF00173043

[10.85] GIAMMARILE, F., CHITI, A., LASSMANN, M., BRANS, B., FLUX, G., EANM procedure guidelines for ^{131}I-meta-iodobenzylguanidine (131I-mIBG) therapy, Eur. J. Nucl. Med. Mol. Imaging **35** 5 (2008) 1039–1047, https://doi.org/10.1007/s00259-008-0715-3

[10.86] FLUX, G., CHITTENDEN, S., SARAN, F., GAZE, M., Clinical applications of dosimetry for mIBG therapy, Q. J. Nucl. Med. Mol. Imaging **55** 2 (2011) 116–125.

[10.87] BUCKLEY, S.E., CHITTENDEN, S.J., SARAN, F.H., MELLER, S.T., FLUX, G.D., Whole-body dosimetry for individualized treatment planning of ^{131}I-MIBG radionuclide therapy for neuroblastoma, J. Nucl. Med. **50** 9 (2009) 1518–1524, https://doi.org/10.2967/jnumed.109.064469

[10.88] CHIESA, C., CASTELLANI, R., MIRA, M., LORENZONI, A., FLUX, G., Dosimetry in ^{131}I-mIBG therapy: Moving toward personalized medicine, Q. J. Nucl. Med. Mol. Imaging **57** 2 (2013) 161–170.

[10.89] REUBI, J.C., et al., Affinity profiles for human somatostatin receptor subtypes SST1–SST5 of somatostatin radiotracers selected for scintigraphic and radiotherapeutic use, Eur. J. Nucl. Med. **27** 3 (2000) 273–282, https://doi.org/10.1007/s002590050034

[10.90] BODEI, L., et al., Long-term tolerability of PRRT in 807 patients with neuroendocrine tumours: The value and limitations of clinical factors, Eur. J. Nucl. Med. Mol. Imaging **42** 1 (2015) 5–19, https://doi.org/10.1007/s00259-014-2893-5

[10.91] STROSBERG, J., et al., Phase 3 trial of ^{177}Lu-Dotatate for midgut neuroendocrine tumors, N. Engl. J. Med. **376** 2 (2017) 125–135, https://doi.org/10.1056/NEJMoa1607427

[10.92] KWEKKEBOOM, D.J., et al., ENETS consensus guidelines for the standards of care in neuroendocrine tumors: Peptide receptor radionuclide therapy with radiolabeled somatostatin analogs, Neuroendocrinology **90** 2 (2009) 220–226, https://doi.org/10.1159/000225951

[10.93] EBERLEIN, U., CREMONESI, M., LASSMANN, M., Individualized dosimetry for theranostics: necessary, nice to have, or counterproductive? J. Nucl. Med. **58** Suppl. 2 (2017) 97S–103S, https://doi.org/10.2967/jnumed.116.186841

[10.94] KWEKKEBOOM, D.J., et al., [^{177}Lu-DOTAOTyr3]octreotate: Comparison with [^{111}In-DTPAo]octreotide in patients, Eur. J. Nucl. Med. **28** 9 (2001) 1319–1325, https://doi.org/10.1007/s002590100574

[10.95] WERNER, R.A., et al., The impact of ^{177}Lu-octreotide therapy on ^{99m}Tc-MAG3 clearance is not predictive for late nephropathy, Oncotarget. **7** 27 (2016) 41233–41241, https://doi.org/10.18632/oncotarget.9775

[10.96] OSBORNE, J.R., et al., A prospective pilot study of ^{98}Zr-J591/prostate specific membrane antigen positron emission tomography in men with localized prostate cancer undergoing radical prostatectomy, J. Urol. **191** 5 (2014) 1439–1445, https://doi.org/10.1016/j.juro.2013.10.041

[10.97] TAGAWA, S.T., et al., Phase II study of Lutetium-177-labeled anti-prostate-specific membrane antigen monoclonal antibody J591 for metastatic castration-resistant prostate cancer, Clin. Cancer Res. **19** 18 (2013) 5182–5191, https://doi.org/10.1158/1078-0432.CCR-13-0231

[10.98] ZECHMANN, C.M., et al., Radiation dosimetry and first therapy results with a (124) I/(131)I-labeled small molecule (MIP-1095) targeting PSMA for prostate cancer therapy, Eur. J. Nucl. Med. Mol. Imaging **41** 7 (2014) 1280–1292, https://doi.org/10.1007/s00259-014-2713-y

[10.99] KRATOCHWIL, C., et al., [^{177}Lu]Lutetium-labelled PSMA ligand-induced remission in a patient with metastatic prostate cancer, Eur. J. Nucl. Med. Mol. Imaging **42** 6 (2015) 987–988, https://doi.org/10.1007/s00259-014-2978-1

[10.100] WEINEISEN, M., SIMECEK, J., SCHOTTELIUS, M., SCHWAIGER, M., WESTER, H.-J., Synthesis and preclinical evaluation of DOTAGA-conjugated PSMA ligands for functional imaging and endoradiotherapy of prostate cancer, EJNMMI. Res. **4** 1 (2014) 63, https://doi.org/10.1186/s13550-014-0063-1

[10.101] WEINEISEN, M., et al., ^{68}Ga- and ^{177}Lu-labeled PSMA I&T: Optimization of a PSMA-targeted theranostic concept and first proof-of-concept human studies, J. Nucl. Med. **56** 8 (2015) 1169–1176, https://doi.org/10.2967/jnumed.115.158550

[10.102] AHMADZADEHFAR, H., et al., Early side effects and first results of radioligand therapy with ^{177}Lu-DKFZ-617 PSMA of castrate-resistant metastatic prostate cancer: A two-centre study, EJNMMI. Res. **5** 1 (2015) 114, https://doi.org/10.1186/s13550-015-0114-2

[10.103] DELKER, A., et al., Dosimetry for ^{177}Lu-DKFZ-PSMA-617: A new radiopharmaceutical for the treatment of metastatic prostate cancer, Eur. J. Nucl. Med. Mol. Imaging **43** 1 (2016) 42–51, https://doi.org/10.1007/s00259-015-3174-7

[10.104] GHOSH, A., HESTON, W.D., Tumor target prostate specific membrane antigen (PSMA) and its regulation in prostate cancer, J. Cell. Biochem. **91** 3 (2004) 528–539, https://doi.org/10.1002/jcb.10661

[10.105] MARCHAL, C., et al., Expression of prostate specific membrane antigen (PSMA) in prostatic adenocarcinoma and prostatic intraepithelial neoplasia, Histol. Histopathol. **19** 3 (2004) 715–718.

[10.106] CHANG, S.S., et al., Five different anti-prostate-specific membrane antigen (PSMA) antibodies confirm PSMA expression in tumor-associated neovasculature, Cancer Res. **59** 13 (1999) 3192–3198.

[10.107] VERBURG, F.A., KROHN, T., HEINZEL, A., MOTTAGHY, F.M., BEHRENDT, F.F., First evidence of PSMA expression in differentiated thyroid cancer using [^{68}Ga]PSMA-HBED-CC PET/CT, Eur. J. Nucl. Med. Mol. Imaging **42** 10 (2015) 1622–1623, https://doi.org/10.1007/s00259-015-3065-y

[10.108] KRATOCHWIL, C., et al., 225Ac-PSMA-617 for PSMA-targeted alpha-radiation therapy of metastatic castration-resistant prostate cancer, J. Nucl. Med. **57** 12 (2016) 1941–1944, https://doi.org/10.2967/jnumed.116.178673

[10.109] SILVER, D.A., PELLICER, I., FAIR, W.R., HESTON, W.D., CORDON-CARDO, C., Prostate-specific membrane antigen expression in normal and malignant human tissues, Clin. Cancer Res. **3** 1 (1997) 81–85.

[10.110] EMAMI, B., et al., Tolerance of normal tissue to therapeutic irradiation, Int. J. Radiat. Oncol. Biol. Phys. **21** 1 (1991) 109–122, https://doi.org/10.1016/0360-3016(91)90171-Y

[10.111] BODEI, L., et al., Long-term evaluation of renal toxicity after peptide receptor radionuclide therapy with ^{90}Y-DOTATOC and ^{177}Lu-DOTATATE: The role of associated risk factors, Eur. J. Nucl. Med. Mol. Imaging **35** 10 (2008) 1847–1856, https://doi.org/10.1007/s00259-008-0778-1

[10.112] CREMONESI, M., et al., Correlation of dose with toxicity and tumour response to ^{90}Y- and ^{177}Lu-PRRT provides the basis for optimization through individualized treatment planning, Eur. J. Nucl. Med. Mol. Imaging **45** 13 (2018) 2426–2441, https://doi.org/10.1007/s00259-018-4044-x

[10.113] HEY, J., et al., Parotid gland-recovery after radiotherapy in the head and neck region — 36 months follow-up of a prospective clinical study, Radiat. Oncol. **6** 1 (2011) 125, https://doi.org/10.1186/1748-717X-6-125

[10.114] DEASY, J.O., et al., Radiotherapy dose–volume effects on salivary gland function, Int. J. Radiat. Oncol. Biol. Phys. **76** 3 Suppl. 3 (2010) S58–S63, https://doi.org/10.1016/j.ijrobp.2009.06.090

[10.115] FENDLER, W.P., et al., Preliminary experience with dosimetry, response and patient reported outcome after ^{177}Lu-PSMA-617 therapy for metastatic castration-resistant prostate cancer, Oncotarget **8** 2 (2017) 3581–3590, https://doi.org/10.18632/oncotarget.12240

[10.116] KABASAKAL, L., et al., Lu-177-PSMA-617 prostate-specific membrane antigen inhibitor therapy in patients with castration-resistant prostate cancer: Stability, bio-distribution and dosimetry, Mol. Imaging Radionucl. Ther. **26** 2 (2017) 62–68, https://doi.org/10.4274/mirt.08760

[10.117] SCARPA, L., et al., The ^{68}Ga/^{177}Lu theragnostic concept in PSMA targeting of castration-resistant prostate cancer: Correlation of SUV_{max} values and absorbed dose estimates, Eur. J. Nucl. Med. Mol. Imaging **44** 5 (2017) 788–800, https://doi.org/10.1007/s00259-016-3609-9

[10.118] OKAMOTO, S., et al., Radiation dosimetry for ^{177}Lu-PSMA I&T in metastatic castration-resistant prostate cancer: Absorbed dose in normal organs and tumor lesions, J. Nucl. Med. **58** 3 (2017) 445–450, https://doi.org/10.2967/jnumed.116.178483

[10.119] VIOLET, J., et al., Dosimetry of ^{177}Lu-PSMA-617 in metastatic castration-resistant prostate cancer: Correlations between pretherapeutic imaging and whole-body tumor dosimetry with treatment outcomes, J. Nucl. Med. **60** 4 (2019) 517–523, https://doi.org/10.2967/jnumed.118.219352

[10.120] PARKER, C., et al., Alpha emitter radium-223 and survival in metastatic prostate cancer, N. Engl. J. Med. **369** 3 (2013) 213–223, https://doi.org/10.1056/NEJMoa1213755

[10.121] CHITTENDEN, S.J., et al., A phase 1, open-label study of the biodistribution, pharmacokinetics, and dosimetry of ^{223}Ra-dichloride in patients with hormone-refractory prostate cancer and skeletal metastases, J. Nucl. Med. **56** 9 (2015) 1304–1309, https://doi.org/10.2967/jnumed.115.157123

[10.122] CARRASQUILLO, J.A., et al., Phase I pharmacokinetic and biodistribution study with escalating doses of ^{223}Ra-dichloride in men with castration-resistant metastatic prostate cancer, Eur. J. Nucl. Med. Mol. Imaging **40** 9 (2013) 1384–1393, https://doi.org/10.1007/s00259-013-2427-6

[10.123] LASSMANN, M., NOSSKE, D., Dosimetry of ^{223}Ra-chloride: Dose to normal organs and tissues, Eur. J. Nucl. Med. Mol. Imaging **40** 2 (2013) 207–212, https://doi.org/10.1007/s00259-012-2265-y

[10.124] PACILIO, M., et al., Dosimetry of bone metastases in targeted radionuclide therapy with alpha-emitting ^{223}Ra-dichloride, Eur. J. Nucl. Med. Mol. Imaging **43** 1 (2016) 21–33, https://doi.org/10.1007/s00259-015-3150-2

[10.125] VAN HAZEL, G.A., et al., SIRFLOX: Randomized phase III trial comparing first-line mFOLFOX6 (plus or minus bevacizumab) versus mFOLFOX6 (plus or minus bevacizumab) plus selective internal radiation therapy in patients with metastatic colorectal cancer, J. Clin. Oncol. **34** 15 (2016) 1723–1731, https://doi.org/10.1200/JCO.2015.66.1181

[10.126] WASAN, H.S., et al., First-line selective internal radiotherapy plus chemotherapy versus chemotherapy alone in patients with liver metastases from colorectal cancer (FOXFIRE, SIRFLOX, and FOXFIRE-Global): A combined analysis of three multicentre, randomised, phase 3 trials, Lancet Oncol. **18** 9 (2017) 1159–1171.

[10.127] VILGRAIN, V., et al., Efficacy and safety of selective internal radiotherapy with yttrium-90 resin microspheres compared with sorafenib in locally advanced and inoperable hepatocellular carcinoma (SARAH): An open-label randomised controlled phase 3 trial, Lancet Oncol. **18** 12 (2017) 1624–1636.

[10.128] KENNEDY, A., Radioembolization of hepatic tumors, J. Gastrointest. Oncol. **5** 3 (2014) 178–189.

[10.129] CREMONESI, M., et al., Radioembolization of hepatic lesions from a radiobiology and dosimetric perspective, Front. Oncol. **4** (2014) 210, https://doi.org/10.3389/fonc.2014.00210

[10.130] SIRTEX MEDICAL LIMITED, SIR-Spheres® Y-90 resin microspheres (Yttrium-90 microspheres) (2017) 1–3, https://www.sirtex.com/media/55rprxv2/ssl-us-14-sir-spheres-microspheres-ifu-us.pdf

[10.131] BOSTON SCIENTIFIC, TheraSphere® Yttrium-90 Glass Microspheres (2014), 1–32, https://www.bostonscientific.com/content/dam/elabeling/pi/OTT-00221_Rev1_TheraSphere_en_s.pdf

[10.132] DEZARN, W.A., et al., Recommendations of the American Association of Physicists in Medicine on dosimetry, imaging, and quality assurance procedures for ^{90}Y microsphere brachytherapy in the treatment of hepatic malignancies, Med. Phys. **38** 8 (2011) 4824–4845, https://doi.org/10.1118/1.3608909

[10.133] KENNEDY, A.S., et al., Treatment parameters and outcome in 680 treatments of internal radiation with resin ^{90}Y-microspheres for unresectable hepatic tumors, Int. J. Radiat. Oncol. Biol. Phys. **74** 5 (2009) 1494–1500, https://doi.org/10.1016/j.ijrobp.2008.10.005

[10.134] CHIESA, C., et al., Radioembolization of hepatocarcinoma with ^{90}Y glass microspheres: Development of an individualized treatment planning strategy based on dosimetry and radiobiology, Eur. J. Nucl. Med. Mol. Imaging **42** 11 (2015) 1718–1738, https://doi.org/10.1007/s00259-015-3068-8

[10.135] GARIN, E., et al., Dosimetry based on ^{99m}Tc-macroaggregated albumin SPECT/CT accurately predicts tumor response and survival in hepatocellular carcinoma patients treated with ^{90}Y-loaded glass microspheres: Preliminary results, J. Nucl. Med. **53** 2 (2012) 255–263, https://doi.org/10.2967/jnumed.111.094235

[10.136] MIKELL, J.K., MAJDALANY, B.S., OWEN, D., PARADIS, K.C., DEWARAJA, Y.K., Assessing spatial concordance between theranostic pairs using phantom and patient-specific acceptance criteria: Application to ^{99m}Tc-MAA SPECT/^{90}Y-microsphere PET, Int. J. Radiat. Oncol. Biol. Phys. **104** 5 (2019) 1133–1140, https://doi.org/10.1016/j.ijrobp.2019.04.012

[10.137] WONDERGEM, M., et al., ^{99m}Tc-macroaggregated albumin poorly predicts the intrahepatic distribution of 90Y resin microspheres in hepatic radioembolization, J. Nucl. Med. **54** 8 (2013) 1294–1301, https://doi.org/10.2967/jnumed.112.117614

[10.138] BASTIAANNET, R., et al., The physics of radioembolization, EJNMMI Phys. **5** 1 (2018) 22, https://doi.org/10.1186/s40658-018-0221-z

Chapter 11

IMPLEMENTING DOSIMETRY IN THE CLINIC

M. BARDIÈS, E. MORA RAMIREZ, G. SGOUROS, M. KONIJNENBERG

Clinical dosimetry is a multistep procedure (see Fig. 11.1); each step is essential to obtain an accurate estimate of the absorbed dose delivered to one or more tumours or normal tissues.

The first step in the clinical dosimetry workflow is the calibration procedure (step 1). This is a prerequisite for activity determination and may require phantom image acquisition with a known amount of activity that should ideally be traceable to a standard laboratory. Procedures for obtaining quantitative information on the activity or activity concentration from images were presented in Chapter 4 and will include sensitivity determination and may include partial volume and dead time corrections. The calibration procedure is a key step in accurately determining the activity distribution. The calibration step and patient image/data acquisition step (step 2) are linked; the camera settings used in the quantitative imaging calibration procedure should be used for all patient imaging. For single photon emission computed tomography (SPECT) quantitative imaging this may mean that the acquisition matrix size, the type of collimator or the number and position of energy windows should remain constant between phantom calibration and patient imaging. Calibration should be repeated whenever the acquisition

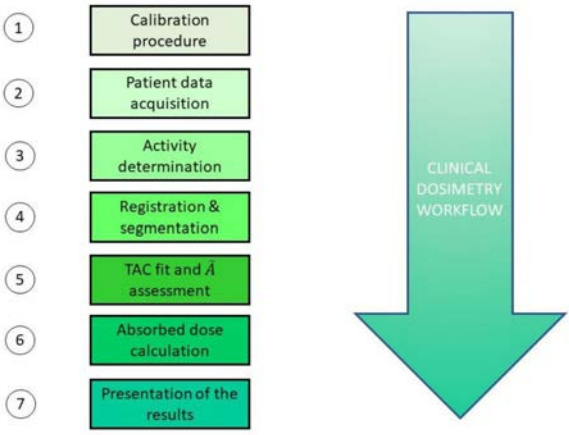

FIG. 11.1. Clinical dosimetry workflow.

device (counter or gamma camera) experiences changes that may impact its performances (e.g. hardware or software upgrades).

The procedures used in steps 1 and 2 vary substantially across different institutions and potentially across radiopharmaceutical therapy agents. Standardization and consensus protocols [11.1–11.7] are essential in enabling comparison of absorbed dose values obtained at different centres and for different agents.

The activity determination (step 3) is the phase leading from the raw acquired counts or voxel values to activity. Depending on step 2 this may be done for non-imaging procedures, or for 2-D (pixel) or 3-D (voxel) images. Reconstruction (SPECT) and corrections for the various effects that limit the quantitative information of images are performed at this stage and were presented in Chapter 4. Even though the final voxel values may be in counts (such as those of a typical reconstructed SPECT image) and not in units of activity, it should be possible to derive the voxel activity at the end of this step (e.g. via a calibration factor).

As for the first two steps in Fig. 11.1, it is important to implement the same processing and reconstruction parameters for calibration and patient images. Step 4 is only relevant in the case of image based dosimetry. It allows the determination of activity from regions or volumes of interest (VOIs) by segmenting and registering images acquired at different time points. This is essential to derive time activity curves, as discussed in Chapter 6. In some commercial software, co-registration is one of the first steps, because in sequential imaging it is preferable to represent all images in a common coordinate frame, allowing for one set of VOIs to be used for all images. Depending on the algorithms implemented, these four steps lead to the characterization of the activity present in the patient in various organs/regions/tissues of interest (or in the locations represented by the voxel positions) at different time points.

The time-integrated activity (TIA) (formerly termed cumulated activity) in a source region r_S, $\tilde{A}(r_S)$, or the time-integrated activity coefficient (formerly residence time) $\tilde{a}(r_S)$ (step 5) are calculated by integrating the time activity curves derived from sequential activity measurements (probes) or from various VOIs in patient images. There are several ways to assess the TIA, depending on how the integration is performed between time points and how extrapolation is dealt with before the first and after the last time points. Depending on the software, this can be achieved for VOIs or at the voxel level. In most scenarios the same set of VOIs is used for all time point images, assuming that the mass does not change over the imaging period. However, if the VOIs are defined for each imaging time point, any change in organ mass and shape can be considered in the dosimetric calculation.

The absorbed dose calculation (step 6) can be performed in different ways as described in Chapter 7, using pre-computed values (*S* values) or by implementing different algorithms (local energy deposition, convolution in homogeneous or heterogeneous media, Monte Carlo modelling of radiation transport). The absorbed dose calculation step can lead to different results, ranging from mean absorbed doses to absorbed dose maps at the voxel level. The post-processing of dosimetric results (step 7), can generate further dosimetry indices, such as quantities derived from absorbed dose volume histograms, absorbed dose rates at the voxel or organ level. Also of interest is the possibility to generate radiobiological indices such as the biologically effective dose (BED), or equivalent uniform BED (EUBED, etc.), as presented in Chapter 8.

The overall uncertainty in the estimated absorbed dose is conditioned by the uncertainty introduced in each step (Chapter 9). Since not all clinical centres may have the resources to optimize all steps that compose the procedure, compromises may have to be made, impacting the accuracy of the dosimetry estimate.

Figure 11.1 presents a **generic** clinical dosimetry workflow. However, the dosimetry procedure is always conditioned by a clinical objective, and therefore cannot be dissociated from the rationale that motivates the dosimetry study.

As can be seen in Chapter 10, depending on the clinical end point, different dosimetry protocols can be implemented, although dosimetry is not always taken into account when planning radiopharmaceutical therapy (RPT). Depending on **when** dosimetry is implemented in the therapeutic workflow it may not immediately impact patient therapy management but could be used for verification purposes.

11.1. CURRENT STATUS OF DOSIMETRY IN CLINICAL PRACTICE

The role and relevance of dosimetry in clinical practice is still a matter of debate [11.8–11.10]. The current situation of RPT is most often that of a '**radioactive chemotherapy**'. Typically, the administered activity is fixed ('one size fits all') or modulated by patient mass or body surface area (BSA). The maximum tolerated activity (maximum tolerated dose (MTD) — where 'dose' here means the quantity of the drug administered) is determined during clinical trials, where patients who are often pretreated and who can thus be more susceptible to toxicity are included to establish administered activity/dosing limits for all. The observation period between subsequent (activity) dose-escalation steps is in most cases limited to one or two months and total follow-up to one year, to keep clinical trials within a reasonable time frame. Therefore, since the maximum tolerated activity/dose will be based on mostly acute toxicity end

points, late toxicity end points such as radiation-induced kidney damage could easily be missed.

This **radioactive chemotherapy** approach neglects inter-patient pharmacokinetic variability. In addition, an advantage of RPT as opposed to chemotherapy is that it is most often possible to monitor the fate of the radioactive administered drug via scintigraphic imaging, blood counting or other means, and therefore assess the absorbed dose delivered to the tumour and to absorbed dose-limiting tissues in the patient. The possibility of dosimetry opens the rationale for considering RPT as a form of **radiotherapy**. This implies that monitoring the delivered absorbed dose (clinical dosimetry) is of importance to personalize and optimize the treatment.

This was expressed in 2007 by Stabin and Brill [11.11]:

> "patients given radiopharmaceuticals for therapy deserve the same individualized attention and optimization of their radiation therapy as do patients treated with external sources of radiation, which has been undergoing constant improvement for decades".

This parallel with external beam radiation therapy (EBRT) is both appealing and misleading. On the one hand, RPT should learn from the decades of experience in EBRT, involving research on absorbed dose–effect studies and routine implementation of dosimetry and treatment planning. On the other hand, the dissimilarities between the two modalities need to be considered, such as the non-uniform absorbed dose distributions in RPT, including at the microscale level, and the vastly different absorbed dose rates that in RPT are also time dependent. Moreover, knowledge on dose–effect relationships in RPT is still scarce, thus limiting the possibility to plan for a specific therapeutic effect. The reason for this scarce knowledge is the current lack of clinical research studies in RPT that include dosimetry.

11.2. ABSORBED DOSE–EFFECT RELATIONSHIP

Among the justifications given for **not** implementing clinical dosimetry is that the absorbed dose alone may not be a good predictor of the effect in RPT. This really points at the need, for the physicist, to go beyond the calculation of the absorbed dose and to consider the clinical end point. Sgouros stressed this in 2007 [11.12]: "The objective of dosimetry in targeted radionuclide therapy is to provide information that will help improve patient care. With this objective, estimated absorbed dose is useful to the extent that it relates to response". With

that in mind, a major objective of ongoing clinical dosimetry studies is to put in evidence the **absorbed dose–effect relationship**.

In 2004, the Radionuclide Therapy Committee of the European Association of Nuclear Medicine (EANM) published an article entitled Clinical radionuclide therapy dosimetry: The quest for the "Holy Gray" [11.13]. The conclusions were that "[d]ata in the literature which underscore the potential of dosimetry to avoid under- and overdosing and to standardise radionuclide therapy methods internationally are very scarce".

Afterwards, the Dosimetry Committee of the EANM performed a bibliographic search on the use and achievements of clinical dosimetry in terms of relationships of absorbed dose vs effect [11.14]. The conclusions were that "the evidence strongly implies a correlation between the absorbed doses delivered and the response and toxicity, indicating that dosimetry-based personalized treatments would improve outcome and increase survival".

This demonstrates an important evolution in a decade, but also highlights remaining challenges that must be overcome to establish clinical dosimetry as an accepted companion to RPT.

For decades, physicists have been focusing on improving clinical dosimetry. This means improving and standardizing quantification of activity, assessment of time integrated activity and radiation transport calculations. However, a major aspect of dose–effect assessment is related to the definition and appraisal of the clinical effect.

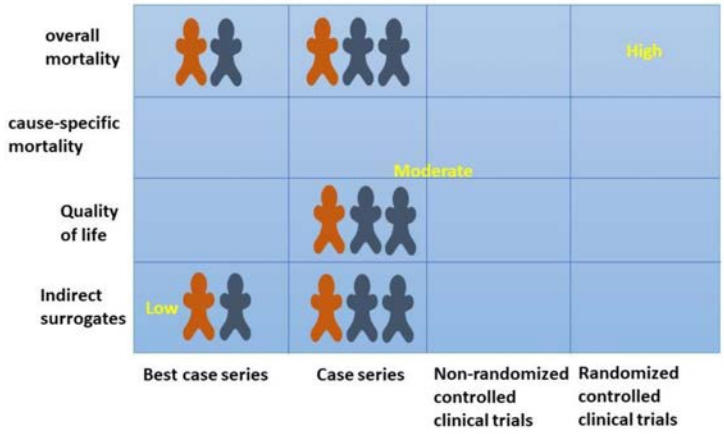

FIG. 11.2. Clinical relevance (indicated as low moderate high) according to the National Cancer Institute (NCI, USA) guidelines in absorbed dose–effect studies summarized in [11.14]. Adapted from [11.14]. For definitions see NCI [11.15].

Strigari et al. [11.14] observed that in many studies reporting absorbed dose–effect relationships, the clinical relevance was low to moderate (Fig. 11.2).

11.3. CLINICAL END POINT: EFFICACY AND TOXICITY

Dosimetry-guided treatments aiming for improved efficacy rely on the definition of a well defined target, as is the case for EBRT. However, the situation in RPT is often that of multiple, diffuse targets with variable uptake: in that context, it is difficult to prescribe a unique absorbed dose (to which representative target?). In addition, it has been shown (e.g. in radioimmunotherapy, but not only) that radiopharmaceutical uptake is relatively more important in small, residual disease, even sub-clinical and disseminated metastases, for which no volume is known (and therefore no absorbed dose can be computed). Defining a treatment based on efficacy (i.e. modulating the administered activity to deliver a given absorbed dose to the tumour) is more difficult for RPT than for EBRT. However, it has been attempted in some clinical studies, including ^{90}Y microsphere therapy aiming for an absorbed dose of >205 Gy to the lesion, while respecting absorbed dose constraints for normal liver [11.16]. For the multiple metastases in end-stage prostate cancer it was concluded that mean whole body tumour dose correlates better with biochemical response than conventional index-lesion dosimetry would do [11.17]. Whole body tumour volume was defined by Violet et al. [11.17] as all voxels with an absorbed dose >5 Gy, excluding voxels over regions with physiological uptake.

The second possibility is to base activity administration on the absorbed dose delivered to the most critical organ/tissue, and to deliver an activity that is ‘as high as safely achievable’ (AHASA) [11.18]. Basing the treatment on only avoiding toxicity, though, raises other issues. For example, available toxicity data are scarce, essentially because the design of clinical trials involves avoiding toxicity as much as possible. Most available toxicity data (i.e. toxicity thresholds in Gy) are derived from EBRT and may not necessarily apply to RPT. For therapies applied against end-stage disease, late toxicity will not be the first concern, whereas therapies in patients with longer life expectancy will need to be more conservative. Palliative therapies will be aimed to avoid acute toxicities, while reducing the tumour burden, either by volumetric reduction or by symptomatic relief.

The conclusion is that the clinical aim will condition the dosimetry protocol definition.

11.4. EXAMPLES

What follows is not meant to be a comprehensive bibliographic study of clinical dosimetry examples, but rather an attempt to point at specific aspects of clinical dosimetry that should be considered when defining a new protocol. The three examples presented highlight that clinical dosimetry protocols will have to be defined taking the end point into consideration — there will not be a unique, generic clinical dosimetry protocol.

11.4.1. Different protocols can be used for the same pathology/clinical end point

In the treatment of differentiated thyroid cancer (DTC) two studies [11.19, 11.20] proposed different ways to relate the absorbed dose to the probability of ablation success with the same clinical end point (efficacy).

To discriminate between potential thyroid remnant ablation failure and success, Verburg et al. [11.19] used the blood absorbed dose. Blood absorbed doses >350 mGy (144 patients) led to a 63.9% successful ablation rate, whereas the successful ablation rate for blood absorbed doses <350 mGy (305 patients) was 3.1%, a statistically different value ($p = 0.03$).

To assess the potential for the same biological outcome, Flux et al. [11.20] performed a voxelized absorbed dose calculation to the remnant and then used the maximum absorbed dose delivered to the remnants (i.e. to the voxel with the highest delivered absorbed dose). This required quantitative 3-D SPECT imaging (3 or 4 time points). The conclusion (based on 23 patients) was that the response depended on the maximum remnant absorbed dose: a maximum absorbed dose to the remnants of 99 ± 128 Gy led to complete ablation; 25 ± 17 Gy did not lead to remnant ablation (significant difference $p = 0.03$).

11.4.2. Very simple protocols can sometimes have a huge impact on patient management

In the treatment of neuroblastoma with ^{131}I mIBG, Buckley et al. [11.21] implemented a very simple protocol to compute the so-called whole body absorbed dose. Whole body count rate was measured with an external probe fixed into the ceiling, 2 m above the patient's bed. This simple design allowed up to 60 readings per administration. The time-integrated activity, obtained by integrating the resulting time activity curves over time, was assumed to be uniformly distributed throughout the patient's body. This provided the input needed to calculate whole body absorbed doses by adjusting the medical internal radiation dose (MIRD) S values to the specific mass of the patient. This relatively

simple approach made it possible to obtain an absorbed dose–toxicity correlation: the mean whole body absorbed dose for patients with grade 4 neutropenia after therapy was significantly higher than for those with grade 1 neutropenia (1.63 vs 0.90 Gy; $P < 0.05$). Furthermore, that very simple approach allowed for personalizing the treatment, with administered activities varying between 1.8 and 32.9 GBq.

11.4.3. Mean absorbed dose computation may not be sufficient to explain absorbed dose–effect relationships

For ^{90}Y microsphere therapy of cancer in the liver both Chiesa et al. [11.22] and Strigari et al. [11.23] presented normal tissue complication probability (NTCP) versus absorbed dose relationships for hepatic toxicity. For the study by Chiesa et al., an inflexion point at approximately 100 Gy was identified, while for the study by Strigari et al., the corresponding absorbed dose value was 50 Gy. These seemingly discordant results could possibly be explained by the different types of microspheres used in the two studies. In the study by Chiesa, glass microspheres were used with a higher specific activity (2500 Bq/sphere) thereby requiring a lower number of spheres resulting in a relatively more non-uniform distribution at the microscopic level. Meanwhile, Strigari et al. used resin microspheres (50 Bq/sphere), with a higher number of spheres administered, resulting in a more uniform distribution at the microscopic level. One conclusion may be that the mean absorbed doses may have to be higher for the glass microspheres in order to compensate for absorbed dose gradients present at the microscopic scale [11.24, 11.25].

11.5. IMPACT OF THE DOSIMETRY PROTOCOL ON THE CONCLUSIONS OF DOSE–EFFECT RELATIONSHIPS

For the same clinical end point, the implementation of the dosimetry protocol will impact the conclusion. A very interesting example is given in the context of peptide receptor radionuclide therapy (PRRT) in the article by Barone et al. [11.26]. The study considered a subset of 18 patients with neuroendocrine tumours (NETs) enrolled in a phase I multicentric study intended to establish the maximum tolerated ‘doses’ of ^{90}Y DOTATOC in patients with metastatic, somatostatin-receptor positive tumours. Absorbed doses delivered to the kidneys were evaluated before therapy through the administration of ^{86}Y DOTATOC and positron emission tomography (PET)/ computed tomography (CT) imaging at 3 time points [11.27]. The therapy was delivered in 2 to 5 cycles, and the therapeutic activity was modulated so that no patient would receive

more than 27 Gy to the kidneys. For this subset of patients, kidney toxicity was assessed by monitoring kidney function (serum creatinine and creatinine clearance) over a period of time longer than one year, as prescribed for the phase I study [11.28, 11.29].

Figure 11.3. shows the resulting dose–effect relationship with three different dosimetry approaches. Absorbed doses were initially computed using MIRDOSE 3.1, under the assumption that all patients had the same kidney volume, and differentiating between male and female patients (Fig. 11.3A). A second (retrospective) study considered the actual volume of each patient's kidney and rescaled the *S* values obtained from MIRD Pamphlet No. 19 [11.30] to a patient-specific *S* value. Moreover, the absorbed dose considered was the one to the cortex rather than that to the whole kidney (Fig. 11.3B). A third approach included radiobiological parameters (from EBRT) to derive the BED delivered to the kidney cortex (Fig. 11.3C).

The reported correlation between the loss of kidney function (toxicity) and either the kidney absorbed dose or the BED clearly demonstrates how the dosimetry protocol impacts the absorbed dose–effect relationships. In addition, from a dosimetry point of view, it also highlights how different aspects of the dosimetry chain play a role in the identification of a dose–effect relationship: even when a very sophisticated activity quantification method is used (in this case based on quantitative ^{86}Y DOTATOC PET imaging), it may not be sufficient to resolve the dose–effect relationship when the same reference *S* value is used for all patients.

Parallel to this study, phase II trials were conducted at the maximum tolerated activity of 13.3 GBq (given in 3 cycles of 4.4 GBq), the activity that was assessed to be safe based on follow-up was limited to one year. Repeated cycles of 3.7 GBq/m^2 BSA of ^{90}Y DOTATOC eventually led to 9% incidence (103 out

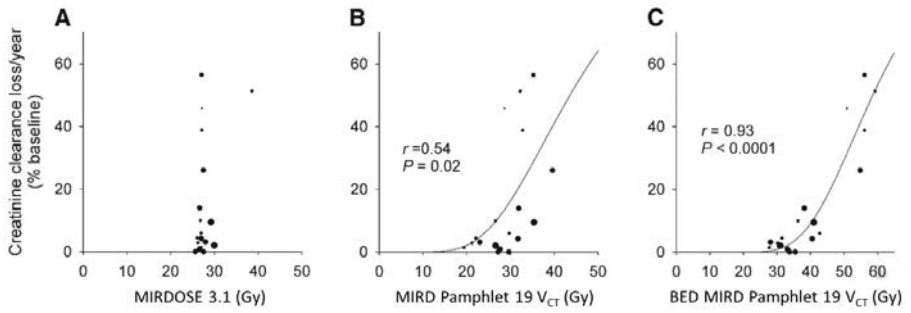

FIG. 11.3. Evolution of the dose–effect relationship according to the clinical dosimetry protocol (adapted from Barone et al. [11.26]). Reproduced with permission from Journal of Nuclear Medicine publishing.

of 1109 patients) of severe permanent or even fatal renal toxicity [11.31]. The prescription of the activity to administer based on BSA led to this devastating outcome. Even without dosimetry, radiobiological analyses could have been applied to consider that some of the prescriptions, which were as high as 6.5 GBq in 2 cycles (for a patient with 1.75 m^2 BSA), would have led to a higher BED than the maximum tolerated activity of 3 cycles of 4.4 GBq.

Other examples can be found in different clinical situations that highlight how the implementation of clinical dosimetry may impact the evidence of absorbed dose–effect relationships [11.32–11.34].

11.6. IMPLEMENTING DOSIMETRY: TREATMENT PLANNING OR THERAPY VERIFICATION?

Clinical dosimetry in a context of therapy can be performed with different aims, and this conditions how and when the dosimetry protocol will be implemented:

11.6.1. Dosimetry for treatment planning

If absorbed dose–effect relationships have been demonstrated for a given therapy, it is possible to use those results to optimize the therapy prescription.

The first scenario that can be qualified for treatment planning considers pre-therapeutic dosimetry. A rationale for pre-therapeutic dosimetry is to set a go/no-go checkpoint for the therapeutic administration (i.e. to assess if the patient will benefit from the therapy or if an alternative therapeutic modality must be considered). In addition, **pre-therapeutic dosimetry** can be performed with the aim of defining the therapeutic activity to administer to the patient. This relies on the a priori knowledge of absorbed dose thresholds for efficacy or toxicity. Pre-therapeutic dosimetry involves a tracer (low activity) administration of the same or a surrogate radiopharmaceutical before the actual treatment. A major assumption is that the uptake will scale linearly with the administered activity and that the tracer administration will not modify the pharmacokinetics of the radiopharmaceutical during the therapeutic phase (e.g. stunning effect for ^{131}I therapy of thyroid diseases, induction of human anti-mouse antibodies in radioimmunotherapy, biodistribution differences due to different fraction of radiolabelled vs unlabelled peptides) [11.35].

Pre-therapeutic dosimetry may allow the modulation of the therapeutic administration, and therefore can be considered treatment planning — that is, providing information to the clinicians that can help them identify and prescribe an administered activity that accounts for individual patient parameters.

However, pre-therapeutic dosimetry requires an additional administration of the radiopharmaceutical (albeit with a reduced activity), additional scans, additional patient visits in the medical centre and the like. This is sometimes considered too demanding (for the patient or for the clinic) and is not necessarily implemented in routine clinical practice.

The second scenario is to deliver the therapy sequentially. This relatively recent approach is implemented in a context of repeated therapies (i.e. when the radiopharmaceutical is administered in cycles separated by several weeks, as it is done for chemotherapy). In this case, the first administration is usually based on a fixed activity (or activity modulated by patient weight, BSA or clinical factors such as kidney function). Dosimetry is then performed in order to calculate the absorbed dose resulting from the first administration fraction to several tissues of interest (critical organs/tissues or tumours), with the aim of personalizing further therapeutic administrations. This relies on a priori knowledge of absorbed dose thresholds (or dosimetry indices derived from the absorbed dose) in order to guide clinicians in their decision. Giving a therapeutic absorbed dose of a radiopharmaceutical in multiple fractions might change its toxicity profile due to radiobiological fractionation effects, similar to what happens in EBRT.

Another required assumption is that the biokinetics of the radiopharmaceutical in organs/tissues within the patient will not vary from one cycle to another. A good example of this approach is that of ^{131}I mIBG therapy of neuroblastoma where the second administration is modulated in order to maintain the whole body absorbed dose below 2 or 4 Gy [11.21].

PRRT treatment is another example of where this concept has been applied. The treatment is normally administered in 4 fractions of fixed activity (7.4 GBq). However, Sundlöv et al. [11.36] demonstrated that, based on the BED delivered to the kidneys, activity administered could be varied by a factor of 3 (3 to 8 cycles). This study provides a very good insight on intra- and inter-patient pharmacokinetics variability.

Dosimetry based multiple-cycle treatments represent a possibility to reduce the extra workload associated with pre-therapeutic dosimetry as there is no need for extra administration of the radiopharmaceutical, or additional measurements, while preserving the possibility to modulate the prescription.

11.6.2. Dosimetry for therapy verification

Dosimetry can be performed after a therapeutic administration for verification of the absorbed doses and to document the therapy delivered. In this context, the approach helps in assessing thresholds of efficacy/toxicity based on data acquired after the therapeutic administration is delivered. Dosimetry performed after therapeutic administration of radiopharmaceuticals may suffer from radiation

safety issues, which may limit data (image) acquisition to times when the patient can return for scanning without excessive exposure of the medical personnel. Additionally, the dead time of gamma cameras may be an issue, thereby limiting the access to early time points. This type of approach is usually performed when no re-treatment is possible/planned, and/or when the next therapy administration is after six months or more. For instance, in the case of thyroid cancer treatment, iodine administration is planned after six months or every year (according to the physician's judgement), therefore every administration can be considered a new one, and the clinical condition of the patient may differ from that of the previous treatment. In other words, the dosimetry performed is not used to assess the activity to administer to a patient. One may argue that post-therapeutic dosimetry has no direct benefit for the patient. However, in a context where radiation damage is supposed to increase during the patient's lifetime, documenting the procedure is a means to allow for further irradiation if needed (i.e. EBRT, or further

TABLE 11.1. DIFFERENT CHARACTERISTICS OF THERAPEUTIC DOSIMETRY

(courtesy of M. Bardiès)

	Treatment planning		Therapy verification
	Pre-therapeutic dosimetry Scenario 1	Dosimetry for repeated cycles Scenario 2	Post-therapeutic dosimetry
Requires tracer activity and additional measurements	YES	NO	NO
May be impacted by high activity at early time points	NO	YES	YES
Requires therapy cycles	NO	YES	NO
Requires preliminary knowledge of the relevant dosimetry or radiobiologic index	YES	YES	NO
Allows treatment stratification	YES	YES	NO
Suffers potentially from altered biokinetics	YES	YES	NO

administration of the radiopharmaceutical long after the first cycles, as can be the case in DTC therapy). This type of approach is becoming more and more useful with the increasing survival of patients.

The main characteristics of each approach are summarized in Table 11.1.

11.7. CLINICAL TRIALS

The need for rigorous, consistent, well validated and accurate dosimetry is perhaps greatest in the context of early phase trial evaluation of a novel therapeutic radiopharmaceutical. This is also the context in which pharmaceutical developers are most amenable to incorporating exploratory (secondary) end points in the trial design. In recent trial designs, the exploratory end points are typically related to biomarker and gene expression investigations that can help identify, a priori, the patient population most likely to benefit from the investigational agent. To a substantial extent, radionuclide dosimetry serves the same purpose — identifying patients most likely to experience toxicity or to demonstrate an objective tumour response — for RPT. Since the results obtained at this stage will influence how dosimetry is implemented in subsequent studies, it is particularly important that the dosimetry implemented is well validated and accurate. Although standardization is always important, it is especially so if the trial is conducted across multiple centres. Almost all discussions on how to incorporate dosimetry begin with a negotiation: the trial principal investigator wants to minimize the logistics and expense associated with additional imaging and other dosimetry related procedures, while the physicist is focused on obtaining a dataset that will provide the most accurate dosimetry possible. A compromise that is too accommodating to the concerns of any one party will lead to an outcome that serves neither over the long term. For example, too few imaging time points or activity quantification that is expedient but not well validated will lead to inaccurate dosimetry estimates and a failure to adequately evaluate the potential utility of dosimetry. Over the long term, this will preclude dosimetry incorporation from either identifying patients more likely to benefit from the treatment or optimizing the treatment to benefit the greatest patient population. Likewise, a procedure that is too involved and burdensome for the patient will lead to reduced patient compliance and accrual. In general, the dosimetry and pharmacokinetic data collected during early phase trial evaluation of a new agent should be sufficient to make it possible to evaluate simpler alternatives that could be implemented routinely.

11.8. CONCLUSIONS

There is no unique way to implement clinical dosimetry and the required equipment and tools can vary. In addition, the absorbed dose alone may not be sufficient to characterize a given biologic response and radiobiology input is needed.

Therefore, a 'reference' or 'generic' clinical dosimetry protocol adapted to all situations is not realistic/feasible. There are some situations where clinical dosimetry that impacts a patient's management is simple. In some other instances, very refined approaches are required. At this stage, it is essential to document the dosimetry approach in the best possible way, to increase the reproducibility/robustness of presented results [11.2].

There is substantial evidence that dosimetry can be used as a 'biomarker of response'. Absorbed dose–effect relationships have been obtained in many cases when a sound methodology was implemented that considered not only the absorbed dose but also the clinical/biological end point assessments.

REFERENCES

[11.1] GEAR, J.I., et al., EANM practical guidance on uncertainty analysis for molecular radiotherapy absorbed dose calculations, Eur. J. Nucl. Med. Mol. Imaging **45** 13 (2018) 2456–2474, https://doi.org/10.1007/s00259-018-4136-7

[11.2] LASSMANN, M., CHIESA, C., FLUX, G., BARDIÈS, M., EANM DOSIMETRY COMMITTEE, EANM Dosimetry Committee guidance document: Good practice of clinical dosimetry reporting, Eur. J. Nucl. Med. Mol. Imaging **38** 1 (2011) 192–200, https://doi.org/10.1007/s00259-010-1549-3

[11.3] LJUNGBERG, M., et al., MIRD Pamphlet No. 26: Joint EANM/MIRD guidelines for quantitative ^{177}Lu SPECT applied for dosimetry of radiopharmaceutical therapy, J. Nucl. Med. **57** 1 (2016) 151–162, https://doi.org/10.2967/jnumed.115.159012

[11.4] DEWARAJA, Y.K., LJUNGBERG, M., GREEN, A.J., ZANCONICO, P.B., FREY, E.C., MIRD Pamphlet No. 24: Guidelines for quantitative ^{131}I SPECT in dosimetry applications, J. Nucl. Med. **54** 12 (2013) 2182–2188, https://doi.org/10.2967/jnumed.113.122390

[11.5] DEWARAJA, Y.K., et al., MIRD Pamphlet No. 23: Quantitative SPECT for patient-specific 3-dimensional dosimetry in internal radionuclide therapy, J. Nucl. Med. **53** 8 (2012) 1310–1325, https://doi.org/10.2967/jnumed.111.100123

[11.6] LASSMANN, M., et al., EANM Dosimetry Committee series on standard operational procedures for pre-therapeutic dosimetry I: Blood and bone marrow dosimetry in differentiated thyroid cancer therapy, Eur. J. Nucl. Med. Mol. Imaging **35** 7 (2008) 1405–1412, https://doi.org/10.1007/s00259-008-0761-x

[11.7] HÄNSCHEID, H., et al., EANM Dosimetry Committee series on standard operational procedures for pre-therapeutic dosimetry II. Dosimetry prior to radioiodine therapy of benign thyroid diseases, Eur. J. Nucl. Med. Mol. Imaging **40** 7 (2013) 1126–1134, https://doi.org/10.1007/s00259-013-2387-x

[11.8] CHIESA, C., et al., The conflict between treatment optimization and registration of radiopharmaceuticals with fixed activity posology in oncological nuclear medicine therapy, Eur. J. Nucl. Med. Mol. Imaging **44** 11 (2017) 1783–1786, https://doi.org/10.1007/s00259-017-3707-3

[11.9] GIAMMARILE, F., et al., Dosimetry in clinical radionuclide therapy: The devil is in the detail, Eur. J. Nucl. Med. Mol. Imaging **44** 12 (2017) 2137–2139, https://doi.org/10.1007/s00259-017-3820-3

[11.10] FLUX, G.D., et al., From fixed activities to personalized treatments in radionuclide therapy: Lost in translation? Eur. J. Nucl. Med. Mol. Imaging **45** 1 (2018) 152–154, https://doi.org/10.1007/s00259-017-3859-1

[11.11] STABIN, M., BRILL, A.B., Physics applications in nuclear medicine: Carpe photon, J. Nucl. Med. **48** 2 (2007) 35N–38N.

[11.12] SGOUROS, G., Toward patient-friendly cell-level dosimetry, J. Nucl. Med. **48** 4 (2007) 496–497, https://doi.org/10.2967/jnumed.106.036749

[11.13] BRANS, B., et al., Clinical radionuclide therapy dosimetry: The quest for the "Holy Gray", Eur. J. Nucl. Med. Mol. Imaging **34** 5 (2007) 772–786, https://doi.org/10.1007/s00259-006-0338-5

[11.14] STRIGARI, L., et al., The evidence base for the use of internal dosimetry in the clinical practice of molecular radiotherapy, Eur. J. Nucl. Med. Mol. Imaging **41** 10 (2014) 1976–1988, https://doi.org/10.1007/s00259-014-2824-5

[11.15] NATIONAL CANCER INSTITUTE, Levels of Evidence for Human Studies of Integrative, Alternative, and Complementary Therapies (PDQ®)–Health Professional Version, https://www.cancer.gov/publications/pdq/levels-evidence/cam

[11.16] GARIN, E., et al., Boosted selective internal radiation therapy with ^{90}Y-loaded glass microspheres (B-SIRT) for hepatocellular carcinoma patients: A new personalized promising concept, Eur. J. Nucl. Med. Mol. Imaging **40** 7 (2013) 1057–1068, https://doi.org/10.1007/s00259-013-2395-x

[11.17] VIOLET, J., et al., Dosimetry of ^{177}Lu-PSMA-617 in metastatic castration-resistant prostate cancer: Correlations between pretherapeutic imaging and whole-body tumor dosimetry with treatment outcomes, J. Nucl. Med. **60** 4 (2019) 517–523, https://doi.org/10.2967/jnumed.118.219352

[11.18] VERBURG, F.A., et al., The "reset button" revisited: Why high activity ^{131}I therapy of advanced differentiated thyroid cancer after dosimetry is advantageous for patients, Eur. J. Nucl. Med. Mol. Imaging **44** 6 (2017) 915–917, https://doi.org/10.1007/s00259-017-3649-9

[11.19] VERBURG, F.A., et al., The absorbed dose to the blood is a better predictor of ablation success than the administered ^{131}I activity in thyroid cancer patients, Eur. J. Nucl. Med. Mol. Imaging **38** 4 (2011) 673–680, https://doi.org/10.1007/s00259-010-1689-5

[11.20] FLUX, G.D., et al., A dose-effect correlation for radioiodine ablation in differentiated thyroid cancer, Eur. J. Nucl. Med. Mol. Imaging **37** 2 (2010) 270–275, https://doi.org/10.1007/s00259-009-1261-3

[11.21] BUCKLEY, S.E., CHITTENDEN, S.J., SARAN, F.H., MELLER, S.T., FLUX, G.D., Whole-body dosimetry for individualized treatment planning of ^{131}I-MIBG radionuclide therapy for neuroblastoma, J. Nucl. Med. **50** 9 (2009) 1518–1524, https://doi.org/10.2967/jnumed.109.064469

[11.22] CHIESA, C., et al., Radioembolization of hepatocarcinoma with ^{90}Y glass microspheres: Development of an individualized treatment planning strategy based on dosimetry and radiobiology, Eur. J. Nucl. Med. Mol. Imaging **42** 11 (2015) 1718–1738, https://doi.org/10.1007/s00259-015-3068-8

[11.23] STRIGARI, L., et al., Efficacy and toxicity related to treatment of hepatocellular carcinoma with ^{90}Y-SIR spheres: Radiobiologic considerations, J. Nucl. Med. **51** 9 (2010) 1377–1385, https://doi.org/10.2967/jnumed.110.075861

[11.24] D'ABADIE, P., HESSE, M., JAMAR, F., LHOMMEL, R., WALRAND, S., ^{90}Y TOF-PET based EUD reunifies patient survival prediction in resin and glass microspheres radioembolization of HCC tumours, Phys. Med. Biol. **63** 24 (2018) 245010, https://doi.org/10.1088/1361-6560/aaf205

[11.25] WALRAND, S., HESSE, M., CHIESA, C., LHOMMEL, R., JAMAR, F., The low hepatic toxicity per Gray of ^{90}y glass microspheres is linked to their transport in the arterial tree favoring a nonuniform trapping as observed in posttherapy PET imaging, J. Nucl. Med. **55** 1 (2014) 135–140, https://doi.org/10.2967/jnumed.113.126839

[11.26] BARONE, R., et al., Patient-specific dosimetry in predicting renal toxicity with ^{90}Y-DOTATOC: Relevance of kidney volume and dose rate in finding a dose-effect relationship, J. Nucl. Med. **46** Suppl. 1 (2005) 99S–106S.

[11.27] WALRAND, S., et al., Quantitation in PET using isotopes emitting prompt single gammas: Application to yttrium-86, Eur. J. Nucl. Med. Mol. Imaging **30** 3 (2003) 354–361, https://doi.org/10.1007/s00259-002-1068-y

[11.28] JAMAR, F., et al., ^{86}Y-DOTA0)-D-Phe1-Tyr3-octreotide (SMT487) — a phase 1 clinical study: Pharmacokinetics, biodistribution and renal protective effect of different regimens of amino acid co-infusion, Eur. J. Nucl. Med. Mol. Imaging **30** 4 (2003) 510–518, https://doi.org/10.1007/s00259-003-1117-1

[11.29] BUSHNELL, D., et al., Assessment of hepatic toxicity from treatment with ^{90}Y-SMT 487 (OctreoTher(TM)) in patients with diffuse somatostatin receptor positive liver metastases, Cancer Biother. Radiopharm. **18** 4 (2003) 581–588, https://doi.org/10.1089/108497803322287664

[11.30] BOUCHET, L.G., et al., MIRD Pamphlet No 19: Absorbed fractions and radionuclide S values for six age-dependent multiregion models of the kidney, J. Nucl. Med. **44** 7 (2003) 1113–1147.

[11.31] IMHOF, A., et al., Response, survival, and long-term toxicity after therapy with the radiolabeled somatostatin analogue [^{90}Y-DOTA]-TOC in metastasized neuroendocrine cancers, J. Clin. Oncol. **29** 17 (2011) 2416–2423, https://doi.org/10.1200/JCO.2010.33.7873

[11.32] FERRER, L., et al., Comparisons of dosimetric approaches for fractionated radioimmunotherapy of non-Hodgkin lymphoma, Q. J. Nucl. Med. Mol. Imaging **56** 6 (2012) 529–537.

[11.33] FERRER, L., et al., Three methods assessing red marrow dosimetry in lymphoma patients treated with radioimmunotherapy, Cancer **116** Suppl. 4 (2010) 1093–1100, https://doi.org/10.1002/cncr.24797

[11.34] DEWARAJA, Y.K., et al., 131I-tositumomab radioimmunotherapy: Initial tumor dose–response results using 3-dimensional dosimetry including radiobiologic modeling, J. Nucl. Med. **51** 7 (2010) 1155–1162, https://doi.org/10.2967/jnumed.110.075176

[11.35] KLETTING, P., et al., Investigating the effect of ligand amount and injected therapeutic activity: A simulation study for ^{177}Lu-labeled PSMA-targeting peptides, PLoS One **11** 9 (2016) e0162303, https://doi.org/10.1371/journal.pone.0162303

[11.36] SUNDLÖV, A., et al., Individualised ^{177}Lu-DOTATATE treatment of neuroendocrine tumours based on kidney dosimetry, Eur. J. Nucl. Med. Mol. Imaging **44** 9 (2017) 1480–1489, https://doi.org/10.1007/s00259-017-3678-4

DEFINITIONS

The definitions given below may not necessarily conform to definitions adopted elsewhere for international use.

deterministic effects, also called tissue reactions. Injury in a population of cells, characterized by a threshold absorbed dose and an increase in the severity of the reaction as the absorbed dose is increased further.

dosimetry. The process whereby the absorbed dose in the relevant organ or tissue is determined by one or several measurements, combined with appropriate calculations.

pharmacokinetics. The fate of externally administered substances in a living organism.

radiopharmaceutical therapy (RPT). Broadly defined as the use of unsealed radionuclides to deliver lethal radiation to tumour cells. Many RPTs are delivered systemically, although oral, intra-cavity and intra-arterial (e.g. microsphere) administrations are also employed. Also called radionuclide therapy, molecular radiotherapy, systemic radiotherapy, nuclear medicine therapy and internal emitter therapy. Other acronyms for this type of therapy include molecular radiotherapy (MRT), radioimmunotherapy (RIT), targeted radionuclide therapy (TRT) and targeted alpha therapy (TAT).

stochastic effects. The induction of malignant disease or heritable effects, where the chance of occurrence (but not the severity) is considered, for radiological protection purposes, to rise with the absorbed dose and does not have a threshold limit.

time activity curve. A parameterized mathematical function that describes the activity in the relevant tissue, as a function of time. Often the parameters are obtained by fitting a model curve to activity data, by use of a numerical method.

time activity data. Time activity data consist of a time sequence of activity values needed to calculate the absorbed dose. The sequential data can be in the format of images from an imaging device, or scalar values (e.g. activity measurements from a detector probe).

ABBREVIATIONS

ATD	anti-thyroid drug
BED	biologically effective dose
BIPM	Bureau International des Poids et Mesures
BSA	body surface area
CDR	collimator detector response
CSDA	continuous slowing down approximation
CT	computed tomography
CT-AC	CT based attenuation correction
DPK	dose point kernel
DTC	differentiated thyroid cancer
EANM	European Association of Nuclear Medicine
EBRT	external beam radiation therapy
ESSE-SC	effective source scatter estimation scatter correction
EUD	equivalent uniform dose
FBP	filtered back projection
FWHM	full width at half-maximum
GEP-NET	gastroenteropancreatic neuroendocrine tumour
GUM	Guide to the Expression of Uncertainty in Measurement
HCC	hepatocellular carcinoma
HE	high energy
ICRP	International Commission on Radiological Protection
ICRU	International Commission on Radiological Units and Measurements
LEHR	low-energy high-resolution
LET	linear energy transfer
LOR	line of response
LPU	law of propagation of uncertainty
LQ	linear–quadratic
LYSO	yttrium doped lutetium oxyorthosilicate
MAA	macroaggregated albumin
MC-SC	Monte Carlo based scatter correction
ME	medium energy
mIBG	meta-iodobenzylguanidine
MIRD	medical internal radiation dose
ML-EM	maximum-likelihood expectation-maximization
MRI	magnetic resonance imaging
MTD	maximum tolerated dose
NET	neuroendocrine tumour

OS-EM	ordered-subsets expectation-maximization
PET	positron emission tomography
PRRT	peptide receptor radionuclide therapy
PSMA	prostate-specific membrane antigen
PVC	partial volume correction
PVE	partial volume effect
RBE	relative biological effectiveness
RC	recovery coefficient
ROI	region of interest
RPT	radiopharmaceutical therapy
SPECT	single photon emission computed tomography
TAC	time activity curve
TCP	tumour control probability
TEW	triple-energy window
TEW-SC	triple-energy-window scatter correction
TOF	time-of-flight
VOI	volume of interest

CONTRIBUTORS TO DRAFTING AND REVIEW

Bardiès, M.	Cancer Research Institute of Montpellier, France
Celler, A.	University of British Columbia, Canada
Cox, M.	National Physical Laboratory, United Kingdom
Dewaraja, Y.	University of Michigan, United States of America
Gear, J.	Royal Marsden Hospital and Institute of Cancer Research, United Kingdom
Hänscheid, H.	Würzburg University, Germany
Knoll, P.	International Atomic Energy Agency
Konijnenberg, M.	Erasmus University Medical Center, Netherlands
Lassmann, M.	Würzburg University, Germany
Ljungberg, M.	Lund University, Sweden
Madsen, M.	University of Iowa, United States of America
Mora Ramirez, E.	Institute of Health and Medical Research, France
Poli, G.L.	International Atomic Energy Agency
Sgouros, G.	Johns Hopkins University, United States of America
Sjögreen-Gleisner, K.	Lund University, Sweden
Smyth, V.	National Physical Laboratory, United Kingdom
Verburg, F.A.	Würzburg University, Germany
Vergara Gil, A.	Institute of Health and Medical Research, France
Zimmerman, B.	National Institute of Standards and Technology, United States of America

Consultants Meetings

Vienna, Austria: 3–6 November 2015; 21–25 August 2017; 26–30 November 2018

IAEA
International Atomic Energy Agency

No. 26

ORDERING LOCALLY

IAEA priced publications may be purchased from the sources listed below or from major local booksellers.

Orders for unpriced publications should be made directly to the IAEA. The contact details are given at the end of this list.

NORTH AMERICA

Bernan / Rowman & Littlefield
15250 NBN Way, Blue Ridge Summit, PA 17214, USA
Telephone: +1 800 462 6420 • Fax: +1 800 338 4550
Email: orders@rowman.com • Web site: www.rowman.com/bernan

REST OF WORLD

Please contact your preferred local supplier, or our lead distributor:

Eurospan Group
Gray's Inn House
127 Clerkenwell Road
London EC1R 5DB
United Kingdom

Trade orders and enquiries:
Telephone: +44 (0)176 760 4972 • Fax: +44 (0)176 760 1640
Email: eurospan@turpin-distribution.com

Individual orders:
www.eurospanbookstore.com/iaea

For further information:
Telephone: +44 (0)207 240 0856 • Fax: +44 (0)207 379 0609
Email: info@eurospangroup.com • Web site: www.eurospangroup.com

Orders for both priced and unpriced publications may be addressed directly to:

Marketing and Sales Unit
International Atomic Energy Agency
Vienna International Centre, PO Box 100, 1400 Vienna, Austria
Telephone: +43 1 2600 22529 or 22530 • Fax: +43 1 26007 22529
Email: sales.publications@iaea.org • Web site: www.iaea.org/publications

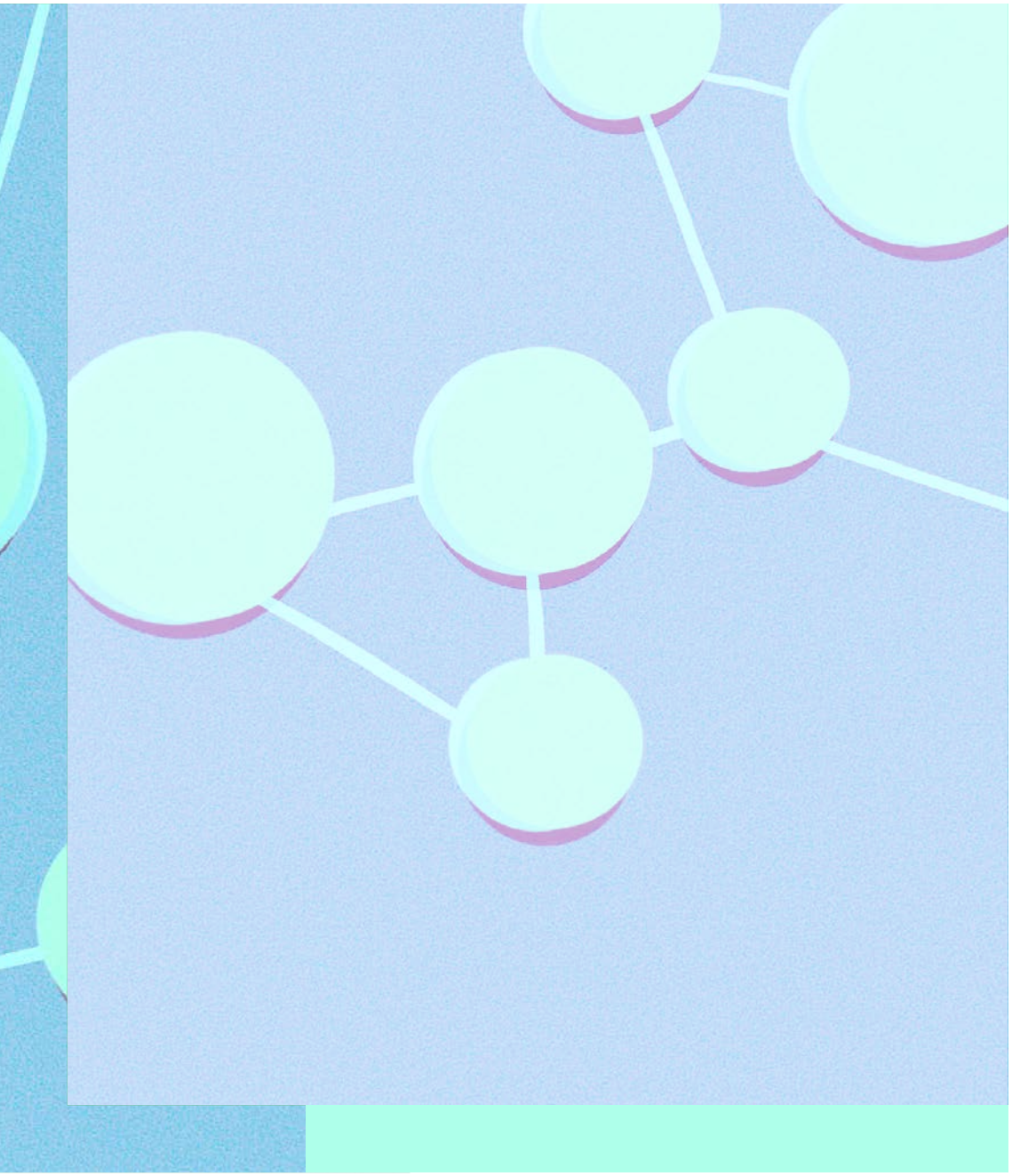

IAEA.ORG

APRIL 2024
INTERNATIONAL ATOMIC ENERGY AGENCY, VIENNA